UNIVERSIDAD NACIONAL AUTÓNOMA DE MÉXICO

DOCTORADO EN CIENCIAS BIOMÉDICAS

FACULTAD DE MEDICINA

ESTUDIO DEL ACOPLAMIENTO ELECTROMECÁNICO EN CANALES DE POTASIO DEPENDIENTES DE VOLTAJE CON COMPUESTOS DE RUTENIO

TESIS QUE PRESENTA:

ANDRÉS JARA OSEGUERA

PARA OBTENER EL GRADO DE:

DOCTOR EN CIENCIAS

TUTOR DE TESIS:

DR. LEÓN DAVID ISLAS SUÁREZ

Facultad de Medicina, UNAM

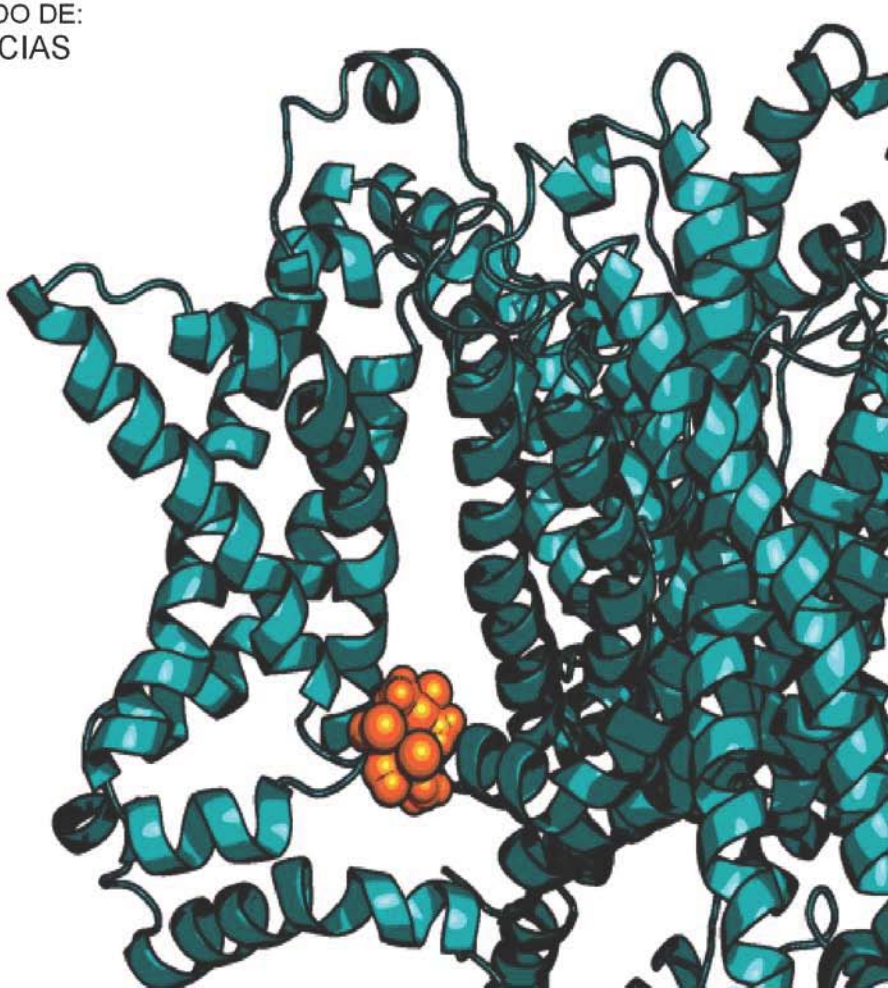

México, D.F., 2012.

UNIVERSIDAD NACIONAL AUTÓNOMA DE MÉXICO

FACULTAD DE MEDICINA

PROGRAMA DE DOCTORADO EN CIENCIAS BIOMÉDICAS

ESTUDIO DEL ACOPLAMIENTO ELECTROMECÁNICO EN CANALES DE POTASIO DEPENDIENTES DE VOLTAJE CON COMPUESTOS DE RUTENIO

TESIS QUE PRESENTA:

ANDRÉS JARA OSEGUERA

PARA OBTENER EL GRADO DE:

DOCTOR EN CIENCIAS

TUTOR DE TESIS:

DR. LEÓN DAVID ISLAS SUÁREZ

FACULTAD DE MEDICINA

AGRADECIMIENTOS

Deseo expresar mi profundo agradecimiento al Dr. León David Islas Suárez, por todo lo que ha compartido conmigo en estos años, como tutor de doctorado y como amigo, por haberme dado las herramientas para formarme como científico y haberme enseñado cómo hacer ciencia.

También deseo agradecer a la Dra. Rosenbaum, por todo lo que me ha enseñado, por su apoyo constante y su amistad.

Agradezco también a los miembros del jurado, la Dra. Marcia Hiriart Urdanivia, el Dr. Daniel Alejandro Fernández Velasco, la Dra. Laura Escobar Pérez y el Dr. José Bargas Díaz, por sus correcciones y comentarios sobre esta tesis.

Agradezco también a los miembros de mi comité tutoral, los Drs. Froylán Gómez Lagunas y Arturo Hernández Cruz, por contribuir a mi formación académica durante todo el doctorado y al desarrollo de mi proyecto de investigación.

Al Dr. Antonmaria Minzoni Alessio, por esos seminarios de matemáticas tan interesantes en donde todos aprendimos muchas cosas.

A la Dra. Gisela Rangel Yescas y a Biol. Alejandra Llorente Gil, por su ayuda y apoyo durante el curso de mi doctorado y por su amistad.

A mis compañeros y amigos del laboratorio, Víctor de la Rosa, Eva Soto, Félix Sierra, Ernesto Ladrón de Guevara y Guillermina Ramírez.

Quiero agradecer especialmente a Itzel González Ishida, por su apoyo y ayuda en todos los aspectos, y sobre todo por compartir conmigo todo este tiempo que ha sido tan valioso para mí.

A mi mamá, María Eugenia Jara, por su apoyo y cariño en todo momento,. A Enrique Fragoso, por su cariño y por todo lo que ha hecho por mí. Muchas

gracias. A mi hermana María Fragoso, muchas gracias tambien. A mis abuelos María Eugenia Oseguera y Mauricio Jara, y a mis tíos Susana Jara, Mauricio Jara, e Itele López Vega, a Carlos Fragoso y Guadalupe Fragoso, muchas gracias también.

Quiero agradecer también a mis amigos, Héctor Salazar, Christian Camacho, Santiago Cendejas, Francisco Ohem, Paul Walther, Silvina Romero, Enrique Hernández y Gaby Michel.

Este trabajo se realizó con ayuda de los donativos del Consejo Nacional de Ciencia y Tecnología (48990), de la Dirección General de Asuntos del Personal Académico-PAPIIT (IN209209) y del Instituto de Ciencia y Tecnología del Distrito Federal (PIFUTP09-262) otorgados al Dr. León David Islas Suárez.

Andrés Jara Oseguera recibió beca de doctorado de CONACyT (No. De becario 268254) por el período de agosto de 2008 a julio de 2011 y de la Coordinación de Estudios de Posgrado de la Universidad Nacional Autónoma de México por el período de agosto de 2011 a agosto de 2012.

1. ÍNDICE

2.1. RESUMEN

La apertura y cierre dependientes del voltaje de los canales iónicos es la base molecular de la actividad eléctrica en las células excitables. Esta actividad de los canales en función del potencial transmembranal depende de la acción concertada de dos regiones presentes en estas proteínas: el dominio sensor de voltaje, el cual interacciona directamente con el campo eléctrico transmembranal y sufre cambios conformacionales en función del voltaje, y el dominio del poro, el cual controla la apertura y cierre de la vía de conducción iónica. Ambos dominios constituyen unidades capaces de funcionar independientemente, sin embargo se encuentran fuertemente acoplados en este tipo de proteínas. El mecanismo mediante el cual el dominio sensor de voltaje controla la apertura o cierre del poro en función del voltaje se llama acoplamiento electromecánico.

A pesar de su importancia para la función de los canales iónicos activados por voltaje, y sus implicaciones para la fisiología celular, se sabe poco del mecanismo molecular subyacente al acoplamiento electromecánico. En este trabajo se encontró que una molécula liberadora de monóxido de carbono, el dímero de tricarbonil-dicloro rutenio o CORM-2 (*Carbon Monoxide Releasing Molecule – 2*), es un inhibidor alostérico de los canales de potasio dependientes de voltaje Kv2.1 y *Shaker*. Esta inhibición depende de la molécula del compuesto, y no del gas que libera. También se encontró que el CORM-2 interfiere con el mecanismo de acoplamiento electromecánico en estos canales, al afectar considerablemente las transiciones de apertura y cierre del canal sin tener un efecto tan grande sobre el movimiento de carga que refleja la actividad de los sensores de voltaje. Finalmente, se identificó un posible sitio de unión del CORM-2 localizado en la interfase entre el poro del canal y los dominios sensores de voltaje, precisamente en la región responsable del acoplamiento electromecánico.

Los datos obtenidos indican que el CORM-2 puede resultar una herramienta útil para estudiar el mecanismo de acoplamiento en los canales activados por voltaje, además de demostrar que una de las moléculas liberadoras de

monóxido de carbono más utilizadas en la investigación puede tener efectos importantes secundarios al gas que libera.

2.2. ABSTRACT

The voltage-dependent opening and closing of ion channels underlies the electrical activity of excitable cells. The control of ionic conductivity by voltage depends on the concerted action of two different domains within the protein: the voltage-sensing domain (VSD), which directly interacts with the transmembrane electric field, and the pore domain, which opens and closes the ion conduction pathway. The mechanism by which the two domains are strongly coupled in these proteins is termed electromechanical coupling, and its molecular basis is not fully understood.

Here, by using a combination of electrophysiological recordings and molecular biology, we found that the carbon monoxide-releasing molecule 2 (CORM-2), tricarbonyl-dichlororuthenium dimer, is an allosteric inhibitor of the voltage-gated potassium channels Kv2.1 and Shaker, and that this effect is independent of the released CO. Moreover, CORM-2 interferes with the electromechanical coupling of these channels by inhibiting channel opening without largely impeding voltage-sensor movement.

Finally, we identified a possible binding site located at the interphase between the VSD and the pore, in a region that has been shown to be essential for the coupling mechanism. These results suggest that CORM-2 may be a useful tool for the study of electromechanical coupling in voltage-gated channels, and also raise awareness that CO-releasing molecules structurally related to CORM-2, which are widely used in research and are beginning to be used in the pharmaceutical industry, could have serious secondary effects.

3. INTRODUCCIÓN

3.1. Transporte, membranas excitables y canales iónicos

Las células son compartimentos físicamente separados del exterior, lo que permite que la composición química del medio intracelular sea distinta a la del medio extracelular, una condición necesaria para la vida. La función de separar al interior de la célula del exterior lo cumple la membrana plasmática, una bicapa lipídica de aproximadamente 30 Å de grosor formada principalmente por fosfolípidos anfipáticos. El carácter anfipático (Fig. 1) de los lípidos de la membrana tiene varias consecuencias importantes. Primero, como las interacciones entre las colas hidrofóbicas de los lípidos son, en general, interacciones débiles, la movilidad de los lípidos y demás elementos de la membrana dentro del plano de la misma es muy alta, similar a la de moléculas dentro de un fluido (Vereb et al., 2003). Segundo, las cabezas hidrofílicas de los lípidos en ambas caras de la membrana interaccionan favorablemente con el agua, lo que permite la formación espontánea de dos compartimentos acuosos cuando una bicapa lipídica de este tipo es expuesta a una solución acuosa (Fig. 1). Finalmente, el carácter hidrofóbico del interior de la bicapa reduce significativamente su permeabilidad para solutos cargados o polares.

La existencia de una barrera física en la célula que permita tener una composición química intracelular distinta de la extracelular es esencial. Sin embargo, el intercambio de solutos también es necesario para la célula, y puede ocurrir por medio de diversos mecanismos. Por un lado, las moléculas de gas, como el oxígeno y el dióxido de carbono, además de otras moléculas hidrofóbicas como lípidos, pueden difundir libremente a través de la membrana plasmática, siempre a favor de su gradiente químico. Otros solutos como los azúcares, iones y otras moléculas polares o cargadas que permean muy pobremente a través de la membrana, pueden ser transportados por proteínas trasportadoras a favor de su gradiente químico. Algunos de estos transportadores acoplan reacciones altamente energéticas, como la hidrólisis de trifosfato de adenosina (ATP), con cambios conformacionales que permiten

la transferencia del soluto de un lado de la membrana a otro en contra de su gradiente químico (Dahl et al., 2004).

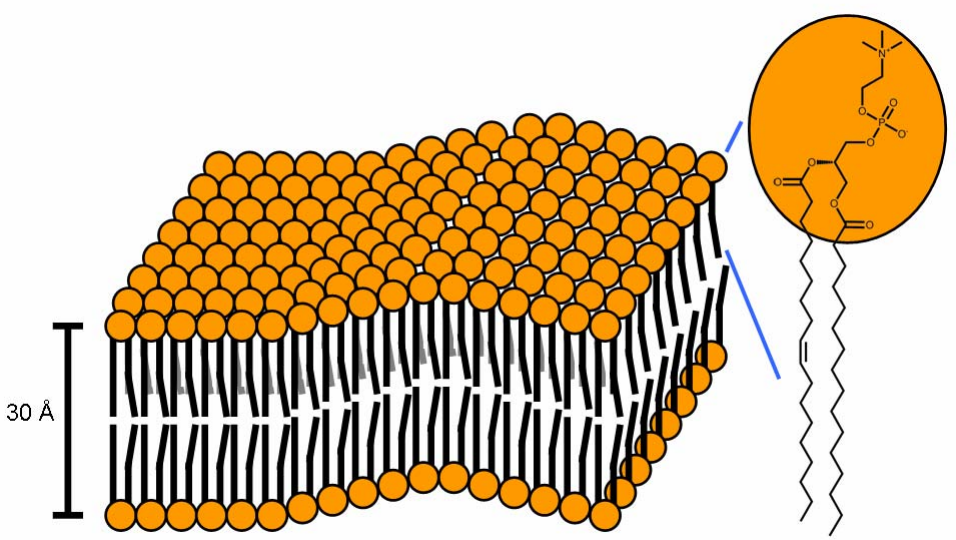

Figura 1. Esquema de una bicapa lipídica. La naturaleza anfipática de los lípidos que constituyen la membrana permite que las cabezas polares (círculos amarillos) estén favorablemente expuestas al agua en ambas caras de la bicapa, mientras que las colas hidrofóbicas se ocultan del agua en el interior de la bicapa. Cerca del 50% en masa de la membrana plasmática celular está constituida por proteínas, las cuales no se muestran en el esquema. De los lípidos en la membrana, los más abundantes son los fosfolípidos, aunque también hay cantidades importantes de colesterol y glucolípidos en la monocapa externa. En la figura se muestra un esquema de la fosfatidilcolina, uno de los fosfolípidos más abundantes en la cara externa de la membrana. El círculo amarillo indica la posición de la cabeza polar en la molécula. La composición de lípidos en la membrana varía entre tipos celulares, durante el desarrollo y entre las caras interna y externa de la bicapa.

A lo largo de la evolución, las células desarrollaron proteínas transportadoras que no son solamente capaces de almacenar energía en forma de un gradiente químico al concentrar algún soluto dentro de la célula, sino que también son capaces de transportar iones de manera asimétrica y generar un gradiente electroquímico transmembranal. Un ejemplo de esto es la bomba de sodio/potasio (Morth et al., 2011), que en cada ciclo de transporte transfiere tres iones de sodio desde interior hasta el exterior de la célula, y dos iones de potasio en la dirección opuesta (del exterior al interior). La salida de 3 iones positivos junto con la entrada de sólo 2 cationes produce una deficiencia de carga positiva en las cercanías de la cara intracelular de la membrana

plasmática (el bulto del citoplasma permanece electroneutral). Además, otro resultado es una concentración intracelular de potasio alta y extracelular baja, y una concentración intracelular de sodio baja y extracelular alta. La mayoría de las células en los mamíferos presentan este perfil de concentraciones iónicas debido a la acción de esta proteína (Glynn, 2002).

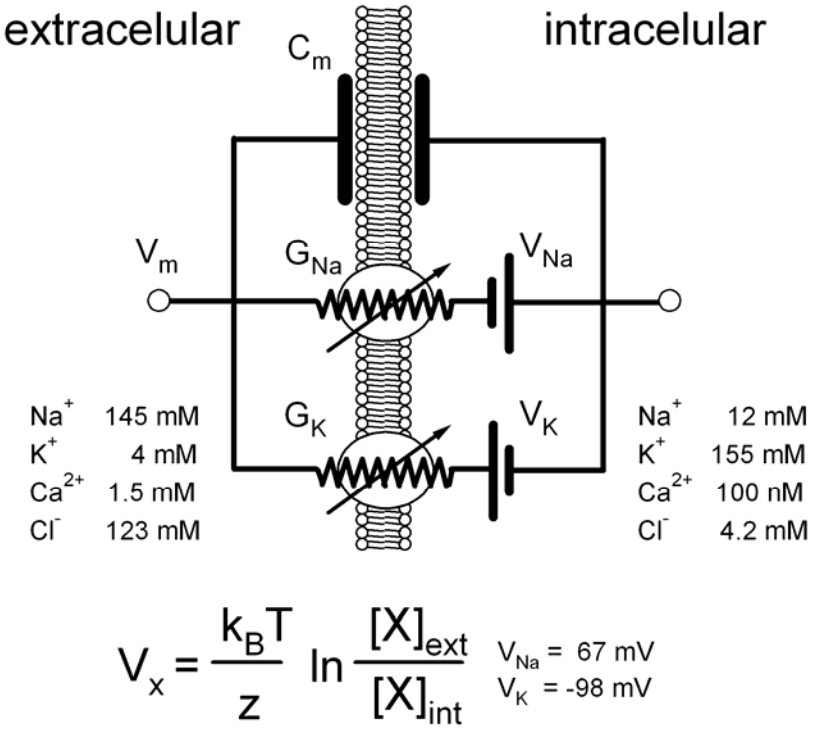

Figura 2. Esquema simplificado del circuito eléctrico equivalente a la membrana de una célula excitable. La membrana celular se considera como un capacitor con capacitancia C_m. La fuerza impulsora asociada a cada tipo de ion y debida al potencial electroquímico que se genera por el transporte activo de iones a través de la membrana, se considera como una fuente de poder con voltaje V_x, cuyo valor se obtiene de la ecuación de Nernst, mostrada en la parte inferior de la figura. En la ecuación, k_B es la constante de Boltzmann, T la temperatura absoluta, z la carga del ion y [X] es la concentración molar del ion en la solución intra- o extracelular. Las concentraciones de iones intra- y extracelulares para una típica célula de músculo liso de un mamífero se muestran en la figura, junto con los potenciales de equilibrio para el sodio (V_{Na}) y el potasio (V_K) calculados a partir de dichas concentraciones utilizando la ecuación de Nernst. Los canales iónicos se consideran como conductancias (G) modulables para cada tipo de ion, conectadas en paralelo con el capacitor de la membrana celular. El potencial transmembranal (V_m) es la diferencia en el voltaje entre los compartimentos intra- y extracelulares.

La energía almacenada por la célula en forma de un gradiente electroquímico se utiliza para el transporte de solutos y nutrientes como la glucosa, al acoplar el transporte de un ion, e.g. sodio, a favor de su gradiente electroquímico (de fuera a dentro de la célula), con el transporte del soluto en dirección opuesta a su gradiente químico, e.g. el transporte de glucosa desde el medio extracelular al intracelular (Wright et al., 2011). Pero además, la distribución asimétrica de iones tiene otras consecuencias importantes: la membrana se puede analizar como un capacitor, donde el desbalance de carga entre las soluciones que bañan directamente las caras intra- y extracelulares de la membrana plasmática genera una diferencia de potencial eléctrico (Fig. 2). Si se estableciera una vía de conducción que conectara ambas caras de la membrana, una corriente podría fluir a velocidades cercanas al límite de la difusión (electrodifusión en este caso), de un lado de la membrana al otro, hasta que se equilibre el número de cargas entre ambos compartimentos, descargando el capacitor. Esta función se lleva a cabo por proteínas transmembranales llamadas canales iónicos, los cuales forman vías de conducción iónica a través de la membrana y permiten la generación de señales eléctricas con muy alta velocidad (~ 10^7 iones fluyen cada segundo a través de un canal iónico). La elevada velocidad de conducción de los canales iónicos se contrasta con el mecanismo de transporte facilitado mediado por proteínas transportadoras, cuya velocidad es significativamente más lenta que la de los canales (~ 10^2 moléculas por segundo).

La acción de la bomba de sodio/potasio, la apertura de canales selectivos a potasio en condiciones basales (i.e. células no estimuladas) y la presencia de una gran cantidad de aniones grandes no permeables a la membrana, como proteínas, nucleótidos, etc. dentro de la célula, generan un perfil de distribución de iones específico para cada tipo celular, pero que posee ciertas características comunes a la mayoría de las células: un potencial eléctrico intracelular negativo con respecto al extracelular y que es aproximadamente igual al potencial de equilibrio del potasio (V_K) dado por la ecuación de Nernst (Fig. 2) y la asimetría antes mencionada con respecto a las concentraciones de sodio y de potasio intra- y extracelulares.

Dada la cercanía del potencial de reposo de la célula con el potencial de equilibrio del potasio (V_K, Fig. 2), la apertura de un canal de potasio (G_K) no produciría un gran efecto en el potencial de reposo. Por otro lado, si en una célula en reposo se abre una vía selectiva a sodio (G_{Na}) se generaría una corriente de sodio entrante debido a que el gradiente electroquímico transmembranal de sodio es grande cuando la célula está en reposo. Esta corriente perduraría hasta que el potencial transmembranal fuera igual al potencial de equilibrio del sodio (V_{Na}, Fig. 2). Si posteriormente se abriera una vía de conducción de potasio, se generaría una corriente entrante de potasio que, de la misma manera, perduraría hasta que el potencial transmembranal igualara al potencial de equilibrio del potasio, regresando al punto de partida. Con este ejemplo se hace evidente que la capacidad de tener vías de conducción selectivas al menos para sodio o potasio permite generar señales eléctricas rápidas con direccionalidad, dependiendo de la condición inicial del potencial transmembranal. Más aún, dada la pequeña capacitancia específica de las membranas celulares (1 μFcm^{-2}), el flujo de unas pocas cargas (~ 10^7 iones de sodio por potencial de acción en una célula esférica de 20 µm de diámetro (Carter and Bean, 2009)), comparadas con la cantidad absoluta de iones dentro y fuera de la célula, basta para generar un cambio considerable en el potencial eléctrico. Por lo tanto, la generación de las señales eléctricas no tiene un impacto significativo sobre las concentraciones de los iones dentro y fuera de la célula: el potencial químico para cada especie iónica se mantiene constante (Sten-Knudsen, 2002).

Finalmente, algunos canales iónicos tienen la propiedad de ser modulados por distintos estímulos, entre ellos el voltaje transmembranal, abriendo o cerrando la vía de conducción iónica en función del potencial eléctrico. Esta modulación dependiente del voltaje, aunada a la capacidad de algunos canales de discriminar entre la permeación de sodio o potasio (selectividad) y a la presencia de potenciales químicos opuestos para cada tipo de ion, constituyen la base de la excitabilidad eléctrica (Armstrong and Hille, 1998; Bezanilla, 2008): la apertura y cierre concertados de vías de conducción iónica (Cole and Curtis, 1939) para sodio y potasio (Hodgkin and Huxley, 1952a, b; Hodgkin and Katz, 1949) permite cambiar la polaridad del potencial transmembranal

dependiendo del tipo de canal activo en cada momento (Hodgkin and Huxley, 1952c). Este fenómeno puede propagarse por medio de perturbaciones locales en el potencial intra- y extracelular, debidas al influjo o eflujo de iones (corrientes pasivas) (Hodgkin, 1937a, b; Hodgkin and Huxley, 1952c) en las microáreas en donde hay canales activos, que a su vez impactan en la actividad de los canales iónicos vecinos. A las señales eléctricas resultantes se les denomina potenciales de acción (Bean, 2007), y son los responsables de la transmisión de los impulsos nerviosos que subyacen la actividad neural, el control motor, la percepción sensorial, etc.

Cada tipo de canal iónico dependiente de voltaje cumple un papel distinto durante la señalización eléctrica celular (Bean, 2007). Específicamente los canales de potasio participan en la "estabilización" del potencial transmembranal (Hille, 2001), ya que son los responsables de determinar el potencial de reposo de la célula, su capacidad para responder a estímulos y de repolarizar la membrana durante un potencial de acción; dependiendo de su cinética de activación, cierre e inactivación, pueden determinar la duración de un potencial de acción, la frecuencia de disparo de una neurona, la duración de una ráfaga de potenciales de acción y el espacio entre ráfagas, entre otras funciones (Bean, 2007). Además, dada su compleja modulación por moléculas que participan en la señalización intra- y extracelular (Yi et al., 2001), pueden modular la excitabilidad celular en función del estado metabólico de la célula o el tejido circundante, por ejemplo. En este contexto, se puede ver como las principales propiedades de los canales iónicos dependientes de voltaje, la selectividad y su capacidad de abrir o cerrar la vía de conducción iónica en función de los estímulos presentes, impactan directamente en la fisiología de las células excitables y los organismos que dependen de su actividad.

3.2. Canales de potasio dependientes de voltaje

3.2.1. Características generales y estructura global

Los canales de potasio se encuentran en organismos procariontes, eucariontes y archaeas, y en todos los tipos celulares en donde se han buscado. Esto sugiere que su aparición durante la evolución ocurrió relativamente temprano con respecto a los demás canales iónicos, y se piensa que constituyen el origen evolutivo de otros canales estructuralmente relacionados (Derst and Karschin, 1998; Ranganathan, 1994).

Los canales de potasio dependientes de voltaje (Kv) pertenecen a la superfamilia de canales dependientes de voltaje, a la cual también pertenecen los canales de sodio (Nav) y calcio (Cav). A esta familia pertenecen 40 genes que codifican para canales Kv en mamíferos, los cuales han sido agrupados en 12 subfamilias (Kv1 – Kv12) con propiedades biofísicas distintas (Gutman et al., 2005). No todas las subfamilias de canales Kv contienen genes que codifican para canales funcionales: la expresión de genes pertenecientes a las subfamilias Kv5, Kv6, Kv8 y Kv9 resulta en la producción de subunidades "silentes" que no forman canales funcionales por sí mismas, pero pueden asociarse con subunidades de la subfamilia Kv2 (Kv2.1 y Kv2.2) y formar canales con características funcionales distintas. Por otro lado, las subunidades pertenecientes a las subfamilias Kv1, Kv2, Kv4, Kv7 y Kv10 pueden formar heterotetrámeros entre miembros de su propia subfamilia (Gutman et al., 2005). Algunos canales pueden asociarse con subunidades accesorias que modulan su función, además de presentar empalme alternativo durante la maduración de sus mRNAs (Gutman et al., 2005), lo que multiplica su diversidad funcional. También es importante mencionar que las primeras cuatro subfamilias (Kv1 - Kv4) son ortólogas de las cuatro familias de canales de potasio inicialmente clonadas de *Drosophila melanogaster*: *Shaker*, *Shab*, *Shaw* y *Shal*, respectivamente (Chandy and Gutman, 1993). *Shaker* fue el primer gen de un canal Kv cuya secuencia fue determinada para ser clonado (Baumann et al., 1988; Kamb et al., 1988; Papazian et al., 1987; Tempel et al., 1987), por lo que ha sido estudiado más extensamente y actualmente constituye el modelo de

estudio predilecto para comprender los mecanismos de funcionamientos de estas proteínas. Sin embargo, en términos generales, tanto los mecanismos moleculares que gobiernan la función de *Shaker*, como sus correlatos estructurales, especialmente en el poro y el dominio sensor de voltaje, parecen estar conservados en los demás canales Kv (Alabi et al., 2007; Lee et al., 2009; Lu et al., 2001; MacKinnon et al., 1998; Magidovich and Yifrach, 2004).

Los canales Kv funcionales son proteínas tetraméricas (Long et al., 2005a; MacKinnon, 1991) (Fig. 3A y B) cuyas subunidades están constituidas por un dominio transmembranal y dos dominios intracelulares que corresponden con los extremos amino- y carboxilo-terminales. El dominio transmembranal, a su vez, está formado por seis segmentos transmembranales (S1-S6) alfa-helicoidales (Fig. 3C y D), de los cuales los segmentos S1-S4 forman el sensor de voltaje, y la región que incluye los segmentos S5 y S6 forma el dominio del poro del canal, como se puede observar en un modelo estructural del canal Kv1.2 (Fig. 3) (Khalili-Araghi et al., 2010) obtenido mediante dinámica molecular a partir de la estructura del canal en el estado abierto determinada por difracción de rayos X (Long et al., 2005a).

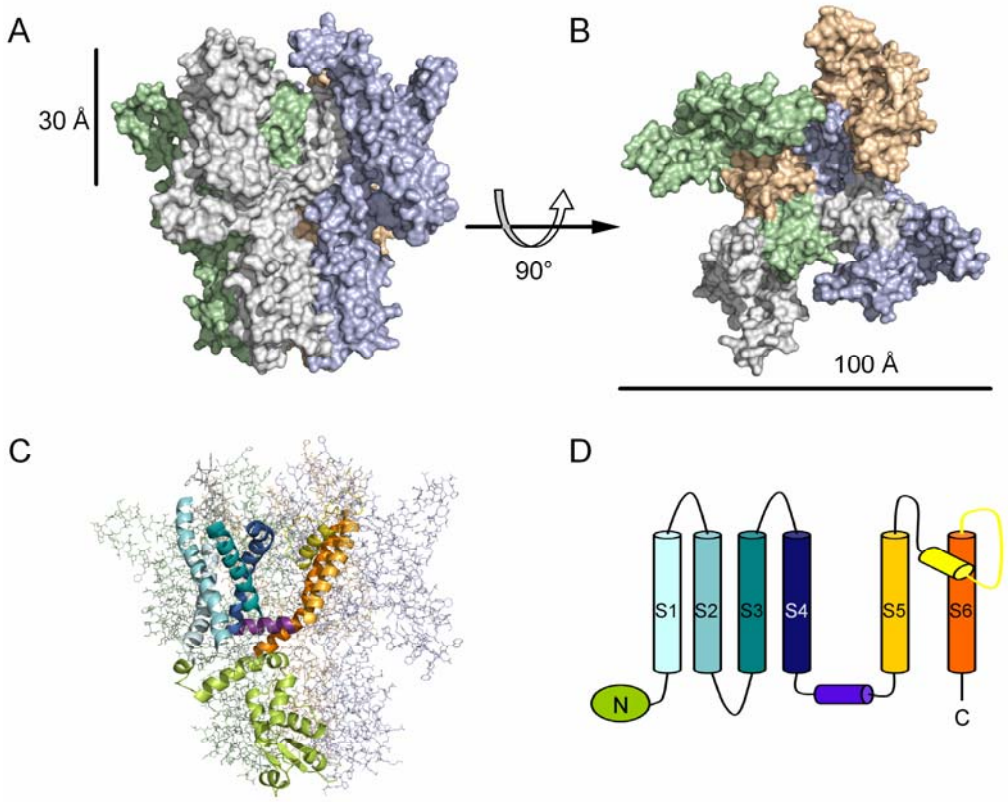

Figura 3. Esquema de la estructura cuaternaria del canal Kv1.2. (A) Vista de lado del canal Kv1.2, con cada subunidad mostrada de un color distinto. La subunidad beta asociada al dominio T1 se excluyó de la figura. La longitud (30 Å) del dominio transmembranal del canal se indica en la figura, y corresponde con el ancho de la membrana plasmática. La "góndola" intracelular con el dominio T1 N-terminal se encuentra localizada debajo del dominio transmembranal. (B) Vista de la cara extracelular del canal, donde se observa la simetría del tetrámero. El dominio sensor de voltaje de cada subunidad, localizado en la periferia, es adyacente al dominio del poro de la subunidad vecina. (C) Vista en listones de los segmentos transmembranales de una de las subunidades del canal. La estructura del resto de las subunidades se muestra en líneas. El dominio T1 está en verde, el dominio sensor de voltaje en azul, el asa de unión entre los segmentos S4-S5 en morado, el segmento S5 en naranja claro, la hélice del poro y el filtro de selectividad en amarillo y el S6 en naranja. Las asas que conectan cada uno de los segmentos, con excepción del asa S4-S5, se muestran en gris. (D) Esquema de los segmentos transmembranales de una subunidad de un canal de potasio representados como cilindros, con los mismos colores que en (C). La cara extracelular corresponde a la porción superior del esquema, y la inferior corresponde con la cara intracelular del canal. La hélice del poro y el asa S4-S5 se representan como cilindros debido a su estructura alfa-helicoidal. La torreta extracelular conecta el segmento S5 con la hélice del poro. Las figuras (A-C) fueron hechas en Pymol a partir de las estructuras reportadas en (Khalili-Araghi et al., 2010), las cuales se obtuvieron mediante dinámica molecular utilizando la estructura del canal Kv1.2 (pdb 2A79).

La región citosólica de los canales Kv es altamente variable, tanto en tamaño como en sus funciones. Por ejemplo, algunos canales de la familia de *Shaker* y Kv1 poseen una región en el amino-terminal (a.a. 6 – 46) que actúa como un bloqueador del poro una vez que éste se ha abierto, lo que resulta en la inactivación rápida del canal (Hoshi et al., 1990). Un dominio que contribuye a la tetramerización de los canales Kv, el dominio T1, también se encuentra en el extremo amino-terminal (Fig. 3A y C). Se ha demostrado que los dominios T1 de cada subunidad se asocian formando una estructura tetramérica que le da estabilidad a la estructura cuaternaria del canal (Gulbis et al., 2000; Kreusch et al., 1998; Long et al., 2005a), además de determinar la selectividad de la asociación de algunas subunidades con respecto a la formación de heterómeros (Mederos et al., 2009). Cabe mencionar que aunque esta región es importante para la tetramerización de los canales, no es esencial (Kobertz and Miller, 1999), y se ha demostrado que otras regiones, incluyendo algunos segmentos transmembranales, también contribuyen a la formación de la estructura cuaternaria funcional de estos canales (Sheng et al., 1997; Tu et al., 1996).

Los dominios T1 en el tetrámero se encuentran próximos al dominio transmembranal, y forman una estructura intracelular de “góndola” que por medio de conductos con carga neta negativa localizados en la región que une a la góndola con el dominio transmembranal del canal, permite el acceso de iones y moléculas mayores, como el dominio N-terminal de inactivación, al interior del poro (Kobertz et al., 2000; Long et al., 2005a). Además de mediar la tetramerización del canal, el dominio T1 provee una superficie de unión para subunidades moduladoras, como las subunidades β pertenecientes a la superfamilia de aldo-ceto reductasas que tienen actividad catalítica (Tipparaju et al., 2008) y que se encuentran asociadas con la mayoría de estos canales (Nakahira et al., 1996). Estas subunidades participan en el tráfico de los canales a la membrana (Campomanes et al., 2002), en la modulación de la inactivación de algunos canales en función del estado de óxido-reducción de la célula (Bahring et al., 2001; Weng et al., 2006) y quizás en otros procesos aún desconocidos.

Al eliminar los segmentos C-terminales de la estructura los canales mantienen su funcionalidad, aunque alterada (Mohapatra et al., 2008). A pesar de que no son esenciales, estas regiones juegan un papel importante en la modulación de la función de algunos canales, como hERG y Kv2.1 (Wray, 2009), y se ha propuesto que en éste último, los extremos N- y C-terminal interactúan en función de la actividad de compuerta del canal y participan directamente en el mecanismo de apertura y cierre (Kobrinsky et al., 2006). Llama la atención que el canal Kv2.1 tiene al menos 16 sitios de fosforilación localizados en el extremo C-terminal, los cuales determinan el voltaje medio de activación en función del estado fosforilado/defosforilado de cada uno de los sitios (Park et al., 2006) mediante un mecanismo que requiere una interacción entre los extremos N- y C-terminales (Mohapatra et al., 2008). Más aún, el extremo C-terminal determina la formación de cúmulos de este canal en la membrana (Mohapatra and Trimmer, 2006). La transferencia de la región C-terminal del Kv2.1 a otros canales Kv es suficiente para conferirle al canal aceptor la modulación por fosforilación propia del canal Kv2.1 y las características topológicas de su expresión en la membrana, tales como la formación de cúmulos (Mohapatra and Trimmer, 2006).

3.2.2. El poro, la permeación y la selectividad

3.2.2.1. El dominio del poro

La característica distintiva de los canales iónicos con respecto a otras proteínas de transporte es su capacidad de conducir iones a velocidades comparadas con la difusión a través de una región altamente desfavorable para el paso de solutos con carga: la membrana plasmática. Para lograr la transferencia de los iones a través de la membrana, los canales iónicos poseen distintos mecanismos que permiten estabilizar a las cargas en la vía de conducción en el poro, y logran una alta velocidad de conducción gracias a las interacciones repulsivas entre los iones durante la permeación (Doyle et al., 1998; Roux et al., 2004).

El poro de los canales de potasio dependientes de voltaje está formado por los segmentos transmembranales S5, S6, y el asa que los comunica, la cual forma la estructura extracelular del canal denominada torreta, la hélice del poro y el filtro de selectividad (Fig. 4) (Long et al., 2005a; Long et al., 2007). Las paredes del poro están formadas por los segmentos S6 de las cuatro subunidades y el filtro de selectividad está localizado en la mitad superior del canal. Este dominio es muy similar entre distintos canales Kv y algunos canales de potasio de porcariontes cuyas subunidades constan únicamente de dos segmentos transmembranales, análogos a los segmentos S5 y S6 de los canales Kv (Doyle et al., 1998; Jiang et al., 2002; Jiang et al., 2003; Long et al., 2005a; Long et al., 2007). Esta similitud permitió extrapolar los conocimientos sobre los mecanismos de permeación obtenidos a partir de la estructura cristalográfica del canal KcsA de *Streptomyces lividans* (Doyle et al., 1998), con el mecanismo de permeación en los canales de potasio dependientes de voltaje, antes de contar con estructuras en alta resolución de canales Kv de mamífero.

El poro de cada canal de potasio contiene cuatro sitios de unión a potasio localizados en el filtro de selectividad, además de dos sitios externos mutuamente excluyentes en la entrada de la cavidad extracelular, y un sitio interno localizado en la cavidad central acuosa en la región del poro (Doyle et al., 1998; Long et al., 2005a; Zhou et al., 2001) que es continua con el medio intracelular y contiene entre 40 y 50 moléculas de agua y un ion en el estado abierto del canal (Fig. 4A) (Jensen et al., 2010). El filtro de selectividad, que contiene la secuencia característica de los canales de potasio (TVGYG) (Heginbotham et al., 1994), está formado por los carbonilos de la cadena principal del asa que conecta los segmentos S5 y S6 (Doyle et al., 1998; Long et al., 2005a).

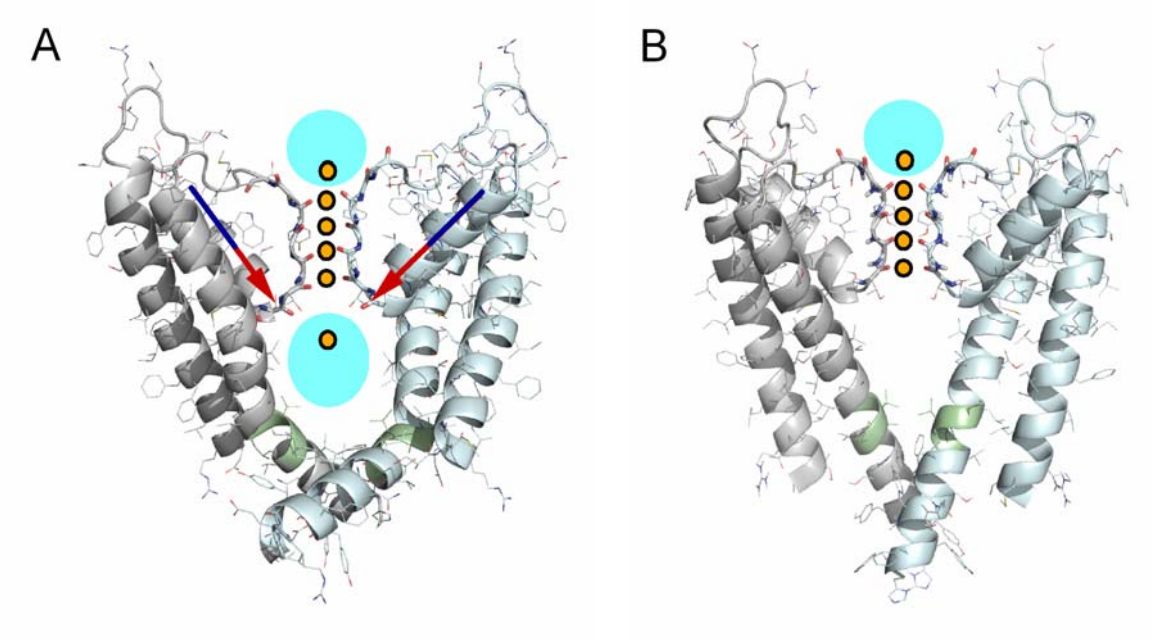

Figura 4. Esquema del poro del canal Kv1.2 en el estado abierto y un modelo del canal *Shaker* en el estado cerrado. (A) Estructura del poro del canal Kv1.2 (de S5 a S6) en el estado abierto reportada en (Khalili-Araghi et al., 2010) y obtenida a partir de dinámica molecular a partir del pdb 2A79. Dos subunidades se muestran en azul claro y gris. Por simplicidad, se omitieron las dos subunidades que salen del plano de la figura. Los átomos están coloreados según el elemento: oxígeno rojo, carbono azul o gris, dependiendo de la subunidad, nitrógeno azul. Los sitios de unión a iones en el filtro de selectividad y en los vestíbulos intra- y extracelulares se indican con círculos amarillos. Los oxígenos de los carbonilos de la cadena principal de la proteína están orientados hacia el centro del filtro, coordinando los iones. La hidratación de los iones en ambos vestíbulos se indica con círculos azules. El momento dipolar de la hélice del poro se representa con flechas, con el polo negativo cerca de la cavidad intracelular. La región del S6 que funciona como una bisagra para abrir y cerrar la vía de conducción iónica, el motivo Pro-Val-Pro, se indica en color verde en los segmentos S6 de ambas subunidades. (B) Modelo estructural del poro del canal *Shaker* en el estado cerrado, obtenido a partir de dinámica molecular (Chanda et al., 2005). Los colores son los mismos que en (A). Con base en la estructura en el estado abierto y al modelo en el estado cerrado, se puede sugerir que el movimiento que realiza el S6 al pasar del estado abierto al cerrado es una torsión en la hélice. Las cadenas laterales se muestran en líneas delgadas. La cavidad interna se encuentra deshidratada (Jensen et al., 2010). Las figuras se generaron en Pymol.

3.2.2.2. El mecanismo de permeación

Los carbonilos del filtro de selectividad proveen a los iones un ambiente electrostático similar al que están expuestos cuando se encuentran hidratados (Fig. 4A) (Berneche and Roux, 2001; Morais-Cabral et al., 2001; Noskov et al., 2004; Zhou et al., 2001). Por tanto, el paso de un ion del sitio en el vestíbulo extracelular del poro, en donde se encuentra hidratado, al primer sitio de unión dentro del filtro, en donde se encuentra rodeado por los carbonilos de la proteína y dos moléculas de agua, una en el siguiente sitio del filtro y la otra en el vestíbulo extracelular, no es energéticamente demandante. Lo mismo ocurre para el paso de un ion de la cavidad intracelular al sitio más intracelular del filtro.

Datos estructurales y modelos teóricos sugieren que únicamente dos sitios dentro del filtro de selectividad (1 y 3 ó 2 y 4) se encuentran ocupados al mismo tiempo durante la permeación, mientras que los sitios restantes están ocupados por moléculas de agua (Morais-Cabral et al., 2001; Zhou and MacKinnon, 2003; Zhou et al., 2001). Los cuatro sitios en el filtro son relativamente equivalentes en cuanto a la energía de unión del potasio, y las barreras que separan el paso de los iones de un sitio al otro son pequeñas (Berneche and Roux, 2001; Morais-Cabral et al., 2001; Zhou and MacKinnon, 2003), mientras no se encuentren dos iones en sitios directamente contiguos, lo que resulta en una fuerte energía electrostática repulsiva. A causa de lo anterior, el movimiento de cada par de iones en el filtro durante la permeación es concertado (Aqvist and Luzhkov, 2000; Berneche and Roux, 2001; Jensen et al., 2010; Jensen et al., 2012; Morais-Cabral et al., 2001), y ocurre junto con la permeación de las moléculas de agua unidas al filtro en proporción 1:1, al menos a concentraciones altas de potasio (Ando et al., 2005; Iwamoto and Oiki, 2011; Jensen et al., 2010; Jensen et al., 2012). Además, la concentración intra- y extracelular de iones afecta la ocupación de los sitios externos al filtro.

Los iones unidos a estos sitios externos establecen interacciones electrostáticas repulsivas con los iones del filtro, lo que modifica el perfil de energía de los sitios de unión dentro y fuera del filtro e influye en la velocidad y

direccionalidad neta del flujo de los iones en función de las concentración interna y externa de potasio (Aqvist and Luzhkov, 2000; Berneche and Roux, 2001; Morais-Cabral et al., 2001). Dado que ambos sitios externos al filtro de selectividad son aproximadamente continuos con el medio intra- o extracelular, la caída mayoritaria del potencial transmembranal en un canal abierto ocurre en el filtro de selectividad (Contreras et al., 2010; Jogini and Roux, 2005), por lo que los iones atraviesan casi la totalidad del campo eléctrico de la membrana al pasar por los cuatro sitios del filtro de selectividad. El campo eléctrico fuertemente enfocado en el filtro provee parte de la fuerza impulsora que, junto con la repulsión electrostática entre iones, permite las altas tasas de flujo a través de estas proteínas.

Finalmente, la hélice del poro (Fig. 4A y B) también tiene una contribución grande en el mecanismo de permeación: como todas las hélices alfa, ésta posee un momento dipolar debido a la naturaleza del enlace peptídico. El momento dipolar de la hélice del poro está orientado hacia el centro de la cavidad acuosa del canal (Doyle et al., 1998). Debido a que el ambiente que rodea a la hélice es de baja constante dieléctrica, la magnitud del campo eléctrico que ésta genera es grande, lo que resulta en una importante contribución de este campo al ambiente electrostático de los iones en el poro, estabilizándolos (Jogini and Roux, 2005).

3.2.2.3. El mecanismo de selectividad

Se ha propuesto que la elevada selectividad de estos canales ($P_K \approx 1000\ P_{Na}$, donde P_x indica permeabilidad del ion x (Hille, 2001)) se debe a un balance energético entre la afinidad de los iones permeantes por los sitios de union en el filtro de selectividad, y la energía conformacional intrínseca del sitio mismo (Noskov et al., 2004): la conformación de menor energía del filtro, considerando las torsiones de los enlaces en la proteína, las distancias entre los carbonilos que forman los sitios de unión en el filtro y la repulsión electrostática entre oxígenos, coincide con la distancia óptima de hidratación de los iones de potasio. Como consecuencia de esto, aunque el paso del potasio de la solución acuosa al filtro implica el cruce de una barrera energética pequeña, la energía

potencial del ion en el filtro con respecto a cuando está completamente hidratado es muy similar. Además, la unión del ion a su sitio en el filtro contribuye a la estabilidad de la estructura funcional de la proteína en esa región (Noskov et al., 2004; Zhou and MacKinnon, 2003). Otros cationes más pequeños, como el sodio, pueden permear a través de los canales de potasio, pero únicamente en ausencia del ion preferencial, dado que su presencia en el filtro resulta en una conformación de mayor energía con respecto a la observada en presencia de potasio (Noskov et al., 2004). Este mecanismo de selectividad dinámica le permitiría al poro mantener el alto grado de selectividad sin requerir que el filtro sea rígido, como se pensaba inicialmente (Hille, 2001). Consistentemente, se ha observado que la presencia de potasio dentro del filtro es necesaria para que éste mantenga una conformación funcional (Gomez-Lagunas, 1997; Khodakhah et al., 1997). De igual forma, el potasio tiene una influencia importante sobre la inactivación lenta (tipo C) en los canales de la subfamilia Kv1, dado que su presencia contribuye a la manutención del estado conductivo del canal y enlentece la entrada al estado inactivado (Baukrowitz and Yellen, 1995).

3.2.2.4. La compuerta de activación: la apertura y cierre de la vía de conducción iónica

Otra región de gran importancia para la función de los canales localizada en el poro es la compuerta de activación. Ésta es la región que permite o impide el flujo de iones en función del estado de los dominios sensores de voltaje. La presencia de una compuerta de activación en los canales de potasio del axón gigante de calamar se sugirió desde inicios de los años 70 por Clay Armstrong (Armstrong, 1971). Utilizando bloqueadores intracelulares de las corrientes de potasio en el axón, Armstrong demostró que en presencia de éstos el canal no puede cerrarse, y a su vez éstos no pueden acceder a su sitio en un canal cerrado (Armstrong, 1971).

Posteriormente, mediante estudios de la accesibilidad de moléculas modificadoras de cisteínas a sitios reactivos a lo largo del S6 en función del estado (abierto o cerrado), se demostró que existe una constricción localizada

en la posición 478 de *Shaker* que impide el flujo de iones cuando el canal está en el estado cerrado (del Camino and Yellen, 2001; Liu et al., 1997). Basándose en estos datos y la estructura del canal KcsA (Doyle et al., 1998), en la que el poro está cerrado, se sugirió que las hélices del segmento S6 en los canales Kv se cruzan en el estado cerrado del canal, formando una estructura de *teepee* invertido, que constituye una barrera física para el flujo de los iones. Por el contrario, en el estado abierto, los segmentos S6 sufren una torsión de aproximadamente 30° alrededor de la secuencia Pro-X-Pro (Pro-Val-Pro en Shaker y Kv1.2, Pro-Ile-Pro en Kv2.1) (del Camino et al., 2000; Long et al., 2005a; Webster et al., 2004), un motivo altamente conservado entre canales Kv, que resulta en el rompimiento de la hélice justo en esa posición y un incremento dramático en el diámetro del poro interno (~4 Å en el estado cerrado vs 12 Å en el abierto (Long et al., 2005a)), parecido a la apertura del diafragma en una cámara (Fig. 4). Este cambio conformacional se favorece por la tendencia de las prolinas a romper hélices alfa y funcionar como puntos de flexibilidad local. Consistente con su importancia para la función de los canales, sustituciones de residuos en estas posiciones tienen efectos dramáticos sobre la función de los canales (Labro et al., 2003; Sukhareva et al., 2003).

Cabe agregar que el estado de hidratación del poro interno juega un papel esencial en la estabilidad del estado abierto vs el estado cerrado del canal: dada la reducción en volumen que experimenta el poro interno cuando éste se cierra, una cantidad significativa de moléculas de agua deben salir del poro para que éste pueda cerrarse (Jensen et al., 2010; Jensen et al., 2012; Zimmerberg et al., 1990). El estado cerrado se favorece tanto por la deshidratación de una cavidad principalmente hidrofóbica en el estado cerrado como por las interacciones favorables entre los segmentos S6, empaquetados más íntimamente que en el estado abierto.

Finalmente, es importante considerar que el canal posee una segunda "compuerta de activación" localizada en el filtro de selectividad que impide la conducción de iones mediante un mecanismo denominado inactivación lenta o tipo-C (Baukrowitz and Yellen, 1995; Cuello et al., 2010). Es interesante que la

apertura y cierre de la compuerta de activación intracelular, el movimiento del sensor de voltaje del canal y la inactivación lenta (tipo C) se influyen mutuamente por medio de interacciones alostéricas (Azaria et al., 2010; Wang et al., 2011; Yifrach et al., 2009).

3.2.3. La detección de cambios en el voltaje

3.2.3.1. Los dominios sensores de voltaje son módulos independientes

La sensibilidad de los canales dependientes de voltaje a los cambios en el potencial transmembranal depende de la acción de un dominio altamente especializado: el dominio sensor de voltaje, el cual es capaz de cambiar de conformación en función del voltaje transmembranal (Catterall, 2010). Los dominios sensores de voltaje (DSV) se encuentran covalentemente asociados al dominio del poro en los canales dependientes de voltaje por medio de la hélice de unión entre los segmentos S4 y S5 (Long et al., 2005a), denominada asa S4-S5. La estructura y la función de los DSV en los canales Kv son muy similares a los de otros canales activados por voltaje, como los canales de sodio (Payandeh et al., 2012), con la diferencia de que en estos últimos las cuatro subunidades que forman a un canal funcional se encuentran unidas covalentemente y están contenidas secuencialmente dentro de un sólo marco de lectura codificado en el genoma.

Por otro lado, se han identificado otras proteínas sin un poro análogo al de los canales Kv (i.e. S5-S6) que contienen dominios que parecen ser muy similares, tanto en función como en estructura, a los DSV de los canales activados por voltaje. Tal es el caso de la fosfolipasa dependiente de voltaje de *Ciona intestinalis* (CiVSP, (Murata et al., 2005)) y los canales de protones activados por voltaje (Hv, (Ramsey et al., 2006; Sasaki et al., 2006)). Más aún, se ha demostrado que ciertas regiones de la enzima CiVSP y del canal Hv pueden sustituir regiones equivalentes en los DSV de canales de potasio y mantener su función (Alabi et al., 2007), lo que indica que estos dominios son módulos independientes del resto de la proteína (e.g. el poro del canal o la enzima citosólica en caso de CiVSP) que, al menos en los canales Kv, se encuentran

fuertemente acoplados con el funcionamiento del dominio del poro (Islas and Sigworth, 1999).

La naturaleza modular de los DSV se refleja también en su función dentro de los canales Kv: se ha demostrado que cada uno de los cuatro DSV en los canales Kv sufre una serie de cambios conformacionales iniciales en función del voltaje (Catterall, 2010), e.g. durante su activación después de una despolarización, de manera independiente, sin presentar signos de cooperatividad entre DSV (Gagnon and Bezanilla, 2010; Mannuzzu and Isacoff, 2000). Consistentemente, los modelos funcionales capaces de representar la actividad dependiente del voltaje de los canales Kv consideran que casi la totalidad de los cambios conformacionales asociados a la activación o desactivación en cada uno de los sensores de voltaje ocurre de manera prácticamente independiente del estado de los demás sensores en el canal (Bezanilla et al., 1994; Schoppa and Sigworth, 1998c; Zagotta et al., 1994a). Por el contrario, los últimos cambios conformacionales en la vía de activación de los sensores de voltaje son altamente cooperativos, al ocurrir de manera concertada con respecto a los cuatro DSV y la apertura del canal (Gagnon and Bezanilla, 2009; Ledwell and Aldrich, 1999; Mannuzzu and Isacoff, 2000; Pathak et al., 2005; Schoppa and Sigworth, 1998c; Zagotta et al., 1994a). Es principalmente durante estos cambios conformacionales concertados en donde opera el mecanismo de acoplamiento electromecánico, por medio del cual el DSV controla el estado del poro del canal: abierto o cerrado. Análogamente, durante la desactivación de los sensores desde el estado activado, los primeros cambios conformacionales son altamente concertados y llevan al cierre del poro, mientras que el resto del proceso de desactivación ocurre de manera independiente en cada subunidad del canal.

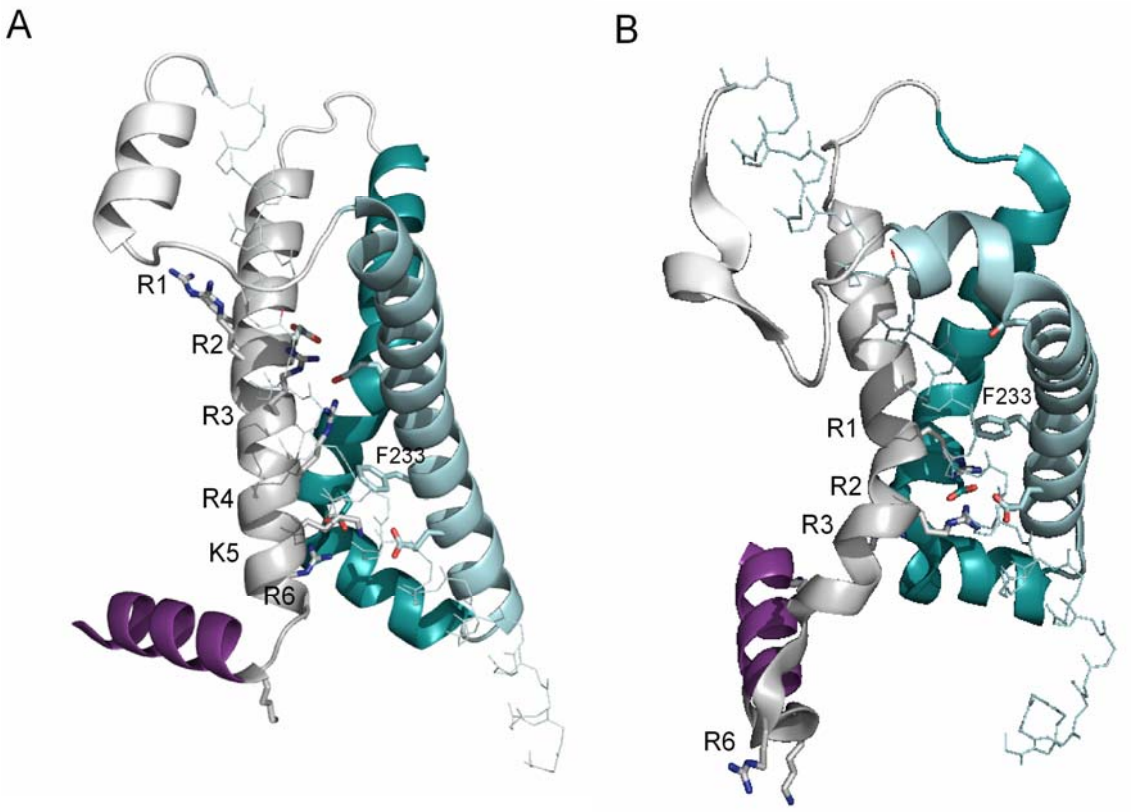

Figura 5. Esquema de un dominio sensor de voltaje del canal Kv1.2 en el estado activado y desactivado. (A) Estructura de un dominio sensor de voltaje en el estado activado. Del S1 se muestra únicamente la cadena principal en representación de líneas color azul claro. El S2 está en azul claro, el S3 en cian, el S4 en gris y el asa S4-S5 en morado. Las demás asas que conectan segmentos transmembranales están en blanco. Se indica la posición de las cadenas laterales de los primeros seis residuos básicos del S4 (R1, R2, R2, R4, K4 y R6) que constituyen las cargas de compuerta. También se muestra la fenilalanina 233 (F233) que separa las cavidades acuosas intra- y extracelulares. Dos cúmulos de residuos ácidos en ambos extremos del DSV también se resaltan en la figura. Estos residuos son D182 (S1), D226 (S2), D236 (S2) y E259 (S3). Los átomos de los residuos resaltados están coloreados por elemento: oxígeno en rojo, carbono del color del resto de segmento transmembranal, nitrógeno en azul. (B) Modelo estructural de un dominio sensor de voltaje en el estado desactivado. Se han resaltado las cadenas laterales de los mismos residuos que en (A), con el mismo código de colores, aunque no se aprecian mucho por estar detrás de la hélice S4. Se puede inferir el movimiento de las cargas de compuerta hacia la región intracelular del canal durante el proceso de desactivación al comparar la posición relativa entre las cargas de compuerta y F233 en las estructuras en el estado activado y desactivado. También se nota el cambio en el ángulo del asa S4-S5 (morado) con respecto al S4 (gris) al cerrarse el canal. Las figuras fueron hechas en Pymol a partir de las estructuras reportadas en (Khalili-Araghi et al., 2010), las cuales se obtuvieron mediante dinámica molecular utilizando la estructura del canal Kv1.2 (pdb 2A79).

3.2.3.2. El movimiento de carga y la estructura del sensor de voltaje

El mecanismo mediante el cual los DSV son capaces de cambiar su conformación en función del potencial eléctrico depende de la interacción con el campo eléctrico transmembranal de una serie de residuos con carga positiva localizados en el cuarto segmento transmembranal (S4) (Fig. 5) (Aggarwal and MacKinnon, 1996; Papazian et al., 1991; Seoh et al., 1996). Estos residuos cargados se encuentran posicionados a lo largo del S4 de forma altamente regular, al presentar un patrón de una arginina o lisina por cada dos residuos hidrofóbicos, para un total de entre 6 y 7 cargas positivas en el S4 en los canales Kv (Fig. 5A).

Una gran cantidad de estudios funcionales, principalmente realizados en *Shaker*, indican que el dominio S4 y la región carboxilo-terminal (C-terminal) del S3 (S3b) se trasladan a lo largo del plano perpendicular a la membrana una distancia de entre 7 y 15 Å en respuesta a cambios en el potencial transmembranal (Fig. 5B) (Broomand and Elinder, 2008; Campos et al., 2007; Jensen et al., 2012; Larsson et al., 1996; Pathak et al., 2007; Starace and Bezanilla, 2004). Como resultado de esto, las cadenas laterales de los residuos básicos R2 y R3 (Fig. 5) se trasladan completamente del medio intracelular al extracelular durante la activación del sensor, y viceversa durante la desactivación.

La accesibilidad de los residuos básicos R1 y R4 desde el medio extra- o intracelular, respectivamente, también se modifica significativamente durante la activación o desactivación (Larsson et al., 1996; Starace and Bezanilla, 2001, 2004). Estas observaciones son consistentes con experimentos en donde se demostró que en *Shaker* son los primeros cuatro residuos cargados (R1-R4) los que interactúan con el campo eléctrico transmembranal, y por lo tanto contribuyen energéticamente a los cambios conformacionales del DSV en función del voltaje (Aggarwal and MacKinnon, 1996; Seoh et al., 1996). Esto concuerda con mediciones que indican que durante la activación/desactivación de *Shaker* se mueven a través del campo eléctrico transmembranal entre 12 y 13 cargas elementales por canal (~ 4 e_0 por subunidad), denominadas cargas

de compuerta (Schoppa et al., 1992). Es precisamente esta traslación del S4 (y las cargas contenidas en él) a través del campo eléctrico de la membrana lo que da origen a las corrientes de compuerta (Armstrong and Bezanilla, 1973, 1974).

Una vez que las corrientes iónicas se han suprimido mediante manipulaciones experimentales, las corrientes de compuerta se pueden observar en registros electrofisiológicos como un componente no lineal de la corriente capacitiva. Las mediciones de corrientes de compuerta son una herramienta de gran valor para el estudio de la estructura y la función de canales dependientes de voltaje, ya que permiten obtener información directa sobre la naturaleza de los cambios conformacionales que sufren estas proteínas antes de que se abra el poro.

Otro aspecto importante para la función de los dominios sensores de voltaje son los mecanismos que le confieren estabilidad a las cargas de compuerta localizadas “dentro” de la membrana plasmática. Residuos con carga negativa en los segmentos S1-S3a en ambos extremos del DSV contribuyen a la estabilización de las cargas positivas del S4, con las que establecen interacciones dependientes del estado del sensor (Long et al., 2007; Pless et al., 2011; Silverman et al., 2003). Un residuo aromático (Phe233 en *Shaker*) localizado en el S2, aproximadamente a la mitad del DSV a lo largo del eje perpendicular a la membrana, constituye un “tapón” hidrofóbico que separa dos cavidades acuosas intra- y extracelulares en cada DSV, en las que se encuentran inmersas las cargas del S4 (Long et al., 2007). Además, Phe233 establece interacciones con las cargas del S4 a medida que se trasladan durante la activación o desactivación del sensor, estabilizándolas al pasar de una cavidad acuosa a la otra (Tao et al., 2009). Las moléculas de agua dentro de las cavidades en ambos extremos del sensor contribuyen a la estabilización de las cargas de compuerta (Pless et al., 2011).

Otra consecuencia importante de la presencia de cavidades acuosas químicamente continuas con el medio intra- o extracelular es que la caída del potencial transmembranal ocurre en una fracción pequeña de todo el grosor de la membrana (Islas and Sigworth, 2001; Jensen et al., 2012; Khalili-Araghi et

al., 2010). Debido a esto, pequeños movimientos de traslación en el S4 (menores a 30 Å) permiten la transferencia de cargas elementales a través de todo el campo eléctrico, minimizando la magnitud del cambio conformacional necesario para transferir 4 cargas elementales por subunidad y haciendo más eficiente el trabajo mecánico del sensor en función del voltaje.

Las interacciones de los residuos cargados del S4 con las cabezas polares o cargadas de los lípidos en la membrana (Krepkiy et al., 2009; Long et al., 2007; Milescu et al., 2009) también contribuyen significativamente al funcionamiento del sensor de voltaje (Schmidt et al., 2006; Xu et al., 2008). Finalmente es importante mencionar que los segmentos S1-S3a no sufren grandes cambios conformacionales durante la actividad del sensor, y se piensa que además de contribuir a la formación de cavidades acuosas y estabilizar las cargas del S4 por medio de interacciones electrostáticas, cumplen la función de proveer un punto de anclaje en la membrana a los segmentos S3b-S4 (Banerjee and MacKinnon, 2008; Ruta et al., 2005).

Para finalizar, es importante enfatizar que el movimiento que el S4 realiza durante la activación/desactivación del sensor de voltaje no está limitado a una simple traslación. La evidencia proveniente de las estructuras obtenidas a partir de difracción de rayos X y las simulaciones mediante dinámica molecular indica que junto con la traslación, el S4 sufre movimientos de rotación y torsión (Jensen et al., 2012; Long et al., 2007). Más aún, se ha propuesto que la estructura secundaria de este segmento se modifica durante la actividad del sensor, en donde regiones consecutivas del S4, comenzando desde el extremo C-terminal, pasan de ser una hélice 3_{10} en el estado desactivado a una hélice alfa en el estado activado, lo que permite que dos residuos básicos contiguos se orienten hacia la misma cara de la hélice y establezcan interacciones electrostáticas con residuos localizados en hélices opuestas (Chakrapani et al., 2010; Khalili-Araghi et al., 2010). De acuerdo con los modelos propuestos, a medida que el sensor de voltaje se activa, diferentes regiones alfa-helicoidales del S4 van adquiriendo la conformación 3_{10} y posteriormente la de hélice alfa de nuevo (Jensen et al., 2012; Khalili-Araghi et al., 2010).

Cabe recalcar que aunque haya una gran cantidad de datos funcionales sobre los cambios que el S4 sufre durante la actividad del DSV, los detalles estructurales siguen siendo altamente especulativos, ya que hasta el momento no se cuenta con una estructura de alta resolución de un canal de potasio dependiente de voltaje en el estado cerrado. Asimismo, los detalles obtenidos a partir de la estructura del sensor del canal Kv1.2 (Long et al., 2005a) y la quimera entre los canales Kv1.2 y Kv2.1 (Long et al., 2007) podrían no reflejar directamente la estructura del sensor en el estado activado. Esto se debe a la "inactivación" del DSV, que consiste en el paso del sensor de voltaje a un estado activado altamente estable, denominado estado de reposo, después de despolarizaciones prolongadas, resultando en histéresis para la desactivación del sensor (Villalba-Galea et al., 2008). Debido a que los cristales se obtienen a cero mV, un voltaje en el que los sensores están activados y son altamente susceptibles a caer en el estado de reposo, es probable que las estructuras disponibles reflejen la estructura del sensor en estado de reposo.

3.2.4. El mecanismo de acoplamiento electromecánico

3.2.4.1. El acomplamiento electromecánico en canales activados por voltaje

El acoplamiento electromecánico es el mecanismo mediante el cual el sensor de voltaje se comunica con la compuerta de activación del canal para abrir o cerrar la vía de conducción iónica en función del voltaje transmembranal. La naturaleza del acoplamiento es capaz de determinar la polaridad de la sensibilidad de un canal al voltaje: mientras que los canales Kv se activan por despolarización y se cierran por hiperpolarización, los canales HCN se activan por hiperpolarización y se cierran por despolarización, a pesar de tener dominios sensores de voltaje (Chen et al., 2000; Mannikko et al., 2002; Vemana et al., 2004) y una compuerta de activación (Rothberg et al., 2002) muy similares, tanto en estructura como en función, a los de los canales Kv. Estos resultados sugieren que la sensibilidad opuesta al voltaje entre ambos tipos de canales está determinada por diferencias en el mecanismo de acoplamiento entre el DSV y el poro (Rosenbaum and Gordon, 2004).

Por otro lado, el acoplamiento electromecánico también es capaz de determinar el grado de sensibilidad de un canal al voltaje, dado que la fuerza de este acoplamiento varía entre canales. Por ejemplo, en los canales de potasio de gran conductancia activados por calcio, o BK, este acoplamiento es relativamente débil, lo que le permite a estos canales abrirse aún cuando los sensores de voltaje se encuentran en el estado desactivado (Horrigan and Aldrich, 2002). Por el contrario, el acoplamiento electromecánico en los canales Kv, al menos en los pertenecientes a las subfamilias de *Shaker* y *Shab*, es muy fuerte, y se ha determinado que la probabilidad de observar aperturas de canales con sensores de voltaje desactivados es más pequeña que 10^{-9} (Islas and Sigworth, 1999). Es por esta razón que los modelos funcionales para los canales Kv, con excepción de canales con ciertas mutaciones puntuales, consideran una única vía de activación en la que el canal sólo se abre una vez que los cuatro sensores han alcanzado el estado activado (Bezanilla et al., 1994; Schoppa and Sigworth, 1998c; Zagotta et al., 1994a).

3.2.4.2. La influencia del campo eléctrico transmembranal y el estado del sensor de voltaje sobre la apertura o cierre del poro: aspectos funcionales

Como se ha dicho con anterioridad, se piensa que este mecanismo opera durante las transiciones concertadas que llevan a la apertura o cierre del canal, dado que el poro no parece sufrir cambios conformacionales significativos durante la activación/desactivación independiente de cada uno de los sensores de voltaje (del Camino et al., 2005). Un punto central en relación al mecanismo de acoplamiento electromecánico es la conformación intrínseca del poro en ausencia del sensor de voltaje: ¿abierto o cerrado? Si la energía libre del estado abierto en ausencia del sensor de voltaje fuera mucho menor que la del estado cerrado, el acoplamiento electromecánico consistiría en la aplicación de fuerza por el DSV sobre el poro para cerrarlo, mientras que no requeriría realizar trabajo para abrirlo. Si la conformación de menor energía, o intrínseca, del poro fuera el estado cerrado, entonces el sensor de voltaje debería de ejercer fuerza para abrirlo, mas no para cerrarlo. El hecho de que el canal a 0 mV se encuentre en el estado abierto, indica que la conformación más estable

del sensor de voltaje en ausencia de campo eléctrico transmembranal es el estado activado (Gagnon and Bezanilla, 2009), pero esto no proporciona información sobre la conformación intrínseca del poro en sí mismo.

Se ha sugerido que dado que el empaquetamiento del poro en el estado cerrado es más compacto, este estado podría resultar el más estable, dada la relativa hidrofobicidad de los residuos que forman las paredes del poro (Jensen et al., 2010; Jensen et al., 2012; Yifrach and MacKinnon, 2002). Esto es consistente con que la mayoría de las mutaciones introducidas en el poro de *Shaker* causan una mayor desestabilización del estado cerrado que del abierto, corriendo el voltaje medio de activación ($V_{1/2}$) a potenciales más negativos (Hackos et al., 2002; Yifrach and MacKinnon, 2002).

Consistentemente, mutaciones en *Shaker* que interfieren con el mecanismo de acoplamiento electromecánico permiten que el sensor de voltaje se active a potenciales menos positivos, lo que sugiere que efectivamente el sensor debe ejercer una fuerza sobre el poro para abrirlo, y que al desacoplar ambos procesos, el sensor de voltaje se libera de la "carga" que el poro ejerce sobre él (Haddad and Blunck, 2011). En contraste, perturbaciones en las regiones responsables del acoplamiento entre los DSV y el poro pueden resultar en canales capaces de abrirse de manera independiente del voltaje (Ferrer et al., 2006; Labro et al., 2011; Lu et al., 2001, 2002; Tristani-Firouzi et al., 2002). Esto sugiere, en contra de lo anterior, que la conformación intrínseca del poro en ausencia de la influencia del sensor es el estado abierto (Upadhyay et al., 2009), o al menos arguye en contra de que la energía libre del estado cerrado sea tan baja que éste funcione como un estado absorbente en ausencia del DSV.

Claramente existe evidencia a favor de que la conformación de menor energía del poro es el estado cerrado o el abierto, lo que sugiere que aunque exista efectivamente una conformación de menor energía, que corresponda ya sea con el estado abierto o el cerrado, la diferencia en energía entre ambos estados no es tan grande como para que uno de ellos funcione como un estado absorbente, existiendo entonces un equilibrio efectivo entre el estado cerrado y

el abierto aun en ausencia de los sensores de voltaje. Si este fuera el caso, y dada la gran fuerza del acoplamiento electromecánico en los canales Kv, se esperaría entonces que el sensor tuviera que realizar trabajo sobre el poro tanto para abrirlo como para cerrarlo.

3.2.4.3. Determinantes estructurales del acoplamiento electromecánico

El siguiente punto relevante con respecto al acoplamiento electromecánico es lo referente a su mecanismo molecular, aunque el balance de fuerzas durante el proceso aún se desconozca. Como se puede observar en las dos estructuras disponibles en alta resolución de canales Kv, existen pocos puntos de contacto entre los DSV y el poro del canal (Long et al., 2005a, b; Long et al., 2007). Mediante un análisis computacional de la correlación entre sitios en la secuencia de aminoácidos de distintos canales de potasio dependientes de voltaje (Lee et al., 2009), se identificaron dos probables regiones de interacción entre el DSV y el poro, que efectivamente coinciden con los resultados experimentales disponibles: por un lado, existe un punto de contacto entre el extremo extracelular del S1 en cada uno de los DSV y la hélice del poro en su extremo más extracelular. Se ha propuesto que esta interfase de interacción provee un punto de anclaje al sensor con respecto al poro para que la transferencia de fuerza de un dominio a otro sea óptima (Lee et al., 2009). La otra región de interacción ha sido más extensamente estudiada, y se piensa que juega el rol activo en el mecanismo de acoplamiento. Esta es la interfase a lo largo del grosor de la membrana entre los dominios sensores de voltaje y el poro del canal, la cual contiene la única unión covalente entre ambos dominios: el asa de unión entre los segmentos S4 y S5 (Fig. 6).

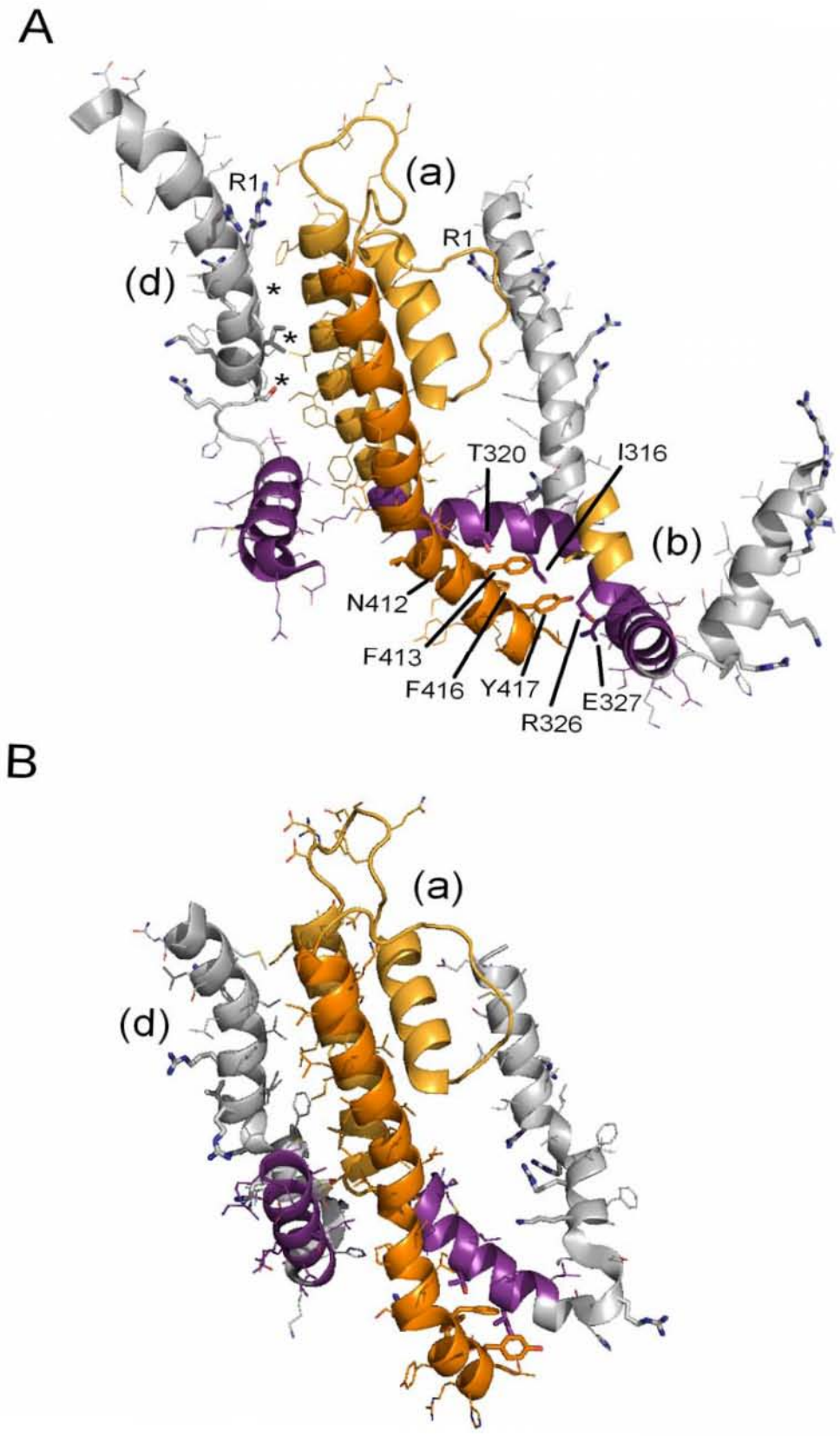

Figura 6. Regiones estructurales que participan en el acoplamiento electromecánico: la interfase entre los DSV y el poro del canal.

Figura 6. Regiones estructurales que participan en el acoplamiento electromecánico: la interfase entre los DSV y el poro del canal. (A) Estructura de la interfase entre un dominio sensor de voltaje en el estado activado y el poro abierto del canal Kv1.2. En amarillo se muestra el S5, la hélice del poro y el filtro de selectividad de una subunidad (subunidad a). De la misma subunidad se incluyó el asa S4-S5 (morado), el S4 (gris) y el S6 (naranja). La posición de la primera carga de compuerta (R1) se indica en la figura. El asa S4-S5 interacciona directamente con el extremo C-terminal del S6 de su propia subunidad, principalmente mediante los residuos I316 y T320 del asa S4-S5 y los residuos N412, F413, F416 y Y417 del S6, según datos funcionales en *Shaker* (Lu et al., 2002), Kv1.5 (Labro et al., 2008) y dinámica molecular de la quimera Kv1.2/Kv2.1 (Jensen et al., 2012). La posición de estos residuos está indicada en la figura, y sus cadenas laterales se han resaltado. Del lado derecho de la subunidad (a) se incluyó el asa S4-S5, parte del segmento S4 y una pequeña porción del S5 de la subunidad vecina (subunidad b). El asa S4-S5 de la subunidad (b) interacciona mediante los residuos R326 y E327 con la porción C-terminal del S6 de la subunidad (a). A su vez, el asa S4-S5 de la subunidad (a) interacciona con el S6 de la subunidad (d), y así sucesivamente, aunque esto no se muestra en la figura. Estos contactos inter-subunidades podrían ser en parte responsables del alto grado de cooperatividad entre subunidades durante las transiciones concertadas de apertura y cierre del poro, y se ha demostrado que dichas interacciones contribuyen a la estabilización del estado abierto en *Shaker* (Batulan et al., 2010). Del lado izquierdo se incluyó el segmento S4 y el asa S4-S5 de la subunidad (d). Se puede notar que varias de las cadenas laterales de residuos en el S4 de la subunidad (d) se encuentran en posición de interaccionar con el S5 de la subunidad (a). La posición de los residuos V301, I304 y S308 se ha marcado con asteriscos. Al ser mutados estos residuos en *Shaker* por I, L y T, respectivamente, dan origen a la mutante ILT en la que las transiciones concertadas están energéticamente desacopladas de la activación de los sensores de voltaje (Ledwell and Aldrich, 1999). El asa S4-S5 de la subunidad (d) también se encuentra en posición de interaccionar con el S6 de (a). Los átomos de las cadenas laterales están coloreados por elemento: oxígeno en rojo, carbono del color del resto de segmento transmembranal y nitrógeno en azul. (B) Modelo estructural de la interfase entre el DSV desactivado y el poro de una subunidad en el estado cerrado. El código de colores y los residuos cuyas cadenas laterales se resaltaron son los mismos que en (A), pero se omitió la subunidad (b). La figura muestra el posible cambio conformacional del asa S4-S5 con respecto al S6, así como el cambio conformacional del S6 mismo al cerrarse el canal. En el estado cerrado, el asa S4-S5 parece retener una posición con respecto al S6 que es favorable para establecer interacciones, aunque de manera diferente que en el estado abierto. Las interacciones entre el S4 de (d) y el S5 de (a) se modifican al cerrarse el canal. Las figuras fueron hechas en Pymol a partir de las estructuras reportadas en (Khalili-Araghi et al., 2010), las cuales se obtuvieron mediante dinámica molecular utilizando la estructura del canal Kv1.2 (pdb 2A79).

En un estudio sistemático de mutagénesis del segmento S5 de *Shaker* se encontró que existen dos cúmulos de residuos importantes para la función del canal, uno de los cuales parece participar directamente en el acoplamiento electromecánico (Soler-Llavina et al., 2006). Interesantemente, casi todas las mutaciones introducidas en esta región resultaron en canales funcionales, lo que indica que esta región es relativamente laxa con respecto al empaquetamiento, y que no hay muchos puntos de contacto entre ambos dominios. Esto es consistente con la independencia relativa entre el poro y el sensor de voltaje. Sin embargo, aunque la mayoría de las mutaciones no resultó en una pérdida absoluta de la actividad de los canales, muchas mutaciones sí alteraron significativamente la función de la proteína. Mutaciones en la región más extracelular del S5, una zona denominada cúmulo externo, desfavorecen la activación del sensor de voltaje sin tener efectos importantes sobre las transiciones concertadas del canal (Soler-Llavina et al., 2006). Esto es consistente con otro estudio en el que se propone que residuos en esa región del S5 establecen contactos con la región más extracelular del S4 de la subunidad adyacente (Pathak et al., 2005; Upadhyay et al., 2009) (Fig. 6).

De acuerdo con lo anterior, se ha demostrado que cisteínas introducidas en los extremos extracelulares del S4 y S5 pueden coordinar zinc en función de la posición del S4 (Phillips and Swartz, 2010). Por otro lado, mutaciones en la región intracelular del S5, o cúmulo interno, facilitan el movimiento de carga pero dificultan la activación del canal (Soler-Llavina et al., 2006). Esto refleja una interferencia con el mecanismo de acoplamiento electromecánico. Estos resultados son similares a otras mutaciones en el asa S4-S5 que también interfieren con el acoplamiento y facilitan la activación del sensor de voltaje y dificultan la apertura del poro (Haddad and Blunck, 2011).

Consistentemente, la región inferior del S5 parece establecer contactos con el S4 de la subunidad adyacente y con el S6 de su misma subunidad (Upadhyay et al., 2009) (Fig. 6), sugiriendo que estas interacciones podrían ser responsables de la singular cooperatividad entre subunidades durante la apertura y cierre del canal. Interesantemente, mutaciones alrededor de dicha

región, como la mutación ILT en el S4 (Ledwell and Aldrich, 1999; Smith-Maxwell et al., 1998) (Fig. 6A), la V2 en el asa S4-S5 (Schoppa and Sigworth, 1998b) o la E395C en el S6 (Holmgren et al., 1996), también interfieren con el acoplamiento electromecánico. Debido a estas observaciones, se ha sugerido que una parte importante de la transferencia de fuerza entre el S4 y el poro ocurre mediante las interacciones entre el S4 y S5, mientras que el S5, a su vez, interactúa con el S6 para inducir la apertura o el cierre del poro (Pathak et al., 2005; Upadhyay et al., 2009).

A pesar de la clara importancia de las interacciones entre los segmentos S4 y S5 a lo largo de la interfase entre ambos dominios, se piensa que la región determinante en el acoplamiento electromecánico es el asa S4-S5 y el extremo intracelular del S6. El asa S4-S5 es una hélice alfa anfipática que interactúa con una cara con el extremo C-terminal del S6 de su misma subunidad (Fig. 6) (Ding and Horn, 2003; Jensen et al., 2012; Labro et al., 2005; Long et al., 2005a, b; Long et al., 2007), y con la otra cara, según se observa en la estructura de la quimera Kv1.2/Kv2.1, con los lípidos de la membrana (Long et al., 2007). Mediante la construcción de quimeras de Shaker, Kv1.5 y Kv2.1 entre ellos o con canales de potasio independientes de voltaje, se ha demostrado que se requiere una completa compatibilidad entre la secuencia del asa S4-S5 y la del extremo C-terminal del S6, es decir, es necesario que ambas secuencias provengan de un mismo canal para que la construcción resultante tenga actividad dependiente del voltaje similar al canal silvestre (Labro et al., 2005; Lu et al., 2001, 2002). Además, mutaciones en esta región introducidas en varios canales dependientes del voltaje, como los canales HCN (Decher et al., 2004), hERG (Tristani-Firouzi et al., 2002), y canales de sodio dependientes de voltaje (Muroi et al., 2010), interfieren con el acoplamiento electromecánico.

En relación a la naturaleza de las interacciones entre el asa S4-S5 y el poro, se ha demostrado que al menos en los canales tipo *Shaker* (Labro et al., 2008) y el canal KCNQ1 (Labro et al., 2011), las interacciones entre el asa S4-S5 y el S6 son de naturaleza hidrofóbica. Más aún, se demostró que la especificidad de estas interacciones depende de la dirección del vector de hidrofobicidad de

ambas hélices (Labro et al., 2008), en donde un pequeño desfase puede resultar en efectos adversos para el acoplamiento. Por otro lado, en los canales HCN y hERG las interacciones entre el asa S4-S5 y el S6 son principalmente debidas a residuos polares o cargados (Decher et al., 2004; Tristani-Firouzi et al., 2002).

Otra diferencia importante entre canales es la dependencia en el estado del canal (abierto o cerrado) para la asociación del asa con el S6: en el canal KCNQ1 el asa parece unirse únicamente al estado cerrado (Choveau et al., 2011), estabilizándolo. Consistentemente, mutaciones en el área putativa de interacción entre ambas regiones de la proteína favorece el estado abierto del canal (Labro et al., 2011).

En el caso del canal hERG, la introducción de una unión covalente del S6 con el asa S4-S5, mediante la inducción de un puente disulfuro entre cisteínas introducidas en ambos sitios, resulta en un canal constitutivamente cerrado, sugiriendo que la interacción entre ambas regiones se da en el estado cerrado (Ferrer et al., 2006). Sin embargo, más recientemente se ha sugerido que el asa S4-S5 podría también interactuar con el estado abierto y contribuir a su estabilización cuando los sensores de voltaje están activados (Ng et al., 2012).

En contraste, en los canales HCN (Prole and Yellen, 2006) y KAT1 (Grabe et al., 2007) el asa S4-S5 interactúa con el S6 únicamente en el estado abierto, lo que podría ser parte del mecanismo que permite que estos canales se activen por hiperpolarización. En el caso de canales tipo *Shaker* (Kv1) y *Shab* (Kv2) este aspecto no está claro. Tanto datos experimentales como las estructuras disponibles sugieren que el asa S4-S5 interacciona con el S6 en el estado abierto, y que estas interacciones contribuyen a la estabilización del canal (Batulan et al., 2010; Jensen et al., 2012; Labro et al., 2011; Labro et al., 2008; Labro et al., 2005; Long et al., 2005a, b; Long et al., 2007). Por otro lado, simulaciones de dinámica molecular y datos experimentales sugieren que el asa S4-S5 podría también interactuar con el S6 en el estado cerrado del canal, estabilizándolo (Choveau et al., 2011; Jensen et al., 2012; Labro et al., 2008; Ng et al., 2012).

En ausencia de datos conclusivos, la interpretación mas sencilla, al igual que con la pregunta sobre el estado intrínseco del poro, es suponer que el S4-S5 es capaz de estabilizar al poro del canal tanto en el estado abierto como en el cerrado, contribuyendo directamente a la dependencia en el voltaje tanto de la transición de apertura como de cierre.

3.2.4.4. El acoplamiento electromecánico: un posible mecanismo

Basándose en lo anterior, se puede proponer un posible mecanismo mediante el cual ocurre el acoplamiento electromecánico (Fig. 7) (Jensen et al., 2010; Long et al., 2005b): tras una despolarización, una vez que los sensores de voltaje han realizado las transiciones independientes necesarias para llegar al estado activado, el canal alcanza el estado activado-cerrado. Se ha propuesto que en este estado tanto el sensor de voltaje como el asa S4-S5 tienen una conformación cercana a la de un canal activado (Jensen et al., 2012; Upadhyay et al., 2009), como en el cristal del canal Kv1.2, mientras que el S5-S6 se encuentra en el estado cerrado (del Camino et al., 2005). La pérdida de interacciones estabilizantes entre el asa S4-S5 y el S6 en el estado cerrado, y quizás una tendencia intrínseca del poro para abrirse, permiten la apertura concertada del canal, estableciendo así un nuevo juego de interacciones entre el asa S4-S5 y el S6 en el estado abierto, en las que la misma región del S4-S5 que estabilizaba al estado cerrado interactúa con el S6 en el estado abierto.

Al ocurrir una hiperpolarización, el sensor de voltaje se traslada hacia la región intracelular del canal, modificando la posición del asa S4-S5 con respecto al S6. Durante estos cambios conformacionales el asa S4-S5 podría trasladarse hacia abajo (Long et al., 2005b; Long et al., 2007) o hacia un lado en el plano paralelo a la membrana (Pathak et al., 2007), sin sufrir movimientos de rotación sobre su eje, y ejercer fuerza sobre el poro por medio de interacciones de van der Waals con el fin de cerrarlo. Una vez que el canal haya alcanzado el estado cerrado, el asa S4-S5 podría establecer interacciones estabilizantes con el S6.

Alternativamente, si la conformación intrínseca del poro fuera el estado cerrado, al trasladarse el S4 hacia la cavidad intracelular, las interacciones entre el S6 y el asa S4-S5 que estabilizaban al estado abierto se romperían, desestabilizando al estado abierto y permitiéndole al poro regresar al estado cerrado, seguido de una posible estabilización del estado cerrado una vez que el poro está cerrado y el sensor de voltaje completamente desactivado. Tanto resultados experimentales (Zimmerberg et al., 1990) como de dinámica molecular (Jensen et al., 2010; Jensen et al., 2012) sugieren que el colapso hidrofóbico de la cavidad interna del poro es la fuerza impulsora que determina el cierre del canal: la hiperpolarización reduce la ocupancia de iones en la cavidad interna, y facilita el colapso de la misma, cerrando al canal. Posteriormente, el reacomodo del sensor de voltaje hacia el estado desactivado podría conferirle al estado cerrado una mayor estabilidad, resultando en la gran fuerza de acoplamiento observada en estos canales.

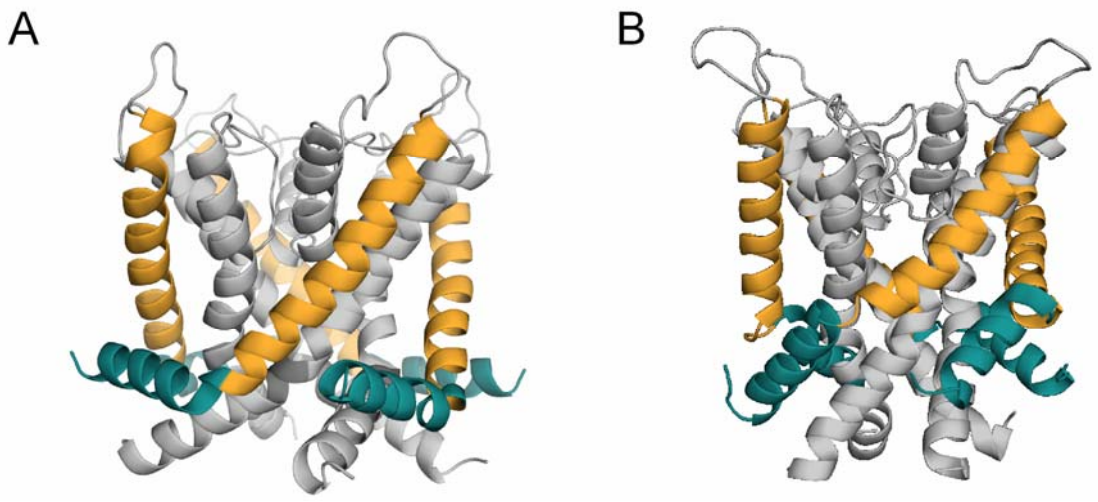

Figura 7. Mecanismo de acoplamiento electromecánico mediado por el asa S4-S5. Modelo estructural del dominio del poro del canal y el asa S4-S5 en el estado abierto (A) y cerrado (B). El segmento S6, la hélice del poro y el filtro de selectividad se muestran en gris, el S5 en amarillo y el asa S4-S5 en verde. Se puede apreciar en la figura el cambio conformacional relativo entre el S6 de cada subunidad y el S4-S5 de su propia subunidad.

4. ANTECEDENTES Y JUSTIFICACIÓN DEL PROYECTO

El objetivo inicial de este proyecto era estudiar el mecanismo de modulación por oxígeno del canal Kv2.1. Se ha demostrado que dicho canal se inhibe por oxígeno cuando se expresa en sistemas de expresión heterólogos, mediante un mecanismo aún desconocido (Hulme et al., 1999; Patel et al., 1997). También se ha propuesto que esta modulación por oxígeno en el músculo liso de las arterias pulmonares contribuye significativamente a la manutención del equilibrio de ventilación-perfusión en los pulmones (Archer et al., 1998; Archer et al., 2000; Archer et al., 2004; Hogg et al., 2002; Yuan et al., 1998).

Por otro lado, se ha identificado que un grupo de enzimas denominadas hemoxigenasas, sintetizan monóxido de carbono (CO) en función de la concentración de oxígeno disuelto en el citoplasma al catalizar una reacción en la que se transforma el grupo hemo en biliverdina utilizando NADPH (Maines and Gibbs, 2005). El monóxido de carbono resultante puede actuar como segundo mensajero dentro de la célula y modular la función de proteínas (Motterlini and Otterbein, 2010), incluyendo canales iónicos (Wilkinson and Kemp, 2011). De hecho, la sensibilidad al oxigeno del canal Slo1 en las células glomosas del cuerpo carotídeo depende de la producción de CO por la Hemoxigenasa 2, mediante la modulación directa del canal por el gas (Williams et al., 2004), el cual interacciona con histidinas localizadas en el dominio de unión a calcio RCK1 del canal (Brazier et al., 2009; Hou et al., 2008; Williams et al., 2008). Este mecanismo es esencial para conferirle sensibilidad al oxígeno al cuerpo carotídeo, el cual señaliza al sistema nervioso central para regular la respiración y la presión sanguínea en condiciones de hipoxia (Lahiri et al., 2006).

Dados los resultados anteriores, se planteó un proyecto dirigido a determinar si el monóxido de carbono es capaz de conferirle sensibilidad al oxígeno al canal Kv2.1 mediante la función de las Hemoxigenasas. Como primera aproximación, se probaron los efectos sobre el canal de una molécula que libera monóxido de carbono con alta eficiencia: el dímero de tricarbonil-dicloro rutenio o CORM-2 (*Carbon Monoxide Releasing Molecule*-2) (Fig. 8). Al estar en solución, el

CORM-2 se disocia en monómeros, tomando un par de moléculas de agua, y en cuestión de segundos libera de forma irreversible hasta dos carbonilos por monómero, uniendo moléculas de agua en su lugar (Fig. 8) (Alessio et al., 1988; Alessio et al., 1995; Brindell et al., 2004; Motterlini et al., 2002). Posteriormente, la molécula puede establecer un equilibrio lento con una forma iónica, en la que una cuarta molécula de agua sustituye un ion cloruro unido al rutenio.

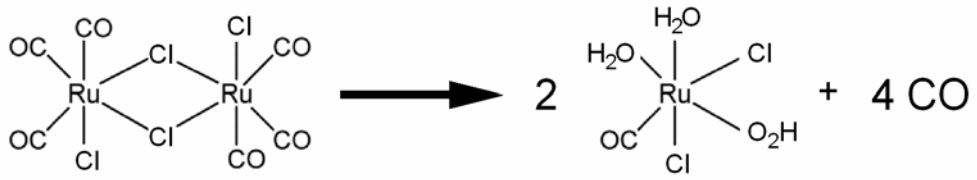

Figura 8. Estructura del CORM-2 y su posible producto de degradación en solución acuosa. En el mecanismo propuesto, el dímero de CORM-2 se disocia en solución acuosa, tomando una molécula de agua en sustitución del cloro que se pierde al romperse el dímero. Los carbonilos liberados (dos por monómero) son igualmente sustituidos por moléculas de agua, resultando en la liberación de cuatro moléculas de CO gaseoso por cada molécula de CORM-2.

Desde un principio, los efectos del CORM-2 sobre el canal resultaron interesantes en sí mismos, ya que el compuesto parecía funcionar como un modulador alostérico del canal, y tener una influencia importante sobre la sensibilidad del canal al voltaje. Dadas estas observaciones, se decidió estudiar con detalle la inhibición del canal Kv2.1 por CORM-2 con el fin último de obtener información sobre el mecanismo mediante el cual este canal detecta cambios en el voltaje y controla el flujo de iones en función del mismo. Como se demostrará a continuación en este trabajo, la molécula de CORM-2, y no el monóxido de carbono, interfiere con el acoplamiento electromecánico tanto de *Shaker* como del canal Kv2.1.

5. OBJETIVO GENERAL

Determinar el mecanismo de inhibición del canal Kv2.1 por CORM-2 y obtener información sobre los procesos que gobiernan la actividad dependiente del voltaje de los canales Kv.

6. OBJETIVOS ESPECÍFICOS

- Caracterizar los efectos del CORM-2 sobre el canal Kv2.1 expresado en sistemas de expresión heteróloga mediante la técnica de fijación de voltaje en microáreas de membrana.
- Determinar si el fenómeno estudiado se debe a la modulación alostérica del canal inducida por el compuesto o a una interferencia directa con la vía de conducción iónica (e.g. bloqueo del poro).
- Determinar si los efectos del compuesto se deben a la molécula donadora o al monóxido de carbono que libera.
- Investigar la influencia del CORM-2 sobre el dominio sensor de voltaje del canal.
- Proponer modelos funcionales que expliquen las observaciones experimentales.
- Localizar posibles sitios para la molécula efectora en el canal.

7. METODOLOGÍA

7.2. Biología molecular

En el trabajo se utilizaron los plásmidos *rKv2.1Δ7*-pBluescript-SK, *mSlo1*-pc-ANAOX, *Shaker H4*-pGEMA y *ShakerW434F*-pGEMA, los cuales nos fueron provistos por los Drs. Kenton Swartz, Larry Salkoff y Fred Sigworth, respectivamente. El canal Kv2.1 Δ*7* contiene siete mutaciones puntuales en el vestíbulo extracelular que le confieren alta sensibilidad a Agitoxina 2 (Aggarwal and MacKinnon, 1996; Li-Smerin and Swartz, 1998). Por simplicidad, en el resto del trabajo se referirá a esta variante del canal Kv2.1 como WT. Tanto Shaker H4 como ShakerW434F contienen una deleción en el amino terminal que elimina la inactivación rápida o tipo N (Hoshi et al., 1990).

Se construyó un canal Kv2.1 fusionado con la proteína amarilla fluorescente (eYFP) por el extremo amino-terminal, llamada aquí eYFP-Kv2.1. Para esto, se amplificó la región que codifica para la proteína fluorescente a partir del plásmido pEYFP-C1 mediante la reacción en cadena de la polimerasa (PCR) utilizando dos oligonucleótidos que introducen cada uno un sitio de restricción distinto en ambos extremos de la región amplificada. Se utilizaron estos sitios de restricción para reintroducir en el plásmido *rKv2.1Δ7*-pBluescript-SK la secuencia amplificada al inicio de la región que codifica para el canal Kv2.1, dejando una secuencia de 10 aminoácidos entre el final de la proteína fluorescente y el inicio del canal. La construcción se verificó por análisis de restricción del plásmido y por secuenciación. Todas las demás mutaciones se verificaron de la misma manera.

El canal eYFP-Kv2.1 se utilizó para introducir el resto de las mutaciones puntuales analizadas en el trabajo. Las mutaciones puntuales individuales A396V, A396W, G337W, L327W, S323M y G312M se introdujeron realizando una sola reacción de PCR con la enzima KOD Hot Start DNA polymerase (Novagen) y dos oligonucleótidos mutagénicos, directo y complementario, de acuerdo con las indicaciones del fabricante. Adicionalmente, los oligonucleótidos utilizados introdujeron un sitio de restricción único para

confirmar la identidad de la construcción. El producto de la PCR se trató con la enzima DpnI hidrolasa (New England Biolabs), y posteriormente se utilizó para transformar células de Escherichia coli DH5α. Las colonias presentes en placas de agar con ampicilina corresponden a células eficientemente transformadas con el plásmido que contiene la mutación puntual.

Las mutantes G317V, G337V y L264M se obtuvieron mediante la técnica de dos PCRs (Rosenbaum and Gordon, 2002). Esta técnica consiste en realizar un primer par de reacciones de PCR, cada una con un oligonucleótido mutagénico que es complementario al de la otra reacción, y un oligonucleótido no mutagénico complementario a una secuencia alejada del sitio a mutar en dirección 5' para una reacción y 3' para la otra (Fig. 9A). Los oligonucleótidos mutagénicos introducen además un sitio de restricción único para verificar el éxito del procedimiento. Por otro lado, los oligonucleótidos no mutagénicos deben flanquear dos sitios de restricción únicos presentes en el plásmido original (Fig. 9C). Con los productos de estas dos reacciones de PCR se realiza una tercera reacción utilizando únicamente los oligonucleótidos no mutagénicos (Fig. 9B). El producto de esta reacción se digiere con las enzimas de restricción correspondientes a los dos sitios que flanquean la región mutagenizada, y el fragmento de DNA resultante se liga con el plásmido que contiene el resto del canal, de donde se ha extraído previamente la secuencia equivalente a la que se mutó (Fig. 9C).

Los plásmidos se linearizaron con la enzima de restricción NotI, y se sintetizó RNA mensajero utilizando un kit de transcripción in vitro con la RNA polimerasa T7 (Ambion). El mRNA se precipitó con etanol y cloruro de litio y se resuspendió en agua tratada con DEPC (dietil-pirocarbonato), para inactivar RNAsas, a una concentración final de entre 0.5 y 1 µg/mL.

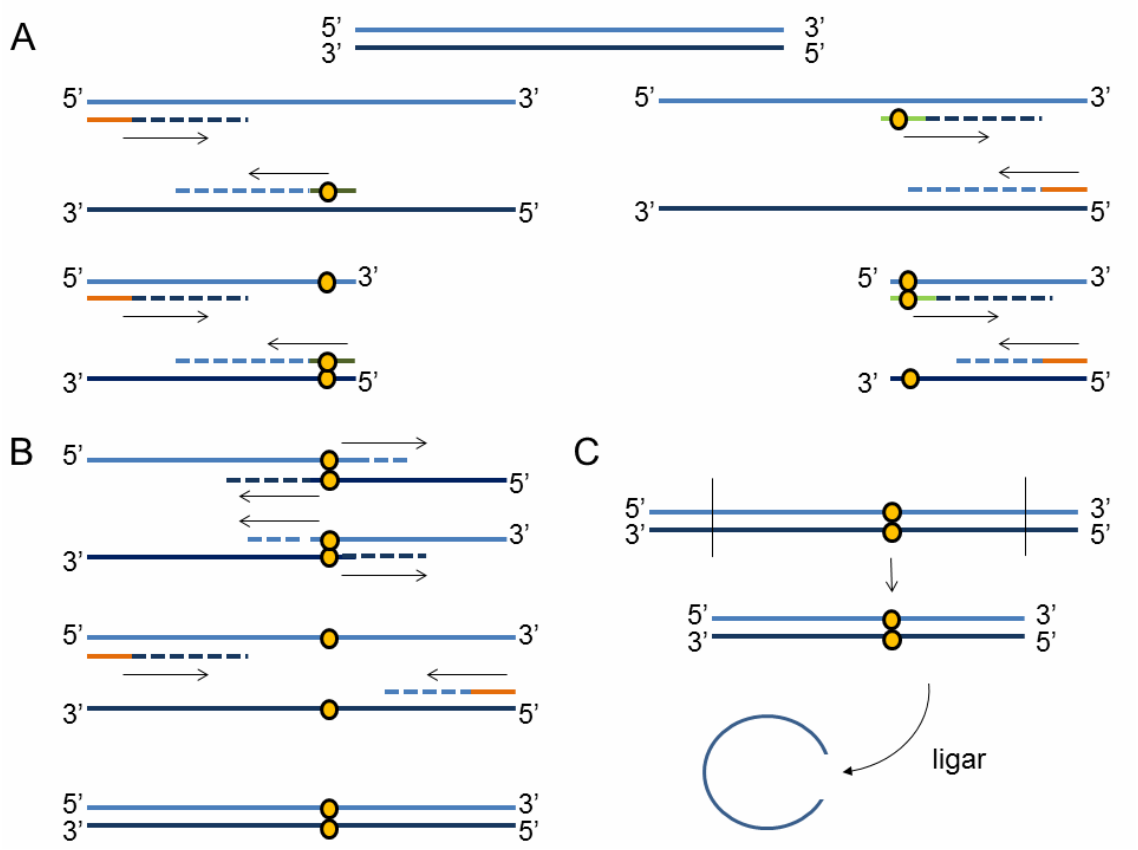

Figura 9. Mutagénesis por la técnica de dos PCRs. (A) Resultado del primer par de reacciones en cadena de la polimerasa para introducir una mutación puntual. En el panel superior se muestra la región del gen a mutagenizar, con la cadena codificante en azul claro y la cadena complementaria en azul obscuro. El panel intermedio muestra los pasos iniciales que ocurren en ambas reacciones de PCR (panel izquierdo y derecho). En el primer par de reacciones se utiliza en cada una un oligonucleótido mutagénico (verde, la posición de la mutación está indicada por el círculo amarillo) y un oligonucleótido no mutagénico que flanquea la región a mutagenizar (naranja). En el transcurso de las reacciones se amplifica la región entre ambos oligonucleótidos, la cual ya contiene la mutación (panel inferior). Esto resulta en dos fragmentos alrededor del sitio mutagenizado, cada uno producto de una de las dos reacciones de PCR. Las flechas negras indican la dirección de polimerización. Las líneas punteadas indican el producto parcial de la reacción de polimerización. (B) En la siguiente PCR se mezclan los productos de las primeras dos reacciones, y se incluyen los dos oligonucleótidos no mutagénicos (naranja) utilizados en el primer par de reacciones. La amplificación de cada una de las hebras de DNA puede ocurrir a partir de ambos templados (panel superior) o a partir de los oligonucleótidos no mutagénicos (panel intermedio). El producto de esta PCR resulta en el mismo par de cadenas de DNA original (ver (A), panel superior), con la mutación introducida (panel inferior). (C) El producto de la segunda PCR se digiere con un par de enzimas de restricción (líneas negras, panel superior), y el fragmento resultante de interés (panel intermedio) se religa en el vector original (panel inferior).

7.3. Expresión en ovocitos de rana *Xenopus laevis*

La extracción de los ovocitos se realizó como ha sido previamente descrito (Goldin, 1992). Previo a la extracción quirúrgica de los ovocitos de rana *Xenopus laevis*, los animales se anestesiaron al sumergirlos en una solución de tricaína al 0.2 % (peso/volumen) y pH 7 (NaOH) durante 5 – 10 minutos. Posteriormente se realizó una incisión en el vientre de la rana y se extrajo una sección del ovario. Las incisiones en el músculo y la piel se suturaron por separado, utilizando suturas degradables y de nylon, respectivamente. La piel de la rana se mantuvo húmeda durante el procedimiento y al final de la cirugía se dejó que la rana se recuperara en un tanque con agua.

Los sacos con los ovocitos se colocaron en solución OR2 (82.5 mM NaCl, 2 mM KCl, 1 mM $MgCl_2$, 5 mM HEPES, pH 7.5 NaOH) y se disgregaron manualmente en cúmulos pequeños. Posteriormente se colocaron en 12 mL de OR2 con colagenasa de *Clostridium hystoliticum* tipo IA (Sigma) a una concentración de 12 mg/mL y se mantuvieron en agitación leve durante 25 – 30 minutos. Después de dos lavados con OR2, los ovocitos se transfirieron a una caja petri con solución ND96 (96 mM NaCl, 2 mM KCl, 1.8 mM $CaCl_2$, 1 mM $MgCl_2$, 5 mM HEPES, pH 7.5 con NaOH) suplementada con piruvato (2.5 mM), gentamicina (20 µg/mL) y, en los ovocitos utilizados para medir corrientes de compuerta, con suero fetal bovino (Invitrogen) al 5%, penicilina/estreptomicina (Invitrogen) al 1% y cloruro de tetraetilamonio (TEA) (10 mM).

Al día siguiente de su extracción, los ovocitos fueron inyectados con 18 – 36 nL de mRNA utilizando un inyector motorizado (Drummond), y se transfirieron a pozos individuales en solución ND96 suplementada como se mencionó anteriormente. Los ovocitos se mantuvieron en una incubadora a 18 °C. Los registros electrofisiológicos se realizaron entre 1 y 5 días despúes de la inyección.

7.4. Compuestos de rutenio

Los compuestos de rutenio *trans,cis,cis*-Ru(CO)(DMS*O*)(DMSO)$_2$Cl$_2$, *cis,cis,cis*-Ru(CO)$_2$(DMSO)(DMS*O*)Cl$_2$, *fac*-Ru(CO)$_3$(DMSO)Cl$_2$, y *cis*-Ru(DMSO)$_4$Cl$_2$ se sintetizaron siguiendo métodos previamente descritos (Alessio et al., 1995; Evans et al., 1973).

Para preparar las soluciones de CORM-2 y los demás compuestos, a excepción de *cis*-Ru(DMSO)$_4$Cl$_2$, se disolvió cada uno de ellos en dimetil-sulfóxido (DMSO) a una concentración de 400 mM. El compuesto *cis*-Ru(DMSO)$_4$Cl$_2$ se disolvió en agua a una concentración de 400 mM. Las soluciones de registro suplementadas con los compuestos se prepararon tomando alícuotas de la solución 400 mM, la cual se preparó cada vez al momento de realizar los experimentos.

Para obtener el CORM-2 inactivado (iCORM), se disolvió el CORM-2 en solución de registro a una concentración de 1 mM y se dejó reposar por una semana a temperatura ambiente.

7.5. Espectrofotometría

Se prepararon soluciones base (2X) de deoximioglobina (Mb) de corazón de caballo (Sigma-Aldrich) a una concentración de 132 µM en la solución 1 de registro electrofisiológico (ver sección 7.5.2) suplementada con 0.1 % (0.118 g/mL) de ditionito de sodio para reducir el hierro del grupo prostético de la mioglobina (Motterlini et al., 2002).

La carboximioglobina (MbCO) se obtuvo mezclando en proporción 1:1 la solución 2X de deoximioglobina con solución de registro previamente burbujeada con monóxido de carbono gaseoso (Infra gas). Las soluciones de deoximioglobina en presencia de los distintos compuestos se prepararon mezclando en proporción 1:1 la solución de deoximioglobina 2X con solución de registro suplementada con cada uno de los compuestos. Como control también se preparó una solución de deoximioglobina y ditionito de sodio 1X en

ausencia de compuestos o monóxido de carbono. Los espectros de absorción se obtuvieron utilizando celdas de cuarzo de 1 cm en un espectrofotómetro Beckman DU7500. Como blanco se utilizó la solución 1 de registro.

7.6. Electrofisiología

7.6.3. La técnica de fijación de voltaje en microáreas de membrana (*patch clamp*): una breve introducción

La técnica de fijación de voltaje en microáreas de membrana revolucionó los campos de estudio de los canales iónicos y la fisiología de las células excitables al permitir obtener registros de la corriente que fluye a través de los canales en la membrana con una relación señal/ruido que permite discernir señales con una amplitud de menos de 1 pA (Hamill et al., 1981). Gracias a esta sensibilidad, se logró registrar la actividad de canales únicos y realizar experimentos de molécula única desde los años 70 (Neher and Sakmann, 1976). Además de alta sensibilidad en cuanto a la amplitud de las señales registrables, la técnica tiene también una altísima resolución temporal, ya que permite detectar señales en decenas de microsegundos y aplicar saltos de voltaje con una velocidad de aproximadamente 30 μs, de acuerdo con la velocidad de respuesta del amplificador.

La parte medular de la técnica consiste en formar sellos de alta resistencia (GΩ) entre la punta de una pipeta de 1 – 10 μm de diámetro y la membrana plasmática de una célula. Esta configuración del *patch clamp* se ha llamado *on-cell* o *cell-attached* (Fig. 10A) (Hamill et al., 1981). Esta configuración permite registrar la actividad de los canales iónicos en el parche manteniendo la composición interna de la célula intacta. La pipeta puede retirarse de la célula una vez formado el sello, lo que da origen a la configuración de *inside-out*, en donde la cara intracelular del parche de membrana adherido a la pipeta está orientada hacia el baño externo (Fig. 10B).

Por otro lado, una vez que se tiene la configuración de *cell-attached*, puede aplicarse succión para romper la membrana localizada en la apertura de la

pipeta, pero manteniendo el sello en los bordes de la misma (Fig. 10C). Esta configuración se denomina de célula completa (*whole-cell*). En *whole-cell* se tiene continuidad eléctrica (y química) entre la pipeta y el interior de la célula, manteniendo intacta la estructura cortical próxima a la membrana de toda la célula.

Finalmente, desde la configuración de célula completa puede desprenderse la pipeta de la célula, llegando a la configuración de *outside-out*, en donde la cara extracelular de la membrana está orientada hacia el exterior de la pipeta (Fig. 10D). Las configuraciones de parche escindido, *inside-out* y *outside-out*, permiten estudiar canales iónicos aislados de los componentes celulares ajenos a la membrana, además de poder controlar la naturaleza de las soluciones que bañan ambas caras del canal. Esto representa una gran ventaja para los estudios de estructura función en este tipo de proteínas.

Una vez que se tiene un sello de alta resistencia en la configuración deseada, el resto de la técnica consiste en mantener el voltaje transmembranal en un valor determinado (fijación de voltaje), y medir las corrientes que fluyen en respuesta a dicho potencial. Estas corrientes se miden utilizando un convertidor de corriente a voltaje, que transforma las pequeñas corrientes debidas a la actividad de los canales en la membrana en una señal de voltaje que se puede registrar en un osciloscopio o digitalizar para ser adquirida por una computadora. Dado que las señales medidas son muy pequeñas, el circuito de fijación de voltaje las amplifica para su adquisición.

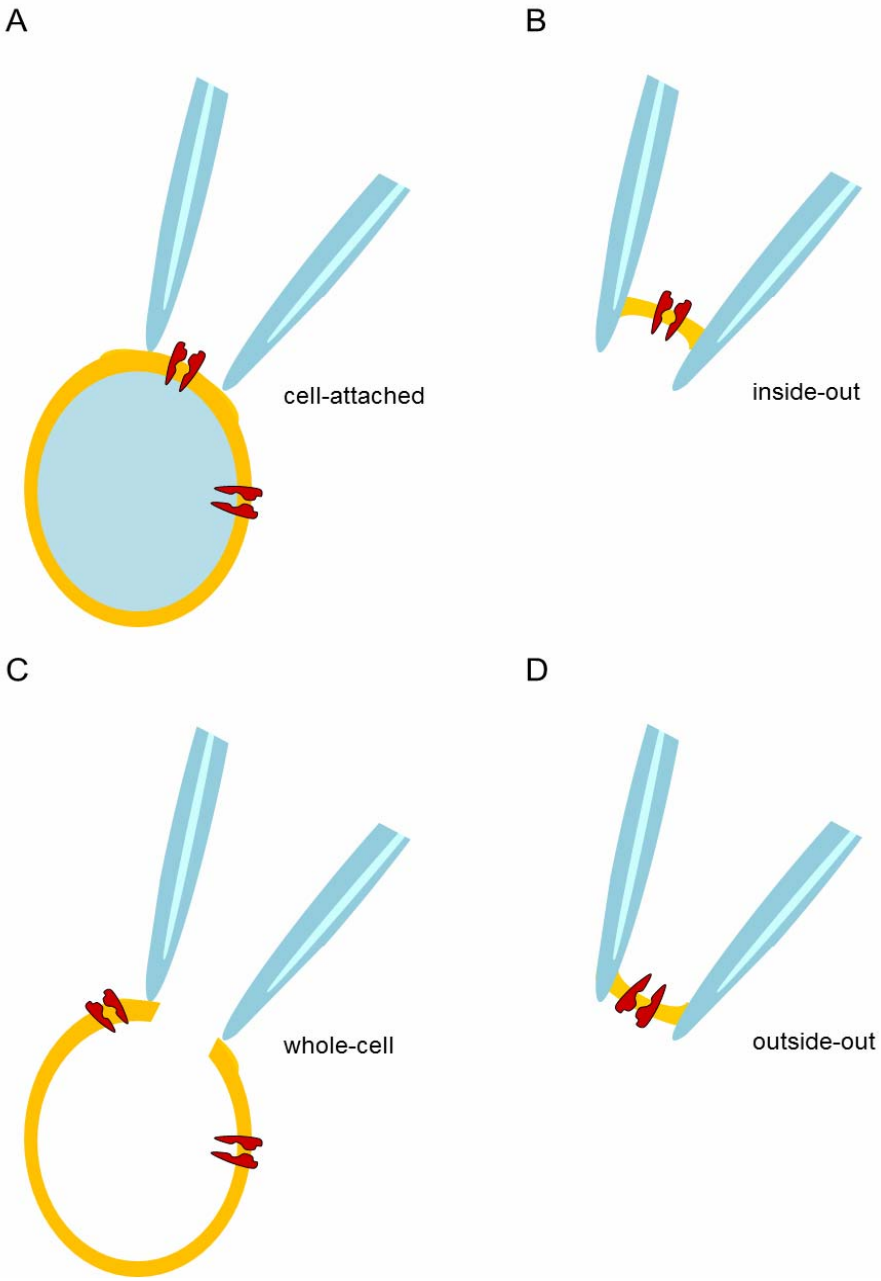

Figura 10. Configuraciones del parche de membrana en la técnica de fijación de voltaje en microáreas de membrana o *patch clamp*. (A) Configuración de *cell-attached* u *on-cell*. La pipeta se esquematiza en azul, la membrana celular en amarillo y la caricatura de un canal iónico se muestra en rojo. (B) Configuración de *inside-out*. El parche de membrana se muestra en amarillo. La cara intracelular del canal se encuentra expuesta al exterior de la pipeta. (C) Configuración de célula completa o *whole-cell*. En esta configuración la solución de la pipeta es continua con el interior de la célula, después de un cierto tiempo de diálisis. (D) Configuración de *outside-out*. En esta configuración de parche escindido, la cara extracelular del canal se expone al medio en el exterior de la pipeta.

Una versión simplificada de un posible circuito de fijación de voltaje se muestra en la Figura 11A. Como resultado del potencial aplicado (V_{ref}) y la apertura de canales en el parche de membrana adherido a la pipeta, una corriente (I_p) fluye a través del electrodo de la pipeta, pasando por la resistencia R. La magnitud de la corriente se puede determinar midiendo la caída de voltaje en la resistencia R. Sin embargo, debido al flujo de la corriente a través de la resistencia, el voltaje en V_p ya no será igual a V_{ref} (habrá una caída de potencial), por lo que el circuito no podrá mantener el voltaje en la pipeta al mismo valor que el voltaje de referencia. Para resolver este problema, se puede medir el voltaje directamente en V_p, y calcular cuánto más voltaje habría que aplicar desde la fuente de poder para compensar por la caída de potencial debida a la corriente a través de la resistencia, y así mantener el voltaje en V_p fijo. La Figura 11B muestra de forma simplificada la manera en que esto se logra en un circuito de *patch clamp* (Sigworth, 1995). Utilizando un amplificador operacional, se compara V_p con V_{ref}, y la diferencia entre ambos potenciales (V_B) se aplica a R_f, utilizando la salida del amplificador como una fuente de poder regulable. La corriente que fluye por la pipeta (I_p) causa una caída en el voltaje entre los extremos de R_f, reduciendo el valor de V_p. Sin embargo, esta caída en V_p se compensa nuevamente aplicando un voltaje extra a la salida del amplificador, para que el valor de V_p sea muy cercano al de V_{ref}. La diferencia entre V_B y V_{ref}, calculada y amplificada por el amplificador diferencial, es igual al producto de la corriente que fluye por los canales, I_p, y la resisencia R_f. Mientras más grande es R_f, mayor es la caída de potencial y por lo tanto se obtiene una mejor sensibilidad, ya que la señal de voltaje V_B con respecto a V_{ref} es mucho mayor. En términos muy generales, el circuito mide, en forma de un voltaje, la corriente que tiene que inyectar al sistema para compensar por la corriente que se está fugando a través de los canales activos, con tal de mantener el voltaje en la pipeta constante (Sigworth, 1995).

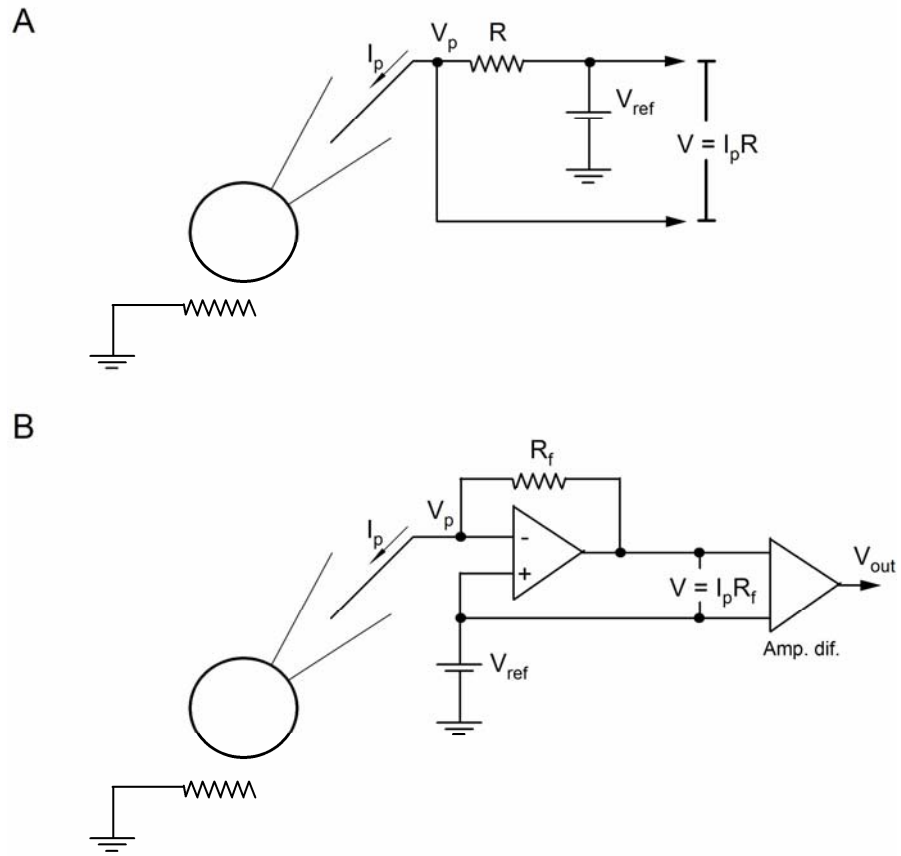

Figura 11. Esquema simplificado de un circuito de fijación de voltaje en microáreas de membrana. (A) Circuito sobresimplificado incapaz de fijar el voltaje en la membrana de la célula. El electrodo de referencia aterrizado se encuentra debajo de la célula (círculo negro) en la esquina inferior izquierda de la figura. La pipeta con el electrodo de medición está en contacto directo con la célula formando un sello de alta resistencia. La corriente que fluye del electrodo a la célula (I_p) se indica con una flecha. V_p es el voltaje en la pipeta, el cual se desea mantener constante al mismo valor que V_{ref}, dado por una fuente de poder. R es una resistencia que conecta la pipeta con la fuente de poder. La corriente I_p está dada por el producto de la diferencia en el voltaje entre V_p y V_{ref} y la resistencia R. (B) Circuito simplificado de patch clamp. El electrodo en la pipeta con potencial V_p, y la fuente de poder al potencial deseado V_{ref} se encuentran conectados a un amplificador operacional, cuya salida es la diferencia entre ambos potenciales. La salida del amplificador operacional está conectada de regreso al electrodo de la pipeta por medio de la resistencia de retroalimentación R_f, funcionando como una fuente de poder que iguala el valor de V_p al de V_{ref}. La diferencia entre el potencial a la salida del amplificador operacional (V_B) y el potencial V_{ref} es proporcional a la corriente que fluye por la pipeta. Esta diferencia de potencial se amplifica en un amplificador diferencial para su adquisición y digitalización.

En realidad, un circuito de *patch clamp* es mucho más complicado, ya que contiene elementos para compensar por múltples efectos debidos a la capacitancia del parche y la pipeta, resistencias en serie, potenciales de unión líquida, etc. Estos detalles se pueden revisar en (Single-Channel Recording, 1995). Finalmente, es importante mencionar que la señal eléctrica contínua adquirida por el amplificador se debe discretizar en el proceso de digitalización. La digitalización de componentes de alta frecuencia cuyas señales varían más rápido que la velocidad de adquisición del sistema introduciría ruido (*aliasing*) en el registro. Con el fin de eliminar todos los componentes de la señal analógica que no pueden ser adecuadamente registrados debido al límite de velocidad de adquisición del sistema, la señal eléctrica analógica se filtra antes de ser digitalizada. Generalmente se utiliza un filtro de Bessel pasa-bajas para filtrar la señal desde el amplificador, y posteriormente se adquieren los datos digitalmente a una frecuencia de al menos el doble de la frecuencia de filtraje (Colquhoun and Sigworth, 1995; Heinemann, 1995), de acuerdo con el teorema de Nyquist. Todas las señales que fluctúen con una frecuencia más baja que la frecuencia de adquisición empleada, que puede ser de hasta 100 kHz, estarán adecuadamente representadas en los registros y podrán ser caracterizadas correctamente.

7.6.4. Soluciones

Soluciones para el registro de corrientes iónicas y corrientes de compuerta del canal *Shaker*W434F:

Solución 1 (intracelular)

130 mM KCl
3 mM HEPES
1 mM EDTA pH 7.4 (KOH)

Solución 2 (extracelular)

60 mM KCl
70 mM N-metil-D-glucamina(NMDG)/Ácido aspártico (Asp)
3 mM HEPES
1 mM EDTA pH 7.4 (KOH)

Soluciones para el registro de corrientes de compuerta en el canal Kv2.1:

Solución 3 (intracelular)

130 mM NMDG
120 mM Asp
10 mM HEPES
10 mM EDTA pH 7.4 (NMDG)

Solución 4 (intracelular)

130 mM cloruro de tetraetilamonio (TEA)
10 mM HEPES
1 mM EDTA pH 7.4 (NMDG)

Solución 5 (extracelular)

1 mM KCl
130 mM NMDG
120 mM Asp
1.8 mM $CaCl_2$
10 mM HEPES pH 7.4 (NMDG)

Solución 6 (extracelular)

5 mM KCl
127 mM NMDG/Asp
1.8 mM $CaCl_2$
10 mM HEPES pH 7.4 (NMDG)

A lo largo de este trabajo, por simplicidad, se referirá a las soluciones de registro en ausencia de compuestos de prueba (e.g. CORM-2) como “salina”. En los experimentos se utilizó un sistema de capilares de plástico (de aproximadamente 2 mm de diámetro) por donde fluyen las diferentes soluciones por simple gravedad y salen a la cámara de registro. La pipeta con el parche de membrana se coloca enfrente de la salida de los capilares, para exponer al parche a los distintos tratamientos experimentales. La posición de la salida de los capilares con respecto a la pipeta se puede cambiar rápidamente utilizando un cambiador de soluciones electrónico.

Cuando se haga referencia a un experimento realizado en “salina”, se está indicando que la pipeta de registro se colocó frente a la salida del capilar que contiene dicha solución, y los registros se realizaron en condiciones de flujo continuo, tanto de salina como de soluciones suplementadas con compuestos

de prueba. La única excepción fue en el registro de corrientes de compuerta, en donde los registros se realizaron en ausencia de flujo, para evitar cambios en la amplitud de las corrientes lineales capacitivas que resultan de los cambios en el nivel del baño en la cámara de registro bajo perfusión constante. Por esta razón, en los registros de corrientes de compuerta se intercambió la totalidad del baño varias veces para modificar la composición de las soluciones a las que el interior del parche estaba expuesto.

7.6.5. Adquisición de datos y protocolos experimentales

En los registros se utilizaron pipetas de vidrio para medición de hematocrito (VWR), cuyas puntas se pulieron en una microforja (Narishige) y se cubrieron con cera dental para reducir los componentes lineales de las corrientes capacitivas durante los registros, además de aumentar la relación señal/ruido en los experimentos. La resistencia de las pipetas al momento del experimento antes de realizar el sello variaba entre 0.3 – 2.0 MΩ. Todos los registros se realizaron en la configuración de *inside-out* de la técnica de fijación de voltaje en microáreas de membrana, la cual permite cambiar las soluciones que bañan la cara intracelular de la membrana.

En todos los experimentos se utilizó un amplificador Axopatch200B (Molecular Devices) y los datos se adquirieron con el programa Pulse (HEKA Elektronik). El análisis de datos se realizó con el programa Igor (Wavemetrics). Las corrientes iónicas macroscópicas y las corrientes de compuerta se adquirieron a 20 kHz y se filtraron a 5 kHz utilizando un filtro de Bessel. Los registros de canal unitario se adquirieron a 10 kHz y se filtraron a 5 kHz, mientras que los registros de corrientes macroscópicas para realizar análisis de ruido no estacionario se adquirieron a 20 kHz y se filtraron a 10 kHz.

Se utilizó un protocolo de sustracción de –p/5 x 6 desde un potencial de mantenimiento de -120 mV. El protocolo de sustracción consiste en aplicar una secuencia de pulsos de voltaje igual a la secuencia de prueba en la que se quiere realizar la sustracción, pero con pulsos 5 veces más pequeños en amplitud (p/5) y de polaridad inversa a la secuencia de prueba (-p/5). Para

reducir el aumento en el ruido de la señal por el reescalamiento de las corrientes registradas en respuesta al protocolo de sustracción, se promediaron al menos 6 pulsos de sustracción a cada voltaje. Para corrientes iónicas macroscópicas, se utilizó un voltaje de mantenimiento de -120 mV, mientras que para las corrientes de compuerta y los registros de corrientes iónicas de los canales Slo1 y Kv2.1G317V, se utilizó un potencial de mantenimiento de -90 mV.

Las curvas dosis a respuesta para el CORM-2 y los demás compuestos de rutenio se adquirieron de la siguiente manera: se aplicó un pulso inicial a 100 mV de 100 ms de duración en presencia de salina. Posteriormente se aplicó solución suplementada con el compuesto de prueba a una concentración dada hasta que la inhibición llegara al equilibrio. Dado que el CORM-2 y algunos de los otros compuestos son relativamente lipofílicos, éstos parecen acumularse en la membrana, por lo que a concentraciones grandes del compuesto la inhibición llega rápidamente a un primer nivel, y después sigue aumentando progresivamente, probablemente debido a la acumulación. Dado que además el canal Kv2.1 sufre cambios dependientes del tiempo en sus propiedades biofísicas al estar en la configuración de parche escindido (Lopatin and Nichols, 1994), la interpretación de los resultados a tiempos largos de experimento resulta complicada. Para minimizar estas fuentes de error, sólo se analizaron los efectos tempranos del CORM-2 y se evitó realizar experimentos muy largos, en la medida en que los protocolos experimentales lo permitieron. Con el fin de no sobre estimar la inhibición por CORM-2 o los otros compuestos, sólo se evaluó una concentración por experimento. El procedimiento descrito al inicio del párrafo se repitió varias veces para cada una de las concentraciones estudiadas. La fracción inhibida se calculó de la siguiente ecuación: $f = 1 - \frac{I_x}{I_{sal}}$ (Ec. 1), donde I_x es la corriente medida en presencia del compuesto X e I_{sal} es la corriente inicial en salina. Las curvas resultantes se ajustaron a la ecuación de Hill: $f = f_{\max} \frac{[X]^s}{K_{1/2}^s + [X]^s}$ (Ec. 2), donde *[X]* es la conentración molar del compuesto, f_{max} es la fracción inhibida máxima, $K_{1/2}$ es la concentración a la cual

se obtiene la mitad de la inhibición y s el el coeficiente de Hill, que indica el grado de cooperatividad del proceso y da un estimado inferior del número de moléculas que participan en la inhibición. La curva dosis a respuesta a CORM-2 para la mutante Kv2.1G317V se graficó como $\frac{I_{corm}}{I_{sal}}$ y se ajustó al siguiente producto de dos ecuaciones de Hill: $\frac{I_{corm}}{I_{sal}} = 1 + \frac{f_{\max}}{(1+\frac{[CORM-2]^{s1}}{K_{1/2,1}^{s1}})(1+\frac{K_{1/2,2}^{s2}}{[CORM-2]^{s2}})}$ (Ec. 3).

Para determinar las curvas de conductancia contra voltaje (curvas G-V) del canal Kv2.1, se aplicaron secuencias de pulsos de 100 ms de duración desde -120 mV hasta 100 mV en incrementos de 20 mV regresando al potencial de mantenimiento de -120 mV. Entre pulsos de prueba se aplicó el protocolo de sustracción y se empleó un intervalo entre pulsos de 200 ms. Se midió la amplitud de las colas de corriente a -120 mV después de cada pulso de prueba, y los valores obtenidos se normalizaron a la amplitud de la cola de corriente medida después del pulso a 100mV. Para determinar la curva G-V del canal Kv2.1 en bajo potasio, se utilizaron la solución intracelular 3 y la solución extracelular 6. En este caso se aplicaron pulsos de prueba de 50 ms de duración, debido a un aumento en la inactivación del canal bajo estas condiciones, y se utilizó un potencial de mantenimiento de -90 mV. Las curvas G-V para *Shaker* se determinaron a partir de la corriente en el estado estacionario a cada voltaje de prueba, suponiendo un comportamiento óhmico para la conductancia. Para hacer esto se construyeron curvas de corriente contra voltaje a partir de los valores de corriente en el estado estacionario, y se ajustó una línea recta a la porción lineal de la curva. La recta se extrapoló a todos los voltajes y se utilizó para normalizar los datos y obtener la curva G-V. Los valores cercanos al potencial de inversión de la corriente (-20mV) se eliminaron debido al error inherente al proceso de normalización. Las curvas se ajustaron a la ecuación de Boltzmann: $G_{norm} = \frac{G_{\max}}{1+e^{\frac{z(V-V_{1/2})}{k_B T}}}$ (Ec. 4), donde G_{max} es la conductancia máxima, z es la carga aparente (en unidades de e_0)

asociada a la transición de apertura y cierre del canal, V es el voltaje de prueba, $V_{1/2}$ es el voltaje medio de activación, k_B es la constante de Boltzmann y T la temperatura. Las curvas G-V en presencia de CORM-2 se normalizaron al mismo valor que se utilizó para normalizar las curvas en salina, y se determinaron después de haber obtenido los registros en ausencia del compuesto.

La cinética de activación de ambos canales se determinó a partir de ajustes de una función exponencial a datos experimentales obtenidos con el mismo protocolo de pulsos que se utilizó para determinar las curvas G-V. Las funciones exponenciales se ajustaron a las corrientes en la segunda mitad del proceso de activación, ignorando los procesos iniciales que confieren sigmoidicidad a las curvas. Para cuantificar la cinética de cierre, se aplicaron secuencias de pulsos que iniciaban en 100 mV durante 100 (Kv2.1) ó 50 ms (*Shaker*), seguidos de pulsos de 100 ms a distintos voltajes, de -150 a -70 mV en incrementos de 20 mV para Kv2.1 o de -170 a -50 mV en incrementos de 10 mV para *Shaker*, finalizando siempre en el potencial de reposo de -120 mV. Se ajustaron funciones mono- o biexponenciales a las colas de corriente para obtener las constantes de velocidad de cierre. Por cada parche se realizaron mediciones en salina y en presencia de CORM-2.

Las mediciones del retraso en la activación de la corriente de *Shaker*, el cual refleja el paso del canal entre estados cerrados previos a la apertura del poro (Cole and Moore, 1960; Schoppa and Sigworth, 1998a), se cuantificó ajustando la siguiente ecuación a los mismos trazos de corriente que se utilizaron para cuantificar la cinética de activación del canal: $I(t) = A - e^{\frac{-(t-\delta)}{\tau}}$ (Ec. 5), donde $I(t)$ es la corriente iónica al tiempo t (t = 0 es el tiempo en que se aplicó el pulso de prueba), A es la amplitud final de la corriente en el estado estacionario, δ es el retraso en la activación y τ es la constante de tiempo para el incremento monoexponencial de la corriente, que corresponde con el inverso del valor de las constantes de velocidad de activación del canal cuya medición se describió con anterioridad.

El análisis de ruido no estacionario se realizó como se ha descrito en (Heinemann and Conti, 1992; Sigworth, 1980). Se aplicaron entre 50-100 pulsos de voltaje de 200 ms de duración a 100 mV a partir del potencial de reposo de -120 mV. En este caso no se aplicó ningún protocolo de sustracción. Se calculó la varianza entre trazos para cada punto en el registro de corriente utilizando el algoritmo de Heinemann y Conti (Heinemann and Conti, 1992). La varianza obtenida se graficó contra la corriente media, y las gráficas se ajustaron a la siguiente ecuación parabólica: $\sigma^2 = \langle I \rangle i - \frac{\langle I \rangle^2}{N}$ (Ec. 6), donde σ^2 es la varianza, $<I>$ es la corriente media, i es la amplitud de corriente de un canal único y N es el número de canales en el parche. Con los valores para el número de canales y la corriente unitaria obtenidos a partir de este ajuste, se calculó la probabilidad de apertura del canal de acuerdo con: $P_o = \frac{\langle I \rangle_{\max}}{Ni}$ (Ec. 7), donde $<I>_{max}$ es la corriente media máxima a cada voltaje (en el estado estacionario).

Para los registros de canal unitario, se aplicaron pulsos de 200 ms de duración a 100 mV. Un promedio de varios trazos de corriente sin aperturas se utilizó para sustraer la corriente de fuga y la corriente capacitiva. Se construyeron histogramas de todos los puntos para la amplitud de la corriente tomando fragmentos de registros que incluyeran eventos de apertura y cierre. Se utilizó una suma de dos curvas gaussianas para ajustar los histogramas obtenidos y estimar el valor de la corriente unitaria media a 100 mV en salina y en presencia de CORM-2. Estos mismos registros se utilizaron para calcular la latencia a la primera apertura. Para ello se utilizó la técnica del cruce del umbral al 50% para detectar aperturas (Colquhoun and Sigworth, 1995): Primero se determinó un valor umbral para la corriente correspondiente a aproximadamente el 50% de la amplitud media de la corriente unitaria a 100 mV. Para cada trazo de corriente se determinó el número de puntos en el registro que había antes de que la corriente tuviera un valor mayor al umbral, lo que se interpreta como una apertura del canal. Se construyeron trazos idealizados para cada trazo experimental, que tomaban el valor de cero para los puntos antes de que se cruzara el umbral por primera vez y 1 para el resto

del pulso una vez cruzado el umbral. La suma de todos los trazos idealizados para un mismo experimento, normalizada al número total de pulsos, es la latencia del canal, que es equivalente a la probabilidad acumulada de que el canal se abra por primera vez dado un voltaje y en función del tiempo. Los trazos que iniciaban con canales abiertos se eliminaron del análisis.

Las corrientes de compuerta se obtuvieron aplicando pulsos de 30 ms de duración desde -90 mV hasta 80 mV en incrementos de 20 mV a partir de un potencial de mantenimiento de -90 mV. Se promediaron al menos 20 trazos de corriente por voltaje para aumentar la relación señal/ruido de los datos. Se utilizó un intervalo entre pulsos de al menos 2 s. En algunos casos se observó una meseta de corriente constante a voltajes por arriba de 0 mV. Este es un artefacto de la sustracción, y se compensó sustrayendo un pulso cuadrado de los trazos de corriente que presentaran la meseta, de tal forma que las corrientes de compuerta sustraídas se relajaran a 0 pA al final del pulso. La carga de compuerta se calculó integrando el área bajo la curva de las corrientes de compuerta. La curva Q-V resultante se ajustó a la ecuación de Boltzmann: $Q_{norm} = \frac{Q_{\max}}{1 + e^{\frac{z(V - V_{1/2})}{k_B T}}}$ (Ec. 8). La cinética de activación y desactivación de las corrientes de compuerta se cuantificó ajustando funciones mono exponenciales a los trazos de corriente.

Los cursos temporales de la inhibición por CORM-2 bajo condiciones de alta probabilidad de apertura se midieron aplicando un tren de pulsos de 100 ms de duración a 100 mV, primero en salina para medir la corriente inicial, y después en presencia de CORM-2. Los cursos temporales de inhibición en el estado cerrado se obtuvieron de la siguiente manera: se midió la corriente inicial en salina a 100 mV y posteriormente se aplicó CORM-2 al potencial de mantenimiento de -120 mV por un tiempo variable, tras el cual se regresó el voltaje a 100 mV para medir la corriente remanente. Este procedimiento se repitió varias veces en parches distintos utilizando diferentes tiempos de exposición al CORM-2 en el estado cerrado para construir el curso temporal.

7.7. Modelado cinético

Los sistemas de ecuaciones diferenciales correspondientes a los modelos presentados en los Esquemas I y II se resolvieron por el método de diferenciación hacia atrás, como se encuentra implementado en Igor Pro.

Las corrientes iónicas se calcularon de acuerdo a: $I(V,t) = P_o(t,V)Ng(V - V_{rev})$ (Ec. 9), donde $P_o(t,V)$ es la ocupancia de los estados abiertos como función del tiempo (la probabilidad de apertura), N es el número de canales, g es la conductancia unitaria, V_{rev} es el potencial de inversión y V es el potencial de prueba. Las corrientes de compuerta se calcularon de acuerdo a: $I_g(t,V) = \sum_{i,j} P_i(t,V)k_{ij}(z_{ij} - z_{ji})$ (Ec. 10), donde $P_i(t,V)$ es la ocupancia del estado i, k_{ij} es la constante de velocidad entre los estados i y j y tiene la siguiente forma: $k_{ij}(V) = k_{ij}(0mV)\exp(-z_{ij}V / k_BT)$ (Ec. 11), z_{ij} y z_{ji} son las cargas parciales asociadas a las constantes de velocidad entre ambos estados.

Para simular las corrientes iónicas y de compuerta se utilizaron las mismas condiciones de voltaje que los registros experimentales. Los valores de las constantes cinéticas predichos por el modelo se calcularon realizando ajustes a funciones exponenciales de las corrientes simuladas de la misma manera en que se hizo con los datos experimentales. Las curvas Q-V y G-V son directamente calculadas por el programa que genera las simulaciones, por lo que lo único que se tuvo que hacer fue normalizarlas de la misma manera en que se normalizaron los datos experimentales.

La calidad de las predicciones de los modelos se evaluó por inspección visual de la correspondencia entre los resultados experimentales (v.g. la forma de las corrientes iónicas y de compuerta en función del voltaje, la cinética de activación y desactivación, las curvas G-V y Q-V) y las predicciones realizadas por el modelo. Debido a esto, los valores numéricos de los parámetros del modelo reportados en este trabajo no son los únicos capaces de reproducir las observaciones experimentales, ni son los mejores en términos de parámetros estadísticos que cuantifican la calidad del ajuste. Esto no representa una

limitación en cuanto a los objetivos del uso de modelos matemáticos en esta tesis, puesto que más que obtener valores específicos para los parámetros, se deseaba identificar rasgos generales requeridos en los parámetros que fueran necesarios para reproducir las respuestas funcionales observadas experimentalmente.

8. RESULTADOS

8.1. El CORM-2 reduce la conductancia macroscópica de un ensamble de canales Kv2.1 por medio de un mecanismo alostérico.

En un estudio dirigido a determinar el mecanismo de modulación del canal Kv2.1 por gases, se decidió probar una serie de compuestos capaces de liberar monóxido de carbono (CO), entre ellos el dímero de tricarbonildicloro rutenio o CORM-2 (*Carbon Monoxide Releasing Molecule-2*) (Fig. 8). Esta molécula es ampliamente utilizada en estudios experimentales de los efectos fisiológicos del monóxido de carbono, un "gasotransmisor" que cuando es sintetizado por el cuerpo parece estar relacionado con un sinnúmero de procesos como la protección contra estrés oxidativo en el sistema nervioso central (Dallas et al., 2011), la regulación vascular (Leffler et al., 2011), la función renal (Csongradi et al., 2012) y la detección de cambios en la concentración de oxígeno (Kemp et al., 2009), entre otros. La preferencia por el CORM-2 como herramienta experimental viene de su alta eficiencia en la liberación del gas, la cual ocurre en unos pocos segundos cuando el compuesto está en solución acuosa (Motterlini et al., 2002), mientras que otros compuestos liberan monóxido de carbono más lentamente o incluso requieren de radiación ultravioleta para catalizar la reacción (Alberto and Motterlini, 2007; Motterlini and Otterbein, 2010). Dado que el monóxido de carbono endógeno que funciona como segundo mensajero se produce dentro de la célula, se decidió probar los efectos del compuesto cuando es aplicado a la cara intracelular del canal Kv2.1, utilizando la técnica de fijación de voltaje en microáreas de membrana en la configuración de *inside-out*.

En la Figura 12A se muestra una familia de corrientes representativas del canal Kv2.1 obtenidas en respuesta a una serie de pulsos desde -120 hasta 100 mV en incrementos de 20 mV registradas de un parche de membrana en la configuración de *inside-out* expuesto a solución salina. Estas corrientes no se observaron en parches de ovocitos inyectados con agua (no se muestran los datos). Al exponer el parche a una solución suplementada con 0.5 mM CORM-2 (Fig. 12A), se obervó una marcada disminución en la amplitud de la corriente, junto con una disminución en la velocidad de activación y cierre del canal.

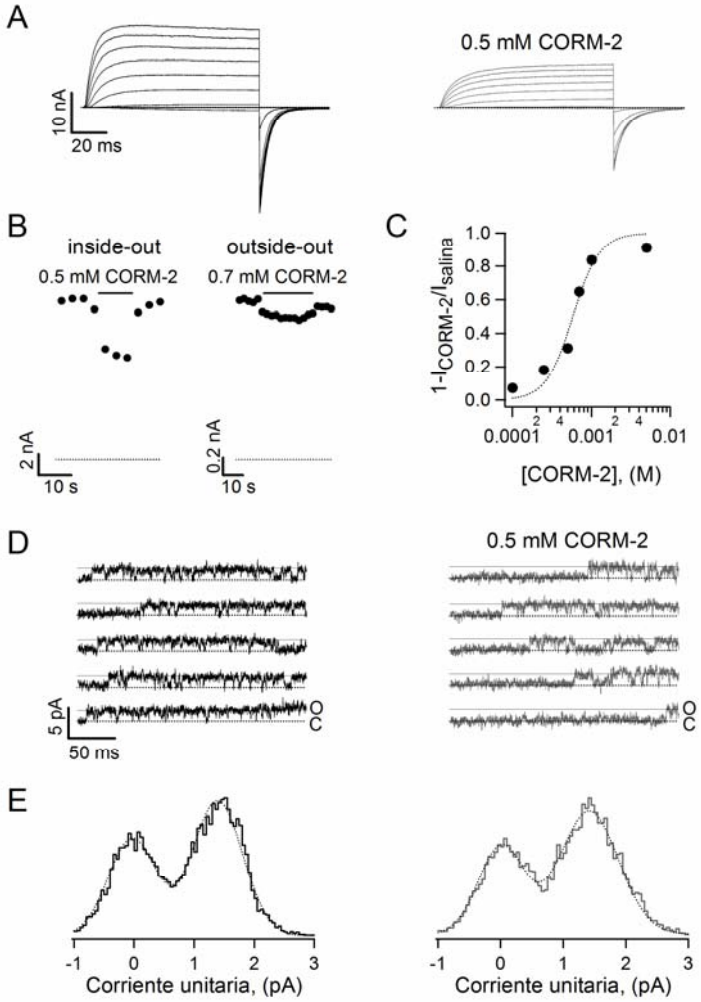

Figura 12. La presencia de CORM-2 induce una inhibición alostérica del canal Kv2.1. (A) Familias de corriente representativas del canal Kv2.1 en salina y en presencia de 0.5 mM CORM-2. Las corrientes se activaron con pulsos desde -120 hasta 100 mV en incrementos de 20 mV. Las líneas punteadas indican el cero de corriente. (B) Cursos temporales representativos a 100 mV de la inhibición del canal por CORM-2 cuando es aplicado a la cara interna (panel izquierdo) o externa (panel derecho) del canal. Las líneas punteadas marcan el nivel de cero corriente. (C) Curva dosis a respuesta a CORM-2 obtenida a 100 mV. La curva punteada es un ajuste a la ecuación de Hill (Ec. 2) con parámetros: $K_{1/2}$ = 0.56 mM y s = 2.8 (n = 3 - 15). (D) Registros de canal unitario representativos en salina y en presencia de 0.5 mM CORM-2 a 100 mV. Las letras O y C indican los niveles de corriente media que corresponden al estado abierto y cerrado del canal, respectivamente. (E) Histogramas de todos los puntos para la amplitud de la corriente unitaria de los registros mostrados en (D). Las curvas punteadas son ajustes a la suma de dos curvas Gaussianas. Los valores de corriente unitaria media obtenidos del ajuste en ausencia y presencia de CORM-2 son: i_{sal} = 1.57 ± 0.16 pA, i_{corm} = 1.51 ± 0.07 pA.

Dado que los gases son capaces de permear a través de las membranas biológicas, es posible que aunque en el experimento mostrado en la Fig. 12A se haya aplicado el compuesto a la cara intracelular del canal, la inhibición ocurriera por la interacción del gas con la cara extracelular del canal, al haber permeado a través de la membrana. Lo mismo es válido para la molécula de CORM-2, la cual es relativamente lipofílica. Para determinar si la inhibición depende de interacciones con la cara intra- o extracelular del canal, se determinó el efecto del CORM-2 cuando es aplicado directamente a la cara extracelular del canal, utilizando parches de membrana en la configuración de *outside-out*. Como se muestra en la Figura 12B, los efectos del CORM-2 cuando éste es aplicado a la cara externa del canal son mucho menores que cuando se aplica a la cara interna. Estos datos sugieren que el sitio de interacción es intracelular, por lo que se decidió enfocarse únicamente en los efectos del CORM-2 cuando es aplicado a la cara intracelular del canal.

Otro aspecto importante de la Fig.12B es la reversibilidad de la inhibición. Aunque al retirar el compuesto se recupera la amplitud inicial de la corriente, la cinética del canal se ve irreversiblemente alterada si la exposición al compuesto es larga o la concentración del compuesto es grande (no se muestran los datos). Esto podría ser resultado de la acumulación del compuesto en la membrana. Por otro lado, el canal en parches escindidos presenta alteraciones dependientes del tiempo (en cuestión de minutos) tanto en la cinética de activación y cierre como en el equilibrio entre el estado abierto y cerrado (Lopatin and Nichols, 1994). Por estos motivos se evitó realizar experimentos utilizando exposiciones largas al CORM-2 y el análisis se limitó a los efectos rápidos del CORM-2, dentro de los límites de los protocolos experimentales utilizados.

Para caracterizar con más detalle la inhibición, se obtuvo una curva de dosis a respuesta para el CORM-2 (Fig. 12C). La inhibición resultó ser dependiente de la concentración de CORM-2, con una $K_{1/2}$ de 0.56 mM y un coeficiente de Hill de 2.8. La alta cooperatividad de la inhibición, reflejada en el coeficiente de Hill mayor a uno, indica la participación de más de una molécula en el proceso. Este resultado arguye en contra de que la inhibición sea el resultado del bloqueo directo de la vía de conducción iónica, ya que el poro intracelular no es

tan grande como para acomodar múltiples moléculas que se unen con cooperatividad positiva. Además, los compuestos que funcionan como bloqueadores del poro de canales catiónicos generalmente son moléculas con carga positiva, mientras que ni el CO ni el CORM-2 tienen carga. Finalmente, no se esperaría que un simple bloqueador del poro tuviera efectos tanto sobre la cinética de activación como la de cierre. Estas consideraciones sugieren que la reducción en la conductancia causada por el CORM-2 resulta de un efecto alostérico sobre el poro, y no del bloqueo directo del mismo.

Una reducción en la conductancia macroscópica de un parche de membrana con muchos canales podría resultar de una reducción en la probabilidad de apertura de los canales, de una reducción en la conductancia unitaria de cada canal o bien de una pérdida total de la funcionalidad de algunos canales en el parche, mientras que el resto permanece intacto. Para descartar que la inhibición resulte de una modificación en la conductancia de los canales, se realizaron registros de canal unitario en ausencia y presencia de 0.5 mM CORM-2 a 100 mV. El CORM-2 no tuvo ningún efecto sobre la corriente unitaria del canal (Fig. 12D y E), lo que es consistente con la ausencia de alteraciones directas o indirectas en las propiedades biofísicas de la vía de conducción iónica cuando el canal está en el estado abierto. La corriente unitaria también se estimó por medio de análisis de ruido no estacionario (no se muestran los datos), donde se obtuvieron valores de corriente unitaria de 1.76 ± 0.17 y 1.66 ± 0.15 pA (n = 10), en ausencia y presencia de 0.5 mM CORM-2, respectivamente. El número de canales activos en el parche calculado a partir de este análisis tampoco varió significativamente (N_{corm}/N_{sal} = 0.84 ± 0.09), indicando que la reducción en la conductancia macroscópica observada en presencia del CORM-2 no resulta de la pérdida de funcionalidad de los canales, sino de una reducción en la probabilidad de apertura.

8.2. La molécula de CORM-2, y no el monóxido de carbono que libera, es responsable de la inhibición.

La siguiente pregunta que se planteó fue si los efectos observados dependen del CO liberado o de la molécula donadora. Como primera aproximación, se determinó si el CORM-2 inactivado (iCORM) es capaz de inhibir al canal Kv2.1. El iCORM es una solución de CORM-2 que ha liberado todo el monóxido de carbono, y está constituida por un conjunto de productos de degradación del donador. Como control inicial se determinó si el iCORM activa al canal Slo1, el cual se modula directamente por CO (Brazier et al., 2009; Hou et al., 2008; Williams et al., 2008). Como se muestra en la Fig. 13A, el iCORM no produjo un aumento en la corriente del canal Slo1, mientras que el CORM-2 fresco causó un incremento significativo en la conductancia macroscópica. En contraste, el iCORM provocó una reducción reversible en la corriente mediada por el canal Kv2.1 (Fig. 13B). El hecho de que la inhibición causada por el iCORM es menor que la provocada por CORM-2 fresco a la misma concentración no es sorprendente, ya que el iCORM es una mezcla de moléculas estructuralmente similares al CORM-2 fresco, pero distintas.

Un problema con el experimento anterior es que la composición molecular del iCORM se desconoce. Para sortear esta dificultad, generalmente se utiliza la molécula $Ru(DMSO)_4Cl_2$ (Fig. 14) como control negativo para la liberación de monóxido de carbono (Williams et al., 2004). En solución acuosa, esta molécula puede liberar entre una y dos moléculas de DMSO y unir agua en su lugar (Alessio et al., 1988; Brindell et al., 2007), por lo que su estructura muy probablemente se asemeja a los compuestos presentes en el iCORM. Sin embargo, las moléculas de DMSO son significativamente diferentes a los carbonilos presentes en el CORM-2, por lo que la molécula de $Ru(DMSO)_4Cl_2$ no es el control ideal. Por esta razón, se sintetizaron una serie de compuestos más parecidos al CORM-2 que la molécula de $Ru(DMSO)_4Cl_2$, y que además poseen distintas capacidades para liberar monóxido de carbono, y contienen distintas proporciones de moléculas de DMSO o CO asociadas al rutenio central (Fig. 14).

Como se muestra en la Figura 13C, todos los compuestos sintetizados fueron capaces de inhibir al canal Kv2.1, aunque con afinidades y potencias distintas a las del CORM-2. Paralelamente se evaluó la capacidad de cada una de las moléculas para liberar CO, al monitorear los cambios en el espectro de absorción de la mioglobina en presencia de cada uno de los compuestos. La mioglobina presenta un drástico cambio en su espectro de absorción cuando no está unida a ningún gas (Fig. 13D, trazo negro punteado) con respecto a cuando une monóxido de carbono (Fig. 13D, trazo negro continuo), por lo que resulta una buena herramienta para monitorear la liberación del CO. Como se esperaba, los compuestos $Ru(DMSO)_4Cl_2$ y $Ru(CO)(DMSO)_3Cl_2$ fueron incapaces de convertir la deoximioglobina (Mb) en carboximioglobina (COMb), indicando que ninguno de estos compuestos libera monóxido de carbono. Sin embargo, ambos inhibieron al canal Kv2.1 con afinidades y potencias distintas, indicando que estas discordancias resultan de las diferencias estructurales entre las moléculas y no de su capacidad para liberar CO. Por otro lado, se espera que cada molécula de $Ru(CO)_2(DMSO)_3Cl_2$ libere una sola molécula de CO, mientras que $Ru(CO)_3(DMSO)Cl_2$ podría liberar dos. Sin embargo, la afinidad de estas moléculas por el canal es la misma (Fig. 13C). Finalmente, tanto un monómero de CORM-2 como la molécula de $Ru(CO)_3(DMSO)Cl_2$ liberan la misma cantidad de moléculas de CO, pero sus afinidades por el canal son distintas, confirmando que la inhibición resulta de la interacción de las moléculas de CORM-2 con el canal, y es independiente del CO liberado.

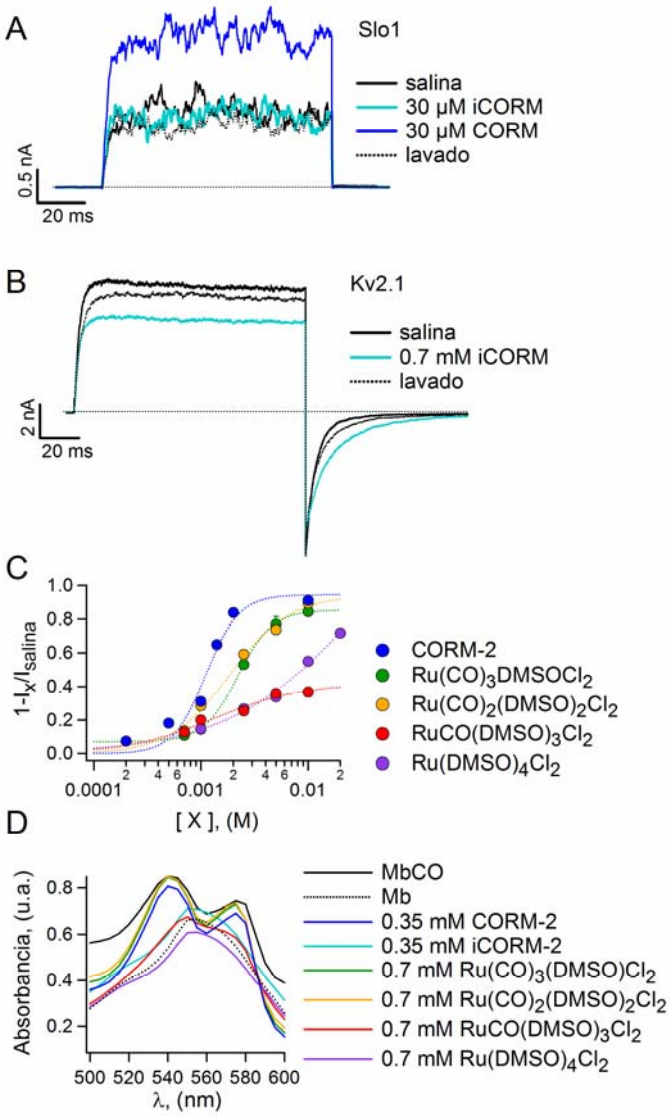

Figura 13. Compuestos de rutenio estructuralmente relacionados con el CORM-2 que no pueden liberar CO inhiben al canal Kv2.1. (A) Corrientes representativas del canal Slo1 activado por pulsos de voltaje a 140 mV desde un potencial de reposo de -90 mV en ausencia de calcio, obtenidas en el mismo parche bajo las condiciones indicadas en la figura. La línea punteada indica el cero de corriente. (B) Corrientes representativas del canal Kv2.1 a 100 mV obtenidas en el mismo parche bajo las condiciones indicadas en la figura. (C) Curvas dosis a respuesta obtenidas a 100 mV para la serie de compuestos cuya estructura se muestra en la Figura 14. I_x se refiere al valor medio de la corriente en estado estacionario medida en presencia del compuesto x. La curva dosis a respuesta para el CORM-2 se corrigió para tomar en cuenta que cada molécula del donador aporta dos monómeros con respecto a los demás compuestos. Las curvas punteadas son ajustes a la ecuación de Hill (Ec. 2). Los parámetros obtenidos son: $Ru(CO)_3(DMSO)Cl_2$, $K_{1/2}$ = 2.04 mM, s = 2.1, Max inh. = 0.88; $Ru(CO)_2(DMSO)_2Cl_2$, $K_{1/2}$ = 1.86 mM, s = 1.54, Max inh. = 0.94; $Ru(CO)(DMSO)_3Cl_2$, $K_{1/2}$ = 1.31 mM, s = 1.08, Max inh. = 0.42; $Ru(DMSO)_4Cl_2$, $K_{1/2}$ = 8.18 mM, s = 0.94, Max inh. = 1.0 (n = 5). (D) Espectros de absorción de la mioglobina bajo las condiciones indicadas en la figura.

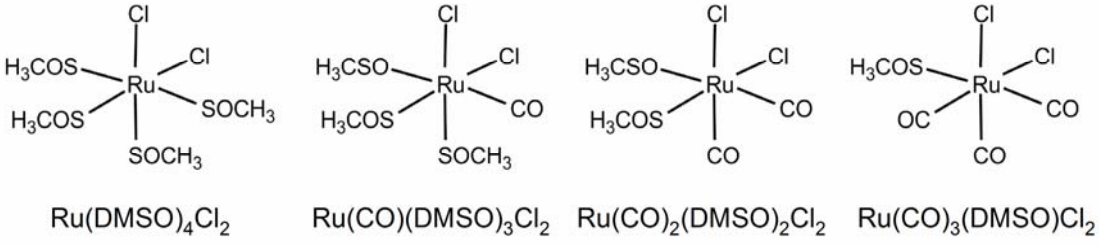

Figura 14. Estructuras de los compuestos de rutenio relacionados al CORM-2.

Para proveer una evidencia más de que la inhibición es independiente del CO, se utilizó hemoglobina como quelante de monóxido de carbono y se determinó si el CORM-2 es capaz de inhibir al canal en presencia de esta proteína. Como era de esperarse, la presencia de hemoglobina en la solución interfirió con la activación del canal Slo1 por CORM-2 (Fig. 15A), indicando que dicha proteína puede utilizarse como un quelante del gas. Al aplicar el CORM-2 en presencia de hemoglobina al canal Kv2.1 no se observó una inhibición mayor que la provocada por la presencia del agente reductor ditionito de sodio, utilizado para reducir el hierro del grupo prostético de la hemoglobina, cuando éste se aplicó por sí sólo. Sin embargo, esta inhibición del efecto del CORM-2 no depende de la hemoglobina, dado que el efecto sobre el canal de la solución con CORM-2 y ditionito en ausencia de hemoglobina fue el mismo que el de una solución con CORM-2, ditionito y hemoglobina (Fig. 15B).

Existen tres explicaciones para el resultado anterior: primero, es posible que el ditionito de sodio modifique covalentemente al canal en un sitio importante para la acción del CORM-2, interfiriendo con los efectos del donador. Segundo, el CORM-2 y el ditionito podrían competir por el mismo sitio en el canal, y la concentración de ditionito utilizada en el experimento podría haber sido saturante, desplazando por completo al CORM-2 de su sitio. Tercero, es posible que el CORM-2 y el ditionito reaccionen químicamente, y la molécula resultante tenga una afinidad tan baja por el canal que no contribuye a la inhibición. Para determinar cuál de estas posibilidades es correcta, se realizó el experimento mostrado en la Figura 15C. El exponer el parche de membrana al ditionito de sodio inicialmente no interfirió con la subsecuente inhibición por CORM-2 cuando éste se aplicó sólo, indicando que el ditionito de sodio no modifica covalentemente al canal para impedir la unión del CORM-2. También se observó que una concentración mayor de ditionito de sodio provoca una mayor inhibición, demostrando que la concentración de ditionito utilizada en el experimento anterior no era saturante. Estos resultados indican que la tercera posibilidad es la correcta, y demuestran que la inhibición del canal por CORM-2 depende de la integridad estructural de la molécula del donador, y no del gas que ésta libera.

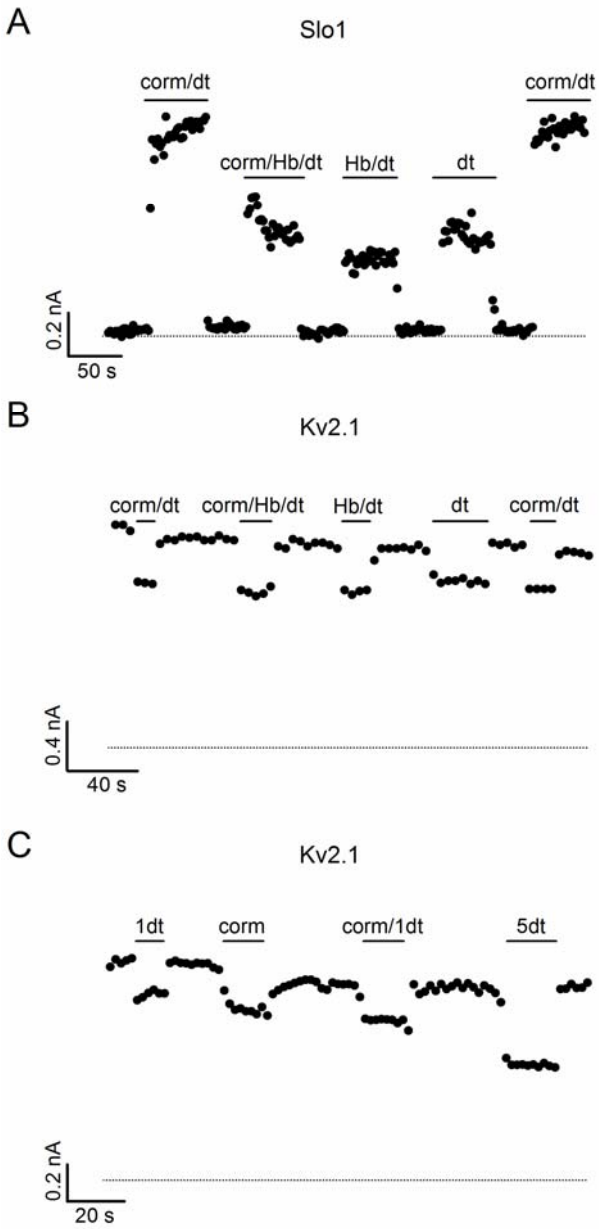

Figura 15. El CORM-2 activa al canal Slo1 por medio del CO liberado, pero inhibe al canal Kv2.1 de manera independiente del gas. (A) Curso temporal de la activación del canal Slo1 por CORM-2 (corm, 0.12 mM) a 80 mV, ya sea en presencia de ditionito de sodio (dt, 1 mM) únicamente, o con deoxi-hemoglobina (Hb, 0.1 mM). (B) Curso temporal de inhibición del canal Kv2.1 por CORM-2 (0.3 mM) a 100 mV por sí solo o en presencia de ditionito de sodio (1 mM) o de ditionito de sodio + deoxi-hemoglobina (0.25 mM). (C) Curso temporal de inhibición del Kv2.1 por CORM-2 (0.3 mM), ditionito de sodio (1dt, 1 mM; 5 dt, 5 mM) y CORM-2 (0.3 mM) + ditionito de sodio (1 mM). Las líneas punteadas marcan el cero de corriente. Los puntos en el curso temporal son la corriente media en el estado estacionario medida bajo cada una de las condiciones indicadas en la figura.

Aunque la inhibición del canal por CORM-2 no tiene relevancia fisiológica, las características de la inhibición, tales como su naturaleza alostérica y los efectos del compuesto sobre la cinética del canal, son interesantes por sí mismas. Dado que la comprensión del mecanismo de acción del CORM-2 sobre el canal podría arrojar información valiosa sobre la manera en la que el canal funciona, se decidió caracterizar los efectos del compuesto con más detalle.

8.3. El CORM-2 afecta la dependencia en el voltaje del canal.

Para determinar si el CORM-2 afecta la dependencia en el voltaje del canal, se obtuvieron curvas de conductancia contra voltaje en ausencia y presencia de dos concentraciones de CORM-2, los datos se muestran en la Figura 16A. Ambas concentraciones de CORM-2 causaron una disminución en la conductancia macroscópica sin provocar un corrimiento significativo en el voltaje medio de activación, como se observa en los ajustes normalizados de la ecuación de Boltzmann a los datos en presencia del donador (Fig. 16A, curvas punteadas). Sin embargo, el compuesto provocó una reducción en la pendiente de las curvas, la cual indica cambios en la carga aparente asociada con las transiciones de apertura y cierre del canal.

La ausencia de un corrimiento en el voltaje medio de activación indica que el compuesto podría estar afectando la cinética de activación y cierre en igual medida. Para determinar si esto ocurre, se determinó el efecto del CORM-2 sobre la cinética del canal. Como se muestra en la Figura 16B, el compuesto causó una reducción en la velocidad de activación y cierre del canal de manera dependiente de la concentración. Para realizar un análisis más cuantitativo, se determinaron las constantes de velocidad de activación y cierre en solución salina y en presencia de 0.5 ó 0.7 mM CORM-2 (Fig. 16C). Sorprendentemente, el compuesto no sólo afectó el tamaño de la barrera de activación asociada a cada una de las constantes de velocidad, lo que se refleja en una disminución del valor de la constante de velocidad a 0 mV, sino que también tuvo un profundo efecto sobre la carga aparente asociada a cada una de las transiciones, especialmente sobre la constante de velocidad de activación en presencia de 0.7 mM CORM-2, la cual se volvió prácticamente independiente del voltaje (Fig. 16C).

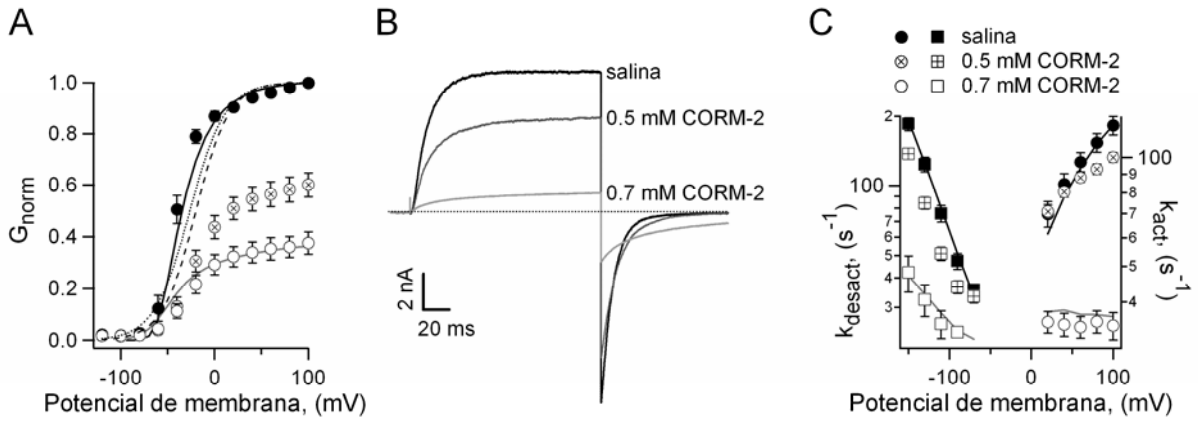

Figura 16. El CORM-2 reduce la dependencia en el voltaje del canal Kv2.1. (A) Curvas G-V obtenidas en salina (●) y en presencia de 0.5 (⊗) ó 0.7 (○) mM CORM-2. Los datos se ajustaron a la ecuación de Boltzmann (Ec. 4) y los parámetros obtenidos son: salina, $V_{1/2}$ = -40 ± 6.1 mV, z = 2.84 ± 0.48 e_0; CORM-2 0.5 mM, $V_{1/2}$ = -22.6 ± 2.46 mV, z = 1.66 ± 0.23 e_0; 0.7 mM CORM-2, $V_{1/2}$ = -26.5 ± 4.9 mV, z = 1.67 ± 0.21 e_0 (n = 4 - 6). Las curvas discontinuas son los ajustes a la ecuación de Boltzmann para los datos en 0.5 (- - - -) y 0.7 (·····) mM CORM-2 normalizadas al valor de conductancia a 100 mV de cada curva. Las curvas sólidas son las predicciones del modelo del Esquema I para salina (curva negra) y 0.7 mM CORM-2 (curva gris). (B) Corrientes representativas del canal Kv2.1 en respuesta a una despolarización a 100 mV y una repolarización a -130 mV en salina (trazo negro), 0.5 (trazo gris obscuro) ó 0.7 (trazo gris claro) mM CORM-2. La línea punteada marca el cero de corriente. (C) Gráficos de las constantes de velocidad de activación (círculos) y cierre (cuadrados) obtenidas de ajustes exponenciales a trazos como los mostrados en (B) a distintos potenciales en salina, 0.5 ó 0.7 mM CORM-2. Los datos se ajustaron a la siguiente ecuación: $k(V) = k(0mV)e^{-\frac{zV}{k_BT}}$ (Ec. 11). Los parámetros obtenidos son: salina, $k_{act}(0)$ = 64.3 ± 5 s^{-1}, z_{act} = 0.18 ± 0.01 e_0, $k_{deact}(0)$ = 7.59 ± 1 s^{-1}, z_{deact} = -0.57 ± 0.03 e_0; 0.5 mM CORM-2, $k_{act}(0)$ = 74.0 ± 13.0 s^{-1}, z_{act} = 0.17 ± 0.01 e_0, $k_{deact}(0)$ = 6.28 ± 1 s^{-1}, z_{deact} = -0.53 ± 0.02 e_0; 0.7 mM CORM-2, $k_{act}(0)$ = 38.4 ± 6.4 s^{-1}, z_{act} = 0.0004 ± 0.0076 e_0, $k_{deact}(0)$ = 5.40 ± 0.45 s^{-1}, z_{deact} = -0.29 ± 0.04 e_0 (n = 4 - 25). Las curvas sólidas son las predicciones del modelo en el Esquema I para salina (curvas negras) y 0.7 mM CORM-2 (curvas grises).

Finalmente se determinó si los efectos del compuesto sobre la cinética de activación del canal observados en mediciones macroscópicas se reproducen en mediciones al nivel de molécula única. Para esto se cuantificó el efecto del CORM-2 sobre la latencia a la primera apertura para un solo canal (Fig. 17). Como era de esperarse, la constante de velocidad asociada al cambio en la latencia en función del tiempo se redujo en presencia del compuesto con

respecto a la determinada en solución salina. Además, el valor de la latencia cuando la curva alcanza el equilibrio es menor en presencia de CORM-2 que en salina, lo que es consistente con una reducción en la probabilidad de apertura debida al compuesto.

El efecto del CORM-2 sobre la dependencia en el voltaje del canal sugiere que el compuesto podría estar interfiriendo con la maquinaria de detección de cambios en el voltaje del canal: el dominio sensor de voltaje. La medición de corrientes de compuerta arroja información directa sobre los cambios conformacionales del DSV, por lo que a continuación se decidió estudiar los efectos del CORM-2 sobre el movimiento de carga del canal.

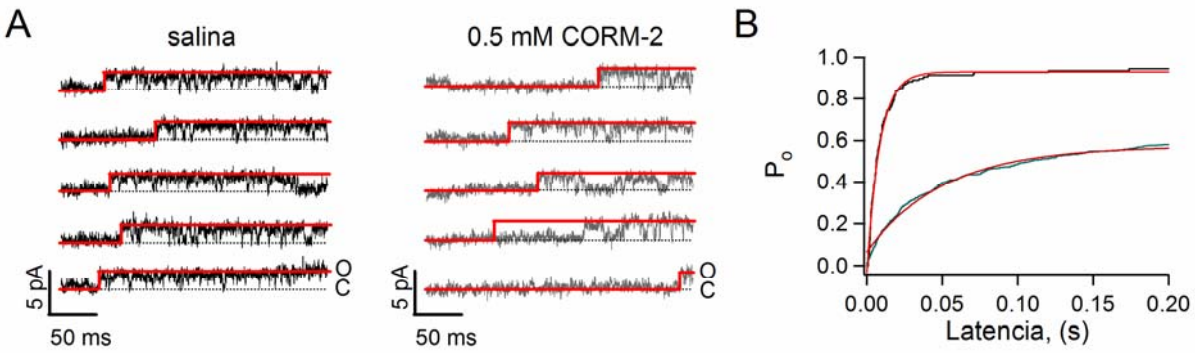

Figura 17. Efecto del CORM-2 sobre la latencia del canal Kv2.1. (A) Registros representativos de canal unitario mostrados en la Fig. 12D (100 mV) con las idealizaciones de los trazos superpuestas en rojo. Los trazos idealizados valen 0 antes de la primera apertura y 1 una vez que se abrió el canal por primera vez en cada pulso. El gráfico en (B) es la suma de los trazos idealizados. (B) Curva representativa de probabilidad acumulada contra latencia a la primera apertura del canal en salina (trazo negro) y en presencia de 0.5 mM CORM-2 (trazo gris). Las curvas punteadas son ajustes a una función exponencial. Los parámetros obtenidos son: k_{sal} = 103 ± 18 s^{-1}, k_{corm} = 23 ± 4 s^{-1} (n = 2).

8.4. Los efectos del CORM-2 sobre el movimiento de carga del canal Kv2.1.

La Figura 18A (panel derecho) muestra familias de corrientes de compuerta del canal Kv2.1 obtenidas de un parche escindido utilizando las soluciones de registro 3 y 5. Inmediatamente después del pulso despolarizante se observa una corriente capacitiva con dependencia no lineal en el voltaje que refleja la activación de los sensores de voltaje y el movimiento de la carga de compuerta asociado a dicho conjunto de transiciones. El rango de voltajes en los que se observa movimiento de carga está determinado por la dependencia en el voltaje de los sensores. Una vez que los sensores alcanzan el estado activado (partiendo desde el estado completamente desactivado), ya no se observan corrientes, porque ya no hay más movimiento de carga de compuerta. Al repolarizar el parche a -90 mV, se observan pequeñas corrientes de compuerta asociadas a la desactivación de los sensores de voltaje.

El tamaño de las corrientes de compuerta depende tanto de la cantidad de carga que se mueve en la transición, como de la velocidad con que ocurre dicha transición. Dado que el paso del estado abierto al primer estado cerrado es lento (Taglialatela and Stefani, 1993), el tamaño de las corrientes de compuerta durante la repolarización es más pequeño que durante la despolarización. Además, se ha observado que el regreso de la carga al estado desactivado es mucho más lento en parches escindidos (Sigg et al., 1994), aunque la razón de esto se desconoce. Cuando el canal no alcanza el estado abierto, a despolarizaciones intermedias (e.g. -40 mV), la desactivación de los sensores de voltaje ocurre más rápidamente, como se observa en el trazo negro de la Figura 18B, panel inferior.

En presencia de 0.7 mM CORM-2 se observaron tres tipos de modificaciones a las corrientes de compuerta: primero, la velocidad de activación de las corrientes durante la despolarización se incrementó, lo cual se observa en los trazos grises de la Figura 18B y en la cuantificación de las constantes de velocidad de activación (Fig. 18C). Interesantemente, la dependencia en el

voltaje de estas transiciones no se vio afectada por la presencia del compuesto (Fig. 18C, valores de z_{Qon}).

En segundo lugar, se observó un decremento en la carga total que se mueve durante la activación de los sensores de voltaje, evaluada mediante la integral bajo los trazos de corriente (Fig. 18D). La curva de carga contra voltaje en presencia de CORM-2 presenta además una pendiente mucho menor que la curva obtenida en salina, sin observarse un corrimiento grande en el voltaje medio de activación. Esto es una indicación de que el compuesto afecta transiciones tardías en la vía de activación del canal, en las que la mayor parte del movimiento de carga ha ocurrido.

Resulta intrigante que el voltaje medio de la curva Q-V en salina (-21.3 mV) es menos negativo que el voltaje medio obtenido de la curva G-V (-40 mV). Este resultado parece contradecir las claras observaciones de que el canal no puede alcanzar el estado abierto hasta que los cuatro sensores de voltaje han alcanzado el estado activado. Sin embargo, se ha observado que la actividad del canal Kv2.1 es modulada directamente por la concentración de potasio (Consiglio and Korn, 2004). Es posible entonces que esta aparente contradicción resulte de los efectos de la ausencia de iones permeantes en las soluciones con las que se realizaron los experimentos. Con el fin de determinar si este era el caso, se midió la curva de activación del canal bajo las mismas condiciones con las que se midieron las corrientes de compuerta, agregando 5 mM de potasio en la solución extracelular para poder registrar corrientes iónicas (solución de registro 6). De acuerdo con lo esperado, la curva resultante tiene un voltaje medio de activación menos negativo que la curva Q-V bajo condiciones experimentales similares (-3.37 mV, Fig. 18D, símbolos grises).

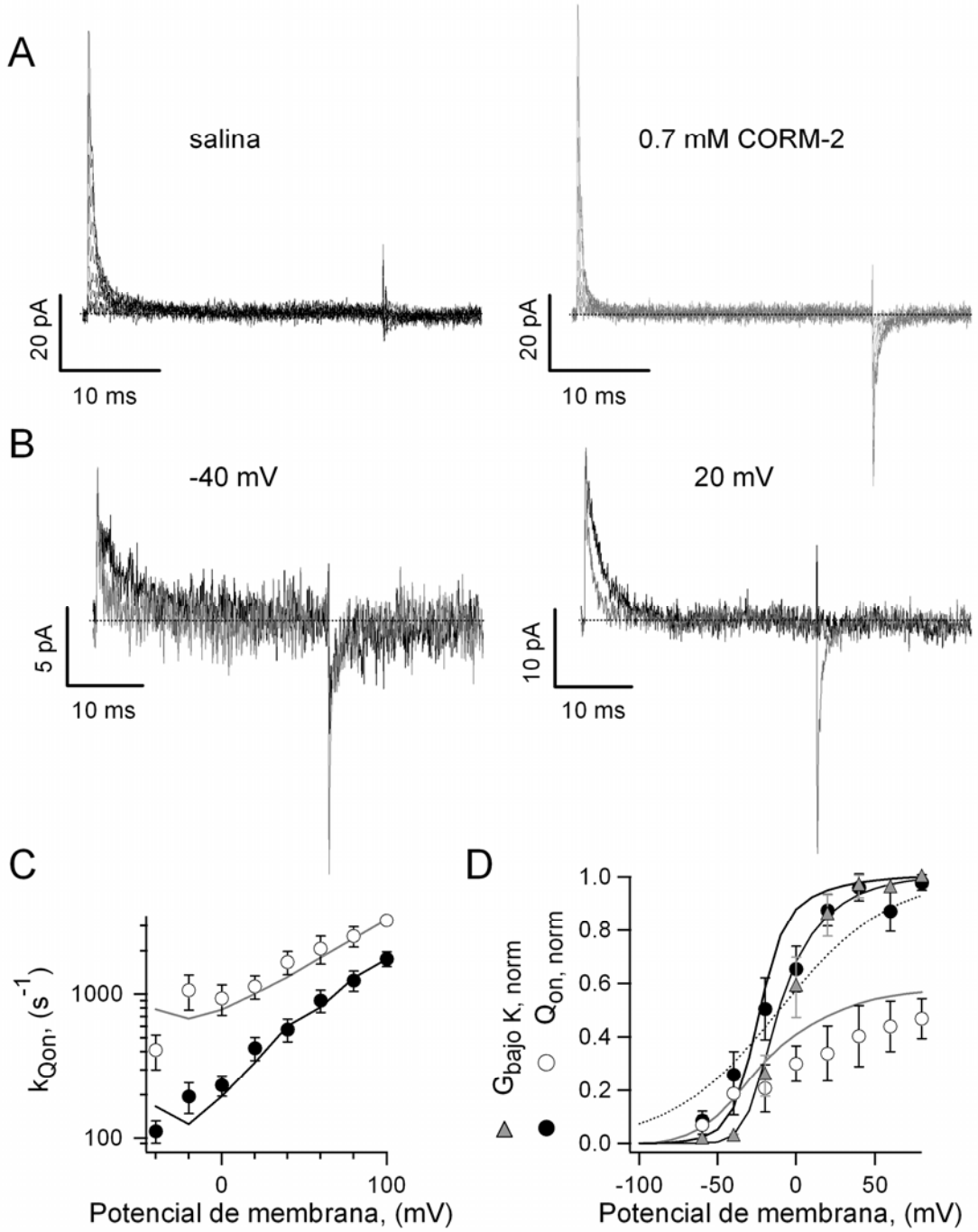

Figura 18. Efectos del CORM-2 sobre las corrientes de compuerta del canal Kv2.1. (A) Familias de corrientes de compuerta representativas medidas en el mismo parche de membrana en respuesta a pulsos entre -60 y 80 mV en incrementos de 20 mV en ausencia y presencia de CORM-2. El voltaje se regresó al potencial de reposo de -90 mV después de cada pulso. (B) Trazos tomados de (A) antes (trazos negros) y durante la aplicación de 0.7 mM CORM-2 (trazos grises) a los voltajes indicados. (C) Constantes de velocidad para la activación de los sensores de voltaje en presencia (símbolos vacíos) o ausencia (símbolos llenos) de

CORM-2. Del ajuste a la ecuación $k_{Qon}(V) = k_{Qon}(0mV)e^{-\frac{z_{Qon}V}{k_BT}}$ se obtuvieron los siguientes parámetros: salina, $k_{Qon}(0)$ = 284 ± 57 s^{-1}, z_{Qon} = 0.47 ± 0.03 e_0, CORM-2, $k_{Qon}(0)$ = 1033 ± 224 s^{-1}, z_{Qon} = 0.27 ± 0.03 e_0 (n = 6). Las curvas continuas son las predicciones del modelo en el Esquema I. (D) Curvas normalizadas de carga (Q_{on}) contra voltaje obtenidas en ausencia (símbolos llenos) o en presencia (símbolos vacíos) de 0.7 mM CORM-2. Las curvas se ajustaron a la ecuación de Boltzmann (Ec. 8) y se obtuvieron los siguientes parámetros: salina, $V_{1/2}$ = -21.3 ± 6.1 mV, z = 1.82 ± 0.13 e_0; CORM-2, $V_{1/2}$ = 8.43 ± 20.56 mV, z = 0.91 ± 0.18 e_0 (n = 6). La curva punteada es el ajuste de la ecuación de Boltzmann a los datos en presencia de CORM-2 normalizada al valor de la carga en el ajuste a 80 mV. Los triángulos grises representan la curva G-V normalizada obtenida en las mismas condiciones que las corrientes de compuerta, pero con 5 mM de potasio extracelular. El ajuste a la ecuación de Boltzmann (Ec. 4) arrojó los siguientes parámetros: $V_{1/2}$ = -3.37 ± 5.76 mV, z = 2.84 ± 0.30 e_0 (n = 9). Las curvas continuas son las predicciones del modelo presentado en el Esquema I.

Finalmente, el tercer efecto del CORM-2 sobre el movimiento de carga del canal radicó en una aceleración en la cinética de desactivación de los sensores de voltaje (Fig. 18B, trazos grises). Esta observación coincide con los resultados de mutaciones que interfieren con el acoplamiento electromecánico, al separar energéticamente la activación de los sensores de voltaje de la apertura del canal (Haddad and Blunck, 2011; Holmgren et al., 1996; Ledwell and Aldrich, 1999). Para obtener más información sobre este fenómeno, se realizaron experimentos en los que se aplicaron pulsos despolarizantes de duración variable y se cuantificó la cinética del regreso del sensor de voltaje al estado desactivado al repolarizar la membrana (Fig. 19A). En solución salina a despolarizaciones cortas, la carga regresó rápidamente al repolarizar la membrana. A medida que la duración del pulso despolarizante se incrementó y los canales fueron alcanzando el estado abierto, la velocidad de la relajación de las corrientes de compuerta de desactivación se redujo (Fig. 19A, panel izquierdo). En presencia de CORM-2 la carga de desactivación regresó rápidamente a todas las duraciones del pulso despolarizante (Fig.19A, panel derecho). Las constantes de velocidad de desactivación del sensor de voltaje se cuantificaron y se muestran en la Figura 19B. Estos resultados sugieren que en presencia de CORM-2 la ocupancia del estado abierto se reduce en gran medida, mientras que persiste un movimiento significativo de los sensores de voltaje.

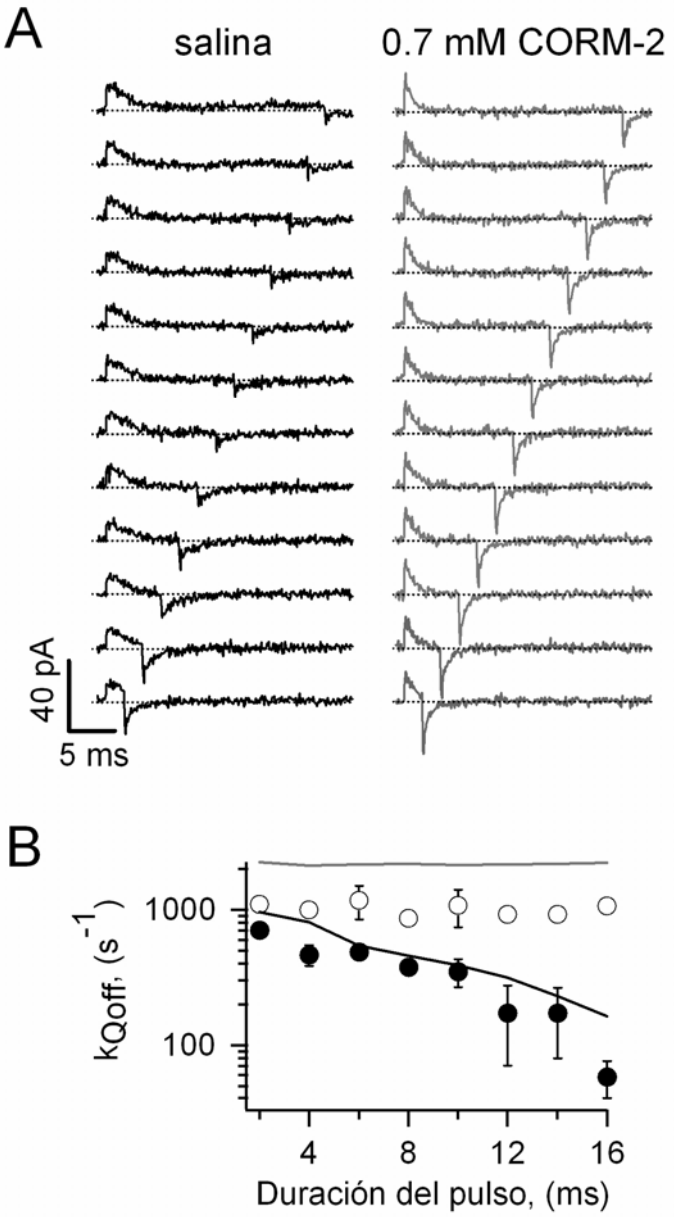

Figura 19. Efecto del CORM-2 sobre la cinética de desactivación de los sensores de voltaje en el canal Kv2.1. (A) Corrientes representativas de compuerta activadas por pulsos de duración creciente a 40 mV, y desactivadas por pulsos repolarizantes a -90 mV. Las líneas punteadas marcan el nivel donde la corriente vale cero. (F) Constantes de velocidad para la desactivación de las corrientes de compuerta medidos de trazos como en (E) en respuesta a despolarizaciones de duración variable a 40 y 60 mV (n = 6). Las curvas continuas son las predicciones del modelo.

Para obtener más evidencia de que el CORM-2 provoca una desestabilización importante del estado abierto del canal, se realizaron experimentos en los que se pudieran detectar corrientes iónicas y corrientes de compuerta simultáneamente. Para lograr esto, se utilizó la solución de registro extracelular 6, que contiene 5 mM de potasio, y la solución intracelular 4, que contiene tetraetilamonio, el cual funciona como un bloqueador del poro en el estado abierto del canal (Armstrong, 1971; Armstrong and Hille, 1972; del Camino et al., 2000), enlenteciendo el cierre y prolongando la duración de las corrientes iónicas entrantes. Las corrientes resultantes en solución salina durante la

repolarización presentan una contribución de la entrada de potasio (corrientes iónicas) que sólo se puede observar a los voltajes en los que el canal alcanza el estado abierto (Fig. 20A, panel izquierdo, y B, trazos negros). En presencia de CORM-2, el componente correspondiente a las corrientes iónicas se vio completamente suprimido, y el movimiento de carga de desactivación ocurrió rápidamente (Fig. 20A, panel derecho, y B, trazos grises), tal y como sucedió en los experimentos anteriores.

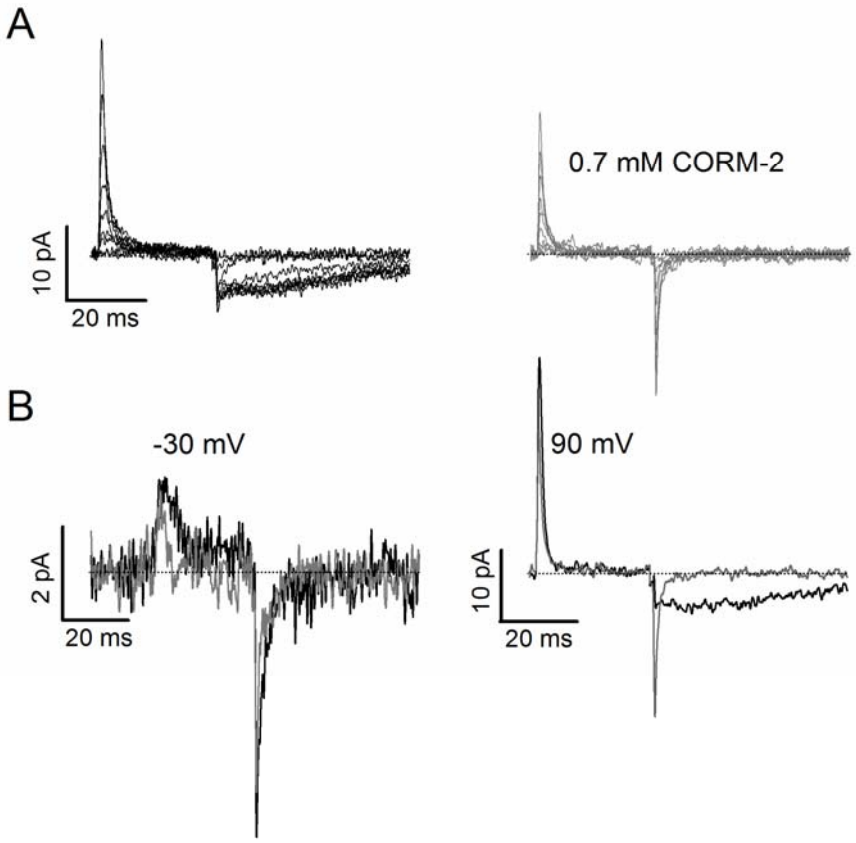

Figura 20. El CORM-2 inhibe la apertura del canal en menor medida que el movimiento de carga. (A) Corrientes de compuerta obtenidas con 5 mM potasio extracelular y 130 mM TEA intracelular en respuesta a pulsos entre -80 mV y 100 mV en incrementos de 20 mV a partir de un potencial de -90 mV. (B) Corrientes tomadas de (A) en ausencia (trazos negros) y presencia (trazos grises) de CORM-2 a dos voltajes.

Estos resultados indican que el CORM-2 desestabiliza al estado abierto en mayor medida que a la activación de los sensores de voltaje. En términos de los modelos propuestos para representar la actividad de estos canales, se podría decir que el donador tiene un efecto importante sobre las transiciones concertadas que llevan a la apertura del canal, y efectos menores sobre las transiciones independientes de los sensores de voltaje. Un problema de esta interpretación es que todos los modelos detallados para la función de canales de potasio dependientes de voltaje se han hecho basados en resultados obtenidos con *Shaker* (Bezanilla et al., 1994; Ledwell and Aldrich, 1999; Schoppa and Sigworth, 1998c; Zagotta et al., 1994a). Aunque existe evidencia de que el canal Kv2.1 se comporta de manera similar (Islas and Sigworth, 1999; Labro et al., 2008; Long et al., 2007), podrían haber diferencias importantes entre ambos canales. Con el fin de comparar directamente los resultados obtenidos aquí con los resultados obtenidos en *Shaker* y los modelos funcionales disponibles, se exploraron los efectos del CORM-2 sobre este canal.

8.5. El mecanismo de inhibición por CORM-2 está conservado entre canales de potasio dependientes de voltaje.

De acuerdo con el alto grado de conservación funcional y estructural entre *Shaker* y Kv2.1, el CORM-2 también tuvo un profundo efecto inhibitorio sobre las corrientes de *Shaker*, como se puede apreciar en las familias de corrientes en la Figura 21A. La afinidad del CORM-2 por *Shaker* resultó ser mayor, puesto que 0.35 mM del compuesto causa una mayor inhibición en este canal que la que causa la misma concentración del compuesto en Kv2.1.

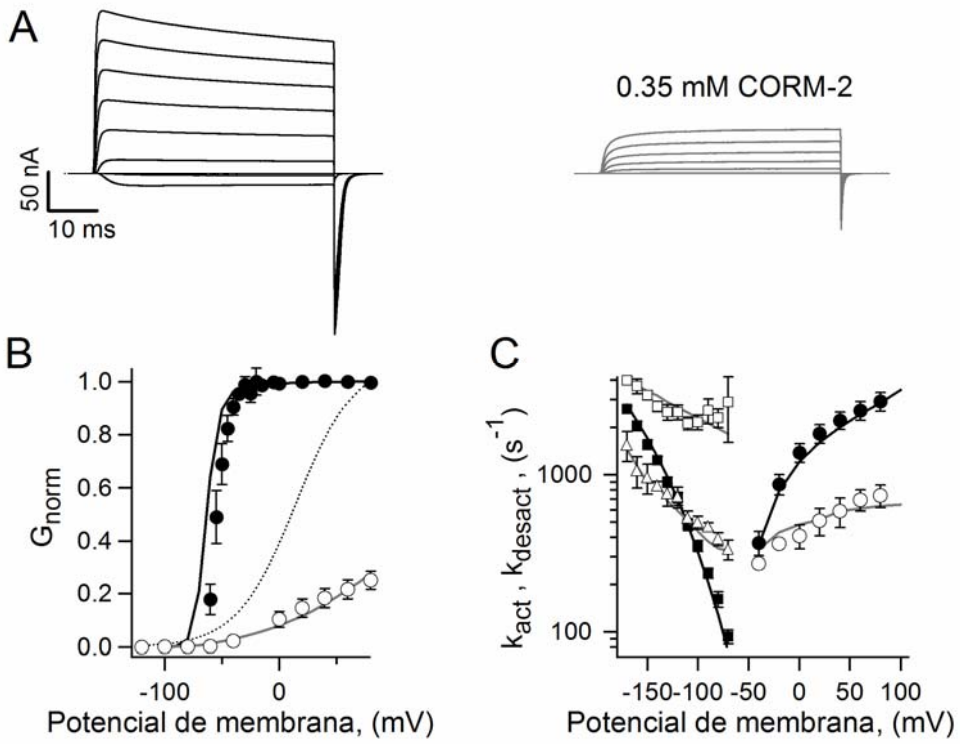

Figura 21. El CORM-2 es un inhibidor alostérico de *Shaker*. (A) Familias de corrientes representativas medidas en el mismo parche de membrana y activadas por pulsos entre -120 y 80 mV en incrementos de 20 mV en salina y en presencia de 0.35 mM CORM-2. (B) Curvas G-V normalizadas de corrientes en salina (símbolos llenos) o en 0.35 mM CORM-2 (símbolos vacíos). Ajustes a la ecuación de Boltzmann (Ec. 4) dieron los siguientes parámetros: salina, $V_{1/2}$ = -39.6 ± 3.1 mV, z = 4.86 ± 0.3 e_0; CORM-2, $V_{1/2}$ = +19.4 ± 8.5 mV, z = 0.99 ± 0.10 e_0 (n = 4). La curva punteada es un ajuste de la ecuación de Boltzmann a los datos en presencia de CORM-2 y normalizada a su valor a 80 mV. Las curvas continuas son las predicciones del modelo en el Esquema I. (C) Constantes de velocidad de activación (círculos) y desactivación (cuadrados y triángulos) en salina (símbolos llenos) o en presencia de 0.35 mM CORM-2 (símbolos vacíos). Los datos se ajustaron a la ecuación 11 y se obtuvieron los siguientes parámetros: salina, k_{act} (0) = 1298 ± 166 s^{-1}, z_{act} = 0.25 ± 0.01 e_0, k_{deact} (0) = 24.5 ± 4.1 s^{-1}, z_{deact} = -0.70 ± 0.02 e_0; CORM-2, k_{act} (0) = 412 ± 64 s^{-1}, z_{act} = 0.175 ± 0.004 e_0, k_{deact1} (0) = 1124 ± 242 s^{-1}, z_{deact1} = -0.19 ± 0.04 e_0, k_{deact2} (0) = 179 ± 31 s^{-1}, z_{deact2} = -0.28 ± 0.05 e_0 (n = 4 - 6). Las curvas continuas son las predicciones del modelo en el Esquema I.

A diferencia del Kv2.1, el compuesto provocó un importante corrimiento a la derecha en la curva de activación del canal (Fig. 21B), además de reducir la pendiente. Esto se debe principalmente a los efectos del compuesto sobre la cinética de activación y cierre del canal, como se observa en el análisis de las constantes de velocidad correspondientes en la Figura 21C. La cinética de

apertura del canal se pudo ajustar bien con una sola exponencial, mientras que el cierre requirió de dos exponenciales, indicando la presencia de al menos dos transiciones con cinética diferente en el paso del estado abierto al cerrado. En contraste con los resultados obtenidos con el canal Kv2.1, en Shaker el componente rápido del cierre se aceleró en presencia del compuesto, lo que sugiere que el compuesto provoca una desestabilización del estado abierto, que resultaría en una reducción aparente en la altura de la barrera energética para pasar del estado abierto al cerrado (Fig. 21C). Por el contrario, la constante de velocidad de apertura del canal se redujo.

El efecto opuesto del CORM-2 sobre las constantes de velocidad de apertura y cierre resulta en una disminución en el valor de la constante de equilibrio a 0 mV, que es equivalente a un corrimiento a la derecha en el voltaje medio de activación de acuerdo con la siguiente ecuación: $K(0mV) = e^{\frac{zV_{1/2}}{k_B T}}$. Una característica común de los efectos del CORM-2 en ambos canales es una importante reducción en la carga aparente asociada a las constantes de velocidad que caracterizan la cinética de las corrientes iónicas, indicando que la dependencia en el voltaje tanto del cierre como de la apertura del canal se reduce en presencia del compuesto. Debido a esta observación, se procedió a analizar los efectos del CORM-2 sobre el movimiento de carga de *Shaker*.

Con el fin de realizar las mediciones de corrientes de compuerta bajo las mismas condiciones que los registros de corrientes iónicas, se utilizó el canal *Shaker* con la mutación puntual W434F, el cual presenta un proceso de inactivación tan rápido que es incapaz de mediar corrientes iónicas, aunque el poro y los sensores de voltaje sí presentan los cambios conformacionales asociados con la apertura del canal (Perozo et al., 1993; Yang et al., 1997).

A diferencia de los efectos del compuesto sobre las corrientes iónicas de *Shaker*, que son cuantitativamente diferentes a los observados en Kv2.1, los efectos sobre las corrientes de compuerta resultaron ser más similares (Fig. 22A). Se observó una reducción en la carga total asociada a la activación de los sensores de voltaje (Fig. 22B), sin que se modificara en gran medida el

voltaje medio de activación, pero provocando una reducción en la pendiente de la misma. La cinética de activación de los sensores no sufrió modificaciones en presencia del donador (Fig. 22C), mientras que la velocidad de desactivación de los sensores se incrementó (Fig. 22A).

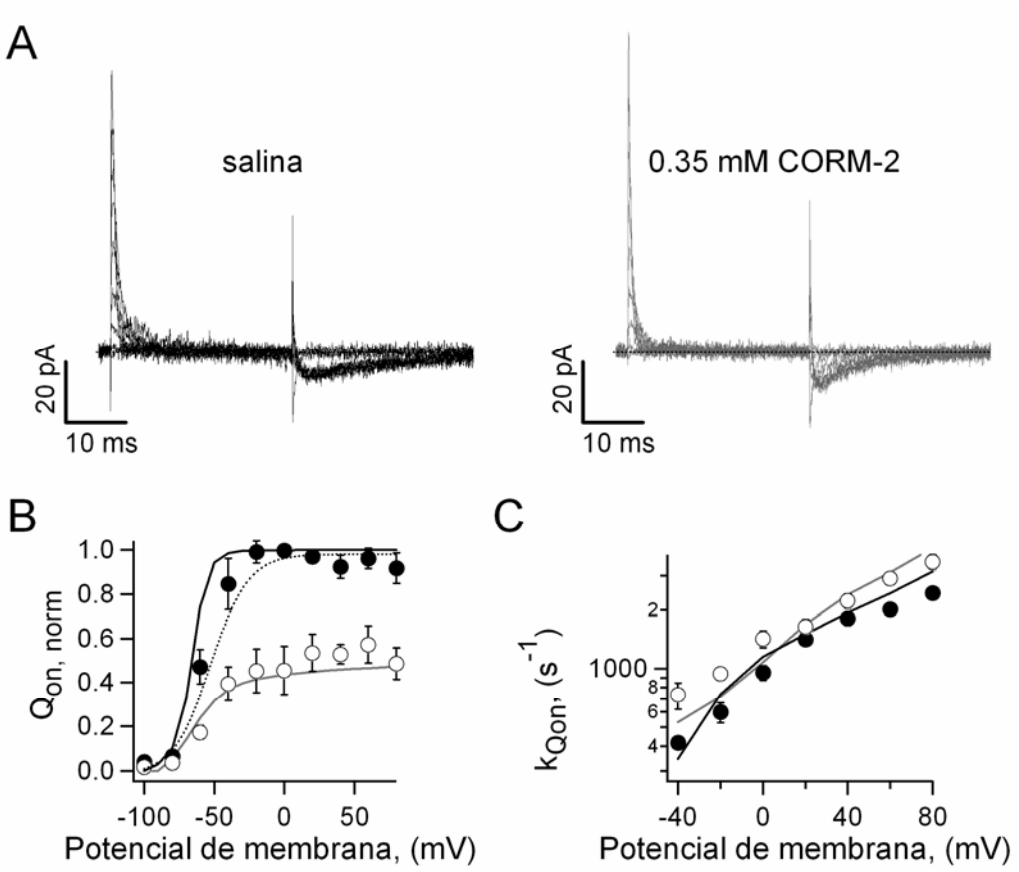

Figura 22. Efectos del CORM-2 sobre las corrientes de compuerta de *Shaker*W434F. (A) Corrientes de compuerta representativas de *Shaker*W434F obtenidas en el mismo parche en respuesta a pulsos desde -100 hasta 80 mV en incrementos de 20 mV en salina y en presencia de 0.35 mM CORM-2. (B) Curva de carga de compuerta de activación (Q_{on}) contra voltaje medida en salina (símbolos llenos) o en presencia de 0.35 mM CORM-2 (símbolos vacíos). Los datos se ajustaron a la ecuación de Boltzmann (Ec. 8) y se obtuvieron los siguientes parámetros: salina, $V_{1/2}$ = -58.3 ± 3 mV, z = 4.0 ± 1.0 e_0; CORM-2, $V_{1/2}$ = -39.0 ± 8.7 mV, z = 1.75 ± 0.53 e_0 (n = 4). La curva punteada es el ajuste a los datos en CORM-2 de la ecuación de Boltzmann, normalizada a su valor a 80 mV. Las curvas continuas son las predicciones del modelo en el Esquema I. (C) Constantes de velocidad de activación de los sensores de voltaje en función del voltaje. Los datos se ajustaron a la ecuación $k_{Qon}(V) = k_{Qon}(0mV)e^{-\frac{z_{Qon}V}{k_BT}}$ y los parámetros resultantes son: salina, k_{Qon} (0) = 966 ± 56 s^{-1}, z_{Qon} = 0.32 ± 0.02 e_0; CORM-2, k_{Qon} (0) = 1306 ± 79 s^{-1}, z_{Qon} = 0.31 ± 0.02 e_0 (n = 4). Las curvas continuas son las predicciones del modelo.

Para caracterizar el efecto del compuesto sobre la cinética de desactivación de los sensores de voltaje en Shaker, se repitió el experimento previamente realizado con el canal Kv2.1 en el que se mide la cinética de desactivación de los sensores de voltaje tras la aplicación de pulsos despolarizantes de duración variable, y el resultado fue muy similar al observado en el canal Kv2.1 (Fig. 23): Mientras que en salina el regreso de la carga de compuerta durante la desactivación de los sensores ocurrió con una cinética lenta, en presencia de CORM-2 la cinética de las corrientes de compuerta fue igual de rápida para todas las duraciones del pulso exploradas. Cabe mencionar que debido a que la velocidad de apertura del poro en *Shaker* es mucho más rápida que la del Kv2.1, la corriente de compuerta de desactivación en salina ocurrió lentamente aún en los pulsos despolarizantes más cortos, puesto que éstos no fueron lo suficientemente breves para que el canal no tuviera tiempo de abrirse.

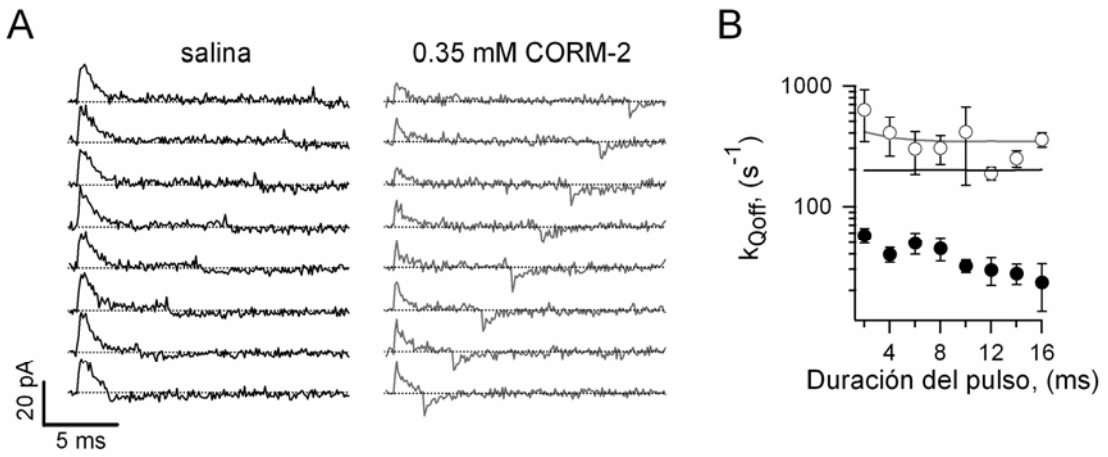

Figura 23. Efecto del CORM-2 sobre la cinética de desactivación de los sensores de voltaje de *Shaker*. (A) Corrientes de compuerta activadas por pulsos de distinta duración a 0 mV y desactivadas a -90 mV. Las líneas punteadas marcan el nivel donde la corriente vale cero. (B) Constantes de velocidad de desactivación obtenidas de ajustes monoexponenciales a trazos como en (A) (n = 3). Las curvas continuas son las predicciones del modelo.

Estos resultados indican que tal y como sucede en el canal Kv2.1, el CORM-2 interfiere con las transiciones tardías en la vía de activación, muy probablemente con las transiciones concertadas que acompañan la apertura y cierre del canal. Otra manera independiente de las corrientes de compuerta

para analizar las transiciones que ocurren antes de que el canal alcance el estado abierto, es cuantificar el retardo que hay entre la aplicación del pulso despolarizante y el inicio en el aumento monoexponencial en la corriente (Fig. 24A). Este análisis es equivalente a determinar el grado de sigmoidicidad de las corrientes iónicas en respuesta a un pulso despolarizante desde un voltaje inicial en el cual los canales se encuentran en el estado cerrado (Schoppa and Sigworth, 1998a; Zagotta et al., 1994b). La magnitud del retardo provee información sobre el número de estados cerrados por los que el canal debe transitar para llegar al estado abierto, y las magnitudes de las constantes de velocidad asociadas a dichas transiciones. Sorprendentemente, el CORM-2 provocó un aumento en la magnitud del retardo en *Shaker* con respecto al retardo en salina (Fig. 24B y C).

Dado que la cinética de las corrientes de compuerta asociadas a la activación de los sensores de voltaje no se alteró significativamente (Fig. 22C), el aumento en el retardo inducido por el CORM-2 debe reflejar una disminución en la velocidad de las transiciones posteriores al movimiento de carga detectado en las mediciones de corrientes de compuerta. Esto es consistente con nuestra hipótesis que establece que el compuesto interfiere con las transiciones tardías en la vía de activación del canal, sin afectar grandemente las transiciones iniciales que llevan a la activación de los sensores de voltaje. Esto es equivalente a considerar que el CORM-2 provoca un desacoplamiento parcial entre los procesos asociados a la detección de cambios en el potencial de membrana y la apertura y cierre del canal.

Con el fin de dar una interpretación mecanística de los efectos del CORM-2 sobre el acoplamiento electromecánico en ambos canales, se realizaron experimentos para localizar posibles sitios de interacción del compuesto en el canal Kv2.1.

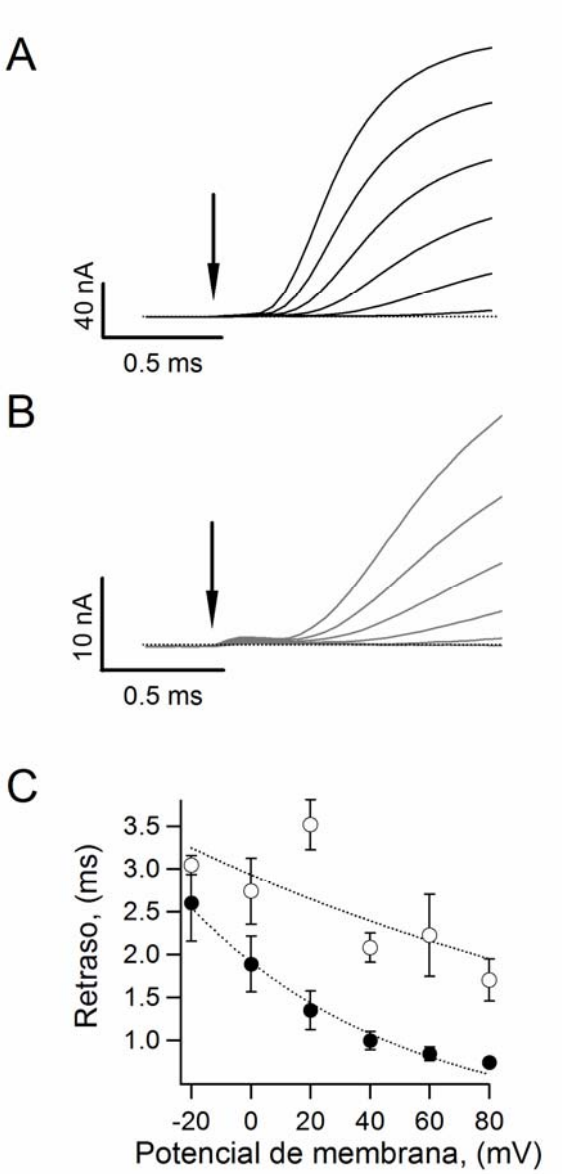

Figura 24. El CORM-2 aumenta el retraso en la activación de las corrientes iónicas de Shaker. (A) Familia de corrientes representativas en respuesta a pulsos entre -20 y 80 mV, en incrementos de 20 mV, en salina. La línea punteada marca el cero de corriente. La flecha indica el inicio del pulso despolarizante a partir del potencial de mantenimiento de -120 mV. (B) Corrientes medidas en el mismo parche que (A), bajo las mismas condiciones de voltaje, pero en presencia de 0.35 mM CORM-2. (C) Retraso en la activación de las corrientes de Shaker en salina (símbolos llenos) o en presencia de CORM-2, determinado a partir de datos como en (A) y (B) ajustados con la ecuación 5 (n = 4). Las líneas punteadas son ajustes a la ecuación 11.

8.6. Localización de un posible sitio de interacción del CORM-2 con el canal Kv2.1.

Como primera aproximación para identificar posibles sitios de unión, se realizó un experimento de *docking* utilizando los modelos estructurales del canal Kv1.2 en el estado abierto y cerrado (Khalili-Araghi et al., 2010), los cuales fueron obtenidos por dinámica molecular a partir de la estructura determinada por difracción de rayos X (Long et al., 2005a). Como ligante se utilizó una molécula de $Ru(DMSO)_2(CO)_2Cl_2$ (Fig. 25A), la cual es estructuralmente similar al CORM-2 e igualmente inhibe al canal, aunque con menor afinidad. El *docking*

se hizo con el servidor Patchdock (Duhovny et al., 2002; Schneidman-Duhovny et al., 2005), el cual busca posibles sitios de unión para un ligante dentro de una proteína únicamente en base a la complementareidad estérica, ignorando las interacciones electrostáticas proteína-ligante. Se ha demostrado que este servidor es altamente eficaz para localizar sitios de unión para ligantes no cargados, como el CORM-2.

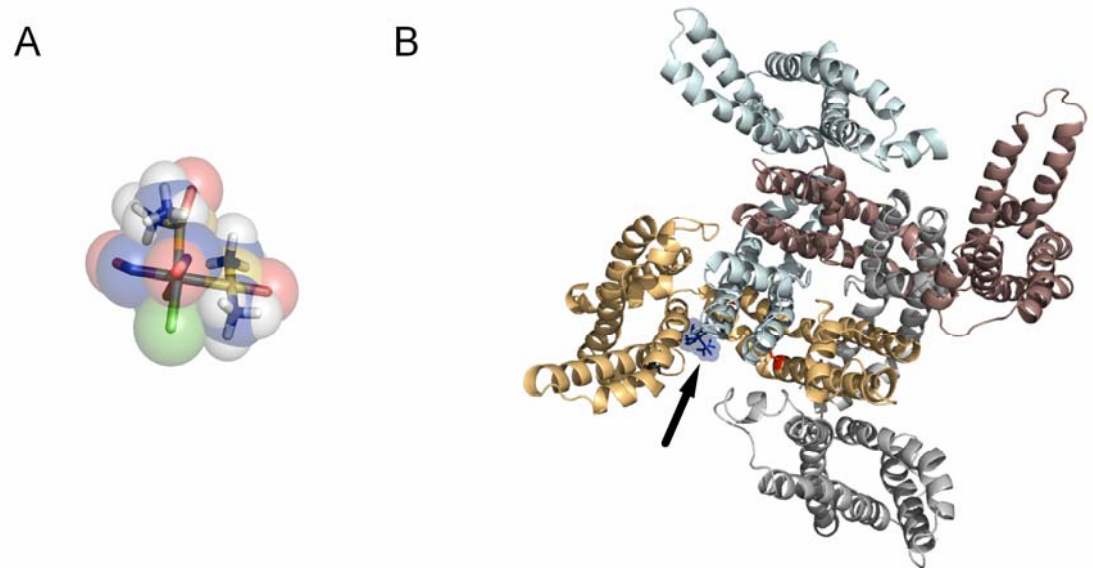

Figura 25. Posible sitio de unión a CORM-2 localizado en la interfase entre los DSV y el poro del canal. (A) Estructura del compuesto $Ru(DMSO)_2(CO)_2Cl_2$. Colores según el tipo de átomo: azufre, amarillo; hidrógeno, blanco; carbono, azul; oxígeno, rojo; rutenio, gris; cloro, verde. Se muestra superpuesta la superficie de van der Waals de la molécula. (B) Vista de la cara extracelular del canal Kv1.2 en el estado abierto. La flecha indica la posición de una molécula de $Ru(DMSO)_2(CO)_2Cl_2$ (azul) en una de las subunidades. Figuras generadas en Pymol.

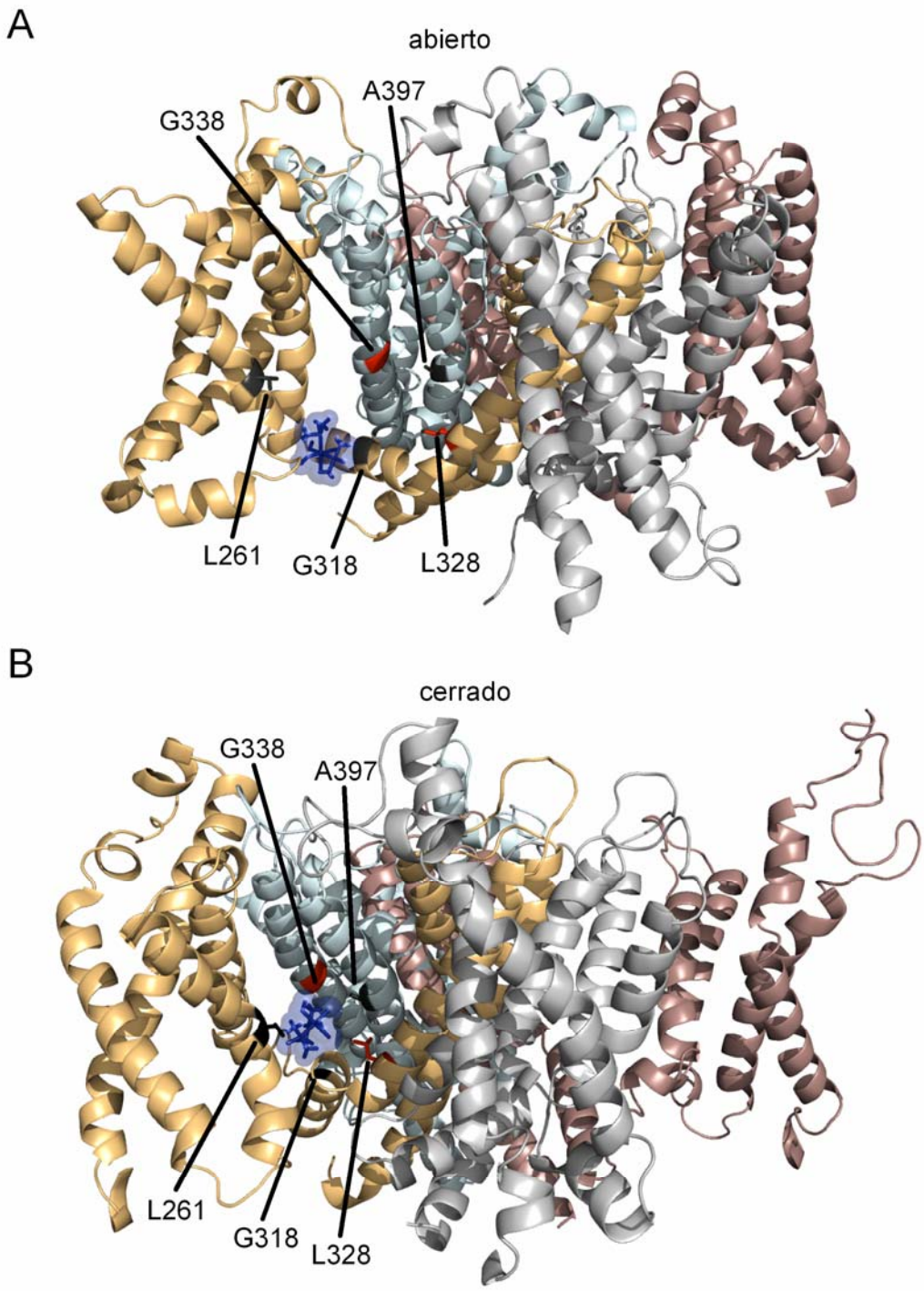

Figura 26. Identificación de residuos que podrían interactuar con el CORM-2. *Docking* del compuesto $Ru(DMSO)_2(CO)_2Cl_2$ en el canal Kv1.2 en su estado (A) abierto y (B) cerrado. Cada subunidad tiene un color distinto. El compuesto $Ru(DMSO)_2(CO)_2Cl_2$ está en azul, con la superficie de van der Waals superpuesta. Los residuos indicados en la figura fueron seleccionados para ser sustituidos por aminoácidos con cadenas laterales más grandes (numeración de residuos de acuerdo con el canal Kv1.2). Los residuos L261 (S3), G318 (asa S4-S5) y A397 (S6), cuya sustitución en Kv2.1 resultó en canales funcionales, se muestran en negro. Los residuos L328 (S5) y G338 (S5), cuya sustitución resultó en canales no funcionales, se muestran en rojo.

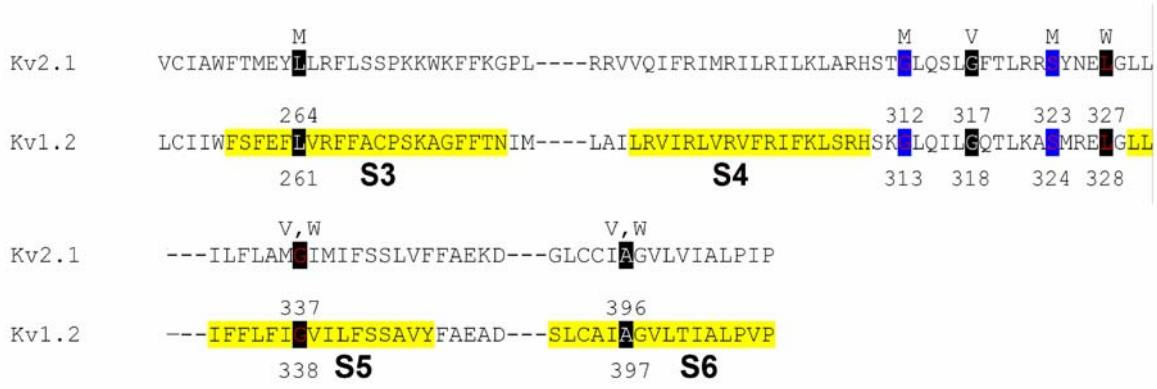

Figura 27 Alineación entre las secuencias de aminoácidos de los canales Kv2.1 y Kv1.2 en la región del posible sitio de unión a CORM-2. Las regiones resaltadas en amarillo denotan segmentos transmembranales. Los residuos resaltados en negro forman parte del posible sitio de unión mostrado en la Fig. 26. Los residuos resaltados en azul corresponden a otro posible sitio de unión localizado detrás del motivo Pro-X-Pro (no se muestra). Caracteres blancos indican mutaciones con expresión funcional, mientras que caracteres rojos indican falta de expresión funcional. La numeración superior es para Kv2.1 y la inferior para Kv1.2. Los caracteres situados encima de la secuencia indican los residuos por los que se sustituyeron los aminoácidos nativos. Por ejemplo, la mutación a metionina del residuo equivalente a L261 de Kv1.2 en el canal Kv2.1 es L264M.

Sorprendentemente, el sitio de unión con mayor ocupación resultó estar localizado en la interfase entre los dominios sensores de voltaje y el poro del canal, tanto en el estado abierto como en el cerrado (Fig. 25B y 26), precisamente en la región responsable del acoplamiento electromecánico (Lee et al., 2009; Long et al., 2005b; Soler-Llavina et al., 2006). Alentados por este resultado, se decidió sustituir residuos cercanos al sitio de unión putativo por aminoácidos con cadenas laterales grandes, con el fin de interferir con la unión del compuesto mediante efectos estéricos. Los residuos elegidos se muestran en la Figura 26. Como los efectos del CORM-2 se estudiaron con mayor detalle en el canal Kv2.1, se decidió introducir las mutaciones en este canal. Para ello, se realizó una alineación entre las secuencias de aminoácidos de los canales Kv1.2 y Kv2.1 y se identificaron los residuos equivalentes en Kv2.1 a los elegidos basándose en la estructura del canal Kv1.2 (Fig. 27). Cabe mencionar que los residuos elegidos están completamente conservados en ambos canales.

Con el fin de tener la capacidad para determinar si los canales mutantes se expresan en la membrana utilizando fluorescencia, se utilizó una construcción en la que se fusionó la proteína amarilla fluorescente al extremo amino-terminal del canal Kv2.1. Como se observa en la Figura 28, esta construcción es muy similar al canal Kv2.1 WT, tanto en la forma de las corrientes (Fig. 28A), la curva de activación (Fig. 28B), la cinética de apertura y cierre (Fig. 28C) y la sensibilidad a CORM-2 (Fig. 28D), indicando que es adecuada para utilizarse como fondo para introducir las mutaciones.

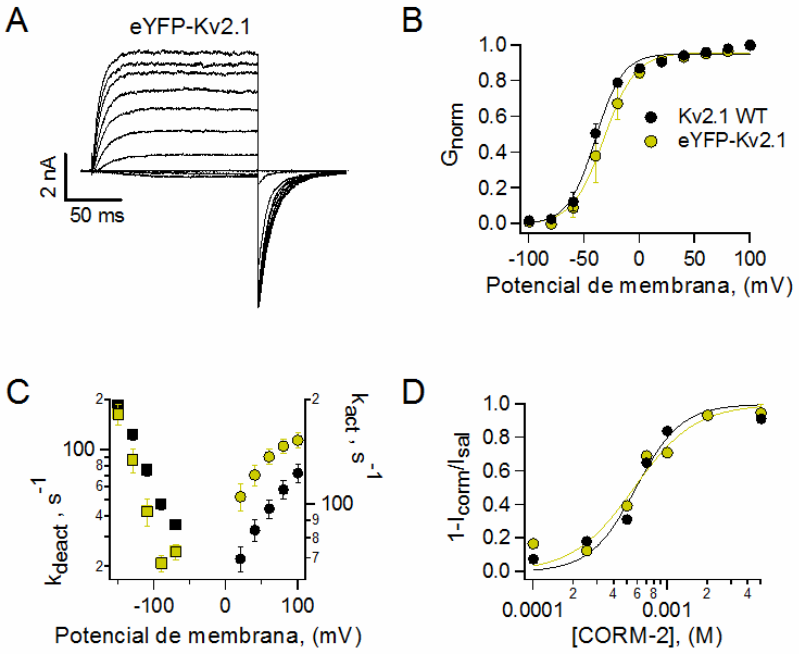

Figura 28. El canal eYFP-Kv2.1 se comporta de forma muy similar al canal WT. (A) Familia de corrientes del canal eYFP-Kv2.1 en respuesta a pulsos desde -120 hasta 100 mV, en incrementos de 20 mV. (B) Curvas de conductancia normalizada contra voltaje para el canal eYFP-Kv2.1 (símbolos verdes) y el canal WT (símbolos negros). Los datos se ajustaron a la ecuación de Boltzmann (Ec. 4) con los siguientes parámetros para eYFP-Kv2.1: $V_{1/2}$ = -33.2 ± 7.0 mV, z = 2.59 ± 0.22 e_0 (n = 4). Las curvas continuas son ajustes a la ecuación de Boltzmann. (C) Constantes de velocidad de activación y cierre para el canal Kv2.1 WT (símbolos negros) y el canal eYFP-Kv2.1 (símbolos verdes). (D) Curva dosis a respuesta a CORM-2 para los canales Kv2.1 WT (símbolos negros) y eYFP-Kv2.1 (símbolos verdes). Las curvas continuas son ajustes a la ecuación de Hill. Los parámetros para el canal fluorescente son: $K_{1/2}$ = 0.56 mM, s = 1.9 (n = 3 - 4).

Todos los canales mutantes parecen haberse expresado en la membrana, ya que se detectó fluorescencia correspondiente a la proteína YFP en la membrana de los ovocitos inyectados con cada una de las construcciones utilizando microscopía confocal (Fig. 29). Sin embargo, la mayoría de los canales mutantes no fueron funcionales, ya que no se pudieron registrar corrientes iónicas de estos canales en registros electrofisiológicos (no se muestran los datos). Este resultado refleja la sensibilidad de la región mutagenizada a perturbaciones estéricas grandes, y muy probablemente sea una indicación de la relevancia funcional de la mayoría de los residuos perturbados. Afortunadamente, al menos tres de los canales mutantes presentaron corrientes iónicas, y se procedió a caracterizarlos.

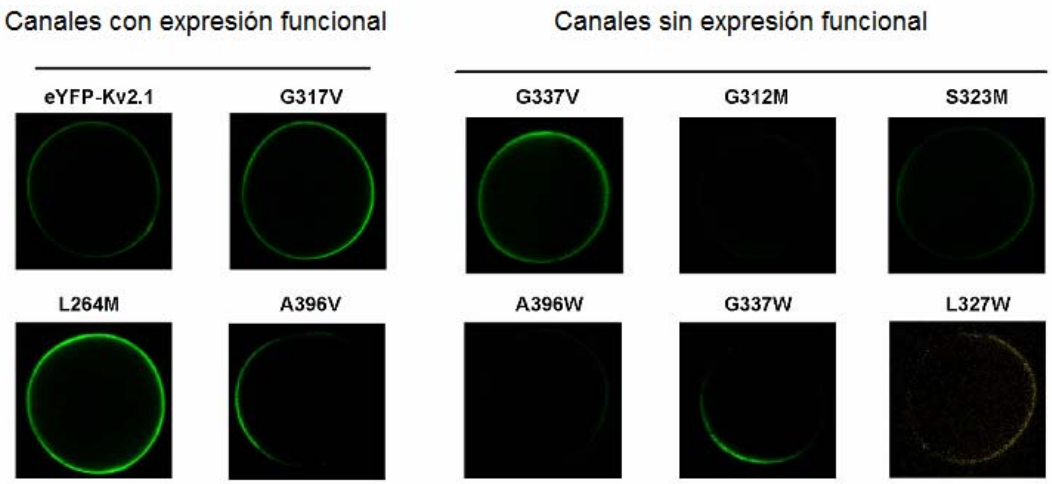

Figura 29. Expresión en la membrana de mutantes del canal eYFP-Kv2.1. Fotografías de microscopía confocal de ovocitos inyectados con el mRNA de cada una de las construcciones fluorescentes. La fluorescencia de eYFP fusionada a los canales se muestra en verde.

En salina, los canales con las mutaciones L264M, en el segmento S3, y A396W, en el S6, se comportaron de manera muy similar al canal WT (Fig. 30A y B). De igual manera, al evaluar la sensibilidad de estas construcciones al CORM-2, se encontró que ambas mutantes presentaban una sensibilidad al compuesto igual a la del canal silvestre (Fig. 30C), indicando que las cadenas laterales de estos residuos no forman parte del sitio de unión.

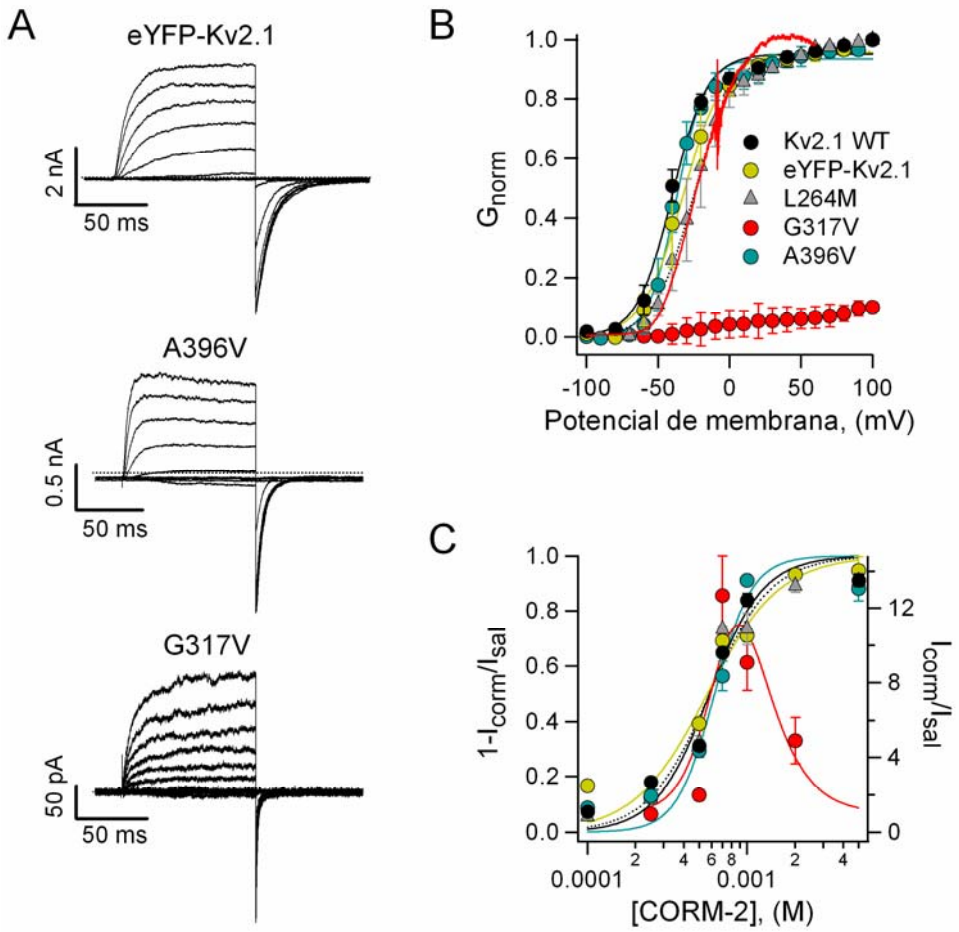

Figura 30. Efectos de las mutantes del sitio de unión putativo a CORM-2. (A) Familias de corrientes representativas de los canales eYFP-Kv2.1, eYFP-Kv2.1A396V y eYFP-Kv2.1G317V medidas en salina en respuesta a pulsos desde -120 hasta 100 mV en incrementos de 20 mV. (B) Curvas G-V para los canales Kv2.1, eYFP-Kv2.1 y las mutantes del sitio de unión putativo a CORM-2. Las curvas continuas son ajustes a la ecuación de Boltzmann (Ec. 4), de los que se obtuvieron los siguientes parámetros: L264M, $V_{1/2}$ = -28.3 ± 5.6 mV, z = 3.05 ± 0.60 e_0; A396V, $V_{1/2}$ = -37.1 ± 4.0 mV, z = 2.84 ± 0.30 e_0, (n = 4). La curva G-V de G317V en salina se normalizó al valor de probabilidad de apertura medido a 100 mV mediante análisis de ruido no estacionario (Fig. 31C). La curva roja continua es la corriente de G317V en presencia de 0.7 mM CORM-2 en respuesta a una rampa de voltaje desde -100 hasta 60 mV y normalizada como se indica en la Figura 31. (C) Curvas dosis a respuesta a CORM-2 para el canal Kv2.1 WT y las distintas construcciones. Las curvas de las mutantes que se inhiben por CORM-2 se expresan como la fracción inhibida $1-I_{corm}/I_{sal}$ (eje izquierdo), mientras que para la mutante G317V las curvas representan la corriente total en CORM-2 normalizada a la corriente en salina I_{corm}/I_{sal} (eje derecho). Las curvas para L264M y A396V se ajustaron a la ecuación de Hill (Ec. 2, curvas continuas), y se obtuvieron los siguientes parámetros: L264M, $K_{1/2}$ = 0.59 mM, s = 2.41; A396V, $K_{1/2}$ = 0.63 mM, s = 3.67 (n = 3-4). La curva de G317V se ajustó al producto de dos ecuaciones de Hill (Ec. 3), con parámetros: I_{max} = 28, $K_{1/2,1}$ = 0.73 mM, s1 = 4.0, $K_{1/2,2}$ = 0.92 mM, s2 = 2.65 (n = 3-6). Los colores de los símbolos son los mismos que en (B).

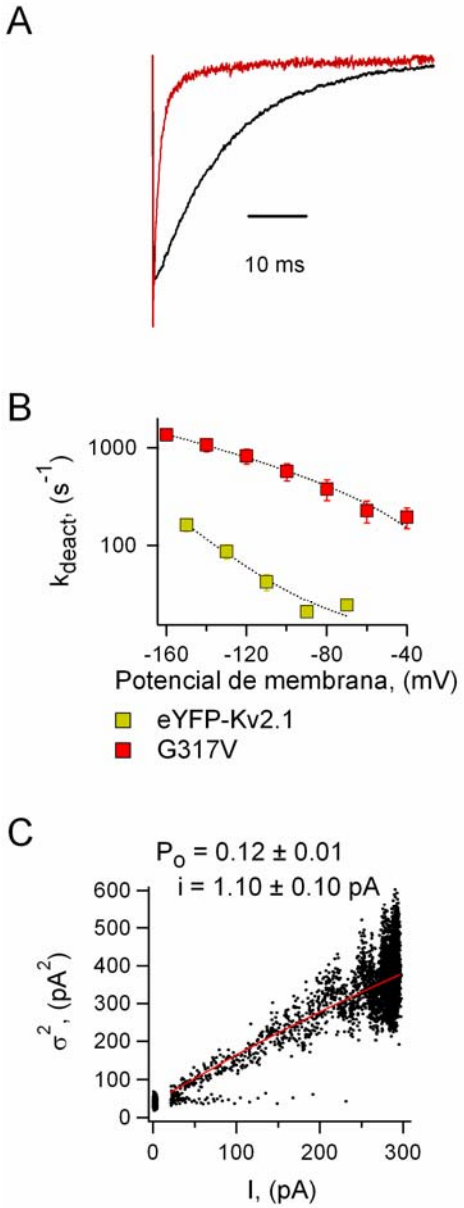

Figura 31. La mutación G317V disminuye la probabilidad de apertura. (A) Colas de corriente representativas a -120 mV desde un potencial de 100 mV (no se muestra) para eYFP-Kv2.1 (trazo negro) y la mutante G317V (trazo rojo). La amplitud de las colas se normalizó al valor máximo de cada una para comparar la cinética. (B) Constantes de velocidad de cierre en función del voltaje para eYFP-Kv.21 y la mutante G317V. Las líneas punteadas son ajustes a una función exponencial. (C) Gráfico representativo de varianza contra corriente media obtenido del análisis de ruido no estacionario a 100 mV para el canal eYFP-Kv2.1G317V. La curva roja es un ajuste a la ecuación 6. La probabilidad de apertura a 100 mV para la mutante, calculada de la Ec. 7 y los parámetros obtenidos del análisis de ruido, incluyendo la corriente unitaria a 100 mV, se indican en la figura (n = 3).

Por otro lado, la mutante G317V, localizada en el asa entre los segmentos S4 y S5, que es la región principal en el mecanismo de acoplamiento electromecánico (Jensen et al., 2012; Labro et al., 2008; Lu et al., 2001, 2002; Tristani-Firouzi et al., 2002), presentó importantes alteraciones en su función con respecto al canal WT. Las corrientes de este canal mutante fueron mucho más pequeñas que las de las otras construcciones y el canal WT, y los trazos de corriente tienen más ruido, lo que sugiere una probabilidad de apertura reducida (Fig. 30A). Consistentemente, la cinética de cierre de este canal se vio significativamente acelerada (Fig. 31 A y B). Con el fin de determinar si la reducción en el tamaño de las corrientes del canal Kv2.1-G317V se debe a una

disminución en la probabilidad de apertura debida a la mutación, se realizó análisis de ruido no estacionario (Fig. 31C). Los resultados obtenidos indican que la mutación efectivamente causa una reducción en la probabilidad de apertura, de 0.80 ± 0.02 (100 mV, n = 12) en el canal WT a 0.12 ± 0.02 (100 mV, n = 3) en G317V. En la Figura 30B se muestra la curva G-V de la mutante G317V escalada al valor de probabilidad de apertura determinado a 100 mV. Resulta muy interesante que no sólo se redujo la probabilidad de apertura, sino que la pendiente de la curva de esta mutante también está significativamente reducida, lo que refleja que muy probablemente la mutación también interfiere con el acoplamiento electromecánico, dificultando la apertura del canal.

A continuación se exploró el efecto del CORM-2 sobre la mutante G317V. Sorprendentemente, en lugar de provocar una inhibición, como en el canal WT, el CORM-2 causó una marcada potenciación casi instantánea de la corriente del canal (Fig. 32 A y B). La potenciación es reversible, como se muestra en el curso temporal de la Figura 32A al regresar el parche a solución salina. Además, la potenciación fue acompañada de un segundo proceso más lento que resulta en la pérdida irreversible de la capacidad del canal para conducir iones.

Para obtener una curva de activación del canal en el estado potenciado, se aplicaron rampas de voltaje en ausencia y presencia de 0.7 mM CORM-2 (Fig. 32C) y se normalizaron con la corriente predicha por un modelo de permeación que considera el salto de una sola barrera de activación (Hille, 2001; Islas and Sigworth, 2001). La curva G-V resultante se muestra en la Figura 30B (trazo rojo). Interesantemente, la curva obtenida se superpone muy bien sobre la curva del canal silvestre, como si el compuesto hubiera revertido momentáneamente el efecto de la mutación. Esto sugiere que el CORM-2 tiene efectos sobre el asa entre los segmentos S4-S5, posiblemente producto de una interacción directa con esta región de la proteína.

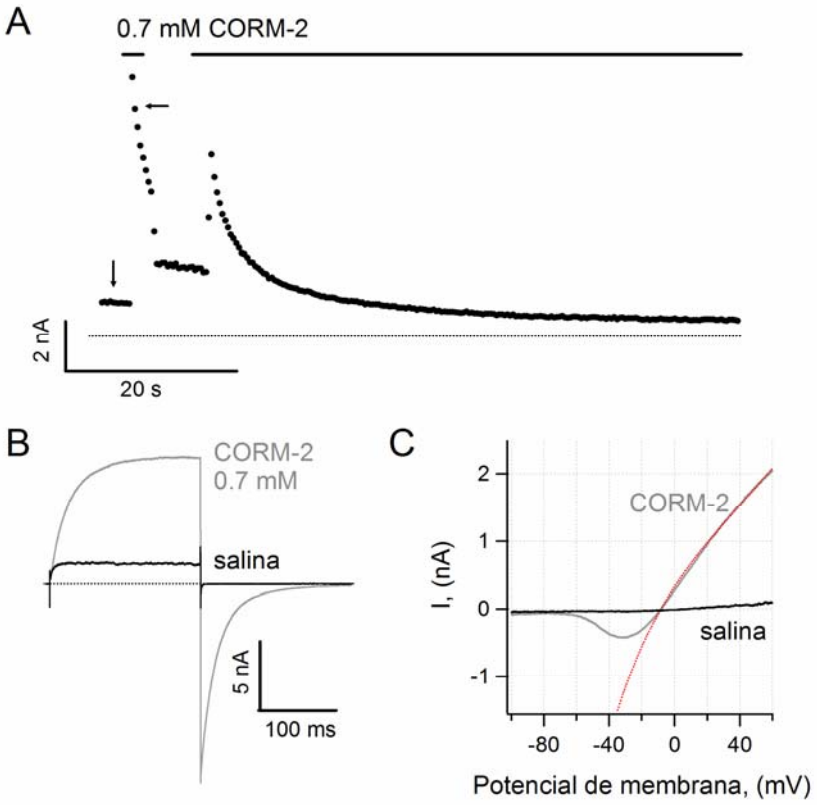

Figura 32. El CORM-2 potencía al canal eYFP-Kv2.1G317V. (A) Curso temporal representativo de los efectos del CORM-2 sobre G317V a 100 mV. La línea punteada indica el cero de corriente y las flechas indican los puntos de donde provienen los trazos en (B). Las líneas horizontales superiores marcan los tiempos en los que el parche estuvo expuesto a CORM-2. (B) Trazos de corriente representativos tomados del experimento en (A) en ausencia y presencia de CORM-2. (C) Rampa de voltaje representativa para la mutante G317V en salina (trazo negro) y en presencia de 0.7 mM CORM-2 (trazo gris). La rampa de voltaje inició en -100 mV y llegó hasta 60 mV con una razón de cambio de 0.48 mV/s. La curva roja es una ajuste a un modelo de permeación a través de una barrera, descrito por la siguiente ecuación: $I(V) = e^{-\frac{\Delta G}{k_B T}}([K]_{\text{int}} e^{-\frac{(1-\delta) z V}{k_B T}} - [K]_{ext} e^{\frac{\delta z V}{k_B T}})$, donde $I(V)$ es la corriente en función del voltaje, $e^{-\frac{\Delta G}{k_B T}}$ es la contribución de la altura de la barrera de energía que separa la solución intracelular de la extracelular, $[K]_{\text{int}}$ y $[K]_{ext}$ son las concentraciones de potasio intra- y extracelulares, respectivamente, z es la carga del ion, δ es la distancia eléctrica que marca la posición de la barrera con respecto a los sitios intra- y extracelulares, V es el voltaje y $k_B T$ tiene su significado usual. Los parámetros utilizados fueron $e^{-\frac{\Delta G}{k_B T}}$ = -6.9 nA/mM y δ = 0.273. La curva roja en la Figura 30B es el cociente entre la corriente predicha por el modelo a cada voltaje de la rampa y la corriente determinada experimentalmente en respuesta a la rampa de voltaje en presencia de CORM-2.

También se determinó una curva de dosis a respuesta para el CORM-2 en la mutante G317V, la cual presenta un comportamiento bifásico, con potenciación a concentraciones intermedias de CORM-2 e inhibición a concentraciones mayores, sugiriendo que la cinética del paso al estado no funcional depende de la concentración del compuesto, y a concentraciones altas ocurre tan rápidamente que la potenciación inicial ya no es detectable (Fig. 30C). La afinidad del canal por el compuesto se vio claramente afectada, sugiriendo nuevamente que la mutación perturbó la región en el canal con la que el CORM-2 interacciona.

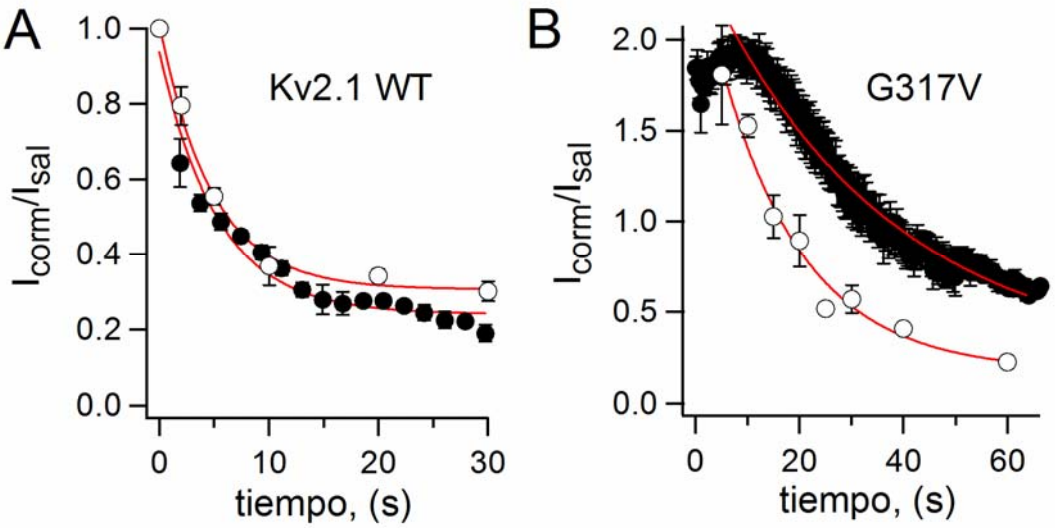

Figura 33. Dependencia en el estado de la inhibición del canal Kv2.1 WT y G317V por CORM-2. Cursos temporales de los efectos del CORM-2 sobre el canal (A) Kv2.1 WT (0.7 mM CORM-2) y (B) la mutante G317V (0.5 mM CORM-2) en los estados abierto (símbolos negros) y cerrado (símbolos blancos) del canal. Las curvas rojas son ajustes a una función exponencial, con parámetros: (A) WT, $k_{abierto}$ = 0.217 ± 0.041 s^{-1}, $k_{cerrado}$ = 0.207 s^{-1} (n = 6); (B) G317V, $k_{abierto}$ = 0.045 ± 0.009 s^{-1}, $k_{cerrado}$ = 0.0625 s^{-1} (n = 3-6).

Finalmente se determinó si los efectos del CORM-2 sobre el canal silvestre y la mutante G317V son dependientes del estado del canal. Para esto se obtuvieron cursos temporales del efecto del CORM-2 cuando este es aplicado en el estado cerrado del canal o en condiciones que promueven una probabilidad de apertura alta. De acuerdo con los resultados del *docking*, que sugieren que el CORM-2 puede unirse a su sitio de manera independiente del estado, los cursos temporales para la inhibición del canal Kv2.1 WT en el

estado cerrado y abierto se superponen casi perfectamente, indicando que el CORM-2 efectivamente puede unirse al canal en el estado abierto y cerrado (Fig. 33A). Por el contrario, tanto la potenciación inicial como la pérdida de la funcionalidad del canal G317V en presencia de CORM-2 ocurrieron más rápidamente cuando el compuesto se aplicó en el estado cerrado (Fig. 33B). El cambio en la dependencia en el estado provocado por la mutación sugiere nuevamente que la mutación provocó perturbaciones estructurales en la región del canal con la que el CORM-2 interacciona.

Tanto los resultados funcionales en los canales silvestres como los resultados obtenidos con la mutante G317V sugieren que efectivamente el CORM-2 interfiere con el mecanismo de acoplamiento electromecánico en canales de potasio dependientes de voltaje. Los posibles mecanismos por los que esto puede ocurrir, y una propuesta para el mecanismo global de acción del CORM-2 sobre los canales Kv2.1, Shaker y Kv2.1G317V se presentará a continuación en la sección de discusión.

9. DISCUSIÓN

9.1. Efectos de compuestos liberadores de monóxido de carbono indepedendientes del CO.

El monóxido de carbono es bien conocido por su alta toxicidad, puesto que puede unirse irreversiblemente a la hemoglobina de la sangre con mayor afinidad que el oxígeno. Sin embargo, una gran cantidad de datos experimentales indican que tanto el monóxido de carbono producido endógenonamente, principalmente por el grupo de enzimas denominadas hemoxigenasas, como el gas administrado exógenamente en condiciones controladas, tiene efectos benéficos para la salud (Motterlini and Otterbein, 2010). Se ha encontrado que el CO tiene efectos antiapoptóticos, protegiendo a células y tejidos de daño durante isquemia o inflamación (Brouard et al., 2000; Kim et al., 2007). Por otro lado, el gas tiene un efecto pro-apoptótico con respecto a células cancerosas, linfocitos T superreactivos y células de músculo liso que presentan proliferación excesiva (McDaid et al., 2005; Song et al., 2004a; Song et al., 2004b; Zhou et al., 2005). Además, varios estudios han demostrado que el CO puede reducir el rechazo o daño isquémico a tejidos transplantados provenientes de pulmón (Fujita et al., 2001), corazón (Clark et al., 2003), riñón (Kaizu et al., 2008; Neto et al., 2006), hígado (Ott et al., 2005), intestino delgado (Nakao et al., 2003) y páncreas (Lee et al., 2007), entre otros, aumentando su supervivencia. Por otro lado, el gas también promueve la supervivencia de animales modelo en condiciones de sepsis por infección bacteriana y choque endotóxico (Desmard et al., 2009; Otterbein et al., 2000; Sarady et al., 2004), y reduce el daño provocado por infarto cardiaco (Guo et al., 2004) y artritis reumatoide (Ferrandiz et al., 2008). Finalmente, el gas también tiene efectos sobre la circulación, por lo que es benéfico en condiciones de hipertensión pulmonar (Zuckerbraun et al., 2006) e insuficiencia renal aguda (Neto et al., 2006; Ryan et al., 2006).

La impactante cantidad de efectos benéficos del CO ante varios padecimientos humanos ha impulsado el desarrollo de moléculas liberadoras de monóxido de carbono con el fin de aplicarlas como tratamiento clínico (Romao et al., 2012;

Santos-Silva et al., 2012). Los avances en síntesis química han permitido incluso desarrollar compuestos liberadores de CO covalentemente asociados a moléculas con especificidad por ciertos tejidos o tipos celulares, permitiendo la liberación dirigida del gas.

Un aspecto importante durante el desarrollo de nuevos tratamientos clínicos son los posibles efectos secundarios de la molécula empleada. Los resultados presentados en esta tesis demuestran que el CORM-2 puede tener efectos importantes sobre la función de canales iónicos de manera independiente del CO que libera. Estos resultados se extienden a moléculas distintas estructuralmente relacionadas al CORM-2 (Fig. 13C), indicando que la inhibición no es selectiva, por lo que otras moléculas podrían tener efectos similares. Más aun, el hecho de que los efectos del CORM-2 sean comunes a dos canales de potasio dependientes de voltaje con estructuras distintas (aunque relacionadas), sugiere que la inhibición podría ocurrir también en otros canales dependientes de voltaje, como los de sodio y calcio, que comparten, en términos generales, el mecanismo de funcionamiento y la topología estructural con los canales Kv. Otros canales Kv de interés clínico, como el canal hERG, que es esencial para la repolarización de los cardiomiocitos, podrían también ser blancos del CORM-2 u otras moléculas similares, conllevando a importantes riesgos para la salud si dichas moléculas se emplearan como tratamiento médico. Notablemente, se ha demostrado que el CORM-2 es capaz de activar una corriente catiónica no selectiva en células endoteliales humanas de manera independiente del CO (Dong et al., 2008).

La existencia de efectos directos de las moléculas liberadoras de CO sobre canales iónicos abre la posibilidad de que algunos de los resultados experimentales fisiológicos obtenidos utilizando estos compuestos sean al menos en parte debidos a estos efectos secundarios. De acuerdo con los resultados de este trabajo, la ausencia de efecto de los controles negativos generalmente empleados, como la molécula de $Ru(DMSO)_4Cl_2$ o el iCORM, no es un buen indicativo para concluir que las moléculas liberadoras de CO son inertes con respecto al objeto de estudio: las acciones directas de las moléculas donadoras sobre el sistema de estudio podrían haber sido pasadas

por alto debido a las concentraciones a las que se emplean normalmente estos compuestos.

Un ejemplo es la reciente demostración de que el CO, y no el CORM-2, inhibe indirectamente al canal Kv2.1 en células completas mediante un mecanismo que requiere especies reactivas de oxígeno y proteincinasa G (Dallas et al., 2011). Dado que la IC_{50} para el efecto del CO reportada en ese estudio es 10 veces menor que la $K_{1/2}$ del CORM-2 medida en este trabajo (y mucho menor que la del iCORM), los efectos directos de la molécula sobre el canal se pasaron por alto. Sin embargo, en estudios clínicos se llega a aplicar hasta 3 mg/kg de CO (Motterlini and Otterbein, 2010). En un cálculo muy grueso, esto corresponde a una concentración de 0.1 mM del gas. Si se tuviera que aplicar la misma concentración de moléculas liberadoras de CO para tener el mismo efecto en la clínica, habría que tomar en cuenta que una concentración de 0.1 mM no se encuentra muy lejos de la $K_{1/2}$ para CORM-2 de Shaker (~ 0.35 mM), sugiriendo que la aplicación clínica de cantidades significativas de compuestos estructuralmente relacionados al CORM-2 podría resultar en efectos directos de las moléculas sobre canales de potasio dependientes de voltaje. En este sentido, el trabajo presentado aquí sirve como una llamada de atención para considerar estos efectos durante la interpretación de resultados fisiológicos y clínicos en experimentos donde se utilicen moléculas liberadoras de monóxido de carbono.

9.2. Evidencias experimentales de que el CORM-2 interfiere con el acoplamiento electromecánico.

Los resultados obtenidos en el curso de los experimentos aquí presentados arguyen en favor de que el CORM-2 funciona como un agente desacoplante entre los dominios sensores de voltaje y el poro del canal. Los argumentos que sustentan esta conclusión se presentan a continuación.

La primera evidencia de que el CORM-2 actúa principalmente sobre el acoplamiento electromecánico proviene de los efectos del compuesto sobre la dependencia en el voltaje de la cinética de activación del canal Kv2.1. Los

datos experimentales demuestran que en presencia de 0.7 mM CORM-2, la activación del canal es prácticamente independiente del voltaje, al ocurrir con la misma velocidad en un rango de 80 mV (Fig. 16C). Esto sugiere que la apertura del canal a potenciales de membrana mayores a 0 mV no se encuentra bajo el control de los sensores de voltaje. Bajo estas condiciones, la probabilidad de apertura estaría únicamente gobernada por el balance de energía libre entre el estado abierto y el estado cerrado-activado (del Camino et al., 2005; Jensen et al., 2012), en el cual los sensores de voltaje han alcanzado el estado activado sin que el poro se abra. Cabe mencionar que debido a lo anterior, el valor de la probabilidad de apertura bajo estas condiciones podría arrojar información sobre la estabilidad intrínseca del estado abierto con respecto al estado cerrado-activado sin la influencia de los sensores de voltaje, siempre y cuando se tome en cuenta el efecto que el CORM-2 mismo podría tener sobre las energías intrínsecas de cada uno de los estados.

En contraste con el efecto del CORM-2 sobre la cinética de activación del canal, el proceso de cierre mantiene una dependencia en el voltaje significativa en presencia del compuesto (Fig. 16C), sugiriendo que los determinantes moleculares responsables del acoplamiento electromecánico para abrir o cerrar al canal son diferentes, dado que responden de manera distinta a la presencia del CORM-2. Esto es consistente con los datos que sugieren que las interacciones del asa S4-S5 con el S6 son diferentes en el estado abierto y cerrado, al menos en algunos canales (Choveau et al., 2011; Ferrer et al., 2006; Labro et al., 2011; Ng et al., 2012). Más aun, el mayor efecto sobre la dependencia en el voltaje de la activación con respecto al cierre sugiere que el cierre del canal es un proceso más robusto que la apertura, consistentemente con el alto grado de acoplamiento entre dominios a voltajes muy negativos para cerrar al canal (Islas and Sigworth, 1999) y la evidencia que sugiere que el estado cerrado del canal es de menor energía que el estado abierto (Jensen et al., 2010; Jensen et al., 2012; Yifrach and MacKinnon, 2002). También es importante mencionar que la dependencia en el voltaje de las constantes de velocidad de cierre para los dos canales se redujo en presencia de CORM-2, lo que es consistente con la acción desacoplante del compuesto.

Los efectos del donador sobre las constantes de velocidad de apertura y cierre en el canal Kv2.1 parecen compensarse de tal modo que las modificaciones resultantes no provocan un corrimiento en el voltaje medio de activación medido de la curva G-V (Fig. 16A). En *Shaker*, por el contrario, la curva G-V se corre por más de 60 mV hacia voltajes más positivos (Fig. 21B). Esto es resultado de efectos asimétricos del CORM-2 sobre las constantes de velocidad de apertura y cierre en este canal (Fig. 21C). En contraste con las diferencias entre ambos canales con respecto a los efectos del CORM-2 sobre las corrientes iónicas, el comportamiento de las corrientes de compuerta en presencia del CORM-2 fue muy similar para Kv2.1 y *Shaker*. Es interesante que el proceso de activación de los sensores de voltaje de canales tipo Shaker (Kv1) y el canal Kv2.1 es muy similar entre ellos, tanto con respecto a las constantes de velocidad asociadas a cada una de las transiciones, como a la carga de compuerta efectiva; por el contrario, los dos tipos de canales difieren significativamente en relación a las transiciones concertadas que llevan a la apertura y cierre del canal (Islas and Sigworth, 1999; Scholle et al., 2004). Las divergencias entre ambos canales en relación a los efectos del CORM-2 sobre las corrientes iónicas podrían derivarse de la acción del CORM-2 sobre las transiciones concertadas de cada canal, que son muy diferentes entre sí.

Una evidencia más de que el CORM-2 afecta las transiciones concertadas proviene de los cambios relativos que el compuesto induce en la $V_{1/2}$ asociada a las curvas G-V y Q-V de ambos canales, aunque esto es más claro en *Shaker*: por un lado se espera que perturbaciones en el movimiento de los sensores de voltaje resulten en corrimientos en la misma dirección en el eje del voltaje en las curvas Q-V y G-V. Por otro lado, una perturbación en las transiciones que ocurren una vez que la mayor parte de la carga de compuerta se movió (i.e. las transiciones concertadas) no podría provocar un corrimiento de la curva Q-V hacia voltajes más positivos. Sin embargo, la misma perturbación podría provocar un corrimiento importante hacia la derecha en la curva G-V. Blunck y colaboradores han ilustrado esto utilizando un modelo secuencial como el que se muestra en negro en el Esquema I, para la activación de *Shaker* (Batulan et al., 2010). Suponiendo que el modelo en el Esquema I se extiende desde C_0 hasta un número n de estados, la ocupancia

en el equilibrio (t→∞) para el estado C_0 estaría dada por: $C_0 = \frac{1}{1+\frac{\alpha_0}{\beta_0}(1+\frac{\alpha_1}{\beta_1}(1+\frac{\alpha_2}{\beta_2}...(1+\frac{\alpha_{n-1}}{\beta_{n-1}})...))}$ (Ec. 12), donde las α's indican constantes de velocidad para transiciones hacia adelante (i.e. hacia el estado abierto) y las β's transiciones hacia atrás (hacia el estado cerrado). Si se supone que el movimiento de la mayor parte de la carga ocurre entre los estados C_0 y C_1, entonces la carga total normalizada $Q_{norm} = \frac{Q}{Q_{\max}} = 1 - C_0$ (Ec. 13). Dado que los términos entre paréntesis en el numerador de la Ec. 12 son siempre mayores o iguales a uno (pero nunca menores), entonces se cumple para la ocupancia de C_0 que: $C_0 < \frac{\beta_0}{\alpha_0 + \beta_0}$ (Ec. 14). Debido a la suposición de que toda la carga se mueve entre C_0 y C_1, se sigue que a la $V_{1/2}$ para la primera transición ($\alpha_0 = \beta_0$, Ec. 14, lado derecho) se ha movido exactamente el 50% de la carga de compuerta. Por lo tanto, la $V_{1/2}$ aparente que resulta de todo el sistema (Ec. 13), y no sólo la primera transición, puede ser más negativa que la $V_{1/2}$ real para el movimiento de la carga, pero nunca más positiva. Ningún cambio sobre las transiciones posteriores a la transición entre C_0 y C_1 puede provocar un corrimiento de la curva Q-V hacia la derecha, aunque sí podría reducir la pendiente de la curva (Batulan et al., 2010).

Consistentemente, el voltaje medio de la curva Q-V de *Shaker* no se alteró demasiado en presencia de CORM-2, aunque sí su pendiente, mientras que la G-V se corrió dramáticamente hacia la derecha, signos claros de perturbaciones en transiciones tardías en las que la mayoría de la carga de compuerta se ha movido. En el caso de Kv2.1, la incertidumbre en los datos de la $V_{1/2}$ para el movimiento de carga en presencia de CORM-2 impide realizar comparaciones confiables.

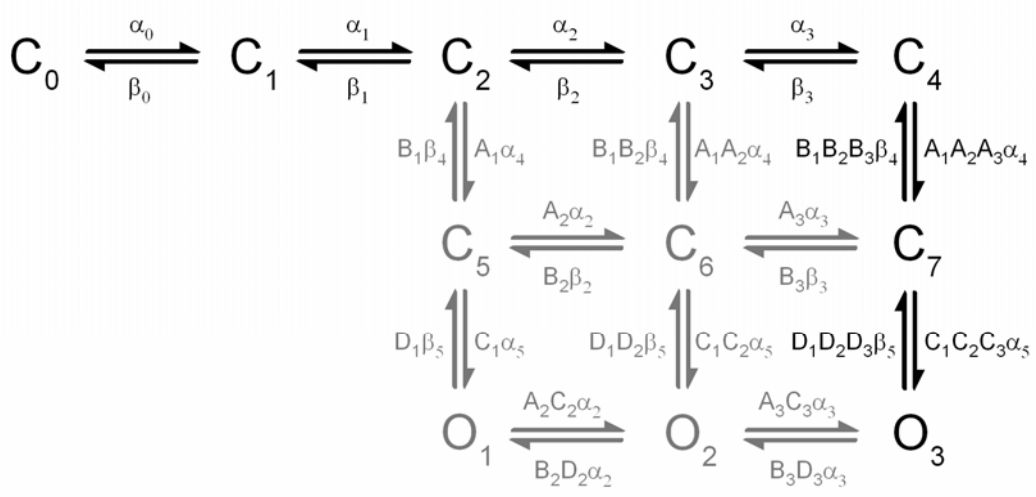

Esquema I. La porción del esquema en negro es suficiente para representar la actividad de los canales en ausencia de CORM-2. En presencia de CORM-2, es necesario utilizar todo el esquema, incluyendo la región en gris. Los estados del canal con la letra C representan estados cerrados, mientras que la O representa estados abiertos. Los parámetros asociados a las constantes de velocidad incluidas en el esquema que se utilizaron para representar los datos se presentan en la Tabla I. Las constantes de velocidad de activación se representan con la letra α, mientras que las constantes de velocidad de desactivación se representan con la letra β. Las letras mayúsculas (A, B o C) son factores alostéricos que representan el efecto de la apertura o cierre del poro sobre la velocidad con que se activan o desactivan los sensores de voltaje, y viceversa.

Otra evidencia importante de que el CORM-2 desacopla el poro de los DSV radica en los efectos del compuesto sobre la cinética del regreso de la carga de compuerta durante la desactivación de los DSV en ambos canales (Figs. 19 y 23). El efecto del CORM-2 sobre este aspecto de la función de los canales es muy similar a los efectos de mutaciones que desacoplan la activación de los sensores de voltaje de la apertura del canal en *Shaker* (Holmgren et al., 1996; Kanevsky and Aldrich, 1999; Ledwell and Aldrich, 1999; Schoppa and Sigworth, 1998b; Smith-Maxwell et al., 1998). En estas mutantes, despolarizaciones de magnitud intermedia que normalmente provocan la apertura del poro en canales silvestres son suficientes para que los cuatro sensores de voltaje realicen las transiciones independientes que llevan al estado activado, pero no proveen suficiente energía para abrir al canal. Al repolarizar la membrana los sensores de voltaje pueden regresar rápidamente al estado desactivado puesto que la transición entre el estado abierto y el primer estado cerrado, que es

lenta, no se observa. En estas mutantes, una despolarización mucho más fuerte de lo normal es capaz de abrir el poro del canal, sin embargo este proceso está energéticamente aislado de la activación de los sensores de voltaje. El 4-AP, un bloqueador del poro de canales Kv, también actúa como un agente desacoplante y elimina el componente lento de las corrientes de compuerta de desactivación, al estabilizar al estado cerrado con respecto al abierto (Armstrong and Loboda, 2001; Loboda and Armstrong, 2001).

Cabe mencionar que la eliminación del componente lento en las corrientes de compuerta de desactivación no necesariamente implica que no se alcance el estado abierto, aunque este sea efectivamente el caso en cuanto al 4-AP y las mutaciones citadas. En un mecanismo alternativo, los sensores de voltaje podrían estar tan desacoplados del poro que serían capaces de regresar rápidamente al estado desactivado sin que el poro se cerrara. Consistentemente, existen reportes de mutaciones en las que el poro y los dominios sensores de voltaje parecen estar completamente desacoplados, permitiéndole al canal abrirse sin que los sensores de voltaje se activen (Ferrer et al., 2006; Hackos et al., 2002; Lu et al., 2001, 2002; Sukhareva et al., 2003).

Finalmente, se ha demostrado que el componente lento en el regreso de la carga de compuerta al estado desactivado no está directamente ligado a la apertura del canal, sino a la estabilización del estado abierto que ocurre de manera posterior a la apertura del poro (Kanevsky and Aldrich, 1999; Batulan et al., 2010). Esta estabilización depende de interacciones entre el extremo N-terminal del asa S4-S5 de una subunidad (R326, E327, Fig. 6A) con el S6 de una subunidad vecina (Y417, Fig. 6A). La ruptura de estas interacciones mediante mutaciones puntuales resulta en la pérdida del componente lento de las corrientes de compuerta de desactivación, pero no le impide al canal abrirse (Batulan et al., 2010).

Es importante mencionar que las tres alternativas que explican la pérdida del componente lento implican distintos grados de desacoplamiento entre los dominios sensores de voltaje y el poro. En el caso del CORM-2 y el canal Kv2.1, las mediciones simultáneas de corrientes de compuerta y corrientes

iónicas (Fig. 20) indican que la pérdida del componente lento está al menos parcialmente ligada a la apertura del canal, puesto que en presencia de CORM-2 ya no se observaron corrientes iónicas a pesar de que se presentara un movimiento significativo de carga de compuerta. Es importante recalcar que los datos experimentales disponibles no permiten distinguir entre las tres posibilidades.

Un quinto argumento a favor de un rol para el CORM-2 como agente desacoplante en canales Kv viene del aumento en el retraso en la activación de *Shaker*: la magnitud del retraso es proporcional al número de estados cerrados por los que transita el canal en la vía de activación y a las constantes de velocidad asociadas con dichas transiciones, mientras que la relajación monoexponencial en la fase tardía de la activación está dada por la transición o transiciones cuya velocidad es limitante (Schoppa and Sigworth, 1998a). Un aumento en el retraso (Fig. 24) implica un aumento en el número de estados cerrados, que resulta poco probable, o bien una disminución en la velocidad de algunas de las transiciones que van al estado abierto. La observación de que la cinética de activación de las corrientes de compuerta de *Shaker* no se altera por la presencia del CORM-2 (Fig. 22C) implica que las transiciones cuya velocidad se redujo para aumentar el retraso de las corrientes iónicas ocurren después del movimiento de al menos el 60% de la carga de compuerta.

Finalmente, la última evidencia a favor de la hipótesis aquí presentada está relacionada con el efecto de la mutante G317V. La mutación en sí misma parece desacoplar los DSV del poro del canal, al impedir la apertura del canal aún a despolarizaciones fuertes. Cabe mencionar que la demostración formal de esta aseveración requeriría medir la dependencia en el voltaje del movimiento de carga de la mutante G317V. Un efecto sobre el acoplamiento electromecánico de una mutación introducida precisamente en esa posición no es algo raro, dado que el asa S4-S5 parece ser el principal determinante molecular del acoplamiento (Labro et al., 2008; Lu et al., 2001, 2002; Tristani-Firouzi et al., 2002). Sin embargo, el hecho de que el CORM-2 sea capaz de revertir el efecto de la mutación y permitir la activación del canal con una dependencia en el voltaje similar a la del canal WT sugiere que efectivamente

el compuesto tiene la propiedad de interferir con el acoplamiento electromecánico en el canal Kv2.1. Los efectos de la mutación y su relación con el mecanismo de acción del CORM-2 se discutirán en la sección final de esta discusión.

9.3. Posible modelo cinético para explicar los efectos del CORM-2 sobre Kv2.1 y Shaker.

Los modelos cinéticos resultan muy útiles para comprender los efectos de una perturbación en la función de un canal, dado que permiten evaluar el tipo de cambios (y su magnitud) que se deben introducir al modelo no perturbado para reproducir los efectos de la perturbación. Estos cambios se pueden interpretar mecanísticamente en términos del modelo cinético, siempre y cuando cada uno de los estados en el modelo y su conectividad tenga una conexión directa bien restringida y establecida con alguna propiedad estructural del sistema bajo estudio. Además, una vez introducidas las modificaciones en el modelo, se pueden generar predicciones para ser verificadas experimentalmente.

Con el fin de comprender mejor el mecanismo de inhibición de ambos canales por CORM-2, se decidió modelar la actividad de ambos canales en salina y en CORM-2 en base a un esquema cinético. Aunque para *Shaker* se han propuesto al menos tres modelos cinéticos de complejidad considerable (Ledwell and Aldrich, 1999; Schoppa and Sigworth, 1998c; Zagotta et al., 1994a), capaces de reproducir la actividad del canal bajo una gran cantidad de condiciones experimentales, no existen modelos bien constreñidos para representar la actividad del canal Kv2.1. Debido a que parte del objetivo del modelado cinético es representar los efectos del CORM-2 sobre ambos canales mediante el mismo mecanismo, se decidió utilizar un modelo simple que fuera capaz de reproducir la actividad de ambos canales en ausencia de CORM-2. En este sentido, los modelos secuenciales lineales (Esquema I, caracteres negros) han sido ampliamente utilizados debido a su simplicidad y a la capacidad que tienen de reproducir exitosamente las principales características de la función de canales iónicos dependientes de voltaje,

incluyendo *Shaker* y Kv2.1 (Armstrong and Loboda, 2001; Bezanilla et al., 1994; Klemic et al., 1998; Scholle et al., 2004; Shieh et al., 1997).

Por las razones aquí expuestas, se decidió utilizar un modelo secuencial lineal de 7 estados (Esquema I, caracteres negros) para representar la actividad de *Shaker* y Kv2.1 en salina. En el modelo, las primeras cuatro transiciones corresponden a la activación secuencial de cada uno de los sensores de voltaje, mientras que las siguientes dos transiciones corresponden a los pasos concertados en el canal. Utilizando los parámetros mostrados en la Tabla I, el modelo fue capaz de reproducir satisfactoriamente las observaciones experimentales en ambos canales en salina, como se puede observar en las Figuras 16A y C, 18C y D, 19B, 21B y C, 22B y C y 23B, las cuales contienen las predicciones del modelo superpuestas en las gráficas. La Figura 34 muestra las predicciones del modelo con respecto a la forma de las corrientes iónicas y de compuerta. Cabe mencionar que la utilización de un modelo cinético más complicado (Ledwell and Aldrich, 1999), como el que se presenta en el Esquema II, no representó una mejora considerable en la calidad de las predicciones para la actividad del canal Kv2.1 en salina (Fig. 35), por lo que se utilizó el modelo simple del Esquema I para estudiar los efectos del CORM-2 en ambos canales.

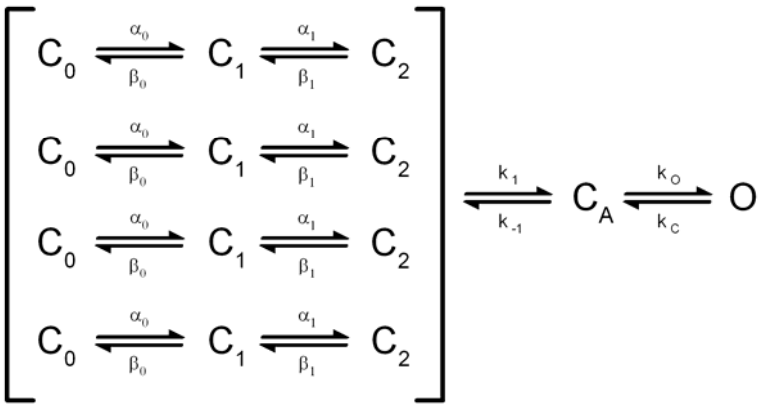

Esquema II. Modelo de 16 estados de Ledwell y Aldrich. C denota estados cerrados, C_A denota un estado en donde los sensores de voltaje han alcanzado el estado activado, pero el poro permanece cerrado, y O denota el estado abierto del canal. Las transiciones entre corchetes representan la activación independiente de cada uno de los cuatro sensores de voltaje, que sufren dos cambios conformacionales independientes (C_1 a C_2, y C_2 a C_3). Además, cada sensor de voltaje sufre un cambio conformacional concertado para alcanzar el estado activado C_A. La apertura del poro ocurre tras otra transición concertada de C_A a O. Los parámetros empleados para representar la actividad del canal Kv2.1 en salina se presentan en la Tabla II.

TABLA I

Parámetros para el modelo descrito en el Esquema I

	Shaker		Kv2.1			
	salina	CORM-2	salina		CORM-2	
				(a)		(b)
$\alpha_0(0)$	1500	3000	900	450	2400	1200
$\beta_0(0)$	250	650	250	500	500	1000
$\alpha_1(0)$	3500	3500	3000	1200	4500	2500
$\beta_1(0)$	250	550	200	450	500	900
$\alpha_2(0)$	3500	2500	3000	1200	1000	400
$\beta_2(0)$	250	50	200	450	500	900
$\alpha_3(0)$	3500	0.0001	3000	1200	0.0001	
$\beta_3(0)$	250	250	200	450	500	900
$\alpha_4(0)$	9000	400	100		20	
$\beta_4(0)$	250	150	55		10	
$\alpha_5(0)$	15000	120	90		40	
$\beta_5(0)$	100	1000	10		70	
$z\alpha_0(0)$	0.2	0.2	0.4		0.4	
$z\beta_0(0)$	-0.4	-0.4	-0.3		-0.3	
$z\alpha_1(0)$	0.4	0.4	0.5		0.5	
$z\beta_1(0)$	-0.5	-0.5	-0.3		-0.3	
$z\alpha_2(0)$	0.5	0.5	0.5		0.5	
$z\beta_2(0)$	-0.7	-0.7	-0.3		-0.3	
$z\alpha_3(0)$	0.5	0.5	0.5		0.5	
$z\beta_3(0)$	-0.7	-0.7	-0.4		-0.4	
$z\alpha_4(0)$	1.1	0.3	0.3		0.05	
$z\beta_4(0)$	-0.8	-0.3	-0.4		-0.4	
$z\alpha_5(0)$	0.18	0.18	0.1		0.001	
$z\beta_5(0)$	-0.5	-0.2	-0.5		-0.005	

(a) Parámetros para Kv2.1 en salina con bajo K^+

(b) Parámetros para Kv2.1 en CORM-2 y bajo K^+

Para *Shaker* A = B = C = D = 1.

Para Kv2.1 todos los factores alostéricos valen uno excepto $A_2 = 1.5$.

TABLA II

Parámetros para el modelo descrito en el Esquema II		
	Kv2.1- salina	
	alto K^+	bajo K^+
$\alpha_0(0)$	600	300
$\beta_0(0)$	300	
$\alpha_1(0)$	1400	800
$\beta_1(0)$	60	100
$k_1(0)$	280	
$k_{-1}(0)$	55	
$k_O(0)$	60	
$k_C(0)$	10	
$z\alpha_0(0)$	0.5	
$z\beta_0(0)$	-0.5	
$z\alpha_1(0)$	0.5	
$z\beta_1(0)$	-0.4	
$zk_1(0)$	0.3	
$zk_{-1}(0)$	-0.5	
$zk_O(0)$	0.2	
$zk_C(0)$	-0.5	

Si se quisieran representar los efectos del CORM-2 sobre ambos canales de la manera más simple, se podrían tomar en cuenta únicamente los dos efectos principales del donador, que consisten en la desestabilización del estado abierto con respecto a los estados cerrados, y el desacoplamiento de los sensores de voltaje con respecto al poro del canal. El efecto desacoplante se puede representar como una reducción en la carga asociada a las transiciones concertadas, mientras que la desestabilización del estado abierto se puede incluir en el modelo en forma de una disminución en la magnitud de las constantes de velocidad asociadas a las transiciones concertadas que llevan hacia el estado abierto y un posible aumento en la magnitud de las constantes de velocidad asociadas a las transiciones concertadas que se alejan del estado abierto. Sin embargo, las modificaciones en la función de los canales causadas por el CORM-2 son mucho más complejas.

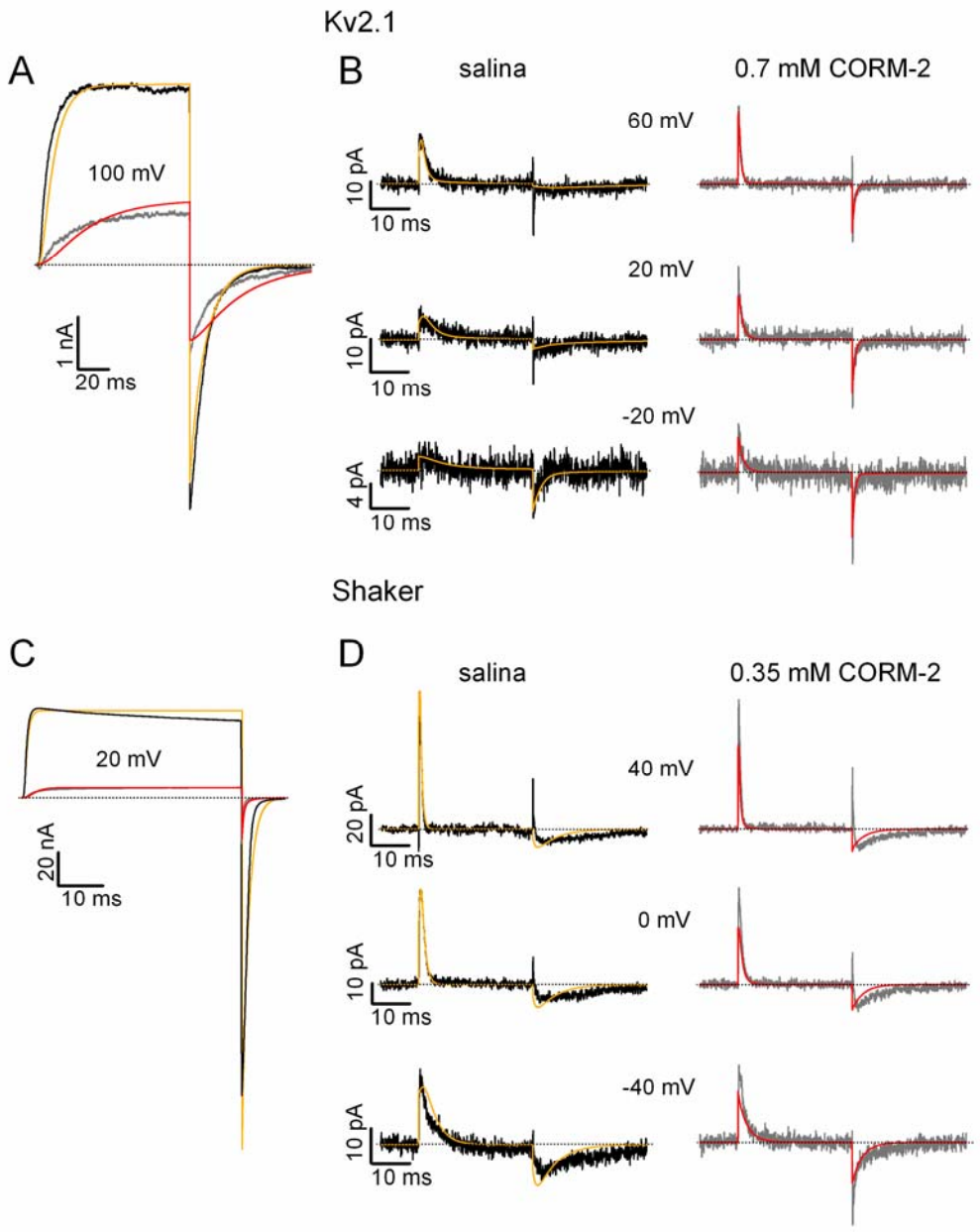

Figura 34. Predicciones del modelo en el Esquema I para las corrientes iónicas y de compuerta para los canales Kv2.1 y *Shaker* en salina y CORM-2. (A) Trazos representativos del canal Kv2.1 en respuesta a una despolarización a 100 mV y una repolarización a -120 mV en salina (trazo negro) y 0.7 mM CORM-2 (trazo gris). Las predicciones del modelo en el Esquema I y los parámetros de la Tabla I (alto K^+) para salina y CORM-2 se muestran en amarillo y rojo, respectivamente. (B) Corrientes de compuerta representativas a activadas a distintos potenciales y repolarizadas a -90 mV en salina y 0.7 mM CORM-2, junto con las predicciones del modelo de acuerdo con los parámetros presentados en la Tabla I (bajo K^+). (C) Trazos representativos de *Shaker* en respuesta a una despolarización a 20 mV y una repolarización a -120 mV en salina (trazo negro) y 0.35 mM CORM-2 (trazo gris). Las predicciones del modelo están superpuestas a los datos. (D) Corrientes de compuerta representativas de ShakerW434F con las predicciones del modelo superpuestas.

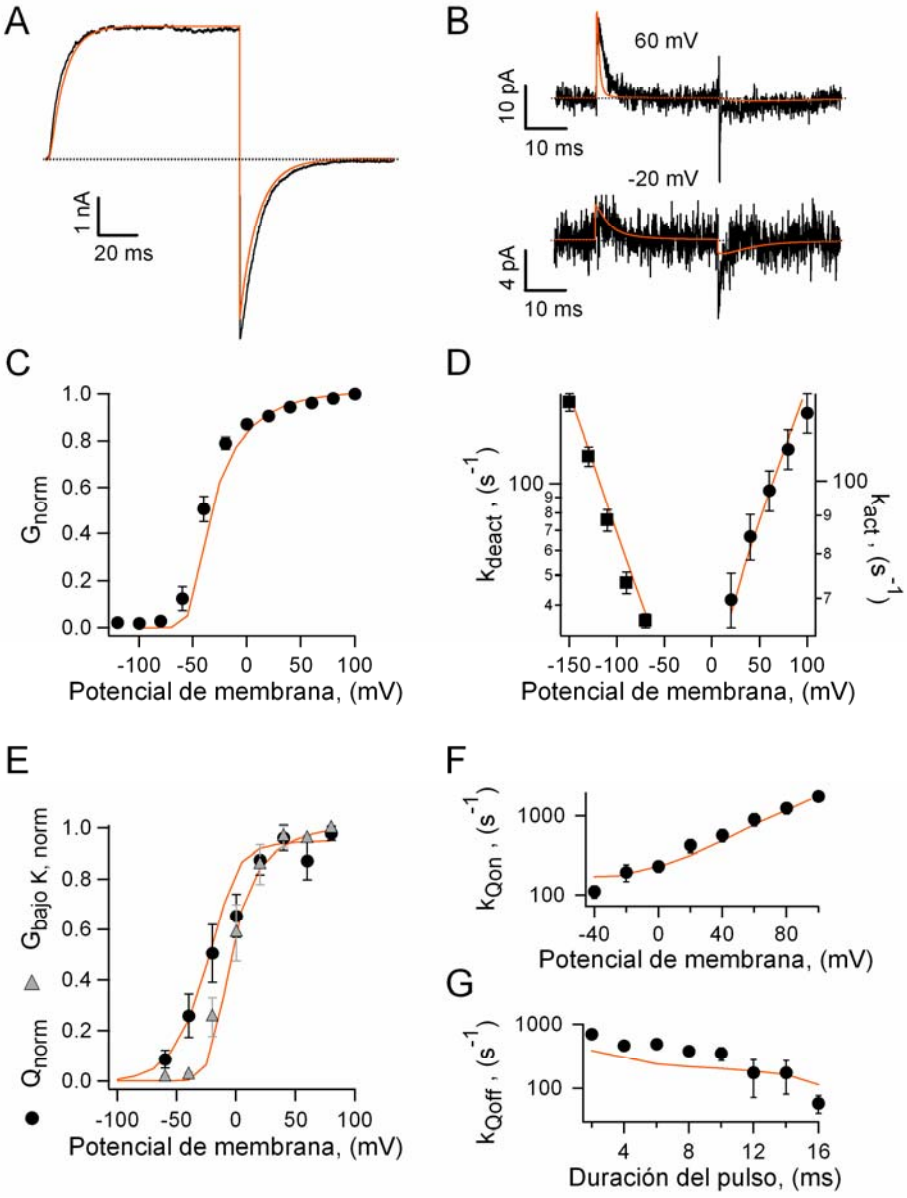

Figura 35. Predicciones del modelo de 16 estados para el canal Kv2.1 en salina. (A) Trazos representativos del canal Kv2.1 en respuesta a una despolarización a 100 mV y una repolarización a -120 mV. (B) Corrientes de compuerta representativas activadas a 60 y 20 mV y desactivadas a -90 mV. (C) Curva G-V normalizada. (D) Constantes de velocidad de activación y cierre en función del voltaje como en la Fig. 16C. (E) Curvas Q_{on}-V y G-V en bajo potasio tomadas de la Fig. 18D. (F) Constantes de velocidad de activación de las corrientes de compuerta tomadas de la Fig. 18C. (G) Constantes de velocidad para la desactivación de los sensores de voltaje a -90 mV en función de la longitud del pulso despolarizante (Fig. 19B). Las predicciones del modelo en el Esquema II de acuerdo con los parámetros de la Tabla II se muestran en la figura como curvas naranjas.

El efecto del compuesto sobre el movimiento de carga de activación es intrigante. La reducción observada en la carga de compuerta total sugiere que si bien el CORM-2 actúa principalmente sobre las transiciones concertadas, en las que se mueve aproximadamente el 10% de la carga de compuerta total (~ 1.8 e_0) (Ledwell and Aldrich, 1999; Pathak et al., 2005; Schoppa and Sigworth, 1998a, b), también tiene un efecto considerable sobre las transiciones independientes de los sensores de voltaje.

Una pérdida de carga en las corrientes de compuerta generalmente se asocia con 1) una reducción en las cargas de compuerta efectivas (e.g. debida a una reorientación de las cadenas laterales de los residuos básicos del S4, de tal forma que ya no interaccionen con el campo eléctrico de la membrana), 2) una remodelación del campo eléctrico transmembranal en el DSV ó 3) un enlentecimiento significativo en alguna de las transiciones que sufren los sensores de voltaje en la vía de activación. Esto se debe a que la amplitud de las corrientes de compuerta está dada por la cantidad de carga que se mueve y por la velocidad a la que ésta se mueve (Ec. 11). Es posible que el CORM-2 disminuya la carga de compuerta de ambos canales al modificar el perfil de potencial alrededor de las cargas de compuerta, e.g. al interactuar directamente con los residuos básicos del S4 o modificar el grado de hidratación de la cavidad acuosa intracelular del DSV. Esto es consistente con que las cargas de compuerta más intracelulares contribuyen al movimiento tardío del sensor de voltaje (Khalili-Araghi et al., 2010; Tao et al., 2009), que parece ser el blanco del CORM-2.

Otra posibilidad igualmente plausible es la que considera la contribución cinética al movimiento de carga. Un problema asociado al enlentecimiento en algunas de las transiciones del sensor de voltaje es que esto debería resultar en un corrimiento hacia la derecha en las curvas G-V y Q-V, puesto que el canal no podría abrirse hasta que los sensores hayan superado las transiciones enlentecidas. Estos efectos se han observado en presencia de toxinas que se unen a los sensores de voltaje (Lee et al., 2003; Phillips et al., 2005; Swartz and MacKinnon, 1997) o tras la modificación covalente de cisteínas en el DSV (Yang et al., 2004), pero no ocurren en presencia de CORM-2. Para que el

enlentecimiento en la activación de los sensores de voltaje sea consistente con las observaciones experimentales, se requiere que el poro sea capaz de abrirse sin que los sensores hayan alcanzado el estado completamente activado, y alternativamente, que los sensores puedan regresar al estado desactivado con el poro abierto. Esto representaría un caso extremo de desacoplamiento, que sin embargo no es una observación del todo rara entre los canales Kv: mutaciones introducidas en el S6 (Sukhareva et al., 2003) o en el asa S4-S5 (Lu et al., 2002) pueden tener efectos de este tipo.

En ausencia de datos para discriminar entre los distintos mecanismos expuestos anteriormente, se escogió modelar los datos de acuerdo a un efecto cinético del CORM-2 sobre el movimiento de los sensores de voltaje.

En el Esquema I se ilustra el modelo cinético capaz de representar los efectos del CORM-2 sobre los canales Kv2.1 y *Shaker*. Para lograrlo se permitió que el poro del canal se abra cuando únicamente dos sensores de voltaje han alcanzado el estado activado, de acuerdo con la discusión anterior. Los efectos del compuesto sobre las transiciones concertadas se incluyeron de la manera descrita al inicio de esta sección, y se muestran en la Tabla I.

Finalmente, la cuarta transición en los sensores de voltaje se enlenteció considerablemente, resultando en una pérdida de carga de compuerta sin comprometer la apertura de los canales. Esto se puede interpretar de dos maneras: 1) que el CORM-2 induzca una forma de cooperatividad negativa entre sensores de voltaje, que dificulte considerablemente la activación del cuarto sensor ó 2) que en realidad la última transición en el modelo no corresponda directamente con la activación del último sensor de voltaje, sino que constituya una representación simplificada de una transición tardía en cada uno de los cuatro sensores de voltaje que resulta desfavorecida por la presencia del CORM-2. Esto también aplica para la suposición de que el canal puede abrirse cuando únicamente dos sensores han alcanzado el estado abierto: Esta aseveración es relativa, ya que las transiciones en el modelo no necesariamente representan cada una de las transiciones de los sensores de voltaje. Dado que el mecanismo de activación de los sensores de voltaje es

más complejo que una sola transición, se puede argumentar que las primeras dos transiciones en el modelo agrupan dos transiciones iniciales en los cuatro sensores de voltaje, las cuales casi no se modifican por la presencia del CORM-2, salvo con respecto a una pequeña aceleración en la velocidad de activación. Esta aceleración se puede explicar aduciendo al efecto desacoplante del CORM-2, que libra a los sensores de voltaje del "peso" del dominio del poro, contra el cual necesitan realizar trabajo para poder abrirlo. Esto les permitiría moverse con mayor facilidad. Consistentemente, se ha demostrado que mutaciones desacoplantes favorecen el estado activado de los sensores de voltaje (Haddad and Blunck, 2011).

El modelo en el Esquema I es capaz de reproducir satisfactoriamente los efectos del CORM-2 sobre ambos canales, tal y como se muestra en las predicciones incluidas en las Figuras 16A y C, 18C y D, 19B, 21B y C, 22B y C, 23B y 34.

Algunas de las deficiencias del modelo son la omisión de la estequiometría de unión del CORM-2 a los canales. Modelos que consideren la unión y disociación del compuesto resultarían más informativos, en caso de que se contara con más datos experimentales para restringir los parámetros. Otra deficiencia del modelo es la sobreestimación de la velocidad de desactivación de los sensores de voltaje en *Shaker* (Fig. 23B). Esto muy probablemente se debe a un mecanismo aun desconocido que provoca un enlentecimiento excesivo la velocidad de desactivación de los sensores de voltaje en parches escindidos (Sigg et al., 1994). El modelo tampoco considera el efecto lento acumulativo del CORM-2 en función del tiempo, que de hecho se ignoró por completo en todos los experimentos e interpretaciones, puesto que este efecto probablemente resulta de la acumulación del compuesto en la membrana durante el curso de los experimentos. La utilización moléculas solubles en agua similares al CORM-2 (Romao et al., 2012) podría permitir la obtención de datos sin el lastre de la contaminación debida a la acumulación del compuesto en la membrana. Esta acumulación podría haber sido considerable en los experimentos donde se realizaron mediciones de corrientes de compuerta, puesto que dichos experimentos son relativamente lentos.

Finalmente, es importante mencionar aquí que los parámetros para el modelo aquí reportados de ninguna manera representan los únicos valores que permiten reproducir la actividad de los canales bajo cada una de las condiciones exploradas, incluídos los datos en presencia de CORM-2. La calidad de los ajustes se evaluó de manera cualitativa mediante inspección visual, y no se utilizaron medidas estadísticas para cuantificar la precisión de los ajustes. El motivo detrás de esto es que el objetivo de este análisis era evaluar el comportamiento del modelo en términos de mecanismos generales (v.g. desestabilización del estado abierto) que se reflejaran en tendencias en los valores de los parámetros (v.g. disminución o aumento de los mismos), mas no en sus valores numéricos precisos. Un análisis cuantitativo de los valores de los parámetros del modelo requeriría una mayor cantidad de restricciones experimentales sobre los mismos, lo cual se ecuentra más allá de los objetivos de este trabajo.

Por otro lado, el modelo aquí presentado se propone como una herramienta para racionalizar los efectos del CORM-2 observados en los experimentos de una forma más cuantitativa, y no como un argumento a favor del mecanismo propuesto. Como se mencionó anteriormente, existen otras posibilidades para representar los datos mediante un modelo cinético. Se requerirá de más experimentos para comprender a todo detalle el mecanismo mediante el cual el CORM-2 inhibe a los canales dependientes de voltaje. Lo que resulta indudable de los datos aquí presentados es el hecho de que una buena parte de la inhibición resulta de la interferencia del compuesto con el mecanismo de acoplamiento electromecánico. A continuación se discuten los datos en relación al posible sitio de unión del compuesto, y se presenta una hipótesis mecanística para la acción del CORM-2 sobre el canal Kv2.1.

9.4. El posible sitio de unión a CORM-2: una interpretación mecanística para los resultados experimentales.

Resulta muy interesante que el experimento computacional de *docking* haya identificado un posible sitio de unión localizado precisamente en la interfase entre los dominios sensores de voltaje y el poro del canal, siendo esto

consistente con los resultados experimentales obtenidos con respecto a la acción del compuesto sobre las transiciones concertadas. En esta interfase están contenidas todas las interacciones responsables del acoplamiento electromecánico: los puntos de contacto entre el segmento S4 de una subunidad y el S5 de la subunidad vecina (Fig. 6A) (Soler-Llavina et al., 2006; Upadhyay et al., 2009), el cúmulo interno de residuos en el S5 que afectan específicamente las transiciones concertadas (Soler-Llavina et al., 2006; Upadhyay et al., 2009), el asa S4-S5 (Labro et al., 2008; Lu et al., 2001, 2002; Tristani-Firouzi et al., 2002) y el segmento S6, incluyendo la región que contiene la bisagra (PVP) que abre y cierra la compuerta de activación y que es determinante para controlar la energía de apertura y cierre del canal (Hackos et al., 2002).

Es intrigante que la mayoría de las mutaciones introducidas a dicho sitio en este trabajo resultaron en canales no funcionales, dado que se ha encontrado que en *Shaker* esta región es considerablemente tolerante a sustituciones agresivas (Soler-Llavina et al., 2006). Nuestros datos sugieren que en Kv2.1 al menos, esta región es sensible a perturbaciones en el empaquetamiento, dado que parece haber una correlación entre la magnitud del cambio en el tamaño de cada residuo sustituido y la funcionalidad del canal resultante: mientras que las mutaciones A396W, G312M, G317V, G337M resultaron en canales no funcionales o con alteraciones significativas en su función, las mutaciones A396V y L264M, donde los cambios en el tamaño de la cadena lateral no son tan grandes, resultaron en canales que se comportan como el canal silvestre.

Esta sensibilidad a perturbaciones grandes es consistente con la idea de que el CORM-2 se asocia con el canal en esta región para modificar su función. Consistentemente, se ha demostrado que los alcanoles, como el 1-butanol, y anestésicos generales como el halotano y el isoflurano se asocian con esta región en el canal Shaw2, al interaccionar con el segmento S4-S5 y el motivo PVP en el S6 (Barber et al., 2011; Bhattacharji et al., 2006; Bhattacharji et al., 2010). Esta interacción resulta en la inhibición del canal, aparentemente mediante una estabilización del estado cerrado. Es muy interesante que una sola mutación puntual en el motivo PVP (PVA) del canal Shaw2, que provoca

una estabilización del estado cerrado con respecto al abierto, es capaz de revertir el efecto del 1-butanol, pasando de un inhibidor a un potenciador de la apertura del canal (Harris et al., 2003). Este hallazgo es muy similar a lo observado en este trabajo para el CORM-2 y la mutante G317V. Es también interesante que los alcanoles, el halotano, el isoflurano, el CORM-2 y sus derivados estudiados en este trabajo, son moléculas anfipáticas con regiones polares y no polares, sugiriendo que ésta es una propiedad general de moléculas distintas con efectos similares en canales dependientes de voltaje. A pesar de compartir un mecanismo general de acción, diferencias específicas en la estructura de cada uno de estos compuestos podrían ser responsables de las diferencias observadas en la sensibilidad de cada canal a estas moléculas: se ha encontrado que tanto el canal Kv2.1 como el canal Kv1.4 tienen una sensibilidad marginal al 1-butanol con respecto al Shaw2, mientras que son sensibles al CORM-2.

El grado de helicidad del asa S4-S5 parece ser un determinante importante en Shaw2 para la inhibición por 1-butanol (Bhattacharji et al., 2006). Una disminución en la propensidad del asa para adoptar una estructura de hélice alfa, causada por la sustitución de una isoleucina por una glicina, tiene como consecuencia una pérdida en la afinidad del canal por el 1-butanol. Los canales insensibles al 1-butanol, como Kv1.4, Kv2.1 y Kv3.4, tienen una glicina en lugar de la isoleucina en el sitio equivalente. Es posible que la sustitución de la glicina G317 reportada en este trabajo afecte la función del canal al modificar la estabilidad de la estructura secundaria en esta región, aunque se requieren experimentos sistemáticos para determinar si esto es cierto.

De acuerdo con la idea de que la interfase entre dominios constituye un sitio de unión a moléculas anfipáticas pequeñas, recientemente se reportó que compuestos alifáticos unidos a un grupo guanidinio se unen también en esta región en *Shaker*, en la porción del S6 que está orientada hacia afuera del poro, cerca del motivo PVP (Kalia and Swartz, 2011), y causan una reducción en la probabilidad de apertura del canal. Es interesante que la afinidad del canal por los derivados del guanidinio aumenta con la cantidad de metilenos presentes en las cadenas alifáticas asociadas al grupo guanidinio, puesto que

esto está relacionado con la hidrofobicidad de las moléculas. Estos compuestos favorecen el cierre del canal sin afectar el movimiento de los sensores de voltaje (Kalia and Swartz, 2011), y aceleran el movimiento de carga durante la desactivación. Cabe mencionar que el segundo sitio con mayor puntaje en el experimento de *docking* realizado en este trabajo está localizado precisamente en esta región.

Los cambios dramáticos en la acción del CORM-2 sobre el canal debidos a la sustitución G317V sugieren que efectivamente el compuesto interacciona con esta región del canal, aunque cabe mencionar que la identificación conclusiva de sitios de unión para moléculas pequeñas que se unen a una proteína con baja afinidad y especificidad es formidablemente complicado. Si bien los datos no implican que el sitio de interacción del compuesto con el canal es necesariamente el asa S4-S5, sí sugieren que la región interactuante en el canal podría estar contenida en la interfase entre dominios, la cual pudo haber resultado perturbada por la mutación.

Como se mencionó anteriormente, la sustitución de la glicina pudo haber modificado la estabilidad de la hélice S4-S5, lo que podría quizás no sólo afectar la interacción del CORM-2 con el canal, sino también alterar la interacción de la misma hélice S4-S5 con el S6, resultando en una profunda desestabilización del estado abierto. La mutación también pudo haber alterado la orientación del asa S4-S5 con respecto al S6, perturbando tanto la interacción del CORM-2 con su sitio de unión en la interfase, como la interacción del asa con el S6. En este respecto se ha demostrado que la orientación mutua entre los vectores de hidrofobicidad del asa S4-S5 y el S6 es un determinante esencial para el correcto acoplamiento electromecánico (Labro et al., 2008). El CORM-2 podría causar un desacoplamiento al modificar la orientación del asa S4-S5 con respecto al S6.

Efectos indirectos de la mutación sobre la interacción del asa S4-S5 resultan más probables que una disrupción directa de interacciones entre el S6 y el asa S4-S5 en la posición 317, puesto que la evidencia funcional y estructural (Labro et al., 2008; Long et al., 2005a, b; Long et al., 2007) sugiere que esa posición

no forma parte de la interfase de interacción entre ambas hélices, sino que está orientada hacia la membrana y participa en interacciones con las cabezas polares de los lípidos (Long et al., 2007). En este sentido es interesante la cualidad hidrofóbica del CORM-2, y su aparente capacidad para acumularse en la membrana e inhibir al canal irreversiblemente después de exposiciones largas (varios minutos). Se puede hipotetizar que el CORM-2 podría interactuar con el asa S4-S5 desde la membrana, promoviendo una conformación de la hélice desfavorable para interactuar con el segmento S6, además de causar un impedimento estérico para los movimientos de esta región de la proteína durante la actividad dependiente del voltaje del canal.

Para racionalizar los efectos del CORM-2 en términos del principal determinante molecular del acoplamiento, el asa S4-S5, se propone el siguiente mecanismo, el cual es consistente con los datos experimentales disponibles: en términos del asa S4-S5, el acoplamiento electromecánico está dado por interacciones específicas entre el asa S4-S5 y el S6 en el estado abierto y cerrado, que estabilizan cada uno de los estados (Fig. 36A). El movimiento del sensor de voltaje rompe dichas interacciones en un estado (e.g. cerrado) y posiciona al asa en un sitio óptimo para establecer contactos con el S6 en el estado opuesto (e.g. abierto).

Este modelo conceptual predice que el acoplamiento para abrir o cerrar al canal podría perturbarse selectivamente, al interferir con las interacciones entre ambas hélices en un estado o en el otro. La ruptura de estas interacciones en el estado abierto resultaría en canales incapaces de abrirse con voltaje, o con una cinética de apertura independiente del voltaje. La ruptura de interacciones en el estado cerrado resultaría en canales incapaces de cerrarse con voltaje, independientemente del estado de los sensores.

Más aún, los resultados experimentales aquí obtenidos sugieren que el CORM-2 interfiere con las interacciones en ambos estados, pero desestabiliza más fuertemente las interacciones en el estado abierto (Fig. 36B). El compuesto también parece tener un efecto sobre la barrera de energía para pasar del estado abierto al cerrado, y viceversa, lo que podría resultar de efectos

estéricos del compuesto posicionado en la interfase, la cual es sensible a perturbaciones en el empaquetamiento.

La mutante G317V parece desestabilizar fuertemente al estado abierto (Fig. 36C), que es diferente a provocar una estabilización del estado cerrado, puesto que esto último resultaría en una cinética de activación lenta para el canal G317V, la cual no se observa. La fuerte desestabilización del estado abierto en esta mutante podría interferir con la interacción del CORM-2 con el canal cuando se encuentra en dicha conformación, lo que podría explicar el cambio en la dependencia en el estado del efecto del CORM-2 en el canal G317V (Fig. 33). La interacción preferente del compuesto con el estado cerrado, y su efecto disruptivo con respecto a la estabilidad de dicha conformación, llevaría a la potenciación del canal.

Finalmente, queda por considerar el efecto inhibitorio aparentemente irreversible del CORM-2 observado en la mutante G317V. Una posible explicación es que los efectos desacoplantes y desestabilizadores de la mutación G317V y el CORM-2 permitan que el canal caiga en un estado no funcional similar a un estado inactivado. Consistentemente, se ha propuesto que la inactivación lenta desde estados cerrados en el canal Kv4.2 es causada por un desacoplamiento en el que se pierden las interacciones entre el asa S4-S5 y el segmento S6 que normalmente permitirían la apertura del canal (Barghaan and Bahring, 2009). El canal Kv2.1 también presenta inactivación pronunciada desde estados cerrados (Klemic et al., 1998), por lo que el desacoplamiento inducido por la mutante y el compuesto bien podrían conducir a la inactivación del canal, de la cual es más difícil recuperarse.

Las características de la inhibición del canal Kv2.1 por CORM-2 indican que esta molécula podría resultar una herramienta útil para el estudio del mecanismo electromecánico, el balance de fuerzas entre el DSV y el poro que lleva a la apertura y cierre del canal, y el rol que juegan distintas regiones del canal en relación al mecanismo de acoplamiento electromecánico.

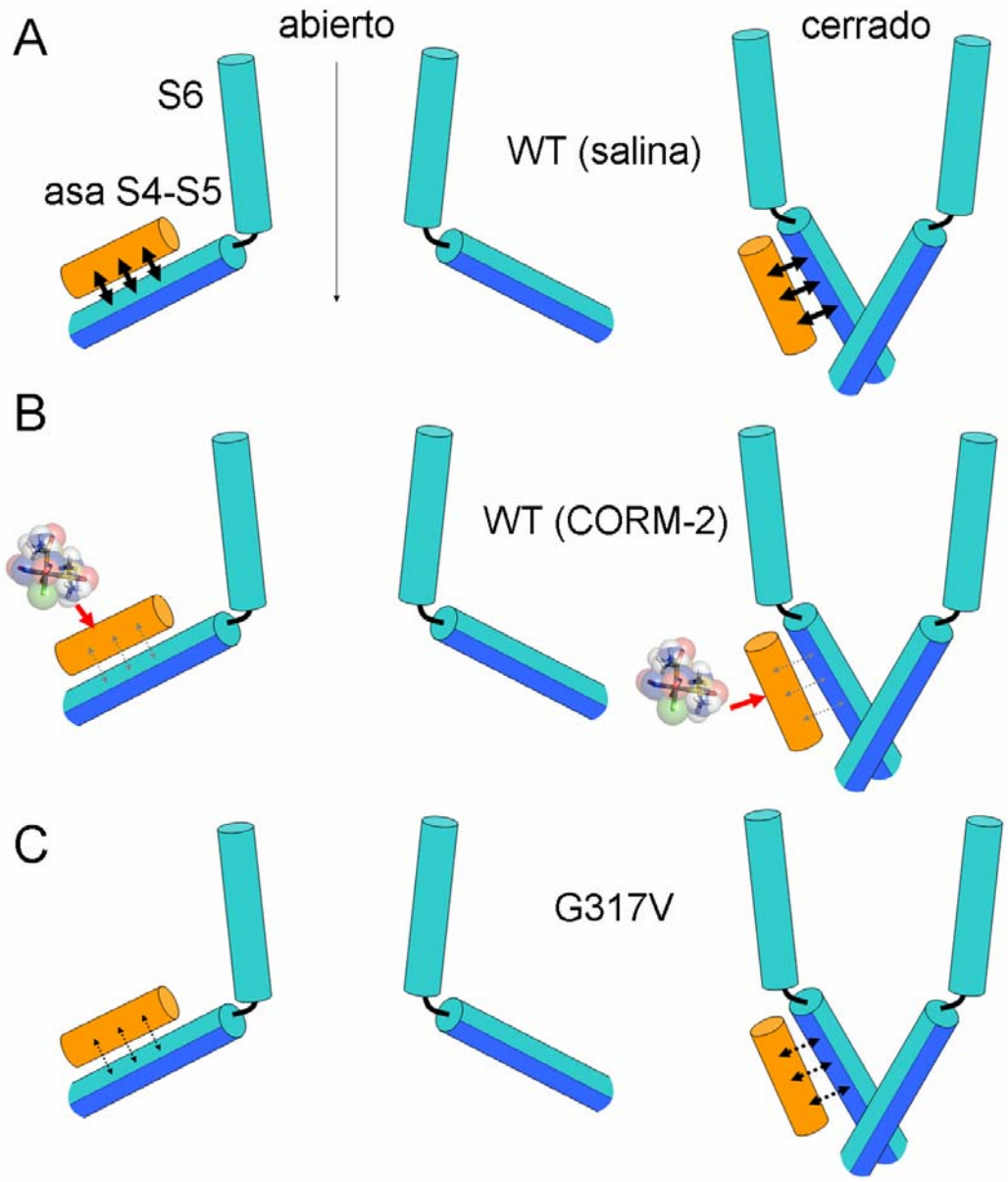

Figura 36. Acoplamiento electromecánico dependiente de la interacción del asa S4-S5 y el extremo C-terminal del S6. (A) El asa S4-S5 (cilindro naranja) interacciona con el extremo C-terminal del S6 (cilindro azul) tanto en el estado abierto como en el cerrado (flechas negras indican interacción). Estas interacciones permiten la estabilización de cada uno de los estados en función de la posición del sensor de voltaje. Las regiones del S6 que interaccionan con el asa S4-S5 en el estado abierto o cerrado son distintas (tonos de azul en la porción inferior del S6). La superficie del asa S4-S5 que interacciona con el S6 es siempre la misma. El motivo PVP se ilustra como una bisagra color negro en la figura. Por simplicidad se muestran unicamente los segmentos S6 de dos subunidades y el asa S4-S5 de una sola subunidad. (B) En presencia de CORM-2 o uno de sus análogos, las interacciones entre el asa S4-S5 se debilitan en ambos estados del canal. Esto podría deberse a una interacción del compuesto con la otra cara del asa. (C) En el canal G317V, las interacciones entre el asa S4-S5 y el S6 también están debilitadas, principalmente en el estado abierto.

10. CONCLUSIONES

- El CORM-2 inhibe a los canales Shaker y Kv2.1 de manera independiente de su capacidad para liberar monóxido de carbono.
- La inhibición no depende de un bloqueo directo de la vía de conducción iónica, sino que está dada por una modulación alostérica de la actividad de compuerta del canal.
- El CORM-2 interfiere con transiciones tardías en la vía de activación, principalmente al desfavorecer las transiciones concertadas que llevan al estado abierto.
- El compuesto actúa como un desacoplante entre los DSV y el poro del canal, lo que provoca una reducción en la dependencia en el voltaje en la cinética de apertura y cierre del poro.
- Las transiciones afectadas por el compuesto incluyen también algunas transiciones independientes de los sensores de voltaje, ya que el compuesto causa una reducción de aproximadamente el 40% en la carga de compuerta asociada con la activación de los sensores.
- Los efectos del CORM-2 parecen depender de una interacción del compuesto con la interfase entre los dominios sensores de voltaje y el poro, y el mecanismo de inhibición podría resultar de interacciones del compuesto con el asa S4-S5.

11. BIBLIOGRAFÍA

(1995). Single-Channel Recording, Second Edition edn (Heidelberg: Springer Verlag).

Aggarwal, S.K., and MacKinnon, R. (1996). Contribution of the S4 segment to gating charge in the Shaker K+ channel. Neuron *16*, 1169-1177.

Alabi, A.A., Bahamonde, M.I., Jung, H.J., Kim, J.I., and Swartz, K.J. (2007). Portability of paddle motif function and pharmacology in voltage sensors. Nature *450*, 370-375.

Alberto, R., and Motterlini, R. (2007). Chemistry and biological activities of CO-releasing molecules (CORMs) and transition metal complexes. Dalton Trans, 1651-1660.

Alessio, E., Mestroni, G., Nardin, G., Attia, W.M., Calligaris, M., Sava, G., and Zorzet, S. (1988). cis- and trans-Dihalotetrakis(dimethyl sulfoxide)ruthenium(II) Complexes (RuX2(DMSO)4; X = Cl, Br): Synthesis, Structure, and Antitumor Activity. Inorg. Chem. *27*, 4099-4106.

Alessio, E., Milani, B., Bolle, M., Mestroni, G., Faleschini, P., Todone, F., Geremia, S., and Calligaris, M. (1995). Carbonyl Derivatives of Chloride-Dimethyl Sulfoxide-Ruthenium(II) Complexes: Synthesis, Structural Characterization, and Reactivity of Ru(CO)x,(DMS0)(4-x),Cl2 Complexes (x = 1-3). Inorg. Chem. *34*, 4722-4734.

Ando, H., Kuno, M., Shimizu, H., Muramatsu, I., and Oiki, S. (2005). Coupled K+-water flux through the HERG potassium channel measured by an osmotic pulse method. The Journal of General Physiology *126*, 529-538.

Aqvist, J., and Luzhkov, V. (2000). Ion permeation mechanism of the potassium channel. Nature *404*, 881-884.

Archer, S.L., Souil, E., Dinh-Xuan, A.T., Schremmer, B., Mercier, J.C., El Yaagoubi, A., Nguyen-Huu, L., Reeve, H.L., and Hampl, V. (1998). Molecular identification of the role of voltage-gated K+ channels, Kv1.5 and Kv2.1, in hypoxic pulmonary vasoconstriction and control of resting membrane potential in rat pulmonary artery myocytes. J Clin Invest *101*, 2319-2330.

Archer, S.L., Weir, E.K., Reeve, H.L., and Michelakis, E. (2000). Molecular identification of O2 sensors and O2-sensitive potassium channels in the pulmonary circulation. Adv Exp Med Biol *475*, 219-240.

Archer, S.L., Wu, X.C., Thebaud, B., Nsair, A., Bonnet, S., Tyrrell, B., McMurtry, M.S., Hashimoto, K., Harry, G., and Michelakis, E.D. (2004). Preferential expression and function of voltage-gated, O2-sensitive K+ channels in resistance pulmonary

arteries explains regional heterogeneity in hypoxic pulmonary vasoconstriction: ionic diversity in smooth muscle cells. Circulation research *95*, 308-318.

Armstrong, C.M. (1971). Interaction of tetraethylammonium ion derivatives with the potassium channels of giant axons. The Journal of General Physiology *58*, 413-437.

Armstrong, C.M., and Bezanilla, F. (1973). Currents related to movement of the gating particles of the sodium channels. Nature *242*, 459-461.

Armstrong, C.M., and Bezanilla, F. (1974). Charge movement associated with the opening and closing of the activation gates of the Na channels. The Journal of General Physiology *63*, 533-552.

Armstrong, C.M., and Hille, B. (1972). The inner quaternary ammonium ion receptor in potassium channels of the node of Ranvier. The Journal of General Physiology *59*, 388-400.

Armstrong, C.M., and Hille, B. (1998). Voltage-gated ion channels and electrical excitability. Neuron *20*, 371-380.

Armstrong, C.M., and Loboda, A. (2001). A model for 4-aminopyridine action on K channels: similarities to tetraethylammonium ion action. Biophysical Journal *81*, 895-904.

Azaria, R., Irit, O., Ben-Abu, Y., and Yifrach, O. (2010). Probing the transition state of the allosteric pathway of the Shaker Kv channel pore by linear free-energy relations. Journal of Molecular Biology *403*, 167-173.

Bahring, R., Milligan, C.J., Vardanyan, V., Engeland, B., Young, B.A., Dannenberg, J., Waldschutz, R., Edwards, J.P., Wray, D., and Pongs, O. (2001). Coupling of voltage-dependent potassium channel inactivation and oxidoreductase active site of Kvbeta subunits. The Journal of Biological Chemistry *276*, 22923-22929.

Banerjee, A., and MacKinnon, R. (2008). Inferred motions of the S3a helix during voltage-dependent K+ channel gating. Journal of Molecular Biology *381*, 569-580.

Barber, A.F., Liang, Q., Amaral, C., Treptow, W., and Covarrubias, M. (2011). Molecular mapping of general anesthetic sites in a voltage-gated ion channel. Biophysical Journal *101*, 1613-1622.

Barghaan, J., and Bahring, R. (2009). Dynamic coupling of voltage sensor and gate involved in closed-state inactivation of kv4.2 channels. The Journal of General Physiology *133*, 205-224.

Batulan, Z., Haddad, G.A., and Blunck, R. (2010). An intersubunit interaction between S4-S5 linker and S6 is responsible for the slow off-gating component in Shaker K+ channels. The Journal of Biological Chemistry *285*, 14005-14019.

Baukrowitz, T., and Yellen, G. (1995). Modulation of K+ current by frequency and external [K+]: a tale of two inactivation mechanisms. Neuron *15*, 951-960.

Baumann, A., Grupe, A., Ackermann, A., and Pongs, O. (1988). Structure of the voltage-dependent potassium channel is highly conserved from Drosophila to vertebrate central nervous systems. The EMBO journal *7*, 2457-2463.

Bean, B.P. (2007). The action potential in mammalian central neurons. Nat Rev Neurosci *8*, 451-465.

Berneche, S., and Roux, B. (2001). Energetics of ion conduction through the K+ channel. Nature *414*, 73-77.

Bezanilla, F. (2008). Ion channels: from conductance to structure. Neuron *60*, 456-468.

Bezanilla, F., Perozo, E., and Stefani, E. (1994). Gating of Shaker K+ channels: II. The components of gating currents and a model of channel activation. Biophysical Journal *66*, 1011-1021.

Bhattacharji, A., Kaplan, B., Harris, T., Qu, X., Germann, M.W., and Covarrubias, M. (2006). The concerted contribution of the S4-S5 linker and the S6 segment to the modulation of a Kv channel by 1-alkanols. Molecular pharmacology *70*, 1542-1554.

Bhattacharji, A., Klett, N., Go, R.C., and Covarrubias, M. (2010). Inhalational anaesthetics and n-alcohols share a site of action in the neuronal Shaw2 Kv channel. British journal of pharmacology *159*, 1475-1485.

Brazier, S.P., Telezhkin, V., Mears, R., Muller, C.T., Riccardi, D., and Kemp, P.J. (2009). Cysteine residues in the C-terminal tail of the human BK(Ca)alpha subunit are important for channel sensitivity to carbon monoxide. Adv Exp Med Biol *648*, 49-56.

Brindell, M., Elmroth, S.K.C., and Stochel, G. (2004). Mechanistic information on the reaction of cis- and trans-[RuCl2(DMSO)4] with d(T2GGT2) derived from MALDI-TOF and HPLC studies. Journal of Inorganic Biochemistry *98*, 1367-1377.

Brindell, M., Stochel, G., Bertolasi, V., Boaretto, R., and Sostero, S. (2007). Photochemistry of trans- and cis-[RuCl2(dmso)4] in Aqueous and Nonaqueous Solutions. Eur. J. Inorg. Chem. *16*, 2353-2359.

Broomand, A., and Elinder, F. (2008). Large-scale movement within the voltage-sensor paddle of a potassium channel-support for a helical-screw motion. Neuron *59*, 770-777.

Brouard, S., Otterbein, L.E., Anrather, J., Tobiasch, E., Bach, F.H., Choi, A.M., and Soares, M.P. (2000). Carbon monoxide generated by heme oxygenase 1 suppresses endothelial cell apoptosis. The Journal of Experimental Medicine *192*, 1015-1026.

Campomanes, C.R., Carroll, K.I., Manganas, L.N., Hershberger, M.E., Gong, B., Antonucci, D.E., Rhodes, K.J., and Trimmer, J.S. (2002). Kv beta subunit oxidoreductase activity and Kv1 potassium channel trafficking. The Journal of Biological Chemistry *277*, 8298-8305.

Campos, F.V., Chanda, B., Roux, B., and Bezanilla, F. (2007). Two atomic constraints unambiguously position the S4 segment relative to S1 and S2 segments in the closed state of Shaker K channel. Proceedings of the National Academy of Sciences of the United States of America *104*, 7904-7909.

Carter, B.C. and Bean, B.P. (2009). Sodium entry during action potentials of mammalian central neurons: incomplete inactivation and reduced metabolic efficiency in fast-spiking neurons. Neuron *64*, 898-909.

Catterall, W.A. (2010). Ion channel voltage sensors: structure, function, and pathophysiology. Neuron *67*, 915-928.

Chanda, B., Asamoah, O.K., Blunck, R., Roux, B. and Bezanilla, F. (2005). Gating charge displacement in voltage-gated ion channels involves limited transmembrane movement. Nature *436*, 852-856.

Clark, J.E., Naughton, P., Shurey, S., Green, C.J., Johnson, T.R., Mann, B.E., Foresti, R., and Motterlini, R. (2003). Cardioprotective actions by a water-soluble carbon monoxide-releasing molecule. Circulation research *93*, e2-8.

Cole, K.S., and Curtis, H.J. (1939). Electric Impedance of the Squid Giant Axon During Activity. The Journal of General Physiology *22*, 649-670.

Cole, K.S., and Moore, J.W. (1960). Potassium ion current in the squid giant axon: dynamic characteristic. Biophysical Journal *1*, 1-14.

Colquhoun, D., and Sigworth, F.J. (1995). Fitting and Statistical Analysis of Single-Channel Records. In Single-Channel Recording, E. Neher, and B. Sakmann, eds. (Heidelberg: Springer Verlag).

Consiglio, J.F., and Korn, S.J. (2004). Influence of permeant ions on voltage sensor function in the Kv2.1 potassium channel. The Journal of General Physiology *123*, 387-400.

Contreras, J.E., Chen, J., Lau, A.Y., Jogini, V., Roux, B., and Holmgren, M. (2010). Voltage profile along the permeation pathway of an open channel. Biophysical Journal *99*, 2863-2869.

Csongradi, E., Juncos, L.A., Drummond, H.A., Vera, T., and Stec, D.E. (2012). Role of Carbon Monoxide in Kidney Function: Is a little Carbon Monoxide Good for the Kidney? Current pharmaceutical biotechnology.

Cuello, L.G., Jogini, V., Cortes, D.M., and Perozo, E. (2010). Structural mechanism of C-type inactivation in K(+) channels. Nature *466*, 203-208.

Chakrapani, S., Sompornpisut, P., Intharathep, P., Roux, B., and Perozo, E. (2010). The activated state of a sodium channel voltage sensor in a membrane environment. Proceedings of the National Academy of Sciences of the United States of America *107*, 5435-5440.

Chandy, K.G., and Gutman, G.A. (1993). Nomenclature for mammalian potassium channel genes. Trends in pharmacological sciences *14*, 434.

Chen, J., Mitcheson, J.S., Lin, M., and Sanguinetti, M.C. (2000). Functional roles of charged residues in the putative voltage sensor of the HCN2 pacemaker channel. The Journal of Biological Chemistry *275*, 36465-36471.

Choveau, F.S., Rodriguez, N., Abderemane Ali, F., Labro, A.J., Rose, T., Dahimene, S., Boudin, H., Le Henaff, C., Escande, D., Snyders, D.J.*, et al.* (2011). KCNQ1 channels voltage dependence through a voltage-dependent binding of the S4-S5 linker to the pore domain. The Journal of Biological Chemistry *286*, 707-716.

Dahl, S.G., Sylte, I., and Ravna, A.W. (2004). Structures and models of transporter proteins. The Journal of pharmacology and experimental therapeutics *309*, 853-860.

Dallas, M.L., Boyle, J.P., Milligan, C.J., Sayer, R., Kerrigan, T.L., McKinstry, C., Lu, P., Mankouri, J., Harris, M., Scragg, J.L.*, et al.* (2011). Carbon monoxide protects against oxidant-induced apoptosis via inhibition of Kv2.1. Faseb J *25*, 1519-1530.

Decher, N., Chen, J., and Sanguinetti, M.C. (2004). Voltage-dependent gating of hyperpolarization-activated, cyclic nucleotide-gated pacemaker channels: molecular coupling between the S4-S5 and C-linkers. The Journal of Biological Chemistry *279*, 13859-13865.

del Camino, D., Holmgren, M., Liu, Y., and Yellen, G. (2000). Blocker protection in the pore of a voltage-gated K+ channel and its structural implications. Nature *403*, 321-325.

del Camino, D., Kanevsky, M., and Yellen, G. (2005). Status of the intracellular gate in the activated-not-open state of shaker K+ channels. The Journal of General Physiology *126*, 419-428.

del Camino, D., and Yellen, G. (2001). Tight steric closure at the intracellular activation gate of a voltage-gated K(+) channel. Neuron *32*, 649-656.

Derst, C., and Karschin, A. (1998). Review: Evolutionary link between prokaryotic and eukaryotic K+ channels. The Journal of experimental biology *201*, 2791-2799.

Desmard, M., Davidge, K.S., Bouvet, O., Morin, D., Roux, D., Foresti, R., Ricard, J.D., Denamur, E., Poole, R.K., Montravers, P.*, et al.* (2009). A carbon monoxide-releasing molecule (CORM-3) exerts bactericidal activity against Pseudomonas aeruginosa and improves survival in an animal model of bacteraemia. Faseb J *23*, 1023-1031.

Ding, S., and Horn, R. (2003). Effect of S6 tail mutations on charge movement in Shaker potassium channels. Biophysical Journal *84*, 295-305.

Dong, D.L., Chen, C., Huang, W., Chen, Y., Zhang, X.L., Li, Z., Li, Y., and Yang, B.F. (2008). Tricarbonyldichlororuthenium (II) dimer (CORM2) activates non-selective cation current in human endothelial cells independently of carbon monoxide releasing. Eur J Pharmacol *590*, 99-104.

Doyle, D.A., Morais Cabral, J., Pfuetzner, R.A., Kuo, A., Gulbis, J.M., Cohen, S.L., Chait, B.T., and MacKinnon, R. (1998). The structure of the potassium channel: molecular basis of K+ conduction and selectivity. Science (New York, N.Y *280*, 69-77.

Duhovny, D., Nussinov, R., and Wolfson, H.J. (2002). Efficient Unbound Docking of Rigid Molecules. In Ed. Proceedings of the 2'nd Workshop on Algorithms in Bioinformatics(WABI) Rome, Italy, Lecture Notes in Computer Science, R. Guigó, and D. Gusfield, eds. (Heidelberg: Springer-Verlag), pp. 185-200.

Evans, I.P., Spencer, A., and Wilkinson, G. (1973). Dichlorotetrakis(dimethylsulfoxide)ruthenium(II) and its use as a source material for some new ruthenium(II) complexes. J. Chem. Soc. Dalton Trans., 204-209.

Ferrandiz, M.L., Maicas, N., Garcia-Arnandis, I., Terencio, M.C., Motterlini, R., Devesa, I., Joosten, L.A., van den Berg, W.B., and Alcaraz, M.J. (2008). Treatment with a CO-releasing molecule (CORM-3) reduces joint inflammation and erosion in murine collagen-induced arthritis. Annals of the rheumatic diseases *67*, 1211-1217.

Ferrer, T., Rupp, J., Piper, D.R., and Tristani-Firouzi, M. (2006). The S4-S5 linker directly couples voltage sensor movement to the activation gate in the human ether-a'-go-go-related gene (hERG) K+ channel. The Journal of Biological Chemistry *281*, 12858-12864.

Fujita, T., Toda, K., Karimova, A., Yan, S.F., Naka, Y., Yet, S.F., and Pinsky, D.J. (2001). Paradoxical rescue from ischemic lung injury by inhaled carbon monoxide driven by derepression of fibrinolysis. Nature medicine *7*, 598-604.

Gagnon, D.G., and Bezanilla, F. (2009). A single charged voltage sensor is capable of gating the Shaker K+ channel. The Journal of General Physiology *133*, 467-483.

Gagnon, D.G., and Bezanilla, F. (2010). The contribution of individual subunits to the coupling of the voltage sensor to pore opening in Shaker K channels: effect of ILT mutations in heterotetramers. The Journal of General Physiology *136*, 555-568.

Glynn, I.M. (2002). A hundred years of sodium pumping. Annual review of physiology *64*, 1-18.

Goldin, A.L. (1992). Maintenance of Xenopus laevis and oocyte injection. Methods in enzymology *207*, 266-279.

Gomez-Lagunas, F. (1997). Shaker B K+ conductance in Na+ solutions lacking K+ ions: a remarkably stable non-conducting state produced by membrane depolarizations. The Journal of Physiology *499 (Pt 1)*, 3-15.

Grabe, M., Lai, H.C., Jain, M., Jan, Y.N., and Jan, L.Y. (2007). Structure prediction for the down state of a potassium channel voltage sensor. Nature *445*, 550-553.

Gulbis, J.M., Zhou, M., Mann, S., and MacKinnon, R. (2000). Structure of the cytoplasmic beta subunit-T1 assembly of voltage-dependent K+ channels. Science (New York, N.Y *289*, 123-127.

Guo, Y., Stein, A.B., Wu, W.J., Tan, W., Zhu, X., Li, Q.H., Dawn, B., Motterlini, R., and Bolli, R. (2004). Administration of a CO-releasing molecule at the time of reperfusion reduces infarct size in vivo. American journal of physiology *286*, H1649-1653.

Gutman, G.A., Chandy, K.G., Grissmer, S., Lazdunski, M., McKinnon, D., Pardo, L.A., Robertson, G.A., Rudy, B., Sanguinetti, M.C., Stuhmer, W., and Wang, X. (2005). International Union of Pharmacology. LIII. Nomenclature and molecular relationships of voltage-gated potassium channels. Pharmacological reviews *57*, 473-508.

Hackos, D.H., Chang, T.H., and Swartz, K.J. (2002). Scanning the intracellular S6 activation gate in the shaker K+ channel. The Journal of General Physiology *119*, 521-532.

Haddad, G.A., and Blunck, R. (2011). Mode shift of the voltage sensors in Shaker K+ channels is caused by energetic coupling to the pore domain. The Journal of General Physiology *137*, 455-472.

Hamill, O.P., Marty, A., Neher, E., Sakmann, B., and Sigworth, F.J. (1981). Improved patch-clamp techniques for high-resolution current recording from cells and cell-free membrane patches. Pflugers Arch *391*, 85-100.

Harris, T., Graber, A.R., and Covarrubias, M. (2003). Allosteric modulation of a neuronal K+ channel by 1-alkanols is linked to a key residue in the activation gate. Am J Physiol Cell Physiol *285*, C788-796.

Heginbotham, L., Lu, Z., Abramson, T., and MacKinnon, R. (1994). Mutations in the K+ channel signature sequence. Biophysical Journal *66*, 1061-1067.

Heinemann, S.H. (1995). Guide to Data Acquisition and Analysis. In Single-Channel Recording, E. Neher, and B. Sakmann, eds. (Heidelberg: Springer Verlag), pp. 53-90.

Heinemann, S.H., and Conti, F. (1992). Nonstationary noise analysis and application to patch clamp recordings. Methods in enzymology *207*, 131-148.

Hille, B. (2001). Ion Channels of Excitable Membranes, Third Edition edn (Sinauer Associates Inc.).

Hodgkin, A.L. (1937a). Evidence for electrical transmission in nerve: Part I. The Journal of Physiology *90*, 183-210.

Hodgkin, A.L. (1937b). Evidence for electrical transmission in nerve: Part II. The Journal of Physiology *90*, 211-232.

Hodgkin, A.L., and Huxley, A.F. (1952a). The components of membrane conductance in the giant axon of Loligo. The Journal of Physiology *116*, 473-496.

Hodgkin, A.L., and Huxley, A.F. (1952b). Currents carried by sodium and potassium ions through the membrane of the giant axon of Loligo. The Journal of Physiology *116*, 449-472.

Hodgkin, A.L., and Huxley, A.F. (1952c). A quantitative description of membrane current and its application to conduction and excitation in nerve. The Journal of Physiology *117*, 500-544.

Hodgkin, A.L., and Katz, B. (1949). The effect of sodium ions on the electrical activity of giant axon of the squid. The Journal of Physiology *108*, 37-77.

Hogg, D.S., Davies, A.R., McMurray, G., and Kozlowski, R.Z. (2002). K(V)2.1 channels mediate hypoxic inhibition of I(KV) in native pulmonary arterial smooth muscle cells of the rat. Cardiovasc Res *55*, 349-360.

Holmgren, M., Jurman, M.E., and Yellen, G. (1996). N-type inactivation and the S4-S5 region of the Shaker K+ channel. The Journal of General Physiology *108*, 195-206.

Horrigan, F.T., and Aldrich, R.W. (2002). Coupling between voltage sensor activation, Ca2+ binding and channel opening in large conductance (BK) potassium channels. The Journal of General Physiology *120*, 267-305.

Hoshi, T., Zagotta, W.N., and Aldrich, R.W. (1990). Biophysical and molecular mechanisms of Shaker potassium channel inactivation. Science (New York, N.Y *250*, 533-538.

Hou, S., Xu, R., Heinemann, S.H., and Hoshi, T. (2008). The RCK1 high-affinity Ca2+ sensor confers carbon monoxide sensitivity to Slo1 BK channels. Proceedings of the National Academy of Sciences of the United States of America *105*, 4039-4043.

Hulme, J.T., Coppock, E.A., Felipe, A., Martens, J.R., and Tamkun, M.M. (1999). Oxygen sensitivity of cloned voltage-gated K(+) channels expressed in the pulmonary vasculature. Circulation research *85*, 489-497.

Islas, L.D., and Sigworth, F.J. (1999). Voltage sensitivity and gating charge in Shaker and Shab family potassium channels. The Journal of General Physiology *114*, 723-742.

Islas, L.D., and Sigworth, F.J. (2001). Electrostatics and the gating pore of Shaker potassium channels. The Journal of General Physiology *117*, 69-89.

Iwamoto, M., and Oiki, S. (2011). Counting ion and water molecules in a streaming file through the open-filter structure of the K channel. J Neurosci *31*, 12180-12188.

Jensen, M.O., Borhani, D.W., Lindorff-Larsen, K., Maragakis, P., Jogini, V., Eastwood, M.P., Dror, R.O., and Shaw, D.E. (2010). Principles of conduction and hydrophobic gating in K+ channels. Proceedings of the National Academy of Sciences of the United States of America *107*, 5833-5838.

Jensen, M.O., Jogini, V., Borhani, D.W., Leffler, A.E., Dror, R.O., and Shaw, D.E. (2012). Mechanism of Voltage Gating in Potassium Channels. Science (New York, N.Y *336*, 5.

Jiang, Y., Lee, A., Chen, J., Cadene, M., Chait, B.T., and MacKinnon, R. (2002). The open pore conformation of potassium channels. Nature *417*, 523-526.

Jiang, Y., Lee, A., Chen, J., Ruta, V., Cadene, M., Chait, B.T., and MacKinnon, R. (2003). X-ray structure of a voltage-dependent K+ channel. Nature *423*, 33-41.

Jogini, V., and Roux, B. (2005). Electrostatics of the intracellular vestibule of K+ channels. Journal of Molecular Biology *354*, 272-288.

Kaizu, T., Ikeda, A., Nakao, A., Tsung, A., Toyokawa, H., Ueki, S., Geller, D.A., and Murase, N. (2008). Protection of transplant-induced hepatic ischemia/reperfusion injury with carbon monoxide via MEK/ERK1/2 pathway downregulation. Am J Physiol Gastrointest Liver Physiol *294*, G236-244.

Kalia, J., and Swartz, K.J. (2011). Elucidating the molecular basis of action of a classic drug: guanidine compounds as inhibitors of voltage-gated potassium channels. Molecular pharmacology *80*, 1085-1095.

Kamb, A., Tseng-Crank, J., and Tanouye, M.A. (1988). Multiple products of the Drosophila Shaker gene may contribute to potassium channel diversity. Neuron *1*, 421-430.

Kanevsky, M., and Aldrich, R.W. (1999). Determinants of voltage-dependent gating and open-state stability in the S5 segment of Shaker potassium channels. The Journal of General Physiology *114*, 215-242.

Kemp, P.J., Telezhkin, V., Wilkinson, W.J., Mears, R., Hanmer, S.B., Gadeberg, H.C., Muller, C.T., Riccardi, D., and Brazier, S.P. (2009). Enzyme-linked oxygen sensing by potassium channels. Annals of the New York Academy of Sciences *1177*, 112-118.

Khalili-Araghi, F., Jogini, V., Yarov-Yarovoy, V., Tajkhorshid, E., Roux, B., and Schulten, K. (2010). Calculation of the gating charge for the Kv1.2 voltage-activated potassium channel. Biophysical Journal *98*, 2189-2198.

Khodakhah, K., Melishchuk, A., and Armstrong, C.M. (1997). Killing K channels with TEA+. Proceedings of the National Academy of Sciences of the United States of America *94*, 13335-13338.

Kim, K.M., Pae, H.O., Zheng, M., Park, R., Kim, Y.M., and Chung, H.T. (2007). Carbon monoxide induces heme oxygenase-1 via activation of protein kinase R-like endoplasmic reticulum kinase and inhibits endothelial cell apoptosis triggered by endoplasmic reticulum stress. Circulation research *101*, 919-927.

Klemic, K.G., Shieh, C.C., Kirsch, G.E., and Jones, S.W. (1998). Inactivation of Kv2.1 potassium channels. Biophysical Journal *74*, 1779-1789.

Kobertz, W.R., and Miller, C. (1999). K+ channels lacking the 'tetramerization' domain: implications for pore structure. Nature structural biology *6*, 1122-1125.

Kobertz, W.R., Williams, C., and Miller, C. (2000). Hanging gondola structure of the T1 domain in a voltage-gated K(+) channel. Biochemistry *39*, 10347-10352.

Kobrinsky, E., Stevens, L., Kazmi, Y., Wray, D., and Soldatov, N.M. (2006). Molecular rearrangements of the Kv2.1 potassium channel termini associated with voltage gating. The Journal of Biological Chemistry *281*, 19233-19240.

Krepkiy, D., Mihailescu, M., Freites, J.A., Schow, E.V., Worcester, D.L., Gawrisch, K., Tobias, D.J., White, S.H., and Swartz, K.J. (2009). Structure and hydration of membranes embedded with voltage-sensing domains. Nature *462*, 473-479.

Kreusch, A., Pfaffinger, P.J., Stevens, C.F., and Choe, S. (1998). Crystal structure of the tetramerization domain of the Shaker potassium channel. Nature *392*, 945-948.

Labro, A.J., Boulet, I.R., Choveau, F.S., Mayeur, E., Bruyns, T., Loussouarn, G., Raes, A.L., and Snyders, D.J. (2011). The S4-S5 linker of KCNQ1 channels forms a structural scaffold with the S6 segment controlling gate closure. The Journal of Biological Chemistry *286*, 717-725.

Labro, A.J., Raes, A.L., Bellens, I., Ottschytsch, N., and Snyders, D.J. (2003). Gating of shaker-type channels requires the flexibility of S6 caused by prolines. The Journal of Biological Chemistry *278*, 50724-50731.

Labro, A.J., Raes, A.L., Grottesi, A., Van Hoorick, D., Sansom, M.S., and Snyders, D.J. (2008). Kv channel gating requires a compatible S4-S5 linker and bottom part of S6, constrained by non-interacting residues. The Journal of General Physiology *132*, 667-680.

Labro, A.J., Raes, A.L., and Snyders, D.J. (2005). Coupling of voltage sensing to channel opening reflects intrasubunit interactions in kv channels. The Journal of General Physiology *125*, 71-80.

Lahiri, S., Roy, A., Baby, S.M., Hoshi, T., Semenza, G.L., and Prabhakar, N.R. (2006). Oxygen sensing in the body. Progress in biophysics and molecular biology *91*, 249-286.

Larsson, H.P., Baker, O.S., Dhillon, D.S., and Isacoff, E.Y. (1996). Transmembrane movement of the shaker K+ channel S4. Neuron *16*, 387-397.

Ledwell, J.L., and Aldrich, R.W. (1999). Mutations in the S4 region isolate the final voltage-dependent cooperative step in potassium channel activation. The Journal of General Physiology *113*, 389-414.

Lee, H.C., Wang, J.M., and Swartz, K.J. (2003). Interaction between extracellular Hanatoxin and the resting conformation of the voltage-sensor paddle in Kv channels. Neuron *40*, 527-536.

Lee, S.S., Gao, W., Mazzola, S., Thomas, M.N., Csizmadia, E., Otterbein, L.E., Bach, F.H., and Wang, H. (2007). Heme oxygenase-1, carbon monoxide, and bilirubin induce tolerance in recipients toward islet allografts by modulating T regulatory cells. Faseb J *21*, 3450-3457.

Lee, S.Y., Banerjee, A., and MacKinnon, R. (2009). Two separate interfaces between the voltage sensor and pore are required for the function of voltage-dependent K(+) channels. PLoS Biol *7*, e47.

Leffler, C.W., Parfenova, H., and Jaggar, J.H. (2011). Carbon monoxide as an endogenous vascular modulator. American journal of physiology *301*, H1-H11.

Li-Smerin, Y., and Swartz, K.J. (1998). Gating modifier toxins reveal a conserved structural motif in voltage-gated Ca2+ and K+ channels. Proceedings of the National Academy of Sciences of the United States of America *95*, 8585-8589.

Liu, Y., Holmgren, M., Jurman, M.E., and Yellen, G. (1997). Gated access to the pore of a voltage-dependent K+ channel. Neuron *19*, 175-184.

Loboda, A., and Armstrong, C.M. (2001). Resolving the gating charge movement associated with late transitions in K channel activation. Biophysical Journal *81*, 905-916.

Long, S.B., Campbell, E.B., and Mackinnon, R. (2005a). Crystal structure of a mammalian voltage-dependent Shaker family K+ channel. Science (New York, N.Y *309*, 897-903.

Long, S.B., Campbell, E.B., and Mackinnon, R. (2005b). Voltage sensor of Kv1.2: structural basis of electromechanical coupling. Science (New York, N.Y *309*, 903-908.

Long, S.B., Tao, X., Campbell, E.B., and MacKinnon, R. (2007). Atomic structure of a voltage-dependent K+ channel in a lipid membrane-like environment. Nature *450*, 376-382.

Lopatin, A.N., and Nichols, C.G. (1994). Internal Na+ and Mg2+ blockade of DRK1 (Kv2.1) potassium channels expressed in Xenopus oocytes. Inward rectification of a delayed rectifier. The Journal of General Physiology *103*, 203-216.

Lu, Z., Klem, A.M., and Ramu, Y. (2001). Ion conduction pore is conserved among potassium channels. Nature *413*, 809-813.

Lu, Z., Klem, A.M., and Ramu, Y. (2002). Coupling between voltage sensors and activation gate in voltage-gated K+ channels. The Journal of General Physiology *120*, 663-676.

MacKinnon, R. (1991). Determination of the subunit stoichiometry of a voltage-activated potassium channel. Nature *350*, 232-235.

MacKinnon, R., Cohen, S.L., Kuo, A., Lee, A., and Chait, B.T. (1998). Structural conservation in prokaryotic and eukaryotic potassium channels. Science (New York, N.Y *280*, 106-109.

Magidovich, E., and Yifrach, O. (2004). Conserved gating hinge in ligand- and voltage-dependent K+ channels. Biochemistry *43*, 13242-13247.

Maines, M.D., and Gibbs, P.E. (2005). 30 some years of heme oxygenase: from a "molecular wrecking ball" to a "mesmerizing" trigger of cellular events. Biochemical and biophysical research communications *338*, 568-577.

Mannikko, R., Elinder, F., and Larsson, H.P. (2002). Voltage-sensing mechanism is conserved among ion channels gated by opposite voltages. Nature *419*, 837-841.

Mannuzzu, L.M., and Isacoff, E.Y. (2000). Independence and cooperativity in rearrangements of a potassium channel voltage sensor revealed by single subunit fluorescence. The Journal of General Physiology *115*, 257-268.

McDaid, J., Yamashita, K., Chora, A., Ollinger, R., Strom, T.B., Li, X.C., Bach, F.H., and Soares, M.P. (2005). Heme oxygenase-1 modulates the allo-immune response by promoting activation-induced cell death of T cells. Faseb J *19*, 458-460.

Mederos, Y.S.M., Rinne, S., Skrobek, L., Renigunta, V., Schlichthorl, G., Derst, C., Gudermann, T., Daut, J., and Preisig-Muller, R. (2009). Mutation of histidine 105 in the T1 domain of the potassium channel Kv2.1 disrupts heteromerization with Kv6.3 and Kv6.4. The Journal of Biological Chemistry *284*, 4695-4704.

Milescu, M., Bosmans, F., Lee, S., Alabi, A.A., Kim, J.I., and Swartz, K.J. (2009). Interactions between lipids and voltage sensor paddles detected with tarantula toxins. Nature structural & molecular biology *16*, 1080-1085.

Mohapatra, D.P., Siino, D.F., and Trimmer, J.S. (2008). Interdomain cytoplasmic interactions govern the intracellular trafficking, gating, and modulation of the Kv2.1 channel. J Neurosci *28*, 4982-4994.

Mohapatra, D.P., and Trimmer, J.S. (2006). The Kv2.1 C terminus can autonomously transfer Kv2.1-like phosphorylation-dependent localization, voltage-dependent gating, and muscarinic modulation to diverse Kv channels. J Neurosci *26*, 685-695.

Morais-Cabral, J.H., Zhou, Y., and MacKinnon, R. (2001). Energetic optimization of ion conduction rate by the K+ selectivity filter. Nature *414*, 37-42.

Morth, J.P., Pedersen, B.P., Buch-Pedersen, M.J., Andersen, J.P., Vilsen, B., Palmgren, M.G., and Nissen, P. (2011). A structural overview of the plasma membrane Na+,K+-ATPase and H+-ATPase ion pumps. Nature reviews *12*, 60-70.

Motterlini, R., Clark, J.E., Foresti, R., Sarathchandra, P., Mann, B.E., and Green, C.J. (2002). Carbon monoxide-releasing molecules: characterization of biochemical and vascular activities. Circulation research *90*, E17-24.

Motterlini, R., and Otterbein, L.E. (2010). The therapeutic potential of carbon monoxide. Nat Rev Drug Discov *9*, 728-743.

Murata, Y., Iwasaki, H., Sasaki, M., Inaba, K., and Okamura, Y. (2005). Phosphoinositide phosphatase activity coupled to an intrinsic voltage sensor. Nature *435*, 1239-1243.

Muroi, Y., Arcisio-Miranda, M., Chowdhury, S., and Chanda, B. (2010). Molecular determinants of coupling between the domain III voltage sensor and pore of a sodium channel. Nature structural & molecular biology *17*, 230-237.

Nakahira, K., Shi, G., Rhodes, K.J., and Trimmer, J.S. (1996). Selective interaction of voltage-gated K+ channel beta-subunits with alpha-subunits. The Journal of Biological Chemistry *271*, 7084-7089.

Nakao, A., Kimizuka, K., Stolz, D.B., Neto, J.S., Kaizu, T., Choi, A.M., Uchiyama, T., Zuckerbraun, B.S., Nalesnik, M.A., Otterbein, L.E., and Murase, N. (2003). Carbon monoxide inhalation protects rat intestinal grafts from ischemia/reperfusion injury. The American journal of pathology *163*, 1587-1598.

Neher, E., and Sakmann, B. (1976). Single-channel currents recorded from membrane of denervated frog muscle fibres. Nature *260*, 799-802.

Neto, J.S., Nakao, A., Toyokawa, H., Nalesnik, M.A., Romanosky, A.J., Kimizuka, K., Kaizu, T., Hashimoto, N., Azhipa, O., Stolz, D.B*., et al.* (2006). Low-dose carbon monoxide inhalation prevents development of chronic allograft nephropathy. Am J Physiol Renal Physiol *290*, F324-334.

Ng, C.A., Perry, M.D., Tan, P.S., Hill, A.P., Kuchel, P.W., and Vandenberg, J.I. (2012). The S4-S5 linker acts as a signal integrator for HERG K+ channel activation and deactivation gating. PloS one *7*, e31640.

Noskov, S.Y., Berneche, S., and Roux, B. (2004). Control of ion selectivity in potassium channels by electrostatic and dynamic properties of carbonyl ligands. Nature *431*, 830-834.

Ott, M.C., Scott, J.R., Bihari, A., Badhwar, A., Otterbein, L.E., Gray, D.K., Harris, K.A., and Potter, R.F. (2005). Inhalation of carbon monoxide prevents liver injury and inflammation following hind limb ischemia/reperfusion. Faseb J *19*, 106-108.

Otterbein, L.E., Bach, F.H., Alam, J., Soares, M., Tao Lu, H., Wysk, M., Davis, R.J., Flavell, R.A., and Choi, A.M. (2000). Carbon monoxide has anti-inflammatory effects involving the mitogen-activated protein kinase pathway. Nature medicine *6*, 422-428.

Papazian, D.M., Schwarz, T.L., Tempel, B.L., Jan, Y.N., and Jan, L.Y. (1987). Cloning of genomic and complementary DNA from Shaker, a putative potassium channel gene from Drosophila. Science (New York, N.Y *237*, 749-753.

Papazian, D.M., Timpe, L.C., Jan, Y.N., and Jan, L.Y. (1991). Alteration of voltage-dependence of Shaker potassium channel by mutations in the S4 sequence. Nature *349*, 305-310.

Park, K.S., Mohapatra, D.P., Misonou, H., and Trimmer, J.S. (2006). Graded regulation of the Kv2.1 potassium channel by variable phosphorylation. Science (New York, N.Y *313*, 976-979.

Patel, A.J., Lazdunski, M., and Honore, E. (1997). Kv2.1/Kv9.3, a novel ATP-dependent delayed-rectifier K+ channel in oxygen-sensitive pulmonary artery myocytes. The EMBO journal *16*, 6615-6625.

Pathak, M., Kurtz, L., Tombola, F., and Isacoff, E. (2005). The cooperative voltage sensor motion that gates a potassium channel. The Journal of General Physiology *125*, 57-69.

Pathak, M.M., Yarov-Yarovoy, V., Agarwal, G., Roux, B., Barth, P., Kohout, S., Tombola, F., and Isacoff, E.Y. (2007). Closing in on the resting state of the Shaker K(+) channel. Neuron *56*, 124-140.

Payandeh, J., Scheuer, T., Zheng, N., and Catterall, W.A. (2012). The crystal structure of a voltage-gated sodium channel. Nature *475*, 353-358.

Perozo, E., MacKinnon, R., Bezanilla, F., and Stefani, E. (1993). Gating currents from a nonconducting mutant reveal open-closed conformations in Shaker K+ channels. Neuron *11*, 353-358.

Phillips, L.R., Milescu, M., Li-Smerin, Y., Mindell, J.A., Kim, J.I., and Swartz, K.J. (2005). Voltage-sensor activation with a tarantula toxin as cargo. Nature *436*, 857-860.

Phillips, L.R., and Swartz, K.J. (2010). Position and motions of the S4 helix during opening of the Shaker potassium channel. The Journal of General Physiology *136*, 629-644.

Pless, S.A., Galpin, J.D., Niciforovic, A.P., and Ahern, C.A. (2011). Contributions of counter-charge in a potassium channel voltage-sensor domain. Nature chemical biology *7*, 617-623.

Prole, D.L., and Yellen, G. (2006). Reversal of HCN channel voltage dependence via bridging of the S4-S5 linker and Post-S6. The Journal of General Physiology *128*, 273-282.

Ramsey, I.S., Moran, M.M., Chong, J.A., and Clapham, D.E. (2006). A voltage-gated proton-selective channel lacking the pore domain. Nature *440*, 1213-1216.

Ranganathan, R. (1994). Evolutionary origins of ion channels. Proceedings of the National Academy of Sciences of the United States of America *91*, 3484-3486.

Romao, C.C., Blattler, W.A., Seixas, J.D., and Bernardes, G.J. (2012). Developing drug molecules for therapy with carbon monoxide. Chemical Society reviews *41*, 3571-3583.

Rosenbaum, T., and Gordon, S.E. (2002). Dissecting intersubunit contacts in cyclic nucleotide-gated ion channels. Neuron *33*, 703-713.

Rosenbaum, T., and Gordon, S.E. (2004). Quickening the pace: looking into the heart of HCN channels. Neuron *42*, 193-196.

Rothberg, B.S., Shin, K.S., Phale, P.S., and Yellen, G. (2002). Voltage-controlled gating at the intracellular entrance to a hyperpolarization-activated cation channel. The Journal of General Physiology *119*, 83-91.

Roux, B., Allen, T., Berneche, S., and Im, W. (2004). Theoretical and computational models of biological ion channels. Quarterly reviews of biophysics *37*, 15-103.

Ruta, V., Chen, J., and MacKinnon, R. (2005). Calibrated measurement of gating-charge arginine displacement in the KvAP voltage-dependent K+ channel. Cell *123*, 463-475.

Ryan, M.J., Jernigan, N.L., Drummond, H.A., McLemore, G.R., Jr., Rimoldi, J.M., Poreddy, S.R., Gadepalli, R.S., and Stec, D.E. (2006). Renal vascular responses to CORM-A1 in the mouse. Pharmacol Res *54*, 24-29.

Santos-Silva, T., Mukhopadhyay, A., Seixas, J.D., Bernardes, G.J., Romao, C.C., and Romao, M.J. (2012). Towards improved therapeutic CORMs: understanding the reactivity of CORM-3 with proteins. Current medicinal chemistry *18*, 3361-3366.

Sarady, J.K., Zuckerbraun, B.S., Bilban, M., Wagner, O., Usheva, A., Liu, F., Ifedigbo, E., Zamora, R., Choi, A.M., and Otterbein, L.E. (2004). Carbon monoxide protection against endotoxic shock involves reciprocal effects on iNOS in the lung and liver. Faseb J *18*, 854-856.

Sasaki, M., Takagi, M., and Okamura, Y. (2006). A voltage sensor-domain protein is a voltage-gated proton channel. Science (New York, N.Y *312*, 589-592.

Schmidt, D., Jiang, Q.X., and MacKinnon, R. (2006). Phospholipids and the origin of cationic gating charges in voltage sensors. Nature *444*, 775-779.

Schneidman-Duhovny, D., Inbar, Y., Nussinov, R., and Wolfson, H.J. (2005). PatchDock and SymmDock: servers for rigid and symmetric docking. Nucleic Acids Res *33*, W363-367.

Scholle, A., Dugarmaa, S., Zimmer, T., Leonhardt, M., Koopmann, R., Engeland, B., Pongs, O., and Benndorf, K. (2004). Rate-limiting reactions determining different activation kinetics of Kv1.2 and Kv2.1 channels. J Membr Biol *198*, 103-112.

Schoppa, N.E., McCormack, K., Tanouye, M.A., and Sigworth, F.J. (1992). The size of gating charge in wild-type and mutant Shaker potassium channels. Science (New York, N.Y *255*, 1712-1715.

Schoppa, N.E., and Sigworth, F.J. (1998a). Activation of Shaker potassium channels. I. Characterization of voltage-dependent transitions. The Journal of General Physiology *111*, 271-294.

Schoppa, N.E., and Sigworth, F.J. (1998b). Activation of Shaker potassium channels. II. Kinetics of the V2 mutant channel. The Journal of General Physiology *111*, 295-311.

Schoppa, N.E., and Sigworth, F.J. (1998c). Activation of Shaker potassium channels. III. An activation gating model for wild-type and V2 mutant channels. The Journal of General Physiology *111*, 313-342.

Seoh, S.A., Sigg, D., Papazian, D.M., and Bezanilla, F. (1996). Voltage-sensing residues in the S2 and S4 segments of the Shaker K+ channel. Neuron *16*, 1159-1167.

Sheng, Z., Skach, W., Santarelli, V., and Deutsch, C. (1997). Evidence for interaction between transmembrane segments in assembly of Kv1.3. Biochemistry *36*, 15501-15513.

Shieh, C.C., Klemic, K.G., and Kirsch, G.E. (1997). Role of transmembrane segment S5 on gating of voltage-dependent K+ channels. The Journal of General Physiology *109*, 767-778.

Sigg, D., Bezanilla, F., and Stefani, E. (1994). Slowing of deactivation kinetics in Shaker B as seen in macropatch recordings of gating and ionic currents. Biophysical Journal *66*, 439.

Sigworth, F.J. (1980). The variance of sodium current fluctuations at the node of Ranvier. The Journal of Physiology *307*, 97-129.

Sigworth, F.J. (1995). Electronic Design of the Patch Clamp. In Single-Channel Recording, E. Neher, and B. Sakmann, eds. (Heidelberg: Springer Verlag), pp. 95-126.

Silverman, W.R., Roux, B., and Papazian, D.M. (2003). Structural basis of two-stage voltage-dependent activation in K+ channels. Proceedings of the National Academy of Sciences of the United States of America *100*, 2935-2940.

Smith-Maxwell, C.J., Ledwell, J.L., and Aldrich, R.W. (1998). Uncharged S4 residues and cooperativity in voltage-dependent potassium channel activation. The Journal of General Physiology *111*, 421-439.

Soler-Llavina, G.J., Chang, T.H., and Swartz, K.J. (2006). Functional interactions at the interface between voltage-sensing and pore domains in the Shaker K(v) channel. Neuron *52*, 623-634.

Song, R., Mahidhara, R.S., Zhou, Z., Hoffman, R.A., Seol, D.W., Flavell, R.A., Billiar, T.R., Otterbein, L.E., and Choi, A.M. (2004a). Carbon monoxide inhibits T lymphocyte proliferation via caspase-dependent pathway. J Immunol *172*, 1220-1226.

Song, R., Zhou, Z., Kim, P.K., Shapiro, R.A., Liu, F., Ferran, C., Choi, A.M., and Otterbein, L.E. (2004b). Carbon monoxide promotes Fas/CD95-induced apoptosis in Jurkat cells. The Journal of Biological Chemistry *279*, 44327-44334.

Starace, D.M., and Bezanilla, F. (2001). Histidine scanning mutagenesis of basic residues of the S4 segment of the shaker k+ channel. The Journal of General Physiology *117*, 469-490.

Starace, D.M., and Bezanilla, F. (2004). A proton pore in a potassium channel voltage sensor reveals a focused electric field. Nature *427*, 548-553.

Sten-Knudsen, O. (2002). Biological Membranes: Theory of Transport, Potentials and Electric Impulses, 1 edn (Cambridge University Press).

Sukhareva, M., Hackos, D.H., and Swartz, K.J. (2003). Constitutive activation of the Shaker Kv channel. The Journal of General Physiology *122*, 541-556.

Swartz, K.J., and MacKinnon, R. (1997). Hanatoxin modifies the gating of a voltage-dependent K+ channel through multiple binding sites. Neuron *18*, 665-673.

Taglialatela, M., and Stefani, E. (1993). Gating currents of the cloned delayed-rectifier K+ channel DRK1. Proceedings of the National Academy of Sciences of the United States of America *90*, 4758-4762.

Tao, X., Lee, A., Limapichat, W., Dougherty, D.A., and MacKinnon, R. (2009). A gating charge transfer center in voltage sensors. Science (New York, N.Y *328*, 67-73.

Tempel, B.L., Papazian, D.M., Schwarz, T.L., Jan, Y.N., and Jan, L.Y. (1987). Sequence of a probable potassium channel component encoded at Shaker locus of Drosophila. Science (New York, N.Y *237*, 770-775.

Tipparaju, S.M., Barski, O.A., Srivastava, S., and Bhatnagar, A. (2008). Catalytic mechanism and substrate specificity of the beta-subunit of the voltage-gated potassium channel. Biochemistry *47*, 8840-8854.

Tristani-Firouzi, M., Chen, J., and Sanguinetti, M.C. (2002). Interactions between S4-S5 linker and S6 transmembrane domain modulate gating of HERG K+ channels. The Journal of Biological Chemistry *277*, 18994-19000.

Tu, L., Santarelli, V., Sheng, Z., Skach, W., Pain, D., and Deutsch, C. (1996). Voltage-gated K+ channels contain multiple intersubunit association sites. The Journal of Biological Chemistry *271*, 18904-18911.

Upadhyay, S.K., Nagarajan, P., and Mathew, M.K. (2009). Potassium channel opening: a subtle two-step. The Journal of Physiology *587*, 3851-3868.

Vemana, S., Pandey, S., and Larsson, H.P. (2004). S4 movement in a mammalian HCN channel. The Journal of General Physiology *123*, 21-32.

Vereb, G., Szollosi, J., Matko, J., Nagy, P., Farkas, T., Vigh, L., Matyus, L., Waldmann, T.A., and Damjanovich, S. (2003). Dynamic, yet structured: The cell membrane three decades after the Singer-Nicolson model. Proceedings of the National Academy of Sciences of the United States of America *100*, 8053-8058.

Villalba-Galea, C.A., Sandtner, W., Starace, D.M., and Bezanilla, F. (2008). S4-based voltage sensors have three major conformations. Proceedings of the National Academy of Sciences of the United States of America *105*, 17600-17607.

Wang, D.T., Hill, A.P., Mann, S.A., Tan, P.S., and Vandenberg, J.I. (2011). Mapping the sequence of conformational changes underlying selectivity filter gating in the K(v)11.1 potassium channel. Nature structural & molecular biology *18*, 35-41.

Webster, S.M., Del Camino, D., Dekker, J.P., and Yellen, G. (2004). Intracellular gate opening in Shaker K+ channels defined by high-affinity metal bridges. Nature *428*, 864-868.

Weng, J., Cao, Y., Moss, N., and Zhou, M. (2006). Modulation of voltage-dependent Shaker family potassium channels by an aldo-keto reductase. The Journal of Biological Chemistry *281*, 15194-15200.

Wilkinson, W.J., and Kemp, P.J. (2011). Carbon monoxide: an emerging regulator of ion channels. The Journal of Physiology *589*, 3055-3062.

Williams, S.E., Brazier, S.P., Baban, N., Telezhkin, V., Muller, C.T., Riccardi, D., and Kemp, P.J. (2008). A structural motif in the C-terminal tail of slo1 confers carbon monoxide sensitivity to human BK Ca channels. Pflugers Arch *456*, 561-572.

Williams, S.E., Wootton, P., Mason, H.S., Bould, J., Iles, D.E., Riccardi, D., Peers, C., and Kemp, P.J. (2004). Hemoxygenase-2 is an oxygen sensor for a calcium-sensitive potassium channel. Science (New York, N.Y *306*, 2093-2097.

Wray, D. (2009). Intracellular regions of potassium channels: Kv2.1 and heag. Eur Biophys J *38*, 285-292.

Wright, E.M., Loo, D.D., and Hirayama, B.A. (2011). Biology of human sodium glucose transporters. Physiological reviews *91*, 733-794.

Xu, Y., Ramu, Y., and Lu, Z. (2008). Removal of phospho-head groups of membrane lipids immobilizes voltage sensors of K+ channels. Nature *451*, 826-829.

Yang, Y., Yan, Y., and Sigworth, F.J. (1997). How does the W434F mutation block current in Shaker potassium channels? The Journal of General Physiology *109*, 779-789.

Yang, Y., Yan, Y., and Sigworth, F.J. (2004). Can Shaker potassium channels be locked in the deactivated state? The Journal of General Physiology *124*, 163-171.

Yi, B.A., Minor, D.L., Jr., Lin, Y.F., Jan, Y.N., and Jan, L.Y. (2001). Controlling potassium channel activities: Interplay between the membrane and intracellular factors. Proceedings of the National Academy of Sciences of the United States of America *98*, 11016-11023.

Yifrach, O., and MacKinnon, R. (2002). Energetics of pore opening in a voltage-gated K(+) channel. Cell *111*, 231-239.

Yifrach, O., Zandany, N., and Shem-Ad, T. (2009). Examining cooperative gating phenomena in voltage-dependent potassium channels: taking the energetic approach. Methods in enzymology *466*, 179-209.

Yuan, X.J., Wang, J., Juhaszova, M., Golovina, V.A., and Rubin, L.J. (1998). Molecular basis and function of voltage-gated K+ channels in pulmonary arterial smooth muscle cells. Am J Physiol *274*, L621-635.

Zagotta, W.N., Hoshi, T., and Aldrich, R.W. (1994a). Shaker potassium channel gating. III: Evaluation of kinetic models for activation. The Journal of General Physiology *103*, 321-362.

Zagotta, W.N., Hoshi, T., Dittman, J., and Aldrich, R.W. (1994b). Shaker potassium channel gating. II: Transitions in the activation pathway. The Journal of General Physiology *103*, 279-319.

Zhou, Y., and MacKinnon, R. (2003). The occupancy of ions in the K+ selectivity filter: charge balance and coupling of ion binding to a protein conformational change underlie high conduction rates. Journal of Molecular Biology *333*, 965-975.

Zhou, Y., Morais-Cabral, J.H., Kaufman, A., and MacKinnon, R. (2001). Chemistry of ion coordination and hydration revealed by a K+ channel-Fab complex at 2.0 A resolution. Nature *414*, 43-48.

Zhou, Z., Song, R., Fattman, C.L., Greenhill, S., Alber, S., Oury, T.D., Choi, A.M., and Morse, D. (2005). Carbon monoxide suppresses bleomycin-induced lung fibrosis. The American journal of pathology *166*, 27-37.

Zimmerberg, J., Bezanilla, F., and Parsegian, V.A. (1990). Solute inaccessible aqueous volume changes during opening of the potassium channel of the squid giant axon. Biophysical Journal *57*, 1049-1064.

Zuckerbraun, B.S., Chin, B.Y., Wegiel, B., Billiar, T.R., Czsimadia, E., Rao, J., Shimoda, L., Ifedigbo, E., Kanno, S., and Otterbein, L.E. (2006). Carbon monoxide reverses established pulmonary hypertension. The Journal of Experimental Medicine *203*, 2109-2119.

THE JOURNAL OF BIOLOGICAL CHEMISTRY VOL. 286, NO. 18, pp. 16414–16425, May 6, 2011

Uncoupling Charge Movement from Channel Opening in Voltage-gated Potassium Channels by Ruthenium Complexes*[S]

Received for publication, October 29, 2010, and in revised form, March 8, 2011 Published, JBC Papers in Press, March 17, 2011, DOI 10.1074/jbc.M110.198010

Andrés Jara-Oseguera[‡1], Itzel G. Ishida[‡], Gisela E. Rangel-Yescas[‡], Noel Espinosa-Jalapa[§], José A. Pérez-Guzmán[¶], David Elías-Viñas[¶], Ronan Le Lagadec[§], Tamara Rosenbaum[‖], and León D. Islas[‡2]

From the [‡]Departamento de Fisiología, Facultad de Medicina, [§]Departamento de Química Inorgánica, Instituto de Química, and [¶]Departamento de Neurodesarrollo y Fisiología, División Neurociencias, Instituto de Fisiología Celular, Universidad Nacional Autónoma de México, Distrito Federal 04510, México and [‖]Sección de Bioelectrónica, Departamento de Ingeniería Eléctrica, Centro de Investigación y Estudios Avanzados, Instituto Politécnico Nacional, Distrito Federal 07360, México

The Kv2.1 channel generates a delayed-rectifier current in neurons and is responsible for modulation of neuronal spike frequency and membrane repolarization in pancreatic β-cells and cardiomyocytes. As with other tetrameric voltage-activated K^+-channels, it has been proposed that each of the four Kv2.1 voltage-sensing domains activates independently upon depolarization, leading to a final concerted transition that causes channel opening. The mechanism by which voltage-sensor activation is coupled to the gating of the pore is still not understood. Here we show that the carbon-monoxide releasing molecule 2 (CORM-2) is an allosteric inhibitor of the Kv2.1 channel and that its inhibitory properties derive from the CORM-2 ability to largely reduce the voltage dependence of the opening transition, uncoupling voltage-sensor activation from the concerted opening transition. We additionally demonstrate that CORM-2 modulates *Shaker* K^+-channels in a similar manner. Our data suggest that the mechanism of inhibition by CORM-2 may be common to voltage-activated channels and that this compound should be a useful tool for understanding the mechanisms of electromechanical coupling.

Voltage-gated potassium channel activation is achieved through extremely tight electromechanical coupling of the S1-S4 voltage-sensing domain (VSD)[3] with the pore domain, which is formed by the S5-S6 transmembrane segments (1–6). The mechanism by which this coupling occurs remains mostly unknown (7, 8).

Based on the high resolution structures of the Kv1.2 and the Kv2.1/Kv1.2 paddle chimera, it has been proposed that, in response to transmembrane voltage changes, S4 motion displaces the S4-S5 linker, which in turn contacts the C-terminal portion of the S6, the pore-lining segment that contains the activation gate (9, 10), and causes it to change conformation. Consistently, a great body of functional data indicates that both the S4-S5 linker and the C terminus of the S6 are essential for the coupling of the VSDs with the pore domain and that the interface between the VSD and the pore domain is also of importance (11–19).

Some of the most detailed models explaining voltage-sensing and pore-gating have been developed for the *Shaker* K^+-channel (18, 20–22). Albeit with some differences, most models and experimental data coincide in the sequential and independent activation of each of the four VSDs, which undergo transitions with high voltage dependence due to a large translocation of charge followed by one or more concerted transitions of all subunits, which lead to channel opening (18, 20, 22, 23). Other Kv channels such as those from the *Shab* family, including Kv2.1 and Kv2.2, seem to share the main features of the gating mechanism found in *Shaker* (6, 24), although detailed models are currently lacking.

In the course of experiments designed to explore the gas sensitivity of Kv2.1 channels, we discovered that the carbon-monoxide releasing molecule 2 (CORM-2) allosterically inhibits its Kv2.1 and that this effect is independent of carbon monoxide itself. We compared ionic and gating currents and found that CORM-2 has a lesser effect on charge movement than on channel opening, partially uncoupling pore-gating and voltage-sensing. Interestingly, we found that CORM-2 inhibits *Shaker* channels through a similar mechanism. Additionally, we identified a possible binding site for CORM-2 in Kv2.1 located at the interface between the voltage-sensing and pore domains. Our results support the notion that there are important similarities in the gating mechanism of different K^+-channels, such as *Shaker* and Kv2.1, and that the inhibitory mechanism of CORM-2 may be general for voltage-gated ion channels. Thus, CORM-2 could be a useful tool for further studies aimed at determining the mechanism of electromechanical coupling.

* This study was supported by Consejo Nacional de Ciencia y Tecnologia Grant 48990, Dirección General de Asuntos del Personal Académico-PAPIIT Grant IN209209, and Instituto de Ciencia y Tecnología del Distrito Federal Grant PIFUTP09-262 (to L. D. I.).

[S] The on-line version of this article (available at http://www.jbc.org) contains supplemental Figs. 1–4, Scheme 1, and Table 1.

[1] This study was performed in partial fulfillment of the requirement for the doctoral degree in Biomedical Sciences at Universidad Nacional Autónoma de México.

[2] To whom correspondence should be addressed: Departamento de Fisiología, Facultad de Medicina, Universidad Nacional Autónoma de México, México, D.F. C.P. 04510. E-mail: islas@liceaga.facmed.unam.mx.

[3] The abbreviations used are: VSD, voltage-sensing domain; CORM-2, carbon-monoxide releasing molecule 2; iCORM-2, inactivated CORM-2; eYFP, enhanced yellow fluorescent protein; NMDG/Asp, *N*-methyl-D-glucamine/aspartate; Mb, myoglobin.

EXPERIMENTAL PROCEDURES

Molecular Biology and Channel Expression in Oocytes—Plasmids *rKv2.1Δ7*-pBluescript-SK, *mSlo1*-pc-ANAOX, *Shaker* H4-pGEMA with N-type inactivation removed, and *Shaker* W434F-pGEMA were kindly provided by Drs. Ken Swartz, Larry Salkoff, and Fred Sigworth, respectively.

A fluorescent Kv2.1 channel (eYFP-Kv2.1) was constructed by amplifying the enhanced yellow fluorescent protein (eYFP) from the pEYFP-C1 plasmid by PCR with primers that introduced flanking restriction sites that were used to ligate the product into *rKv2.1Δ7*-pBluescript-SK, leaving a 10-amino acid linker between the end of the fluorescent protein and the channel. eYFP-Kv2.1 was used as a template for all amino acid substitutions. Mutations A396V, A396W, G337W, L327W, S323M, and G312M were introduced by performing a single-PCR reaction with the KOD Hot Start DNA polymerase (Novagen) and the direct and complementary mutagenic primers according to manufacturer's instructions. The PCR product was digested with DpnI hydrolase (New England Biolabs, Ipswich, MA) and transformed into *Escherichia coli* DH5α cells. Mutants G317V, G337V, and L264M were constructed using the overlapping PCR method as described (25). All mutations were confirmed by sequencing. Plasmids were linearized with NotI, transcribed using a T7 RNA polymerase *in vitro* transcription kit according to the manufacturer's instructions (Ambion, Austin, TX), and RNA transcripts were resuspended in DEPC-treated water to a final concentration of 0.5–1 μg/μl.

Xenopus laevis oocytes were surgically extracted and defolliculated as previously described (26). Oocytes were incubated at 18 °C in ND96 solution containing 96 mM NaCl, 2 mM KCl, 1.8 mM $CaCl_2$, 1 mM $MgCl_2$, 5 mM HEPES, 2.5 mM pyruvate, 20 mM μg/ml gentamycin (pH 7.5, NaOH). In some cases ND96 solution was supplemented with 5% fetal calf serum (Invitrogen), 1% penicillin/streptomycin (Invitrogen), and 10 mM tetraethylammonium (Sigma) to increase oocyte survival. Oocytes were injected with 18–36 nl of mRNA 1 day after harvesting using a Nanostepper injector (Drummond Scientific Co., Broomall, PA). Experiments were performed 1–5 days after injection.

Solutions and Patch Clamp Recording—All experiments were performed in the inside-out configuration of the patch clamp technique unless otherwise indicated following standard recording techniques. For Kv2.1 and *Shaker* ionic current recordings and *Shaker* W434F gating current recordings, the following solutions were employed: intracellular, 130 mM KCl, 3 mM HEPES, 1 mM EDTA (pH 7.4, KOH); extracellular, 60 mM KCl, 70 mM *N*-methyl-D-glucamine/aspartate (NMDG/Asp), 3 mM HEPES, 1 mM EDTA (pH 7.4, KOH).

For Kv2.1 gating current experiments, two different sets of solutions were employed containing: set 1, intracellular: 130 mM NMDG, 120 mM Asp, 10 mM HEPES, 10 mM EDTA (pH 7.4, NMDG); extracellular: 1 mM KCl, 130 mM NMDG, 120 mM Asp, 1.8 mM $CaCl_2$, 10 mM HEPES (pH 7.4, NMDG); set 2, intracellular: 130 mM tetraethylammonium chloride, 10 mM HEPES, 1 mM EDTA (pH 7.4, NMDG); extracellular: 5 mM KCl, 127 mM NMDG/Asp, 1.8 mM $CaCl_2$, 10 mM HEPES. Recording solutions not containing CORM-2 or any other compound tested will be referred to in the text as "saline" solutions for simplicity. Tricarbonyldichlororuthenium dimer $[Ru(CO)_3Cl_2]_2$ (Sigma) was dissolved in DMSO at 400 mM, diluted to the final concentration in recording solution, and used fresh for experiments. "Aged" or inactivated CORM-2 (iCORM-2) was obtained by letting the recording solution with 1 mM CORM-2 stay exposed to air at room temperature for 1 week. Complexes *trans,cis,cis*-$Ru(CO)(DMSO)(DMSO)_2Cl_2$, *cis, cis,cis*-$Ru(CO)_2(DMSO)(DMSO)Cl_2$, *fac*-$Ru(CO)_3(DMSO)Cl_2$, and *cis*-$Ru(DMSO)_4Cl_2$ were synthesized according to the published methods (27, 28).

Stock solutions for the first three compounds were prepared as for CORM-2, whereas $Ru(DMSO)_4Cl_2$ stock solutions were prepared in water. Solutions were delivered to membrane patches via a gravity-fed perfusion system and were changed with a homemade motorized solution changer. For gating-current experiments, the whole bath solution was manually substituted before data acquisition to avoid changes in capacity. All solutions delivered to the patch were applied to the intracellular face of the membrane unless otherwise stated.

Recording pipettes were pulled from glass capillaries (VWR International, Batavia, IL), had a resistance of 0.3–2.0 megaohms, and were covered with dental wax. Currents were recorded with an Axopatch200B amplifier (Molecular Devices, Silicon Valley, CA) and acquired with Pulse software (HEKA Elektronik GMBH, Pfalz, Germany). All data analysis and modeling was done using IgorPro (Wavemetrics Inc., Portland, OR).

Macroscopic ionic currents and gating currents were filtered at 5 kHz and sampled at 20 kHz with a low-pass Bessel filter. A $-p/5 \times 6$ protocol from a holding potential of −120 mV was used for linear current subtraction. For macroscopic ionic current recordings, a holding potential of −120 mV was used. For Slo1 and gating current experiments, a holding potential of −90 mV was employed. Gating currents are the average of at least 20 traces to improve the signal to noise ratio. In some cases the traces at potentials more positive than 0 mV had a plateau of constant current, which was eliminated by subtracting a square pulse from the data. Off-gating currents were measured at −90 mV.

Dose-response curves for CORM-2 and CORM-2-related compounds were measured as follows; steady-state current values at 100 mV in the presence of CORM-2 were normalized to the value obtained in saline and averaged with data obtained at the same compound concentration. A single CORM-2 concentration was evaluated per patch to avoid overestimation of the inhibition due to channel rundown upon patch excision. Kv2.1 conductance *versus* voltage (G-V) curves in 130 mM intracellular K^+ were obtained from the peak values of the tail currents measured at −120 mV and normalized to the tail value after a 100-mV test pulse obtained in saline. G-V curves at low potassium were recorded using the first set of gating-current solutions but with 5 mM extracellular KCl. In that case, a holding potential of −90 mV was used, and 50-ms test pulses were delivered to avoid the increased inactivation observed at zero intracellular potassium. *Shaker* G-V curves were estimated from current to voltage (I-V) curves assuming Ohm's equation. Data were fit to the following form of the Boltzmann equation,

$$G_{norm}(V) = \frac{G_{max}}{1 + \exp(-z(V - V_{1/2})/k_BT)} \quad \text{(Eq. 1)}$$

where z is the apparent charge (in units of e_0) associated with the gating transitions, $V_{1/2}$ is the voltage for half-maximal activation and k_BT has its usual meaning. Q_{on}-V curves were obtained from the time-integral of on-gating current traces and were fitted to an analogous equation.

Single-channel recordings were low pass-filtered at 5 kHz and sampled at 10 kHz. Currents were activated by 200-ms pulses to 100 mV from a holding potential of −120 mV. An average of null traces was used for leak subtraction. Single-channel current amplitude was estimated from all-points histograms of current traces with channel openings. Openings were detected with the 50% threshold crossing technique (29). First latency analysis was carried out according to Sigworth and Zhou (30).

For non-stationary noise analysis, data were sampled at 20 kHz and low pass-filtered at 10 kHz. 50–100 200-ms pulses to 100 mV were applied to patches without leak subtraction. Data analysis was performed as described in Sigworth (31) and Heinemann and Conti (32).

For activation kinetics-measurements, 100 (Kv2.1)- or 50 (*Shaker*)-ms pulses were delivered at several voltages from a holding potential of −120 mV, and single-exponential functions were fit to the second half of the rising current on activation. For deactivation kinetics, a conditioning pulse of 100 (Kv2.1) or 50 (*Shaker*) ms to 100 mV was delivered, and then voltage was stepped from −150 to −70 mV in 20-mV increments for Kv2.1 or from −170 to −70 in 10-mV increments for *Shaker* for 100 ms. Single- or double-exponential functions were fit to the deactivating currents.

The time courses of CORM-2 inhibition in the closed state were measured as follows; after measuring the initial current in saline, the voltage was stepped to −120 mV (WT) or −90 mV (G317V), and CORM-2 was applied for a given time interval, after which a pulse to 100 mV was applied to measure the remaining current still in the presence of CORM-2, to avoid washout effects. The time courses were constructed by varying the duration of CORM-2 application at the negative holding potential and normalizing the data to the initial value in saline. A single data point was obtained per experiment. The time courses at high open probability were measured by applying a train of 100-ms pulses to 100 mV in the presence of the donor. All group data are presented as the mean ± S.E.

Modeling of Kv2.1 and Shaker Gating—The system of differential equations corresponding to Scheme 1 was solved with the Backwards Differentiation Formula method. Ionic currents were calculated according to

$$I = P_o(t)\,Ng(V - V_{rev}) \quad \text{(Eq. 2)}$$

where $P_o(t)$ is the occupancy of the open state(s) as a function of time, N is the number of channels, g is the unitary conductance, V_{rev} is the reversal potential, and V is the test voltage. Gating currents were calculated from

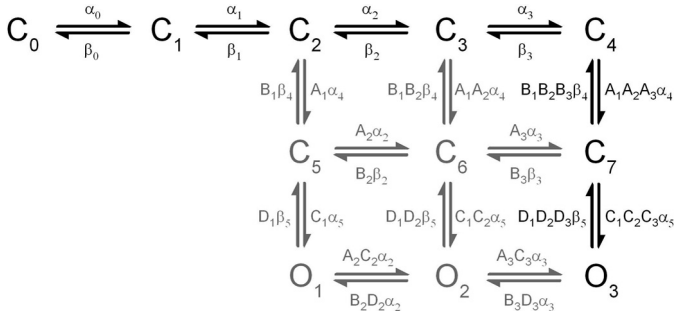

SCHEME 1

$$I_{gating} = \sum_{i,j} P_i(t)k_{ij}(z_{ij} - z_{ji}) \quad \text{(Eq. 3)}$$

where $P_i(t)$ is the occupancy of state i, k_{ij} is the forward rate constant between states i and j and has a form

$$k_{ij}(V) = k_{ij}(0\text{ mV})\exp(-z_{ij}V/k_BT) \quad \text{(Eq. 4)}$$

and z_{ij} and z_{ji} are partial charges of the forward and backward rate constants between states i and j, respectively. Images were generated with PyMOL Molecular Graphics System, Version 1.3 (Schrödinger, LLC).

Spectrophotometric Measurements—132 μM equine heart myoglobin (Sigma) stock solutions were prepared in the intracellular 130 mM KCl-recording solution and supplemented with 0.1% sodium dithionite (118 g/liter). Carboxymyoglobin was prepared by mixing a 2× myoglobin solution in 1:1 proportion with recording solution that had been bubbled with pure carbon monoxide (Infra Gas) for 30 min. Measurements were performed with a 1-cm quartz cell in a Beckman DU7500 spectrophotometer (Beckman Coulter, Brea, CA).

RESULTS

In the context of a survey of gaseous modulators of Kv channels, we examined the effects of tricarbonyldichlororuthenium dimer or CORM-2, an efficient and widely used CO-donor, on the Kv2.1 potassium channel expressed in *X. laevis* oocytes. Intracellularly applied CORM-2 inhibited Kv2.1-mediated currents in inside-out membrane patches (Fig. 1*A*). The inhibition proceeded rapidly and was reversible upon washout (Fig. 1*B*, *left panel*). In addition, CORM-2 inhibited the channel with greater affinity from the intracellular side of the membrane than from the extracellular side (Fig. 1*B*). We also found the inhibition to be concentration-dependent and highly cooperative, reflected in a Hill coefficient of nearly three (Fig. 1*C*).

Given the small affinity of the compound for the extracellular side of the channel, we decided to focus on the intracellular effects of CORM-2. To discard the possibility of CORM-2 being a fast pore blocker, we measured the effects of the donor on the single-channel current amplitude by performing single-channel recordings. We found that CORM-2 does not affect single-channel current amplitude (Fig. 1, *D* and *E*), indicating that the inhibition is not due to fast pore block. Consistent with our single-channel recordings, the current amplitudes obtained from non-stationary noise analysis did not differ significantly between saline and 0.5 mM CORM-2. The number of active channels in the patch, calculated from noise analysis, also

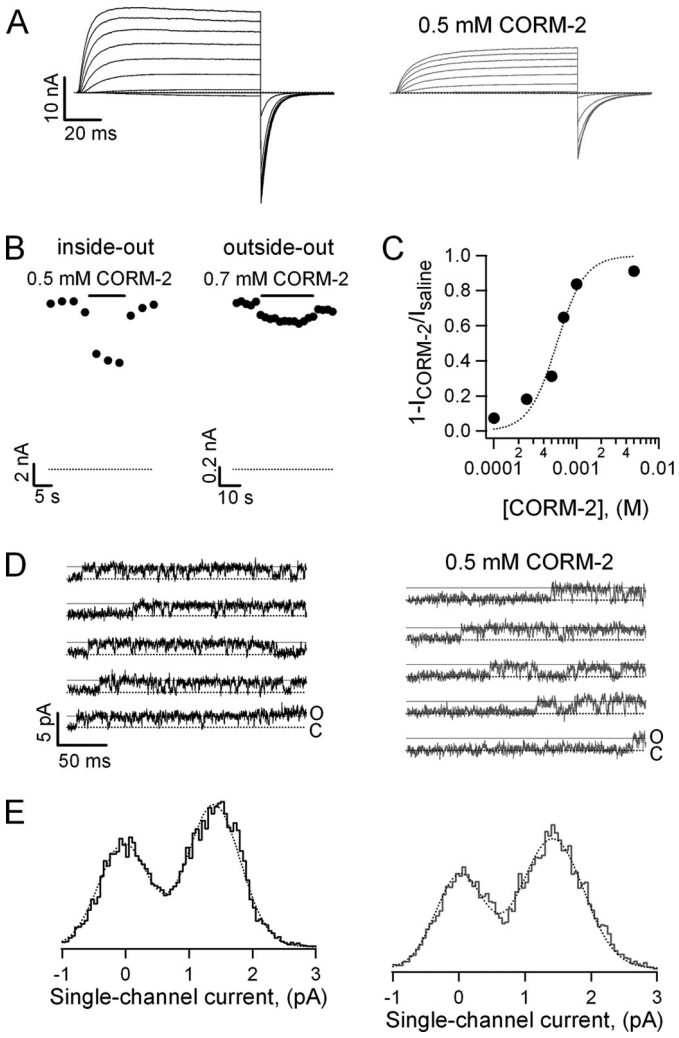

FIGURE 1. **CORM-2 inhibits Kv2.1 channel without changes in single-channel current.** *A*, representative Kv2.1 currents obtained in the absence and presence of CORM-2 are shown. Currents were activated by the application of voltage pulses from −120 to +100 mV in 20-mV increments. *B*, representative time courses for the inhibition of Kv2.1 by CORM-2 applied either from the intracellular or extracellular side of the membrane at 100 mV are shown. *C*, dose-response curve for CORM-2 at a voltage of 100 mV are shown. The *dotted curve* is a fit to the Hill equation. The fitted parameters are: $K_{1/2}$ = 0.56 mM and s = 2.8 (n = 3–15). *D*, representative single-channel recordings obtained with or without CORM-2 at 100 mV are shown. *E*, all-point histograms were obtained from *traces* as in *D*. *Dotted curves* are fits to the sum of two Gaussian functions. The mean single-channel current amplitudes are: i_{sal} = 1.57 ± 0.16 pA, i_{corm} = 1.51 ± 0.07 pA.

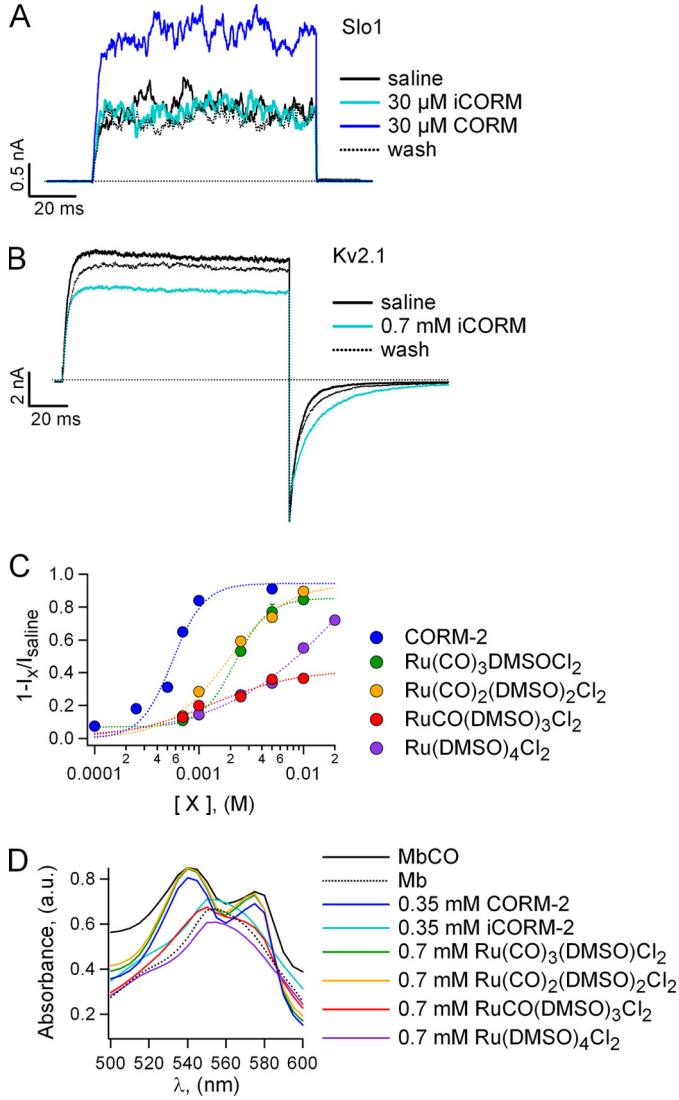

FIGURE 2. **Compounds related to CORM-2 that are unable to release CO inhibit the Kv2.1 channel.** *A*, Slo1 currents activated at 140 mV in the absence of calcium. The *dotted line* indicates the a zero-current level. *B*, Kv2.1-mediated currents at 100 mV are reversibly inhibited by iCORM-2. *C*, shown are dose-response curves of the Kv2.1 channel to CORM-2 and to several related compounds at 100 mV. I_x refers to the steady-state current value at a given compound concentration. *Dotted curves* are fits to the Hill equation. The resulting parameters are: $Ru(CO)_3(DMSO)Cl_2$, $K_{1/2}$ = 2.04 mM, s = 2.1, maximum inhibition = 0.88; $Ru(CO)_2(DMSO)_2Cl_2$; $K_{1/2}$ = 1.86 mM, s = 1.54, maximum inhibition = 0.94; $Ru(CO)(DMSO)_3Cl_2$; $K_{1/2}$ = 1.31 mM, s = 1.08, maximum inhibition = 0.42; $Ru(DMSO)_4Cl_2$; $K_{1/2}$ = 8.18 mM, s = 0.94, maximum inhibition = 1.0 (n = 5). *D*, shown is myoglobin absorption spectra at the conditions indicated in the figure. *a.u.*, absorbance units.

remained nearly constant before and during CORM-2 treatment: N_{corm}/N_{saline} = 0.84 ± 0.09. The small reduction in the ratio probably arises from time-dependent variations in the current due to channel rundown, which is observed in Kv2.1 channels (33).

Carbon monoxide has been shown to up-regulate several ion channels, including P2X receptors and the voltage- and calcium-dependent Slo1 potassium channel (34–36). For this reason, we next addressed whether the effects of CORM-2 depend on the donor molecule itself or on the carbon monoxide it releases. To answer this question, our first approach was to test whether inactivated CORM-2 or iCORM-2, which has already lost all releasable carbonyls, could inhibit the Kv2.1 channel in a similar manner as fresh CORM-2. As a positive control, we used the Slo1 channel. As expected, CORM-2 increased Slo1-mediated currents at 140 mV in the absence of calcium, whereas iCORM-2 at the same concentration was unable to produce any current increase (Fig. 2*A*). On the other hand, iCORM-2 caused a reversible reduction in Kv2.1-mediated currents and a slowing of deactivation kinetics, albeit with a decreased affinity when compared with fresh CORM-2 (Fig. 2*B*), suggesting that the inhibition is CO-independent.

iCORM-2 is a mixture of several degradation products of CORM-2 in which the carbonyls have been substituted by other ligands, such as water, and are, therefore, structurally similar to

CORM-2. Alternatively, the compound $Ru(DMSO)_4Cl_2$ has been used as a negative control for the CO-mediated effects of CORM-2 (35). Because CORM-2 stock solutions were prepared in DMSO, it is likely that some of the carbonyls released by CORM-2 were substituted by DMSO molecules in our experiments. Besides, it has been shown that two DMSO ligands in $Ru(DMSO)_4Cl_2$ are quickly substituted by water molecules (37, 38) as in iCORM-2. However, each ruthenium atom per donor is able to release only two carbonyls, retaining the third (39), making it likely that iCORM molecules contain at least one carbonyl, so we suspected that $Ru(DMSO)_4Cl_2$ may not represent the main constituent of iCORM-2.

The approach we took next was to test whether CORM-2-related compounds in which the carbonyls were substituted one by one by a DMSO molecule were still able to inhibit Kv2.1. All compounds tested did inhibit the channel, although with decreased affinity and cooperativity (Fig. 2*C*). We next asked if these compounds were able to release CO by analyzing the effect they had on the absorption spectrum of myoglobin, whose spectrum is very different if the protein is unliganded or bound to CO. As expected, myoglobin solutions that contained iCORM or the ruthenium complexes that contained a single carbonyl ligand or none had an absorption spectrum identical to that of unliganded myoglobin (Mb), indicating that they did not release CO (Fig. 2*D*). On the contrary, solutions with ruthenium complexes that had two or more carbonyl ligands had a spectrum identical to CO-bound myoglobin (MbCO), indicating that they did release CO. The interesting result is that even ruthenium complexes that are not able to release CO can inhibit the Kv2.1 channel. Our experiments with iCORM and the related compounds we synthesized are a strong indication that the effects of CORM-2 are CO-independent. To further support this assertion we used hemoglobin as a scavenger of CO released by CORM-2. These experiments indicate that hemoglobin is capable of sequestering the CO released locally by CORM-2 and that the presence of the scavenger does not interfere with the inhibition caused by CORM-2 (supplemental Fig. 1).

The fact that CORM-2 did not affect the single-channel current amplitude or the number of active channels in the patch suggests that it may inhibit the channel by shifting its gating equilibrium. Surprisingly, although CORM-2 slightly right-shifted the channel activation curve, the observed changes in $V_{1/2}$ were not nearly sufficient to produce the degree of inhibition at the two concentrations tested, 0.5 and 0.7 mM (Fig. 3*A*). However, the steepness of the activation curve was considerably reduced, probably reflecting a change in subunit cooperativity or an actual reduction in the gating charge.

A large decrease in the open probability without a proportional change in the activation curve would require a change in the activation and deactivation rate constants. Indeed, macroscopic kinetics in the presence of CORM-2 seemed to be slower, so we studied the kinetics with more detail. As shown in Fig. 3, *B* and *C*, solutions containing 0.5 and 0.7 mM CORM-2 produced a slowdown in both the activation and deactivation kinetics of the channel. The most dramatic effect is seen at 0.7 mM; activation and deactivation rates at zero mV were reduced, and the valences for both transitions, reflected in the steepness

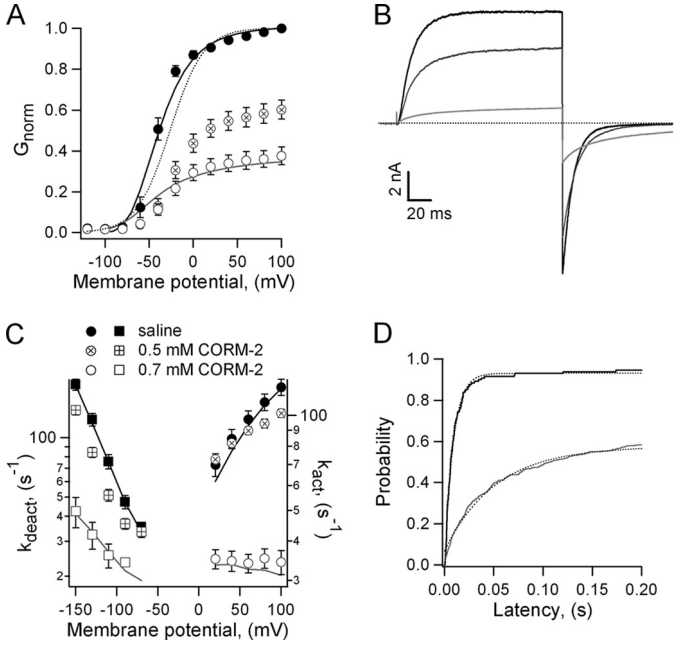

FIGURE 3. **CORM-2 has a small effect on the activation curve and a large effect on channel kinetics.** *A*, G-V curves obtained before (●) or during the application of 0.5 (⊗) or 0.7 (○) mM CORM-2 are shown. Data were fit to Equation 1, and the obtained parameters are: saline, $V_{1/2} = -40 \pm 6.1$ mV, $z = 2.84 \pm 0.48\ e_0$; CORM-2 0.5 mM $V_{1/2} = -22.6 \pm 2.46$ mV, $z = 1.66 \pm 0.23\ e_0$; 0.7 mM CORM-2, $V_{1/2} = -26.5 \pm 4.9$ mV, $z = 1.67 \pm 0.21$ e_0 ($n = 4$ - 6). The scaled-up fit to the 0.7 mM CORM-2 data is included as a *dotted curve*. *Solid curves* are predictions of the model in Scheme 1, for saline (*black*), and 0.7 mM CORM-2 (*gray*). *B*, representative Kv2.1 currents at 100 mV and deactivated at −130 mV in saline (*black traces*) and with 0.5 (*dark gray*) or 0.7 mM CORM-2 (*light gray*) are shown. The *dotted line* indicates the zero-current level. *C*, plots of the activation (*circles*) and deactivation (*squares*) rate constants obtained from single-exponential fits to traces as in *B* at several voltages and at both CORM-2 concentrations. Data were fit to Equation 4, and the resultant values are: saline, $k_{act}(0) = 64.3 \pm 5\ s^{-1}$, $z_{act} = 0.18 \pm 0.01\ e_0$, $k_{deact}(0) = 7.59 \pm 1\ s^{-1}$, $z_{deact} = -0.57 \pm 0.03\ e_0$; 0.5 mM CORM-2, $k_{act}(0) = 74.0 \pm 13.0\ s^{-1}$, $z_{act} = 0.17 \pm 0.01\ e_0$, $k_{deact}(0) = 6.28 \pm 1\ s^{-1}$, $z_{deact} = -0.53 \pm 0.02\ e_0$; 0.7 mM CORM-2, $k_{act}(0) = 38.4 \pm 6.4\ s^{-1}$, $z_{act} = 0.0004 \pm 0.0076\ e_0$, $k_{deact}(0) = 5.40 \pm 0.45\ s^{-1}$, $z_{deact} = -0.29 \pm 0.04\ e_0$ ($n = 4$ - 25). *Solid curves* were calculated from the model in Scheme 1 for saline (*black*) and 0.7 mM CORM-2 (*gray*). *D*, shown is representative probability *versus* first latency plot obtained from single-channel recordings as in Fig. 1*D* in the absence (*black trace*) or presence (*gray trace*) of 0.5 mM CORM-2 at 100 mV. *Dotted curves* are fits to an exponential function. The rates are: $k_{sal} = 103 \pm 18\ s^{-1}$, $k_{corm} = 23 \pm 4\ s^{-1}$ ($n = 2$).

of the curves, were even more affected, rendering opening kinetics almost voltage-independent (Fig. 3*C*). This slowdown of the opening transition was also observed in single-channel recordings in the presence of CORM-2; the latency to first channel opening was increased in a manner consistent with the macroscopic current recordings (Fig. 3*D*).

The large reduction in the voltage dependence of activation and deactivation kinetics and the decrease in the steepness of the steady-state G-V curve suggest that CORM-2 could either affect voltage-sensor function or alter the cooperativity between subunits. To clarify this issue, we measured gating currents in the absence and presence of 0.7 mM CORM-2, a concentration that causes a large reduction in the voltage dependence of activation and deactivation. Gating currents in saline activated rapidly at depolarized potentials and could be accurately measured in the inside-out configuration (Fig. 4*A*, *left panel*). Gating current deactivation kinetics, on the other hand, were much slower due to the first open-to-closed transition,

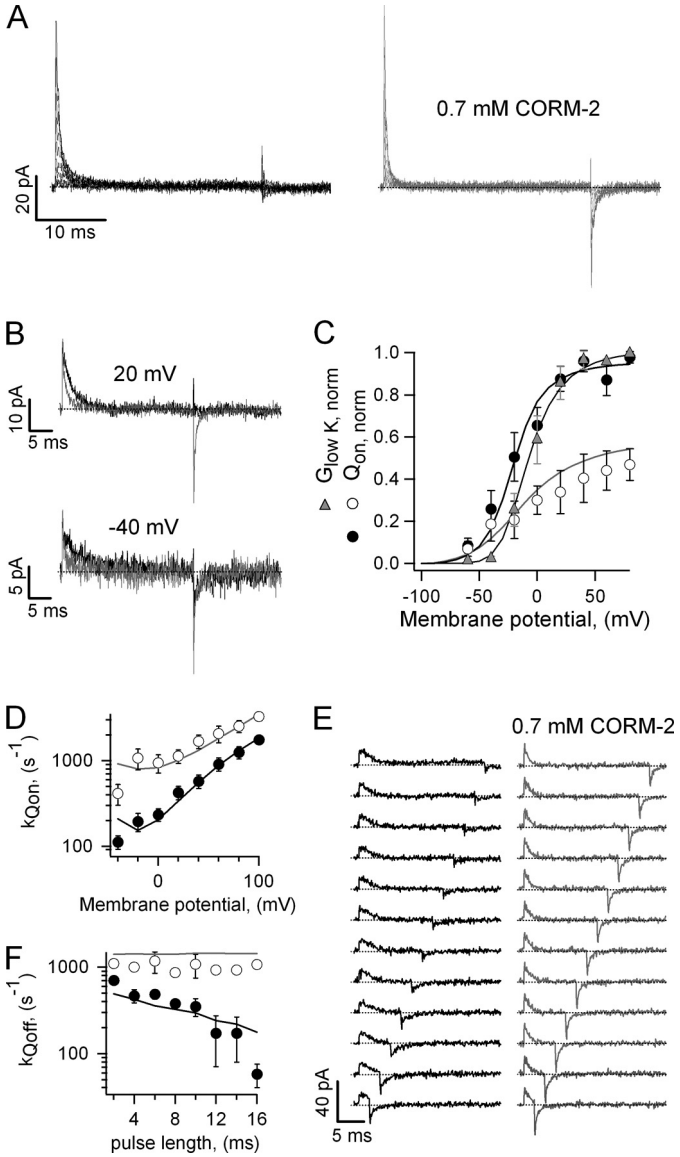

FIGURE 4. **CORM-2 and charge movement in Kv2.1.** *A*, shown are representative Kv2.1 gating current families from the same patch, activated by voltage pulses between −60 and 80 mV in 20-mV increments with or without CORM-2. *B*, shown is a comparison of gating current traces from A at 20 and −40 mV in the presence (*gray traces*) and absence (*black traces*) of CORM-2. *C*, shown is a normalized Q_{on}-V curve obtained either before (*filled symbols*) or in the presence (*empty symbols*) of CORM-2. Data were fit to the Boltzmann equation, and the obtained fits are: saline, $V_{1/2} = -21.3 \pm 6.1$ mV, $z = 1.82 \pm 0.13$ e_0; CORM-2, $V_{1/2} = 8.43 \pm 20.56$ mV, $z = 0.91 \pm 0.18$ e_0 ($n = 6$). The normalized G-V curve was obtained under the same ionic conditions as the gating currents with 5 mM extracellular KCl. A fit to Equation 1 gave the following parameters: $V_{1/2} = -3.37 \pm 5.76$ mV, $z = 2.84 \pm 0.30$ e_0 ($n = 9$). *Solid black* and *gray curves* are the model predictions for saline and CORM-2, respectively. *D*, shown are gating current decay rate constants measured from traces as in *A* in the presence (*empty symbols*) and absence (*filled symbols*) of CORM-2. The parameters of the fit to Equation 4 are: saline, $k_{Qon}(0) = 284 \pm 57$ s^{-1}, $z_{Qon} = 0.47 \pm 0.03$ e_0, CORM-2, $k_{Qon}(0) = 1033 \pm 224$ s^{-1}, $z_{Qon} = 0.27 \pm 0.03$ e_0 ($n = 6$). *Solid curves* are the rates predicted by the model. *E*, representative gating currents were elicited by successive pulses to 40 mV of increasing duration. *Dotted lines* mark the zero-current level. *F*, off-gating current rate constants were obtained from traces as in *E* as a function of depolarizing pulse duration. *Solid curves* are the model predictions.

which is slow (40), making it difficult to accurately quantify the amount of charge that moves upon repolarization. In the presence of CORM-2 (Fig. 4*A*, *right panel*) two important changes in the behavior of the currents could be clearly observed; the magnitude of the currents was smaller, and kinetics were faster. The differences can be seen more clearly in the isolated current traces at two different voltages in Fig. 4*B*. It can also be seen that at voltages in which the open probability is low, *i.e.* −40 mV, off-gating currents can be clearly observed in both saline and CORM-2 (Fig. 4*B*, *lower panel*), whereas at voltages with open probability nearer to 1, *i.e.* 20 mV, off-gating currents are no longer discernible in saline (Fig. 4*B*, *upper panel*).

Comparison of the Q_{on}-V curve in the absence and presence of CORM-2 (Fig. 4*C*) suggests that the compound reduced the maximal gating charge that moves upon depolarization by about 30% and shifted the voltage of half-maximal activation to the right, as estimated from fits to the Boltzmann equation. These changes suggest an energetic destabilization of the activated state of the voltage sensor. Another important observation is that the $V_{1/2}$ for the Q_{on}-V in saline is less negative than the $V_{1/2}$ of the G-V curve in Fig. 3*A*, a result that seems to be in contradiction with a sequential model for K^+-channel gating. However, the recording conditions between both experiments were quite different, so we measured a G-V curve under similar conditions as the gating-current experiments, *i.e.* low K^+ concentrations (Fig. 4*C*, *gray triangles*), and found that under these conditions the G-V curve was right-shifted with respect to the Q_{on}-V curve, which indicates that the channel activation curve depends on the concentration of the permeating ion.

The acceleration of on-gating currents caused by CORM-2 was quantified by fitting single exponentials to the gating current decay (Fig. 4*D*). The rate at 0 mV was increased almost 4-fold with respect to saline, whereas the apparent charge associated with gating current activation was halved. The increased speed in off-gating current kinetics could imply an acceleration of the first closing transition. However, the first closing transition could not be much faster as ionic tail current kinetics was slower in the presence of CORM-2. The other possibility would be that one or more forward (opening) transitions are inhibited by the compound, so that the channel in the presence of CORM-2 does not reach the open state, and therefore, it no longer undergoes the slow first closing-transition upon repolarization.

To test this possibility, we measured gating currents in response to depolarizing voltage pulses of increasing duration in saline and in 0.7 mM CORM-2 (Fig. 4*E*). As has been widely documented for *Shaker* and other Kv channels (40–42), with short pulse durations (Fig. 4*E*, *left panel*, *bottom*) most channels in saline did not reach the open state. As a consequence, gating currents deactivated fast. At longer pulse durations, most channels reached the open state, so the gating currents deactivated slowly. Consistent with our hypothesis, in the presence of CORM-2 the off-gating currents returned fast at all time intervals tested (Fig. 4*E*, *right panel*). These data suggest that CORM-2 affects the concerted transitions, so that channels in the presence of the compound open with a much slower rate. Off-gating current kinetics with and without CORM-2 was quantified by fitting single-exponential functions to the current decay time course, and the results are depicted as a function of depolarizing pulse duration in Fig. 4*F*.

To further test this hypothesis, we performed experiments in which gating and ionic currents could be measured in the same

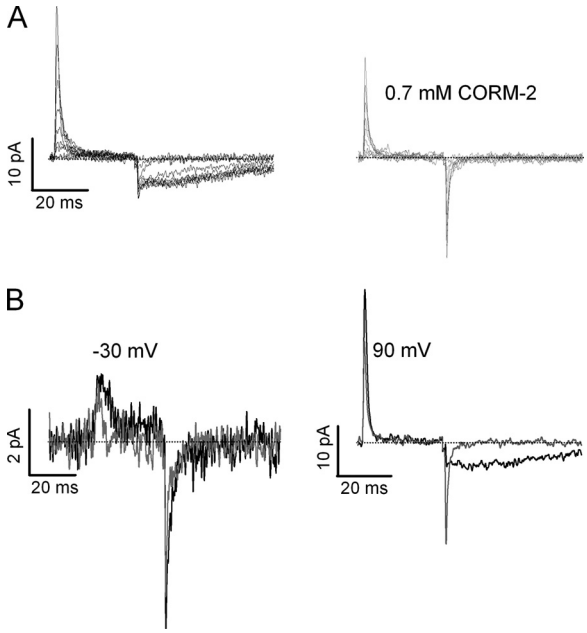

FIGURE 5. **CORM-2 inhibits channel opening without largely inhibiting charge movement.** *A*, gating currents were measured with 5 mM extracellular potassium and 130 mM intracellular tetraethylammonium from a voltage of −80 mV to 100 mV in 20-mV increments. *B*, shown are current traces from *A* at two different voltages, with (*gray traces*) or without (*black traces*) CORM-2.

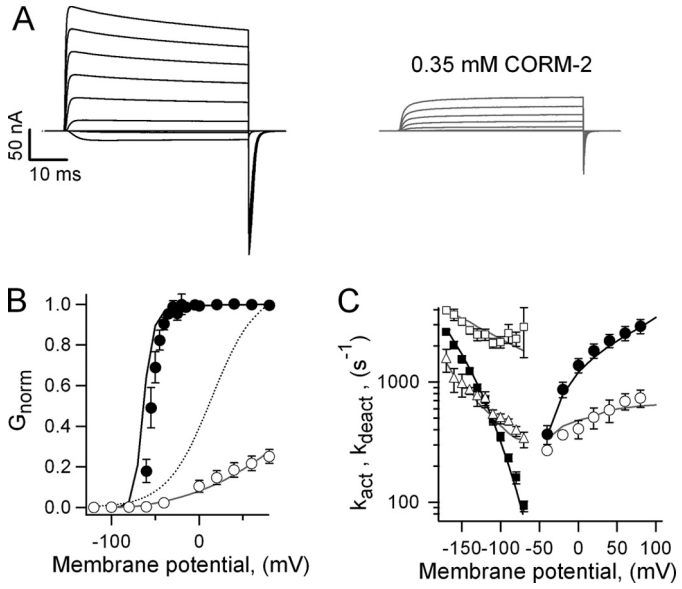

FIGURE 6. ***Shaker* channels are also inhibited by CORM-2.** *A*, *Shaker* WT ionic current families activated by voltage pulses from −120 to 80 mV in 20-mV increments were obtained in saline and in CORM-2. *B*, normalized G-V curves from traces as in *A* are shown, with *closed circles* for *saline* and *open circles* for CORM-2. The parameters obtained from fits to Equation 1 were: saline, $V_{1/2} = -39.6 \pm 3.1$ mV, $z = 4.86 \pm 0.3$ e_0; CORM-2, $V_{1/2} = +19.4 \pm 8.5$ mV, $z = 0.99 \pm 0.10$ e_0 ($n = 4$). The *dotted curve* is a scaled fit of Equation 1 to the CORM-2-data. *Solid curves* are predictions from Scheme 1 for saline (*black*) and CORM-2 (*gray*). *C*, activation (*circles*) and deactivation rate constants (*squares* and *triangles*) for *Shaker* in saline (*filled symbols*) and in 0.35 mM CORM-2 (*empty symbols*) are shown. Data were fit to Equation 4, and the resultant values were: saline, k_{act} (0) = 1298 ± 166 s^{-1}, $z_{act} = 0.25 \pm 0.01$ e_0, k_{deact} (0) = 24.5 ± 4.1 s^{-1}, $z_{deact} = -0.70 \pm 0.02$ e_0; CORM-2, k_{act} (0) = 412 ± 64 s^{-1}, $z_{act} = 0.175 \pm 0.004$ e_0, k_{deact1} (0) = 1124 ± 242 s^{-1}, $z_{deact1} = -0.19 \pm 0.04$ e_0, k_{deact2} (0) = 179 ± 31 s^{-1}, $z_{deact2} = -0.28 \pm 0.05$ e_0 (n = 4 - 6). *Solid curves* are the predictions of Scheme 1.

patch to simultaneously determine the effect of CORM-2 on both. Gating currents were recorded in the presence of 5 mM extracellular potassium and high intracellular tetraethylammonium, which slows the first closing transition even further (43). Under these conditions, current recordings in saline show slow ionic tail currents upon repolarization at potentials where a high open probability is expected (Fig. 5, *A*, *left panel*, and *B*, *right panel*, *black traces*). After the addition of 0.7 mM CORM-2, the ionic currents were no longer visible, and the off-gating currents had faster kinetics (Fig. 5, *A*, *right panel*, and *B*, *gray traces*).

The possibility of CORM-2 acting as an uncoupling agent that affects principally the concerted transitions of the Kv2.1 channel is exciting, as such a compound should be useful for the study of the mechanism of coupling between voltage-sensor activation and pore- opening. However, there is limited experimental information concerning such coupling in Kv2.1, as opposed to *Shaker*, where a considerable amount of functional data is already available (11–19). We, therefore, decided to test whether CORM-2 inhibits *Shaker* channels in a similar fashion.

We found that CORM-2 did inhibit *Shaker*-mediated currents (Fig. 6*A*). The G-V curve in the presence of CORM-2 was dramatically right-shifted (Fig. 6*B*), and the steepness of the curve was also reduced at least 4-fold. As for Kv2.1, CORM-2 had profound effects on *Shaker* activation and deactivation kinetics (Fig. 6*C*); in the presence of the compound two different components of activation and deactivation can be discerned. In the case of activation, both components were slower than the rate measured in saline and had a reduced voltage dependence. The slower component could also be present in saline but obscured by the extensive slow inactivation at more depolarized potentials, so that only the faster component was quantified in Fig. 6*C*. Deactivation tail currents in CORM-2 were biexponential, with one component faster than the deactivation rate in saline and one slower but both less voltage-dependent (Fig. 6*C*). Finally, *Shaker* undergoes slow inactivation at depolarized potentials at a faster rate than Kv2.1 (Fig. 6*A*). Interestingly, CORM-2 eliminated slow inactivation, at least in the studied time scale, probably due to a reduced occupancy of the open state. Because the reduction of the steepness of the G-V curve could reflect a change in gating charge and/or subunit cooperativity, we proceeded to investigate the effect of the donor on *Shaker* gating currents by using the non-conducting *Shaker* mutant W434F (44, 45).

In *Shaker* W434F, gating currents in saline also activated fast and deactivated slowly (Fig. 7*A*, *left panel*). The effects of CORM-2 on *Shaker* gating currents, which consisted of a reduction in on-gating current amplitude and an acceleration of on and off kinetics, were surprisingly similar to the effects seen in Kv2.1 (Fig. 7*A*, *right panel*). The Q_{on}-V curve in the presence of CORM-2 was right-shifted to a similar degree as the Q_{on}-V curve of Kv2.1 (Fig. 7*B*) almost by 20 mV, although not as much as the *Shaker* G-V curve. The steepness was reduced 2-fold, less than the observed reduction in the G-V curve steepness. Additionally, as for Kv2.1, the measured reduction in on-gating charge was smaller than the reduction in patch conductance at the same voltage and CORM-2 concentration. The acceleration in on-gating current kinetics was also quantified and is shown in Fig. 7*C*. We also performed the same experi-

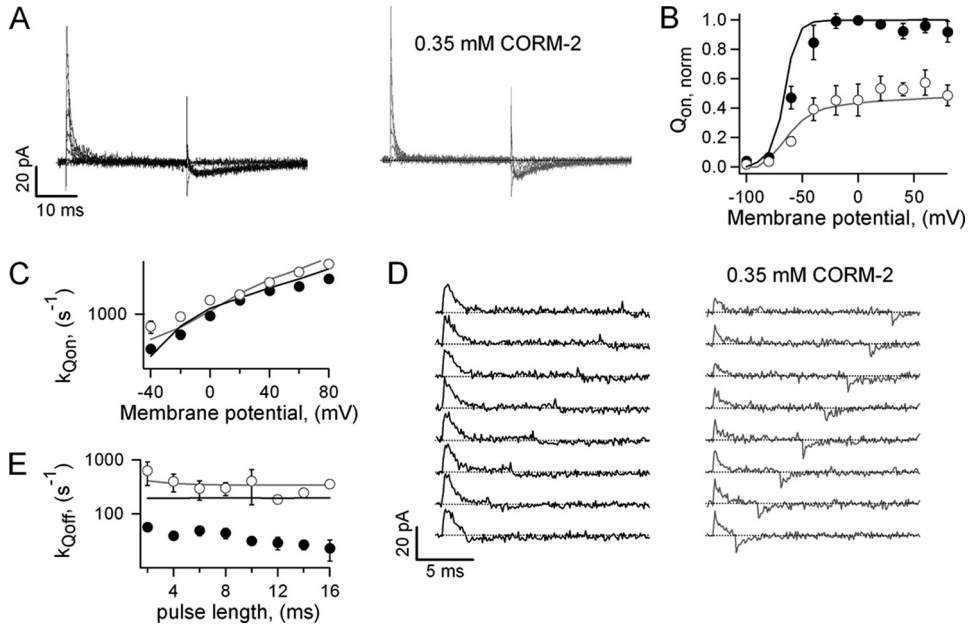

FIGURE 7. **The effects of CORM-2 on *Shaker*-gating currents.** *A*, *Shaker*W434F gating currents measured in saline or with CORM-2 in the same patch are shown. *B*, Q_{on}-V curves were measured from traces as in *A*. Fits to the Boltzmann equation returned the following parameters: saline, $V_{1/2} = -58.3 \pm 3$ mV, z = 4.0 ± 1.0 e_0; CORM-2, $V_{1/2} = -39.0 \pm 8.7$ mV, z = 1.75 ± 0.53 e_0 ($n = 4$). *Solid curves* are predictions from the model in Scheme 1. *C*, rate constants for on-gating current-decay with (*empty symbols*) or without (*filled symbols*) CORM-2 are shown. The parameters obtained from fits to Equation 4 are: saline, k_{Qon} (0) = 966 ± 56 s^{-1}, $z_{Qon} = 0.32 \pm 0.02$ e_0; CORM-2, k_{Qon} (0) = 1306 ± 79 s^{-1}, $z_{Qon} = 0.31 \pm 0.02$ e_0 ($n = 4$). *Solid curves* are the rate constants predicted by Scheme 1. *D*, representative gating currents were elicited by pulses to 0 mV of increasing duration. *Dotted lines* indicate the zero-current level. *E*, off-gating current rate constants were obtained from traces as in *D* as a function of depolarizing pulse duration. *Solid curves* are the model predictions.

ment as in Fig. 4*E*, and found a similar result (Fig. 7, *D* and *E*); although the off-gating currents in saline become progressively slower at longer pulse durations, currents in the presence of CORM-2 retained fast kinetics in the studied time interval.

Our data are consistent with a mechanism in which CORM-2 inhibits the concerted opening transition of Kv2.1 and *Shaker* without fully inhibiting voltage-sensor movement. The question remains as to the location of the CORM-2 binding site. As a first approximation, we carried out docking calculations using the Patchdock server, which assigns possible docking sites according to size and geometry (46, 47). As templates, we used the refined structures of the Kv1.2 channel in the open and closed conformations (48) and the compound $Ru(DMSO)_2(CO)_2Cl_2$, which likely is a major component of CORM-2 solutions after CO release (37, 38). The most common docking observed in both the open and closed states of the channel occurs at a cavity that exists between the voltage-sensing and pore domains of adjacent subunits (Fig. 8*A*). A second high-scored docking site in the channel is located between the S5 and S6 segments, near the Proline-Valine-Proline region (data not shown).

To experimentally confirm the docking results, we tested whether mutations in the predicted binding site altered the channel's interaction with CORM-2. Selected residues in the Kv2.1 channel were substituted with bulkier amino acids based on their position in the putative binding sites in the Kv1.2 structure (Fig. 8*A*) and an amino acid sequence alignment between both channels (supplemental Fig. 2*A*). Point mutations were introduced into an eYFP-Kv2.1 fusion protein, which allowed us to check for membrane expression of the constructs and which has very similar biophysical properties and CORM-2 sensitivity to the WT channel (Fig. 8, *B*–*D*).

Most mutants are trafficked to the plasma membrane but did not generate measurable currents, suggesting that they produced non-functional channels (supplemental Fig. 2*B*). Mutants L264M and A396V were functional but did not largely differ from the WT in regards to their activation curve, kinetics, and CORM-2 sensitivity (Fig. 8, *C* and *D*, and data not shown). On the other hand, the mutant G317V, in which the substituted residue lies in the S4-S5 linker, behaved significantly different from the WT channel, with much faster deactivation kinetics (Fig. 8*B*) and a dramatically right-shifted activation curve (Fig. 8*C*). Non-stationary noise analysis indicated that the steady-state open probability at 100 mV was rather small (0.12 ± 0.02) and that the single-channel current at the same voltage was not largely reduced (1.11 ± 0.10 pA, supplemental Fig. 3*A*), suggesting that the point mutation had shifted the gating equilibrium toward the closed state. When 0.7 mM CORM-2 was applied to the patch, a rather surprising effect was observed; the compound caused an instantaneous, reversible, and quite large increase in the current, which then declined to a value comparable with the leak current (supplemental Fig. 3, *B* and *C*). Apart from causing an increase in current, CORM-2 induced a substantial leftward shift in the G-V curve as estimated from currents activated by rapid voltage ramps (Fig. 8*C* and supplemental Fig. 3*D*). The G317V dose-response curve in Fig. 8*C* displays the peak potentiation of the current as a function of CORM-2 concentration. The potentiation dose-response cannot be accurately determined because the inhibitory process at larger CORM-2 concentrations is so fast that it does not allow quantifying the compound concentration at which the potentiating component saturates. As an approximation, data were fit to the product of two Hill equations, and the obtained parameters differ from those of the WT, suggesting that the residue substi-

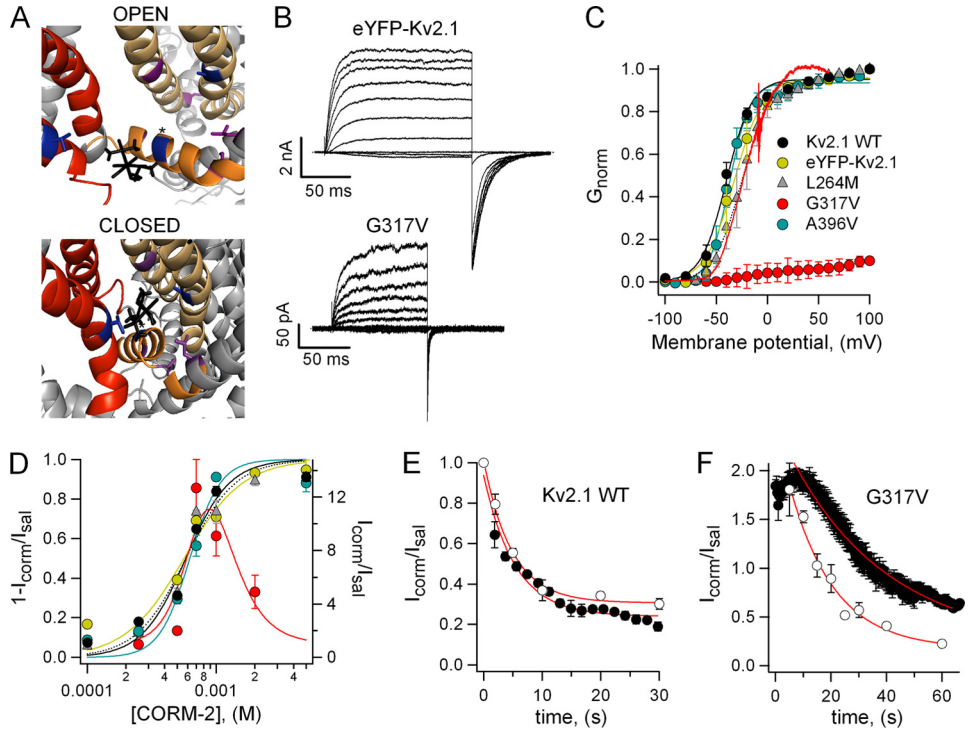

FIGURE 8. **Identification of a possible CORM-2 binding site in the Kv2.1 channel.** *A*, docking of a putative degradation product of CORM-2, $Ru(DMSO)_2(CO)_2Cl_2$ (*black*), with Kv1.2 in the open and closed states is shown. The S3 and S4 are shown in *red*, the S4-S5 linker is in *orange*, and the pore domain of the adjacent subunit is in *light yellow*. Residues Val-261 (S3 segment, Leu-264 in Kv2.1), Gly-318 (S4-S5 linker, Gly-317 in Kv2.1), and Ala-397 (S6, Ala-396 in Kv2.1), whose substitution resulted in functional channels, are shown in *blue*. Residues Ser-324 (S5, Ser-323 in Kv2.1), Gly-313 (S4-S5 linker, Gly-313 in Kv2.1), Leu-328 (S5, Leu-327 in Kv2.1), and Gly-338 (S5, Gly-337 in Kv2.1), when mutated resulted in non-functional channels, are shown in *purple*. Position Gly-318 is marked with an *asterisk*. *B*, representative currents of eYFP-Kv2.1 and eYFP-Kv2.1G317V were activated by voltage pulses from −100 to 100 mV in 20-mV increments and deactivated at −120 mV. *C*, normalized G-V relations for the different Kv2.1 constructs in saline are shown. The G317V curve was normalized to the open probability measured from non-stationary noise analysis at 100 mV. Curves are fits to Equation 1 with following parameters: eYFP-Kv2.1, $V_{1/2} = -33.2 \pm 7.0$ mV, $z = 2.59 \pm 0.22$ e_0; L264M, $V_{1/2} = -28.3 \pm 5.6$ mV, $z = 3.05 \pm 0.60$ e_0; A396V, $V_{1/2} = -37.1 \pm 4.0$ mV, $z = 2.84 \pm 0.30$ e_0, ($n = 4$). The *continuous red curve* is a representative G-V-relation of G317V in the presence of 0.7 mM CORM-2 obtained from a voltage ramp from −100 to 60 mV with 0.48 mV/s normalized to a fit of a single-barrier permeation model as described in supplemental Fig. 3*D*. *D*, CORM-2 dose-response curves for WT and mutant Kv2.1 channels at 100 mV are shown. *Symbols* are as in *C*. *Continuous* and *dotted curves* are fits to the Hill equation with following parameters: eYFP-Kv2.1, $K_{1/2} = 0.56$ mM, s = 1.91; L264M, $K_{1/2} = 0.59$ mM, s = 2.41; A396V, $K_{1/2} = 0.63$ mM, s = 3.67; $n = 3–4$. The G317V data were fit to the following product of two Hill equations: $I_{corm}/I_{sal} = 1 + I_{max}[(1 + [\text{CORM-2}]/K_{1/2,1})^{s1}(1 + K_{1/2,2}/[\text{CORM-2}])^{s2}]^{-1}$ and obtained with the following parameters: $I_{max} = 28$, $K_{1/2,1} = 0.73$ mM, $s1 = 4.0$, $K_{1/2,2} = 0.92$ mM, $s2 = 2.65$ ($n = 3–6$). *E*, time course of Kv2.1 inhibition by 0.7 mM CORM-2 in the open (*black symbols*) and the closed (*white symbols*) state is shown. The first point in the curve marks the beginning of CORM-2 application. *Red curves* are fits to an exponential function with rates: $k_{open\text{-}state} = 0.217 \pm 0.041$ s^{-1}, $k_{closed\text{-}state} = 0.207$ s^{-1} ($n = 6$). *F*, shown is the time course of 0.5 mM CORM-2-action on G317V in the open (*black symbols*) and closed states (*white symbols*). *Red curves* are fits to an exponential with parameters: $k_{open\text{-}state} = 0.045 \pm 0.009$ s^{-1}, $k_{closed\text{-}state} = 0.0625$ s^{-1} ($n = 3–6$).

tution at that position has an effect on CORM-2 interaction with the channel.

The S4-S5 linker is thought to undergo large state-dependent conformational changes, so it is expected that the residue substitution at position 317 would have state-dependent effects on the actions of CORM-2 if it forms part of its binding site. The state dependence of CORM-2 inhibition was estimated by measuring the time courses of CORM-2-action on the closed state of WT and G317V channels and comparing them with time courses obtained during the application of a train of pulses to 100 mV to keep the channel in the open state for a larger fraction of time. Interestingly, both time courses in the WT channel overlap almost perfectly, indicating that CORM-2 inhibits the WT channel in a state-independent manner (Fig. 8*E*). In contrast, CORM-2 appears to have an increased affinity for the closed state of the G317V (Fig. 8*F*). These data suggest that G317 may indeed be part of the compound binding site in the channel.

DISCUSSION

In this paper we describe the effects of CORM-2 as an allosteric modulator of Kv2.1 and *Shaker* Kv channels. The compound behaves as an inhibitor of the coupling between charge movement and channel opening. *Shaker* and Kv2.1 channels seem to share a common gating mechanism in which the VSD in each subunit undergoes independent voltage-dependent transitions followed by a different set of concerted cooperative transitions that lead to the open state. This commonality might be reflected in the similar effects of CORM-2 on both channels. The observed slowing of the opening kinetics and a reduction in overall voltage dependence were accompanied by an increased rate of charge movement, notably of charge return upon repolarization. These changes are reminiscent of the effects observed for several *Shaker* mutants like the ILT (18, 49), V2 (20), F401A (50), R3Q (51), and E395C (52), which selectively shift the gating equilibrium toward the closed state, making the last concerted forward transition rate-limiting. Interestingly, these mutations are distributed in different regions, from the S4 to the S6, indicating that the cooperative interactions that lead to the coupling between the VSD and the pore involve diverse structural regions of the protein. The pore blocker 4-AP has been shown to have analogous effects (53). Interestingly, 4-AP has been shown to inhibit slow inactivation in *Shaker* (54), as does CORM-2 (Fig. 6*A*).

However, the changes caused by CORM-2 are not limited to the last concerted transitions. The observed reduction in gating charge is larger than the fraction of charge that has been associated with the concerted transitions in *Shaker* (18, 20, 55), indicating that CORM-2 also interferes with the independent subunit transitions in both channels. A simple slowing of forward independent transitions would cause a reduction in apparent gating charge at the studied voltage range. However, such a mechanism would also predict slowing of on-gating current kinetics and large depolarizing shifts in the Q_{on}-V and G-V curves. Such observations have been made for methanethiosulfonate ethyltrimethylammonium-modified *Shaker* F370C channels (56) or Kv2.1 channels in the presence of gating-modifying toxins (57–59). In contrast, our Q_{on}-V and G-V curves are not dramatically right-shifted, especially for Kv2.1, and gating current kinetics is significantly accelerated for both channels, indicating that the subunit transitions are altered in a different manner.

In an effort to identify a mechanism that could explain our data, we considered a model based on a mechanistic interpretation of our findings in which CORM-2 uncouples voltage-sensing from pore opening by allowing the channel to open before all voltage sensors have reached the activated state. Additionally, we assume that CORM-2 causes a progressive reduction in voltage sensor activation rate as more sensors reach the activated state, as if CORM-2 induced negative cooperativity between subunits. Such a mechanism has been proposed to explain the effects produced by several uncoupling mutations, which allow Kv channels to open independently of the state of the voltage sensors (11, 12, 60). Furthermore, certain molecules, like local anesthetics and gastropod toxins, have been found to affect or induce cooperative interactions between voltage sensors in different voltage-gated ion channels (61, 62).

In the absence of established kinetic models for Kv2.1, we decided to use a seven-state linear model that provided a good fit of our data (Scheme 1, *black states*; Figs. 3, 4, 6, and 7, and supplemental Fig. 4; parameters are shown in Table 1) even when compared with fits to a 16-state model (supplemental Scheme I) that has been shown to reproduce *Shaker* behavior under a wider range of experimental conditions (18) (supplemental Fig. 5 and Table 1). Furthermore, linear models have been previously used satisfactorily in studies of Kv2.1 and other potassium channels (24, 53, 63–65).

In the context of the linear model, the effects of CORM-2 were explained by assuming that the channels can open after the activation of at least two voltage sensors by undergoing two additional concerted transitions (Scheme 1, *gray states*). The rates for the forward subunit transitions are initially accelerated and become progressively slow, with a major reduction in the last subunit transition. The valences of the independent transitions are unchanged, and changes in valence are only required for the rate-limiting concerted transitions. The reduced valence could be a consequence of the loosened coupling between voltage sensors and the pore. Scheme 1 predictions for CORM-2 are shown in Figs. 3, 4, 6, and 7 as *gray lines* and in supplemental Fig. 3. Another interesting observation that is consistent with Scheme 1 is that Kv2.1 currents at the holding potential are slightly larger in the presence of high concentrations of CORM-2 than in saline (data not shown), which could be a result of channel opening from the states with incomplete voltage-sensor activation.

TABLE 1

Parameter estimates for Scheme 1

For *Shaker*, A = B = C = D = 1. For Kv2.1, all allosteric factors are equal to unity except $A_2 = 1.5$.

Consejo Nacional de Ciencia y Tecnologia	*Shaker*		Kv2.1			
	Saline	CORM-2	Saline		CORM-2	
				Low K^+		Low K^+
$\alpha_0(0)$	1500	3000	900	450	2400	1200
$\beta_0(0)$	250	650	250	500	500	1000
$\alpha_1(0)$	3500	3500	3000	1200	4500	2500
$\beta_1(0)$	250	550	200	450	500	900
$\alpha_2(0)$	3500	2500	3000	1200	1000	400
$\beta_2(0)$	250	50	200	450	500	900
$\alpha_3(0)$	3500	0.0001	3000	1200	0.0001	
$\beta_3(0)$	250	250	200	450	500	900
$\alpha_4(0)$	9000	400	100		20	
$\beta_4(0)$	250	150	55		10	
$\alpha_5(0)$	15000	120	90		40	
$\beta_5(0)$	100	1000	10		70	
$z\alpha_0(0)$	0.2	0.2	0.4		0.4	
$z\beta_0(0)$	−0.4	−0.4	−0.3		−0.3	
$z\alpha_1(0)$	0.4	0.4	0.5		0.5	
$z\beta_1(0)$	−0.5	−0.5	−0.3		−0.3	
$z\alpha_2(0)$	0.5	0.5	0.5		0.5	
$z\beta_2(0)$	−0.7	−0.7	−0.3		−0.3	
$z\alpha_3(0)$	0.5	0.5	0.5		0.5	
$z\beta_3(0)$	−0.7	−0.7	−0.4		−0.4	
$z\alpha_4(0)$	1.1	0.3	0.3		0.05	
$z\beta_4(0)$	−0.8	−0.3	−0.4		−0.4	
$z\alpha_5(0)$	0.18	0.18	0.1		0.001	
$z\beta_5(0)$	−0.5	−0.2	−0.5		−0.005	

Although the model in Scheme 1 succeeds in reproducing the overall channel behavior in saline and CORM-2, it also exhibits some shortcomings. First, the observed off-gating currents are slower than the model predictions (Figs. 4 and 7). A slowing of *Shaker* off-gating kinetics in excised patches, as compared with other recording configurations, is a common observation (66), however unexplained. A second shortcoming of the model is its inability to reproduce the presence of a slower component of CORM-2 inhibition observed after longer patch exposures (several minutes). This effect could be due to CORM-2 binding to a second low affinity site but could also be caused by an accumulation of the compound in the membrane, so that patches were not exposed to CORM-2 for long time intervals unless it could not be avoided. In this respect it must be taken into account that if the forward and backward concerted transitions under longer nearly saturating CORM-2 exposures, like in the gating current experiments, became immeasurably slow albeit still significant, then the open and last closed state could act as inactivated states, causing charge immobilization during the experiment and contributing to the observed decrease in gating charge.

Other mechanisms for CORM-2 actions may be plausible. For example, the CORM-2 effects on both channels can be simulated (data not shown) by decreasing the charge associated with both independent and concerted transitions to almost half of the total and reducing the rate of the forward concerted transitions. Such a mechanism would imply structural rearrangements in the voltage sensor and its surroundings, resulting in a decrease in effective gating charge movement. Although both models of CORM-2 action are quite different in regard to the reduction in the gating charge, both require large

changes in the concerted forward and backward transitions, which seem to be the main targets of the compound.

To correlate our functional data with structural information, we decided to search for possible compound binding sites, and our first approach was to perform a docking experiment using the Kv1.2 structural model (48). There is a high degree of structural conservation between Kv channels, especially in the pore and VSD (10, 11, 67–69), so that structural information on one channel can be usefully applied to others. Moreover, residues that have been identified as important for channel function in *Shaker* have their equivalents in other Kv channels, where they seem to perform a similar function (58, 60, 70). Consistently, several studies have succeeded in generating functional chimeras between different K^+-channel α-subunits (11, 12, 23, 63, 69), like the paddle chimera between the Kv1.2 and Kv2.1 (71), whose structure has been determined at high resolution and has been shown to retain the features observed in the Kv1.2 structure (10).

Interestingly, the highest scored docking results are all located at the interface between the voltage-sensing and pore domains of adjacent subunits, a region that has been shown to be important for the cooperative interactions between both domains (13, 14, 17, 19) and that contains the S4-S5 linker, which is thought to be responsible for the electromechanical coupling mechanism in voltage-dependent K^+ channels (9–12, 15–17, 72).

We introduced mutations in the predicted binding site, mainly substituting small hydrophobic residues for bulkier ones. Notably, most mutations resulted in non-functional channels (supplemental Fig. 2). Because of the nature of the substitutions, it is likely that the mutations altered the packing of the protein in that region in a functionally deleterious fashion. Accordingly, smaller changes in residue size, like in the L264M or A396V mutants, resulted in functional channels with properties similar to WT, whereas larger changes in size, like in the A396W or G317V constructs, resulted in channels that were non-functional or had very different biophysical properties as compared with the WT channel (Fig. 8 and supplemental Figs. 2 and 3). These data suggest that the packing in that region is quite sensitive to perturbations, which is consistent with its importance for conformational changes within the protein.

The observations made with the G317V mutant are also consistent with the involvement of the studied region on electromechanical coupling. The faster deactivation kinetics and the extremely right-shifted activation curve all point to an energetic destabilization of the activated state, which in terms of the seven-state linear model, can be achieved by increasing the closing rate constants and decreasing the forward rates of the concerted transitions. The interactions between the S4-S5 linker and the S6 are thought to depend highly on the orientation of one helix with respect to the other (72), so that the observed changes in G317V channel function could have been caused by a change in orientation of the S4-S5 linker.

Our state dependence data argue that the interaction of CORM-2 with the channel was altered by the mutation, suggesting that the S4-S5 linker may indeed be part of the compound binding site. If so, the effects of CORM-2 on this mutant, although surprising, can also be interpreted in terms of CORM-2-induced reorientations of the S4-S5 linker affecting the gating equilibrium. The G-V curve obtained from voltage ramps in the presence of CORM-2 is consistent with a shift in gating equilibrium toward the open state (Fig. 8*C* and supplemental Fig. 3*D*). A larger destabilization of the closed state could also be the consequence of the apparent higher affinity of the compound for the closed state observed in the mutant.

The cooperativity observed in the WT and mutant channel CORM-2 dose-response curves also suggests that CORM-2 is involved in highly cooperative transitions in the channel, which might correspond to the concerted opening and closing transitions. Other interactions of the compound with the rest of the interface could be responsible for the rearrangements in the voltage-sensing domain or the opening of the gate without fully activated voltage sensors. The inhibitory component of CORM-2 on the G317V channel develops with decreased rate from the apparently instantaneous current potentiation and could be caused by a slower CORM-2-induced transition in the channel or its binding to a second site.

The precise nature of CORM-2 interactions with the channel remains to be elucidated. The fact that the L264M and A396V substitutions did not interfere with CORM-2 effects indicates that the side chains of those residues are not in proximity to the compound in the binding site, possibly reflecting differences between the Kv1.2 and Kv2.1 channels or a relative tolerance of the site to small perturbations. In this respect, the docking results were the same whether CORM-2 or one of its degradation products was used (data not shown), indicating a degree of robustness of the putative binding site.

CORM-2 then appears to have similar effects on two different but related ion channels, interfering with the coupling of the voltage-sensing domain and the gating of the pore. The similarities in the effects on both channels point to a conserved mechanism of electromechanical coupling among voltage-activated potassium channels. CORM-2 could be used as a tool to understand the mechanisms by which different ion channels are able to transduce changes in membrane potential into conformational changes that lead to ion conduction.

Acknowledgments—We thank Manuel Hernández at Facultad de Medicina, Universidad Nacional Autónoma de México, for expert instrument fabrication, Ernesto Ladrón de Guevara and Itzel Llorente for help with molecular biology, and Olga Araceli Patrón Soberano and Gabriel Orozco Hoyuela for assistance with confocal microscopy at Instituto de Fisiología Celular.

REFERENCES

1. Aggarwal, S. K., and MacKinnon, R. (1996) *Neuron* **16,** 1169–1177
2. Schoppa, N. E., McCormack, K., Tanouye, M. A., and Sigworth, F. J. (1992) *Science* **255,** 1712–1715
3. Seoh, S. A., Sigg, D., Papazian, D. M., and Bezanilla, F. (1996) *Neuron* **16,** 1159–1167
4. Bezanilla, F. (2005) *IEEE Trans. Nanobioscience* **4,** 34–48
5. Sigworth, F. J. (2007) *Biophys. J.* **93,** 2981–2983
6. Islas, L. D., and Sigworth, F. J. (1999) *J. Gen. Physiol.* **114,** 723–742
7. Roux, B. (2006) *Neuron* **52,** 568–569
8. Tombola, F., Pathak, M. M., and Isacoff, E. Y. (2006) *Annu. Rev. Cell Dev. Biol.* **22,** 23–52
9. Long, S. B., Campbell, E. B., and Mackinnon, R. (2005) *Science* **309,**

903–908
10. Long, S. B., Tao, X., Campbell, E. B., and MacKinnon, R. (2007) *Nature* **450,** 376–382
11. Lu, Z., Klem, A. M., and Ramu, Y. (2001) *Nature* **413,** 809–813
12. Lu, Z., Klem, A. M., and Ramu, Y. (2002) *J. Gen. Physiol.* **120,** 663–676
13. Caprini, M., Fava, M., Valente, P., Fernandez-Ballester, G., Rapisarda, C., Ferroni, S., and Ferrer-Montiel, A. (2005) *J. Biol. Chem.* **280,** 18253–18264
14. Soler-Llavina, G. J., Chang, T. H., and Swartz, K. J. (2006) *Neuron* **52,** 623–634
15. Lee, S. Y., Banerjee, A., and MacKinnon, R. (2009) *PLoS Biol.* **7,** e47
16. Tristani-Firouzi, M., Chen, J., and Sanguinetti, M. C. (2002) *J. Biol. Chem.* **277,** 18994–19000
17. Lai, H. C., Grabe, M., Jan, Y. N., and Jan, L. Y. (2005) *Neuron* **47,** 395–406
18. Ledwell, J. L., and Aldrich, R. W. (1999) *J. Gen. Physiol.* **113,** 389–414
19. Li-Smerin, Y., Hackos, D. H., and Swartz, K. J. (2000) *Neuron* **25,** 411–423
20. Schoppa, N. E., and Sigworth, F. J. (1998) *J. Gen. Physiol.* **111,** 313–342
21. Zagotta, W. N., Hoshi, T., Dittman, J., and Aldrich, R. W. (1994) *J. Gen. Physiol.* **103,** 279–319
22. Zagotta, W. N., Hoshi, T., and Aldrich, R. W. (1994) *J. Gen. Physiol.* **103,** 321–362
23. Smith-Maxwell, C. J., Ledwell, J. L., and Aldrich, R. W. (1998) *J. Gen. Physiol.* **111,** 399–420
24. Scholle, A., Dugarmaa, S., Zimmer, T., Leonhardt, M., Koopmann, R., Engeland, B., Pongs, O., and Benndorf, K. (2004) *J. Membr. Biol.* **198,** 103–112
25. Rosenbaum, T., and Gordon, S. E. (2002) *Neuron* **33,** 703–713
26. Goldin, A. L. (1992) *Methods Enzymol.* **207,** 266–279
27. Alessio, E., Milani, B., Bolle, M., Mestroni, G., Faleschini, P., Todone, F., Geremia, S., and Calligaris, M. (1995) *Inorg. Chem.* **34,** 4722–4734
28. Evans, I. P., Spencer, A., and Wilkinson, G. (1973) *J. Chem. Soc. Dalton Trans.* 204–209
29. Sakmann, B., and Neher, E. (1995) *Single-channel Recording*, 2nd Ed., pp. 483–585, Plenum Press, New York
30. Sigworth, F. J., and Zhou, J. (1992) *Methods Enzymol.* **207,** 746–762
31. Sigworth, F. J. (1980) *J. Physiol.* **307,** 97–129
32. Heinemann, S. H., and Conti, F. (1992) *Methods Enzymol.* **207,** 131–148
33. Lopatin, A. N., and Nichols, C. G. (1994) *J. Gen. Physiol.* **103,** 203–216
34. Wilkinson, W. J., Gadeberg, H. C., Harrison, A. W., Allen, N. D., Riccardi, D., and Kemp, P. J. (2009) *Br. J. Pharmacol.* **158,** 862–871
35. Williams, S. E., Wootton, P., Mason, H. S., Bould, J., Iles, D. E., Riccardi, D., Peers, C., and Kemp, P. J. (2004) *Science* **306,** 2093–2097
36. Hou, S., Xu, R., Heinemann, S. H., and Hoshi, T. (2008) *Proc. Natl. Acad. Sci. U.S.A.* **105,** 4039–4043
37. Alessio, E., Mestroni, G., Nardin, G., Attia, W. M., Calligaris, M., Sava, G., and Zorzet, S. (1988) *Inorg. Chem.* **27,** 4099–4106
38. Brindell, M., Stochel, G., Bertolasi, V., Boaretto, R., and Sostero, S. (2007) *Eur. J. Inorg. Chem.* **16,** 2353–2359
39. Motterlini, R., Clark, J. E., Foresti, R., Sarathchandra, P., Mann, B. E., and Green, C. J. (2002) *Circ. Res.* **90,** E17–E24
40. Taglialatela, M., and Stefani, E. (1993) *Proc. Natl. Acad. Sci. U.S.A.* **90,** 4758–4762
41. Perozo, E., Papazian, D. M., Stefani, E., and Bezanilla, F. (1992) *Biophys. J.* **62,** 160–168
42. Schoppa, N. E., and Sigworth, F. J. (1998) *J. Gen. Physiol.* **111,** 271–294
43. Armstrong, C. M. (1971) *J. Gen. Physiol.* **58,** 413–437
44. Perozo, E., MacKinnon, R., Bezanilla, F., and Stefani, E. (1993) *Neuron* **11,** 353–358
45. Yang, Y., Yan, Y., and Sigworth, F. J. (1997) *J. Gen. Physiol.* **109,** 779–789
46. Duhovny, D., Nussinov, R., and Wolfson, H. J. (2002) in *Proceedings of the Second Workshop on Algorithms in Bioinformatics* (*WABI*) *Rome, Italy, Lecture Notes in Computer Science* (Guigó, R., and Gusfield, D., eds) pp. 185–200, Springer-Verlagm Heidelberg, Germany
47. Schneidman-Duhovny, D., Inbar, Y., Nussinov, R., and Wolfson, H. J. (2005) *Nucleic Acids Res.* **33,** W363–W367
48. Khalili-Araghi, F., Jogini, V., Yarov-Yarovoy, V., Tajkhorshid, E., Roux, B., and Schulten, K. (2010) *Biophys. J.* **98,** 2189–2198
49. Smith-Maxwell, C. J., Ledwell, J. L., and Aldrich, R. W. (1998) *J. Gen. Physiol.* **111,** 421–439
50. Kanevsky, M., and Aldrich, R. W. (1999) *J. Gen. Physiol.* **114,** 215–242
51. Shao, X. M., and Papazian, D. M. (1993) *Neuron* **11,** 343–352
52. Holmgren, M., Jurman, M. E., and Yellen, G. (1996) *J. Gen. Physiol.* **108,** 195–206
53. Armstrong, C. M., and Loboda, A. (2001) *Biophys. J.* **81,** 895–904
54. Claydon, T. W., Vaid, M., Rezazadeh, S., Kehl, S. J., and Fedida, D. (2007) *J. Pharmacol. Exp. Ther.* **320,** 162–172
55. Pathak, M., Kurtz, L., Tombola, F., and Isacoff, E. (2005) *J. Gen. Physiol.* **125,** 57–69
56. Yang, Y., Yan, Y., and Sigworth, F. J. (2004) *J. Gen. Physiol.* **124,** 163–171
57. Swartz, K. J., and MacKinnon, R. (1997) *Neuron* **18,** 665–673
58. Lee, H. C., Wang, J. M., and Swartz, K. J. (2003) *Neuron* **40,** 527–536
59. Phillips, L. R., Milescu, M., Li-Smerin, Y., Mindell, J. A., Kim, J. I., and Swartz, K. J. (2005) *Nature* **436,** 857–860
60. Sukhareva, M., Hackos, D. H., and Swartz, K. J. (2003) *J. Gen. Physiol.* **122,** 541–556
61. Muroi, Y., and Chanda, B. (2009) *J. Gen. Physiol.* **133,** 1–15
62. Sack, J. T., and Aldrich, R. W. (2006) *J. Gen. Physiol.* **128,** 119–132
63. Shieh, C. C., Klemic, K. G., and Kirsch, G. E. (1997) *J. Gen. Physiol.* **109,** 767–778
64. Klemic, K. G., Shieh, C. C., Kirsch, G. E., and Jones, S. W. (1998) *Biophys. J.* **74,** 1779–1789
65. Bezanilla, F., Perozo, E., and Stefani, E. (1994) *Biophys. J.* **66,** 1011–1021
66. Sigg, D., Bezanilla, F., and Stefani, E. (1994) *Biophys. J.* **66,** 439
67. MacKinnon, R., Cohen, S. L., Kuo, A., Lee, A., and Chait, B. T. (1998) *Science* **280,** 106–109
68. Magidovich, E., and Yifrach, O. (2004) *Biochemistry* **43,** 13242–13247
69. Alabi, A. A., Bahamonde, M. I., Jung, H. J., Kim, J. I., and Swartz, K. J. (2007) *Nature* **450,** 370–375
70. Li-Smerin, Y., Hackos, D. H., and Swartz, K. J. (2000) *J. Gen. Physiol.* **115,** 33–50
71. Tao, X., and MacKinnon, R. (2008) *J. Mol. Biol.* **382,** 24–33
72. Labro, A. J., Raes, A. L., Grottesi, A., Van Hoorick, D., Sansom, M. S., and Snyders, D. J. (2008) *J. Gen. Physiol.* **132,** 667–680

Properties of the Inner Pore Region of TRPV1 Channels Revealed by Block with Quaternary Ammoniums

Andrés Jara-Oseguera,[1] Itzel Llorente,[2] Tamara Rosenbaum,[2] and León D. Islas[1]

[1]Departamento de Fisiología, Facultad de Medicina, and [2]Departamento de Biofísica, Instituto de Fisiología Celular, Universidad Nacional Autónoma de México, D.F., 04510, México

The transient receptor potential vanilloid 1 (TRPV1) nonselective cationic channel is a polymodal receptor that activates in response to a wide variety of stimuli. To date, little structural information about this channel is available. Here, we used quaternary ammonium ions (QAs) of different sizes in an effort to gain some insight into the nature and dimensions of the pore of TRPV1. We found that all four QAs used, tetraethylammonium (TEA), tetrapropylammonium (TPrA), tetrabutylammonium, and tetrapentylammonium, block the TRPV1 channel from the intracellular face of the channel in a voltage-dependent manner, and that block by these molecules occurs with different kinetics, with the bigger molecules becoming slower blockers. We also found that TPrA and the larger QAs can only block the channel in the open state, and that they interfere with the channel's activation gate upon closing, which is observed as a slowing of tail current kinetics. TEA does not interfere with the activation gate, indicating that this molecule can reside in its blocking site even when the channel is closed. The dependence of the rate constants on the size of the blocker suggests a size of around 10 Å for the inner pore of TRPV1 channels.

The Journal of General Physiology

INTRODUCTION

The transient receptor potential vanilloid 1 (TRPV1) channel is a nonselective cation channel primarily expressed in sensory C and Aδ fibers and in neurons from the dorsal root and trigeminal ganglia (Szolcsanyi et al., 1990, 1991; Szallasi et al., 1993, 1995; Caterina et al., 1997; Szallasi and Blumberg, 1999). Being a polymodal receptor, TRPV1 is activated by diverse stimuli such as voltage (Piper et al., 1999; Gunthorpe et al., 2000), temperature (>43°C), protons (pH, <5.4) (Caterina et al., 1997; Tominaga et al., 1998), and several naturally occurring pungent compounds such as capsaicin from chili peppers (Caterina et al., 1997) and allicin from garlic (Macpherson et al., 2005; Salazar et al., 2008).

Accumulating evidence points to a role of the TRPV1 channel in inflammatory processes and the pain pathway, being one of the key signal transducers mediating inflammatory pain detection and hyperalgesia (Hwang et al., 2000; Premkumar and Ahern, 2000; Chuang et al., 2001; Tominaga et al., 2001; Bhave et al., 2002; Moriyama et al., 2003; Numazaki and Tominaga, 2004; Premkumar et al., 2004; Price et al., 2004; Zhang et al., 2005; Cortright et al., 2007; Szallasi et al., 2007).

Despite the numerous physiological processes in which this channel is involved, we currently have little knowledge of the structural characteristics and basic biophysical properties of TRPV1. The available information points to structural conservation between TRP channels and the voltage-dependent potassium channels in regard to overall channel topology and the general structure of the pore domain (Ferrer-Montiel et al., 2004; Voets et al., 2004; Tominaga and Tominaga, 2005; Owsianik et al., 2006). Several lines of evidence indicate that the functional TRPV1 channel is a tetramer with each subunit formed by six transmembrane segments with the pore domain formed by the S5, S6, and the loop between them (Kedei et al., 2001; Cheng et al., 2007). A recent study has provided information regarding the structure of the pore and indicated that it is formed by α-helices that might be forming a bundle crossing, as has been observed for voltage-activated K^+ channels (Susankova et al., 2007). Additionally, TRP channels possess multiion permeation properties, as do several potassium channels (Owsianik et al., 2006; Oseguera et al., 2007).

Mutagenesis experiments have revealed that several point mutations in the putative S5-S6 loop alter the permeation properties of the channel, in accordance with this region being the selectivity filter (Garcia-Martinez et al., 2000; Mohapatra et al., 2003).

Pore blocker molecules constitute a helpful tool in our understanding of the general architecture of the permeation pathway and the gating properties of ion channels. Quaternary ammonium ions (QAs), in particular, are a family of potassium channel blockers that have been successfully used in structure–function studies, providing

Correspondence to León D. Islas: islas@liceaga.facmed.unam.mx

Abbreviations used in this paper: QA, quaternary ammonium ion; TBA, tetrabutylammonium; TPA, tetrapentylammonium; TPrA, tetrapropylammonium; TRPV1, transient receptor potential vanilloid 1.

The Rockefeller University Press $30.00
J. Gen. Physiol. Vol. 132 No. 5 547–562
www.jgp.org/cgi/doi/10.1085/jgp.200810051

information about the properties and dimensions of the pore (French and Shoukimas, 1981, 1985; Guo and Lu, 2001), as well as the first description of an activation gate in a voltage-activated K^+ channel (Armstrong, 1971; Armstrong and Hille, 1972; Bezanilla and Armstrong, 1972).

Here, we showed that QA derivatives are also pore blockers of TRPV1 channels and performed experiments to probe their mechanism of action. We have previously reported that tetrabutylammonium (TBA) blocks open TRPV1 channels and interferes with closing of a gate (Oseguera et al., 2007). We extended this previous study and found that all QAs tested act as voltage-dependent pore blockers that can produce blockade in a manner that depends on the channel being in the open state. Channels that were blocked by tetrapropylammonium (TPrA), TBA, and tetrapentylammonium (TPA) showed considerable slowing of the closure kinetics, consistent with a state-dependent block mechanism and "foot-in-the-door"–like effects on closure as described for Kv channels. Even though TEA also blocks the channel, it does not interfere with the gating mechanism, suggesting that a TEA molecule can reside in its blocking site even when the channel is closed and that the channel pore is large enough to accommodate this small ion.

MATERIALS AND METHODS

Mammalian Cell Culture and Recording

Methods are similar to those described in Oseguera et al. (2007). Recordings were performed using HEK 293 cells expressing large T antigen. Cells were transfected with Lipofectamine (Invitrogen) according to the manufacturer's instructions. The rTRPV1-pCDNA3 plasmid (provided by D. Julius, University of California, San Francisco, San Francisco, CA) was cotransfected with pIRES-GFP (BD Biosciences) to fluorescently visualize transfected cells. Cells plated in coverslips were used for recording 1 d after transfection. Bath and pipette low divalent solutions consisted of 130 mM NaCl, 3 mM HEPES, pH 7.2, and 1 mM EDTA for Ca^{2+}-free conditions, unless otherwise indicated. 4 mM capsaicin (Sigma-Aldrich) stocks were prepared in ethanol and diluted to the desired concentrations in recording solution.

TEA, TPrA, and TPA were purchased from Sigma-Aldrich. TBA was obtained from Fluka. Stock solutions were prepared using the low divalent solution described above and diluted to their final concentrations in the presence of capsaicin. Intracellular solutions in inside-out patches were changed using an RSC-200 rapid solution changer (Biological).

Macroscopic and single-channel currents were low-pass filtered at 2.5 kHz and sampled at 10 kHz with an EPC 10 amplifier and acquired and analyzed with PULSE data acquisition software (HEKA Elektronik GMBH). For macroscopic current recordings, the following voltage protocol was used: Patches were held at 0 mV and given a prepulse of −120 mV for 30 ms. Voltage was then stepped from −150 to 150 mV in 10-mV increments for 100 ms and then stepped back to −120 mV for 30 ms. Steady-state current measurements were taken as the average of the last 30 ms of the test pulse. Channel closure kinetics were measured using a tail current protocol in which the voltage was stepped to −120 mV for 20 ms, and then to 60 mV for 100 ms followed by pulses starting from −220 to 0 mV in 20-mV steps for 100 ms. All tail current recordings are the average of three current traces to reduce noise. Pipettes for recording were pulled from borosilicate glass, covered in Q-Dope (GC Electronics), and had a resistance of 2–4 MΩ. All recordings were performed at room temperature (19°C). For leak subtraction, currents in the absence of capsaicin were subtracted from currents in the presence of capsaicin. This procedure does not influence the shape or size of currents because the voltage-activated TRPV1 currents in the absence of capsaicin at this temperature are negligible (the open probability at 100 mV is 0.01).

Data Analysis

Blocker dose–response relations were obtained from current measurements in the same patch using voltage steps from −120 to 100 mV in 20-mV increments for 200 ms, first in the absence and then in the presence of varying concentrations of blocker. The fraction of current blocked (F_B) was calculated as:

$$F_B = 1 - \frac{I}{I_o},$$

where I is the current in the presence of blocker and I_o is the current in the absence of blocker. For each QA, the apparent dissociation constant, K_D, was obtained at a given voltage by fitting F_B as a function of blocker concentration with the Hill equation:

$$F_B = \frac{[QA]^s}{K_D^s + [QA]^s}, \quad (1)$$

where s is the steepness factor and $[QA]$ is the quaternary ammonium concentration. The voltage dependence of K_D was obtained by plotting the value obtained from the Hill equation fit as a function of voltage.

Burst analysis was performed on single-channel openings in inside-out patches containing multiple channels recorded at low capsaicin concentrations using the same solutions as for macroscopic current recordings. A burst of openings was defined as in Oseguera et al. (2007), using the criterion of Colquhoun and Sakmann (1985). Event detection was performed with the 50% threshold crossing technique. Dwell times were logarithmically binned and exponential probability density functions were fitted with a maximum likelihood method (Sigworth and Sine, 1987; Colquhoun and Sigworth, 1995).

Determination of Blocking Rates Using the β Distribution

Block induced by TEA and TPrA is too fast to be resolved in single-channel recordings. To determine the rates of blocker association (on-rate) and dissociation (off-rate), we made use of the β distribution (Fitzhugh, 1983) to fit amplitude histograms from single-channel openings. As discussed by Yellen (1984), this method was analytically derived for a simple RC filter, but it can be used with modification for data filtered with a multi-pole Bessel filter. As a Gaussian filter is a good numerical approximation to a Bessel filter, we wanted to determine if this method could also be reliably applied to Gaussian-filtered data. A two-state process filtered by a single-pole filter has a probability density function given by:

$$f(y) = \frac{y^{a-1}(1-y)^{b-1}}{B(a,b)}, \quad (2)$$

with $a = \alpha\tau$, $b = \beta\tau$, and

$$B(a,b) = \int_0^1 y^{a-1}(1-y)^{b-1}dy.$$

In these equations, τ is the single-pole filter time constant, α is the blocker dissociation rate constant, β is the association rate

constant, and $B(a,b)$ is the β function, used as a normalization factor. We simulated a noiseless two-state Markov process with a Monte-Carlo algorithm and filtered the data at 2,500 Hz, which is the filter cutoff frequency used in our experiments. The simulation was performed with the two states, identified as blocked and open, having amplitudes of 0 and 1, respectively (Fig. 1 A). Data were simulated with rates α and β = 51,000 s^{-1}. The same data after Gaussian filtering and its corresponding amplitude distribution is shown in Fig. 1 (B and C). To fit Eq. 2 to the amplitude distribution, the single-pole filter time constant, τ, is corrected by a factor ε/f_c, where f_c is the Gaussian corner frequency. The term ε can be determined from fits of Eq. 2 to amplitude distributions derived from simulated data, by holding α and β = 51,000 s^{-1}. We determined a value for ε = 0.418 and thus $\tau = 0.418/f_c$. This value of τ provided the best fits to the amplitude distribution of simulated data over a wide range of values for α and β. All-points histograms collected from individual openings or bursts of openings were scaled in such a way that zero corresponds to the closed channel current level and one is the open-channel amplitude in the absence of blocker. The closed events were subtracted from the histograms to obtain only the open event distribution. Histograms were then normalized so that the area under the curve would be equal to one. To fit the amplitude histograms, β distributions were convolved with a Gaussian function that represents the added noise observed when the channel was fully closed. All data analysis was performed with programs written in Igor Pro (Wavemetrics Inc.).

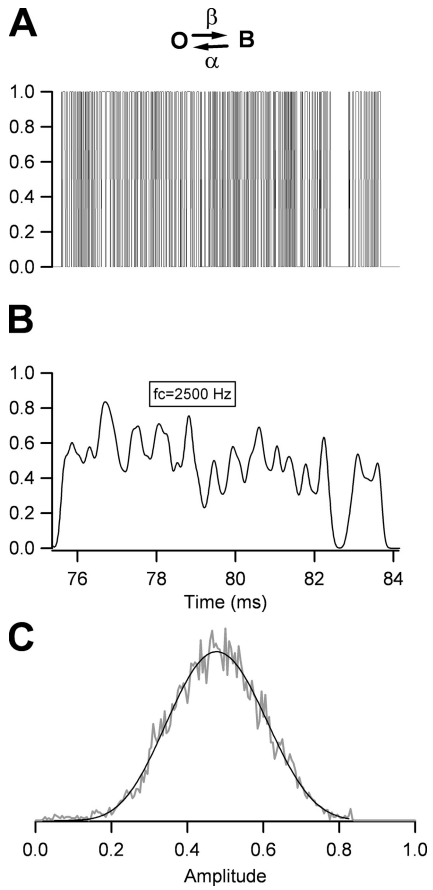

Figure 1. Analysis of a fast two-state process with amplitude histograms and the β distribution. (A) Monte-Carlo simulation of the process with blocking rate β and unblocking rate α = 51,000 s^{-1}. The simulation is set so that the amplitudes of the states in the scheme are O (open) = 1 and B (blocked) = 0. (B) The simulated data in A after filtering with a Gaussian filter with corner frequency, f_c, of 2500 Hz. The data becomes smeared and the amplitude is reduced. (C) Amplitude histogram compiled from all the points from the trace in B (gray trace). The black trace is the fit of the β distribution to the data (Eq. 2) with parameters β = 51,200 s^{-1}, α = 50,950 s^{-1}, and $\tau = 0.418/f_c$.

RESULTS

Quaternary Ammonium Block of TRPV1 Channels Is Voltage Dependent

Here, we have examined some fundamental properties of the effects of QAs on TRPV1 channels. We used TEA, TPrA, TBA, and TPA to determine how block of TRPV1 channels is affected by the different sizes of these QAs and to obtain information on the state dependence of block of TRPV1 channels by these compounds.

Intracellular application of all four QAs readily blocked currents through TRPV1. Fig. 2 A shows macroscopic TRPV1 currents activated by voltage pulses in the presence of saturating 4 μM capsaicin recorded from inside-out patches in the absence of blocker. The addition of QAs effectively induced current block (Fig. 2 B). Fig. 2 C shows the steady-state current to voltage relations obtained from the traces in A and B. The outward rectifying character of the TRPV1 channel can be clearly seen and block seems to be voltage dependent, with QAs blocking with higher affinity at positive membrane potentials. The reversal potential lies near zero mV, as expected under isometric sodium conditions.

Fig. 3 A shows the dose-response curves for the various QAs obtained at 100 mV. Blockade was dose dependent with the apparent dissociation constant, K_D, decreasing with blocker size, indicating an increase in affinity. The steepness of the Hill equation used to fit the data is close to one, suggesting that only a molecule of blocker can bind to the channel at a time (Fig. 3 A). A plot of the apparent dissociation constant, K_D, versus voltage indicates that block is clearly voltage dependent; however, contrary to the expectation from a Woodhull-type model (Woodhull, 1973), the value of K_D for all blockers reaches an asymptotic value at positive potentials (Fig. 3, B and inset). This apparent relief of block has been explained in other types of ion channels by several different mechanisms, including a permeant blocker mechanism (Guo and Lu, 2000), diffusion limitation of the on-rate at positive voltages (Blaustein and Finkelstein, 1990b), and permeant–ion interactions with the blocker in the conduction pathway (Heginbotham and Kutluay, 2004). For TBA, we have previously shown that relief of block can be explained by the latter mechanism (Oseguera et al., 2007), and it is very likely that the same is true for the rest of QA blockers used here. At negative voltages, the K_D does behave as an exponential function of voltage, and we can estimate the valence of the blocking reaction

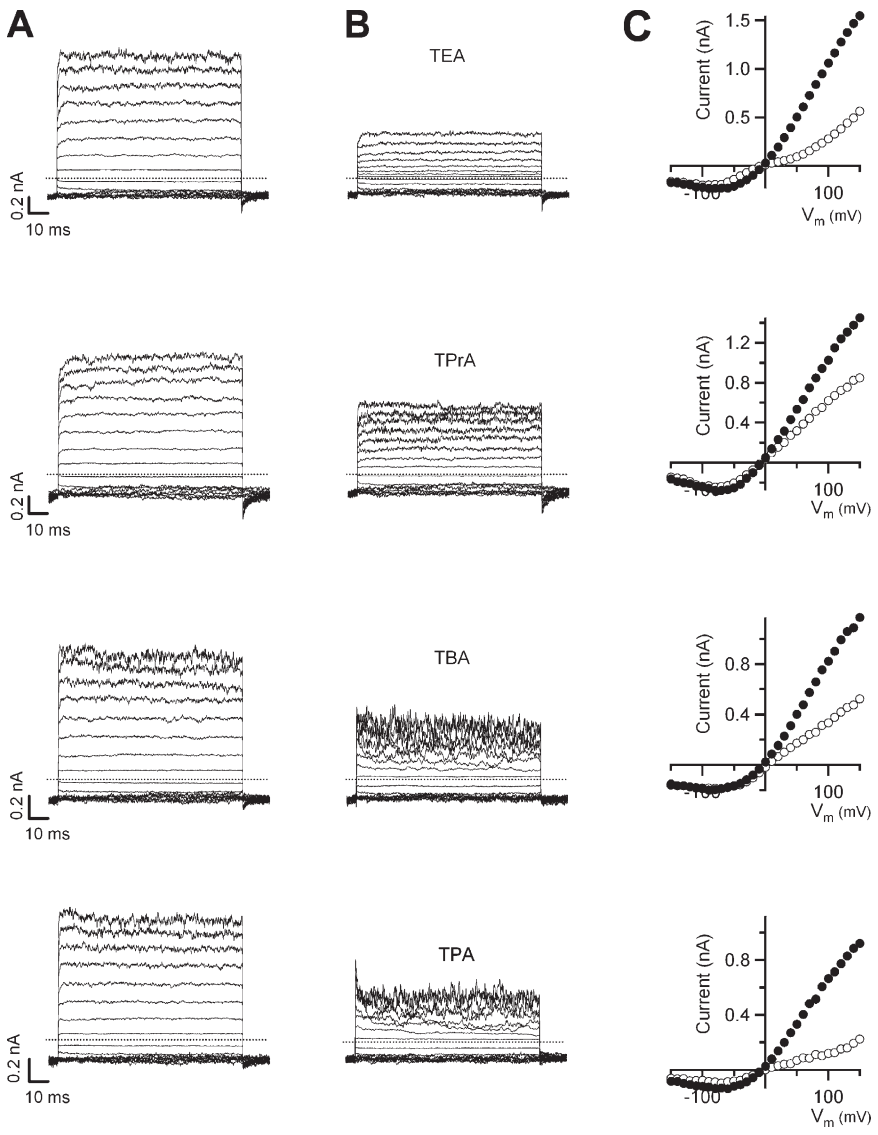

Figure 2. Block of TRPV1 currents by intracellular QAs. Current traces without blockers (A) and with blockers (B). The currents were elicited by stepping membrane voltage from a 0-mV holding potential to −120 mV, and then to various test potentials from −150 to 150 mV in 10-mV increments. For clarity, only the traces at every 20 mV are shown. All current traces in B were obtained after applying the corresponding QA to the patch in A and corrected for leak current in the absence of agonist. The blocker concentrations used are: 10 mM TEA, 0.9 mM TPrA, 250 µM TBA, and 40 µM TPA. The dotted lines identify the zero current levels. (C) Steady-state current to voltage relations obtained from the traces in A (closed symbols) and B (open symbols).

at voltages more negative than 0 mV by fitting Eq. 3 to the data:

$$K_D = K_D(0)\exp(-Z_{app}V/kT), \quad (3)$$

where $K_D(0)$ is the value of K_D at zero mV and Z_{app} is the apparent charge associated with the blocking reaction. These parameters are shown in Fig. 3 C for each blocker. Similar to observations in voltage-dependent potassium channels (Choi et al., 1993), the apparent affinity of the blocker increases with the size and hydrophobicity of the QA derivative (Fig. 3 C). It can also be appreciated that the voltage dependence of TEA, TPrA, and TBA, represented by the value of Z_{app} (Fig. 3 C), is higher than or near a value of one. A similar observation of high apparent valences of blockers in potassium-permeable channels has been shown to be due to the coupling of permeant ion movement with blocker occupancy (French and Shoukimas, 1985; Spassova and Lu, 1998), and we have shown previously that in the case of TBA, a large fraction of this voltage dependence is due to movement of Na^+ ions in the selectivity filter of the TRPV1 channel, which is coupled to blocker occupancy, and not due to the blocker traversing a large fraction of the transmembrane voltage (Oseguera et al., 2007).

Kinetics of Block by TEA

Block of TRPV1 by TEA is a very fast process. The individual blocking events are so short-lived that they are smeared by the filter and, as a result, block appears as an apparent reduction of the single-channel conductance. For this reason and to estimate the kinetic parameters of the blocking reaction, we used an approach to analyze the all-points amplitude histogram from bursts of openings, which makes use of the β distribution. As discussed in Materials and methods, we showed that this approximation can describe a two-state process filtered by a Gaussian filter with reasonable accuracy. Fig. 4 A shows

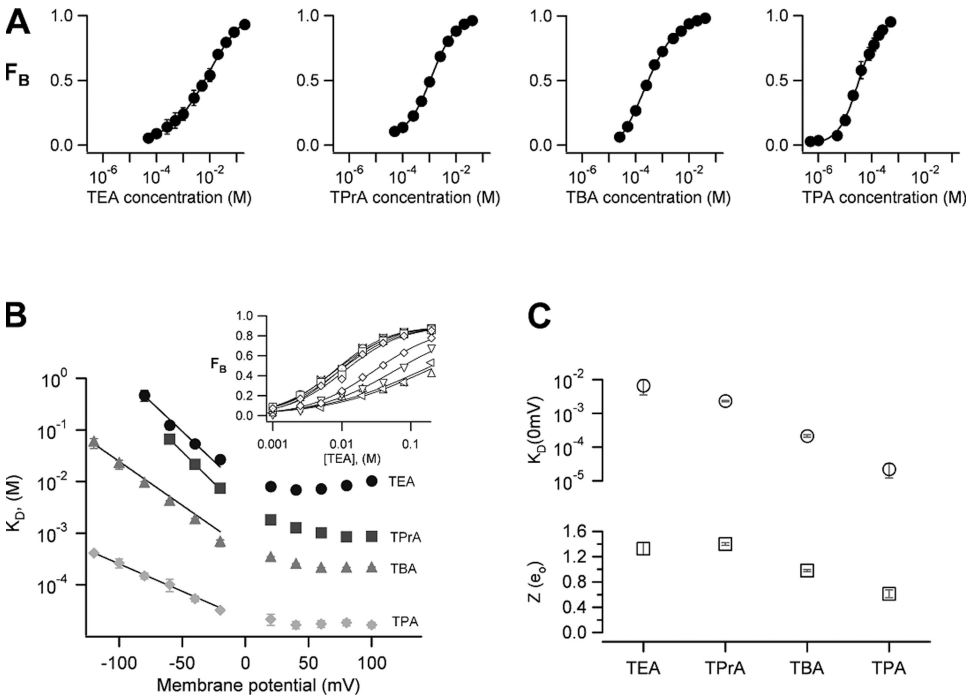

Figure 3. Voltage dependence and steady-state block at negative voltages. (A) Dose-response curves for the different QAs measured at a voltage of 100 mV. The solid lines represent fits to the Hill equation. The parameters are: TEA, $K_D = 8.7 \pm 0.7$ mM, $s = 0.77 \pm 0.08$ ($n = 5$); TPrA, $K_D = 940 \pm 60$ μM, $s = 0.79 \pm 0.04$ ($n = 6$); TBA, $K_D = 327 \pm 25$ μM, $s = 0.88 \pm 0.02$ ($n = 9$); TPA, $K_D = 36 \pm 8$ μM, $s = 1.15 \pm 0.12$ ($n = 3$). All recordings were performed in the presence of 4 μM capsaicin. (B) The apparent dissociation constant, K_D, derived from data as in A at different voltages. The inset shows a complete dataset for TEA for voltages from −80 to 100 mV. Voltage dependence of block was determined at negative voltages by fitting Eq. 3 to the data in B up to −20 mV. (C) The parameters obtained from the fit are plotted as a function of the size of the blocker. K_D at 0 mV (in units of M; top): TEA, $6.65 \times 10^{-3} \pm 3.10^{-3}$ ($n = 4$); TPrA, $2.31 \times 10^{-3} \pm 0.11 \times 10^{-3}$ ($n = 4$); TBA, $21.3 \times 10^{-5} \pm 1.7 \times 10^{-5}$ ($n = 6$); TPA, $2.2 \times 10^{-5} \pm 10^{-5}$ ($n = 5$). The values of Z (bottom) are (in units of e_o): TEA, 1.32 ± 0.097; TPrA, 1.4 ± 0.02; TBA, 0.98 ± 0.02; TPA, 0.61 ± 0.06. The affinity of the channel for the blockers increases with blocker size. Group data are presented as mean ± SEM.

representative single-channel openings in the absence and presence of increasing concentrations of TEA obtained at 60 mV. It is apparent that the effect of the blocker is a reduction of the single channel current. Fig. 4 B shows amplitude histograms for channel openings obtained from traces as in Fig. 4 A and constructed as indicated in Materials and methods. Superimposed on the histograms are fits to Eq. 2 convolved with a Gaussian function, which describes the current amplitude distribution of the closed level in the absence of blocker.

The β distribution provides an excellent description of the data, and blocker association and dissociation rates can be readily extracted. To obtain the pseudo first order on-rate constant, the rate obtained from the β distribution fit was plotted as a function of blocker concentration and the slope was used as an estimate of the association rate constant. The off-rate constant did not depend on the blocker concentration, and the dissociation rate constant was obtained as the zero intercept of the line fitted to the data (not depicted).

The voltage dependence of both the on- and off-rates is shown in Fig. 4 C. There are some striking features of these data. First, the on-rate constant is not a monotonic function of voltage. At voltages between −40 and 40 mV it increases exponentially with an equivalent valence of 0.94 e_o, but at more positive voltages it approaches a maximum asymptotic value. As the estimated on-rate is very fast, a possible explanation for this is that at voltages more positive than 60 mV, the rate is limited by diffusion of the blocker to its binding site, as has been shown to occur for block of Anthrax toxin channels by QAs and in BK channels by Na^+ (Yellen, 1984; Blaustein and Finkelstein, 1990a). A rough estimate of the expected diffusion-limited on-rate for a spherical blocker the size of TEA (8 Å diameter) and an absorbing disk of radius 6 Å, yields a value of 2.5×10^8 $M^{-1}s^{-1}$, which is more than an order of magnitude higher than the observed on-rate of 6.2×10^6 $M^{-1}s^{-1}$ at 100 mV. This result suggests that the plateauing on-rate is not due to diffusion limitation, and thus another mechanism should explain this observation, as will be shown for TPrA.

The other striking feature of the TEA kinetic data is that the off-rate increases with positive voltages. The off-rate cannot be estimated by the amplitude method at negative potentials because, due to the strong outward rectification of the single-channel I-V curve, currents at voltages more negative than −40 mV, even in the absence of blocker, are very small and difficult to separate from the recording noise. Nevertheless, given an overall voltage dependence of block at negative voltages of 1.5 e_o (Fig. 3) and the voltage dependence of the on-rate constant, we estimated that the off-rate constant should have a valence of ∼−0.5 e_o.

Both the saturation of the on-rate constant and the increase of the off-rate constant of TEA at positive voltages are responsible for the observed steady-state relief of block. These two observations seem counterintuitive, as the exit rate for a positively charged blocker is expected

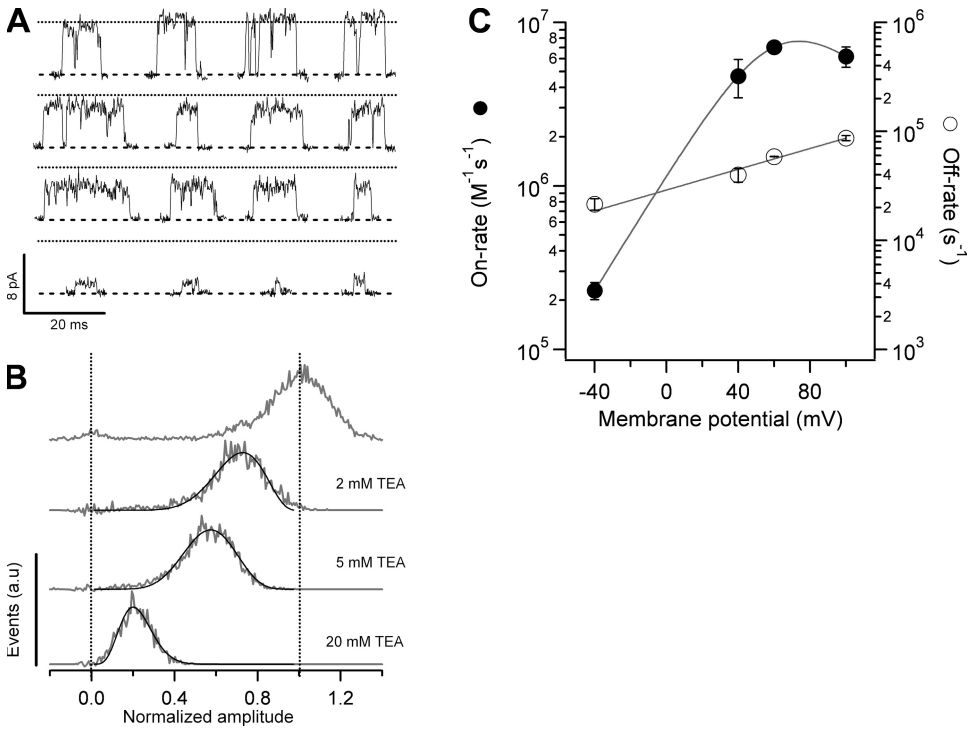

Figure 4. Kinetics of block by intracellular TEA determined with the β distribution. (A) Single-channel openings in the absence (top trace) and in the presence of 2, 5, and 20 mM TEA obtained at 60 mV. The apparent current amplitude decreases as the TEA concentration is increased, as predicted for a fast blocker. The dashed line represents the closed-channel current level, and the dotted line is the mean open-channel level in the absence of TEA. (B) Normalized amplitude histograms obtained from traces as in A. Solid lines are fits to the β distribution with the following parameters: 2 mM, β = 26,679 s^{-1}, α = 61,454 s^{-1}; 5 mM, β = 43,001 s^{-1}, α = 55,882 s^{-1}; 20 mM, β = 156,370 s^{-1}, α = 44,582 s^{-1}. (C) Blocking rate constants obtained from the fits to the β distribution as in B from three separate patches at several voltages and blocker concentrations. The on-rate, k_{on}, increases with voltage and reaches a plateau. The solid line is a fit to a double exponential function reflecting both the voltage dependence of the on-rate and of the relief of block and has the form

$$k_{on} = \frac{1}{k_{ac}(0)\exp z_{ac}V/kT} + \frac{1}{k_{rel}(0)\exp z_{rel}V/kT}.$$

The values of the fit parameters are: $k_{ac}(0) = 1.171 \times 10^6\ M^{-1}s^{-1}$; $z_{ac} = 1.0193$; $k_{rel}(0) = 4.722 \times 10^7\ M^{-1}s^{-1}$; $z_{rel} = 0.48$. The off-rate decreases with increasing voltages but starts to increase at voltages more positive than 60 mV. The values of k_{on} and k_{off} at 0 mV were estimated from an exponential fit to the data between 240 and 60 mV, and the parameters of the fit are: $k_{on}(0) = 1.04 \times 10^6\ M^{-1}s^{-1}$; $z = 0.94\ e_o$; $k_{off}(0) = 28{,}950\ s^{-1}$; $z = 0.27\ e_o$. Group data are presented as mean ± SEM.

to increase at negative voltages and the entry rate to increase at positive potentials. We will come back to this point when we discuss block by TPrA.

Kinetics of Block by TPrA

Just as in the case of TEA, blockade by TPrA is exceedingly fast, and the individual blocking events are not well resolved at our recording bandwidth (Fig. 5). For this reason, we also applied the β distribution approach to estimate the rate constants of TPrA block of TRPV1. Fig. 5 A shows single-channel traces in the absence and presence of TPrA at the concentrations indicated in Fig. 5 B. All-point amplitude histograms derived from single-channel openings can be well described by the β distribution (Eq. 2), and on- and off-rate constants can be derived (Fig. 5, B and C). As with TEA, the on-rate constant for TPrA block saturates at positive potentials, and this happens at a value near $5 \times 10^6\ M^{-1}s^{-1}$, well below the estimated diffusion-limited on-rate of $1.7 \times 10^8\ M^{-1}s^{-1}$ for TPrA (9 Å diameter), which was calculated as for TEA. The voltage dependence of the on-rate constant is exponential at voltages below 40 mV, with a valence of 0.7 e_o. In this same range of voltages, the off-rate constant increases with hyperpolarization with a valence of −0.19 e_o, but, as for TEA block, the off-rate constant also increases at voltages more positive than 40 mV, instead of monotonically decreasing, and this behavior accounts for the marked relief of block at positive potentials that is also observed with TPrA.

Ion Interactions and TPrA Blocker Kinetics

What is the origin of the saturation of the on-rate constant for TEA and TPrA? Given the observation that saturation occurs at rates below the expected diffusion-limited rate, we sought to investigate which other mechanism may be responsible for this effect. As mentioned earlier, we have observed that the voltage dependence of TBA blockade of TRPV1 channels can be explained by the coupled movement of permeant ions and blocker occupancy (Oseguera et al., 2007). This led us to suspect that a similar mechanism may be at work for TPrA and may be responsible for the voltage dependence of the k_{on} at positive voltages. It has been observed that the coupling between permeant ions and the blocker

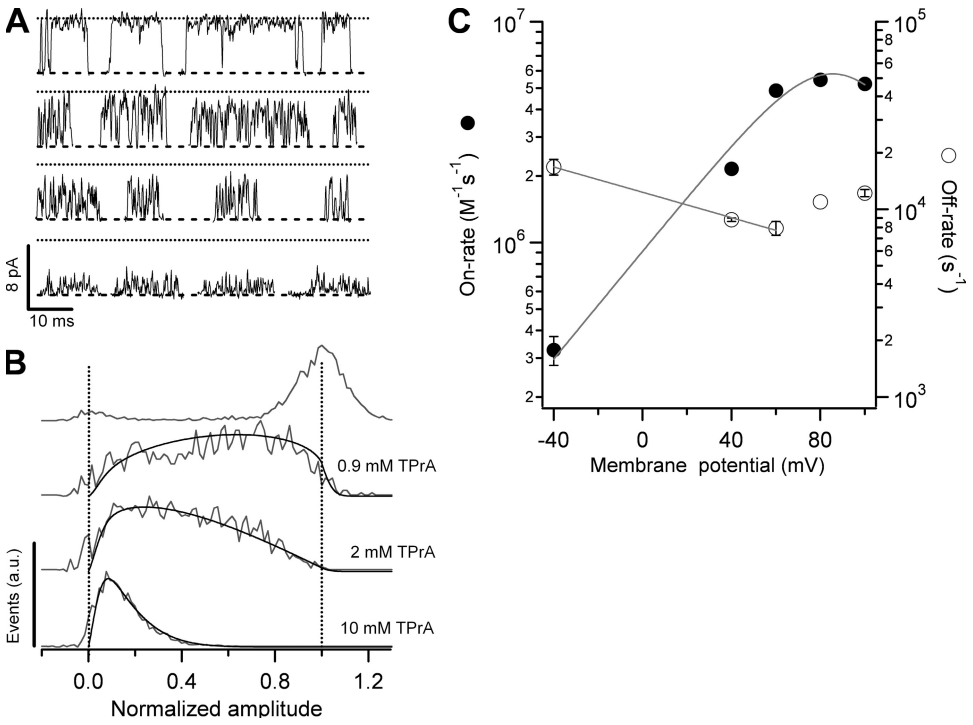

Figure 5. Kinetics of TPrA block. (A) Single-channel openings in the absence (top-most trace) and presence of 0.9, 2, and 10 mM TPrA obtained at 60 mV. The current amplitude decreases as the TPrA concentration is increased, as expected for a fast blocker. The dashed line represents the closed-channel current level, and the dotted line is the mean open-channel level in the absence of TPrA. (B) Normalized amplitude histograms obtained from traces as in A. Solid lines are fits to the β distribution with parameters: 0.9 mM, β = 8,571.7 s^{-1}, α = 7,315.9 s^{-1}; 2 mM, β = 8,563 s^{-1}, α = 12,193 s^{-1}; 10 mM, β = 11,198 s^{-1}, α = 49,061 s^{-1}. (C) Blocking rate constants obtained from the fits to the β distribution as in B in three different patches at several voltages and blocker concentrations. The on-rate increases with voltage and reaches a plateau. The off-rate decreases with increasing voltages but starts to increase at voltages more positive than 60 mV. The solid line is a fit to a double exponential as in Fig. 4. The values of k_{on} and k_{off} at 0 mV were estimated from an exponential fit to the data between −40 and 60 mV, and the parameters of the fit are: $k_{on}(0) = 8.6 \times 10^5$ M^{-1} s^{-1}; z = 0.69 e_o; $k_{off}(0) = 1.23 \times 10^4$ s^{-1}; z = −0.19 e_o. Group data are presented as mean ± SEM.

occurs partially due to electrostatic interactions (Spassova and Lu, 1998). In our experimental conditions, we expect that repulsion of Na^+ by TPrA into the selectivity filter may cause the charge displacement that is manifested as a large valence of the on-rate constant; at the same time, this electrostatic repulsion between the Na^+ ion and TPrA molecule will tend to reduce the entry rate of TPrA to its blocking site and may be responsible for the observed saturation of the on-rate. To test this hypothesis, we performed measurements of the on-rate of TPrA under conditions of reduced extracellular Na^+ concentration. We hypothesized that this maneuver would have the effect of reducing Na^+ occupancy of the pore, causing a reduction of the possible interactions between the permeant ions and TPrA.

The data in Fig. 6 shows that, as expected, blockade of TRPV1 by TPrA is more effective in the low extracellular Na^+ (10 mM; Fig. 6 B) experiments than in the isometric (130 mM) Na^+ concentration experiments (Fig. 6 A), as indicated by the larger reduction of current amplitude produced by TPrA under low extracellular sodium conditions. This reduced current amplitude translates into larger values for the on-rate constant. In addition, the on-rate constant no longer saturates at positive voltages and behaves as an exponential function of voltage for the entire range of voltages tested. The corresponding valence of this exponential is 0.7 e_o (Fig. 6 C), which is the same as that measured at negative potentials under isometric 130 mM Na^+ conditions.

These data support our hypothesis that the entry rate of TPrA is limited at positive voltages by its interaction with the permeant ion. This interaction with Na^+ also suggests that QA blockers bind to an intracellular site in the pore of TRPV1 channels, allowing us to use these molecules as probes for obtaining information about the pore properties of this channel protein.

Block Kinetics of Slower Blockers: TBA and TPA

It has been shown that the kinetics of TRPV1 block by TBA are sufficiently slow to be observed in macroscopic current recordings as an exponential relaxation of current during depolarizing pulses (Oseguera et al., 2007). We observed that TPA is also a slower blocker than TEA and TPrA. In single-channel recordings, TPA does not affect the single-channel conductance, and blocking events can be well resolved (Fig. 7 A). When dwell-time histograms are compiled, blockade is observed as an increase in the number of long-duration events in the closed-time histogram (Fig. 7 B). The voltage-dependent blocking kinetics of TPA can also be observed in macroscopic recordings as a current relaxation during positive voltage steps (Fig. 7 C). This relaxation can be fitted with an exponential function (Fig. 7 C, top). During repolarizing voltage pulses, the channel seems to no longer be able to deactivate and instead the tail current increases with a rate that is voltage dependent. This behavior of the tail current reflects the time course of TPA leaving its binding site in the channel, and an estimate

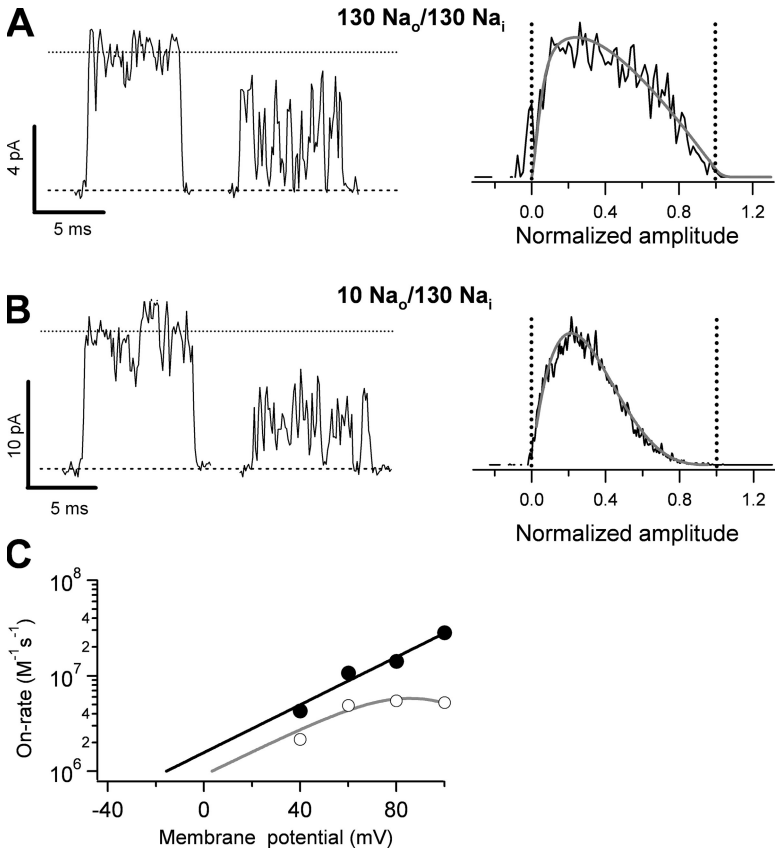

Figure 6. Kinetics of TPrA block depends on the extracellular sodium concentration. (A) Single-channel openings (left) in the absence of TPrA (left trace) and the presence of 2 mM TPrA (right trace) with isometric 130-mM NaCl solutions at 40 mV. The right panel depicts the normalized amplitude histogram from multiple traces as in the left panel. The β distribution fit yielded parameters of $\beta = 8{,}563.7\ s^{-1}$ and $\alpha = 10{,}971\ s^{-1}$. (B) Single-channel openings (left) in the absence of TPrA (left trace) and the presence of 2 mM TPrA (right trace) with 10 mM NaCl in the extracellular and 130 mM in the intracellular solution at 40 mV. The right panel shows the normalized amplitude histogram with the β distribution fit superimposed. The parameters of the fit are: $\beta = 26{,}919\ s^{-1}$, $\alpha = 11{,}661\ s^{-1}$. The amplitude histogram under low extracellular sodium conditions is left-shifted, indicating faster blocker kinetics under these conditions. (C) On-rates obtained from fits of the β distribution to histograms as in B under low sodium conditions, obtained from two different patches (filled circles). The black line is a fit to an exponential of the form:

$$k_{on}(V) = k_{on}(0)\exp(z_{on}V/kT).$$

The values of the fit parameters are: $k_{on}(0) = 1.57 \times 10^6\ M^{-1}\ s^{-1}$; $z_{on} = 0.72\ e_o$. The gray line corresponds to the fit to the on-rate under isometric 130 mM NaCl conditions in Fig. 5 C (open circles). Error bars are smaller than the symbols. The data indicate that the relief of block observed as a plateau for the on-rate at more positive potentials is a result of interactions between the blocker and the Na^+ ions in the selectivity filter, and not due to diffusion limitation. Group data are presented as mean ± SEM.

of this rate can be obtained from the inverse of the time constant of an exponential function fitted to the tail current relaxation (Fig. 7 C, bottom). The summarized data for on- and off-rate constants of block by TPA, obtained from macroscopic current recordings, is presented in Fig. 7 D. Both rates are exponential functions of voltage.

Table I summarizes the results of kinetic analysis for all four blockers. The main observation is that as the size of the blocker increases, so does its apparent affinity. When one compares the smaller blocker, TEA, to the bigger one, TPA, it is observed that the increase in apparent affinity as a function of blocker size is accomplished by a >1,000-fold decrease in the off-rate and only a 10-fold decrease in the on-rate constant.

Closure Kinetics in the Presence of Blockers

The kinetics of channel closure in the presence of a blocker molecule can reflect some aspects of the nature of the gating mechanism. It has been shown that if the blocker is able to only reach its binding site when the channel is open, the time course of channel closure should be slowed down because the blocker needs to leave the open channel before the activation gate can close (Armstrong, 1971; Choi et al., 1993; Li and Aldrich, 2004). To understand the relationship between blocker

TABLE I

Summary of Kinetic Parameters for QA Block of TRPV1[a]

Blocker	Association rate constant k_{on}(0 mV), ($M^{-1}s^{-1}$)	Dissociation rate constant k_{off} (0 mV), (s^{-1})	z_{on} (e_o)	z_{off} (e_o)
TEA ($n = 3$)	$1.04 \times 10^6 \pm 4.8 \times 10^5$	$2.89 \times 10^4 \pm 3.2 \times 10^3$	0.94 ± 0.13	0.27 ± 0.03
TPrA ($n = 3$)	$8.59 \times 10^5 \pm 1.5 \times 10^5$	$1.23 \times 10^4 \pm 186$	0.69 ± 0.14	−0.19 ± 0.01
TBA ($n = 6$)	$2.5 \times 10^5 \pm 2.9 \times 10^4$	83.76 ± 10	0.93 ± 0.03	−0.63 ± 0.03
TPA ($n = 5$)	$1.03 \times 10^5 \pm 4 \times 10^4$	10.73 ± 0.95	0.68 ± 0.06	−0.45 ± 0.02

The table summarizes the on- and off-rates for the four blockers used in this study and their associated valence.
[a]Data are mean ± SEM.

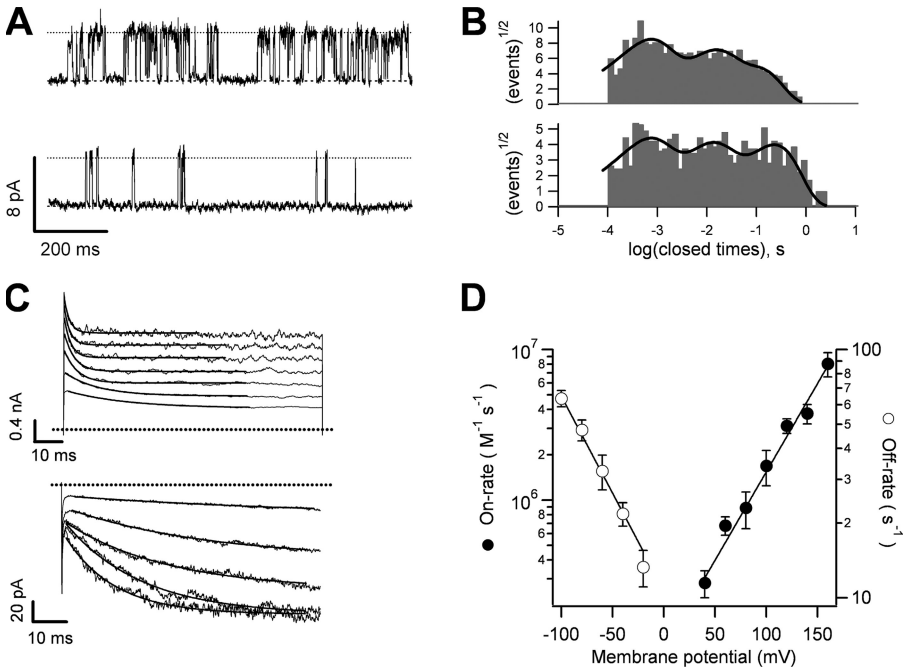

Figure 7. Kinetics of block by TPA. (A) Single-channel traces in the absence (top trace) and presence of 80 μM TPA (bottom trace). (B) Closed time histograms from multiple traces as in A fitted with three exponential components. (C; top) Macroscopic kinetics of block during depolarizing voltage pulses ranging from 40 to 160 mV in the presence of 40 μM TPA. The onset of block can be seen as an exponential decay of the initial current, as expected for a slower blocker. (Bottom) Blocker dissociation observed during tail current experiments. Traces were obtained in the presence of 80 μM TPA at −20, −40, −60, −80, and −100 mV. Blocker dissociation can be seen as an exponential increase in the current. The off-rates were obtained from fits to an exponential (solid lines). (D) The on- and off-rates obtained from traces as in C, plotted as a function of voltage. Both rates are voltage dependent and have the following values estimated from an exponential fit to the data: $k_{off}(0\ mV) = 10.73\ s^{-1}$ ($n = 3$); $z_{off} = 0.45\ e_o$; $k_{on}(0\ mV) = 1.03 \times 10^5\ M^{-1}s^{-1}$ ($n = 5$); $z_{on} = 0.68\ e_o$. Group data are presented as mean ± SEM.

occupancy and gating, we examined channel closure kinetics with tail current protocols, both in unblocked channels and when channels were blocked by the fast blockers, TEA and TPrA, and by the slow blockers, TBA and TPA. The voltage dependence of deactivation of TRPV1 channels is small (z_{-1}, ~0.1 e_o; Figs. 8 B and 9, D and E) when compared with Kv channels, and as a result the channels cannot be completely closed upon repolarization to the voltages we used; nevertheless, tail currents can be reliably recorded at negative voltages.

Block of TRPV1 channels by TEA is more voltage dependent than that produced by the other blockers used in this study, and when this blocker is applied to inside-out patches, tail currents were in fact accelerated, as if TEA made closing easier. The magnitude of the tail current in the presence of TEA is decreased, reflecting steady-state block at the depolarizing prepulse. Tail currents in the absence and presence of blocker could be fitted to an exponential time course (Fig. 8 A). A plot of the inverse of the time constant of this exponential as a function of voltage reveals a weak voltage dependence for channel closure. In the absence of TEA, the channels close with a rate at 0 mV of 196 s^{-1} and a valence of 0.07 e_o, a rather modest voltage dependence. When TEA is present, the closing rate increases up to approximately threefold at 80 mM TEA over all voltages, indicating that channel closure is in fact faster when the channel is blocked by TEA (Fig. 8 B).

This observation can be explained by a model in which the channels are able to close with TEA in the pore or, alternatively, by assuming that TEA can gain access to channels in the closed state. In both cases, one expects an acceleration of the closing rate because the closed blocked states provide a second closing pathway. Another indication that TEA may remain in its binding site when the channel is closed is provided by the observation that the duration of bursts of openings is shorter in the presence of TEA (Fig. 8, C and D). The shortening of burst lengths can again be explained by considering a mechanism that allows occupation of closed states by TEA.

The blocking behavior of TPrA differs from that of TEA. Tail currents of TRPV1 in the presence of TPrA show significant differences in time course when compared with currents in the absence of blocker. Tails were significantly slower in the presence of the blocker (Fig. 9 A). Moreover, tail currents in the presence of TPrA develop a characteristic "hook" indicative of the blocker having to exit the channel before it can close, as has been described in Na and Kv channels (Yeh and Narahashi, 1977; Clay, 1995).

Tail current kinetics behaves in a similar fashion when TBA is present. That is, a significant slowing of closure is obtained and there is a marked appearance of hooks in the tail currents (Fig. 9 B).

Because tail current experiments with TPrA and TBA are consistent with a "foot-in-the-door" mechanism, quantitation of the slowing of tail currents by these blockers was performed in the framework of this mechanism as follows: After a depolarizing step in the presence of a blocker, the channels are mostly in an open but blocked state.

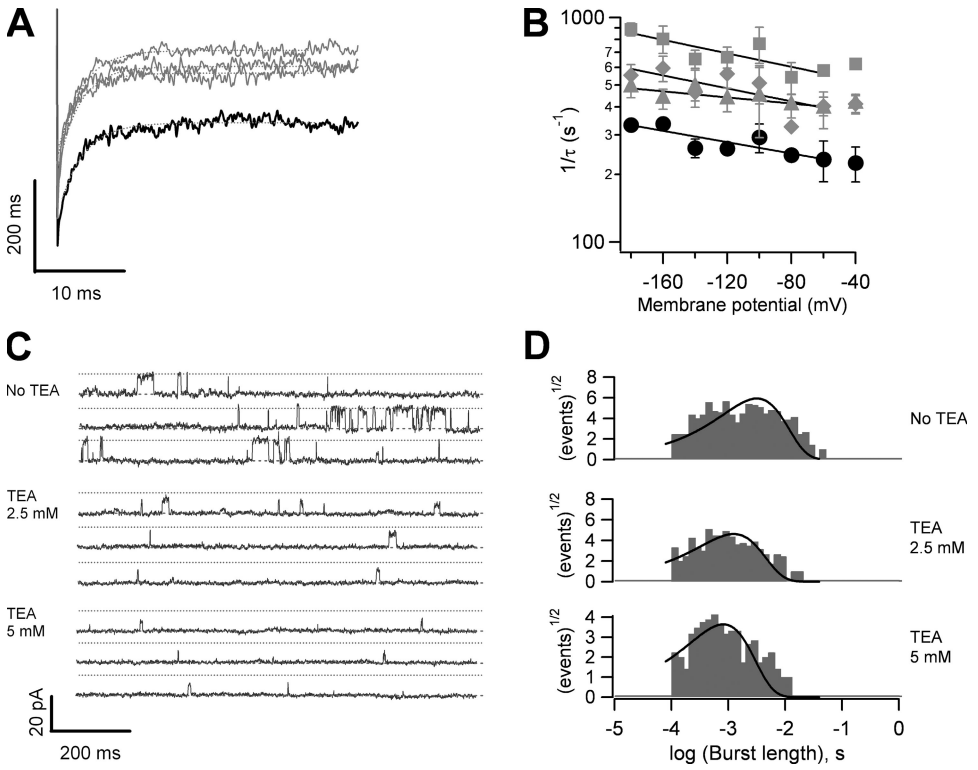

Figure 8. Channel-closing kinetics in the presence of TEA. (A) Representative tail currents obtained at −180 mV after a prepulse of 100 ms at 60 mV in the absence (thick trace) or presence of 20, 40, and 80 mM TEA (gray traces). Dotted lines are fits to a single exponential function. (B) Channel-closing rate as a function of voltage obtained from fits to an exponential as in A. The straight lines are fits to the equation:

$$k_1(V) = k_1(0)\exp(z_1 V/kT).$$

Symbols and parameters of the fit are (n = 4): No TEA $k_1(0)$ = 196.49 s^{-1}, z_1 = 0.073 e_o (filled circles); 20 mM TEA $k_1(0)$ = 364.9 s^{-1}, z_1 = 0.04 e_o (filled triangles); 40 mM TEA $k_1(0)$ = 323.9 s^{-1}, z_1 = 0.083 e_o (filled diamonds); 80 mM TEA $k_1(0)$ = 457.2 s^{-1}, z_1 = 0.086 e_o (filled squares). The closing rate increases with blocker concentration, indicating that TEA speeds up channel closure. (C) Representative traces of single-channel openings in the absence or the presence of the indicated concentration of TEA. The dotted lines indicate the current amplitude in the absence of TEA. (D) Burst length distributions obtained from traces as in C. Burst length was measured and compiled in logarithmically binned histograms in the absence or presence of TEA. The black lines are fits with a single exponential function of time with the following time constants: No TEA, 3.17 ms; 2.5 mM TEA, 1.2 ms; 5 mM TEA, 0.8 ms.

During hyperpolarization, the blocker will first leave the channel with rate k_{off} and then channel closure occurs, with rate k_{-1}, according to Scheme 1.

$$C \xleftarrow{k_{-1}} O \underset{k_{off}}{\overset{[B]k_{on}}{\rightleftharpoons}} OB \qquad \text{(SCHEME 1)}$$

At negative voltages the blocking rate ($[B]k_{on}$) and the reopening rate are small, and thus the time course of the occupancy of the open state is approximately given by:

$$I_{tail}(t) = \frac{k_{off}}{k_{-1} - k_{off}}\left(\exp^{k_{-1}t} - \exp^{-k_{off}t}\right). \qquad (4)$$

The tail currents are proportional to the probability of being in state O, so tail currents were fitted to Eq. 4, and k_{-1} was plotted as a function of voltage to serve as an index of the channel's closing rate. This was compared with the closing rate in the absence of blockers. Fig. 9 compares the voltage dependence of the apparent closing rate (k_{-1}) as the concentrations of TPrA and TBA are increased. We observed that these two blockers behave in similar fashion and markedly slow the closing rate of TRPV1 channels (Fig. 9, D and E).

When TPA is used, the off-rate of the blocker is so slow that the channels close much more slowly than the duration of the hyperpolarizing pulse and, as explained earlier (Fig. 7), only a slow increase in current that is produced by the slow exit of TPA from the channel can be observed (Fig. 9 C). Nevertheless, the results of tail current experiments with TPrA, TBA, and TPA suggest that these blockers occupy a binding site accessible through the intracellular mouth of the channel pore and that these molecules occupy the open state and leave the binding site before channel closure can occur, that is, the blocker acts as a foot in the door (Scheme 1). Mechanistically, these observations of the effects of TPrA, TBA, and TPA on tail current kinetics are consistent with an open-state block mechanism, and suggest that these blockers gain access to a binding site located after a cytoplasmic gate, as has been observed in voltage-dependent potassium channels (Armstrong, 1971; Choi et al., 1993; Li and Aldrich, 2004).

DISCUSSION

The results presented here indicate that the quaternary ammoniums TPrA, TEA, TBA, and TPA interact with TRPV1 channels through different mechanisms, depending on the size of the blocker. Similar to what happens

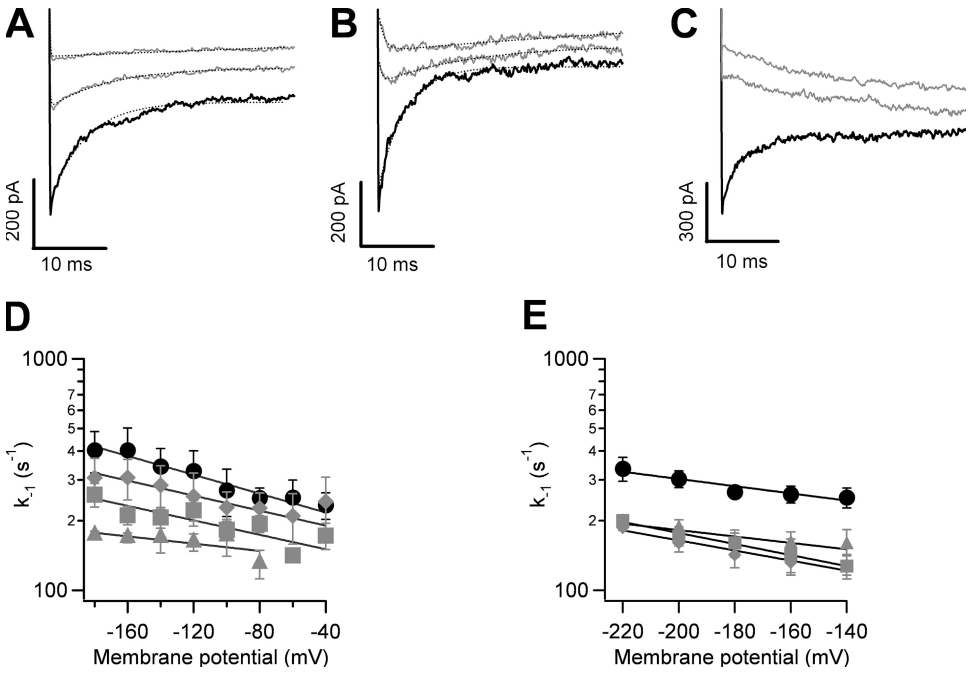

Figure 9. Channel-closing kinetics in the presence of TPrA, TBA, and TPA. (A) Representative traces obtained in the absence (black trace) or presence (gray traces) of 2 and 10 mM TPrA at −100 mV. Tail current kinetics is altered by the presence of the blocker. Channel closure is slowed and the tail currents now display a hook, characteristic of a blocker that interferes with the channel's activation gate. The dotted line represents fits to Eq. 4. (B) Tail currents obtained in the absence (black trace) or presence (gray traces) of 250 µM and 2.5 mM TBA at a voltage of −100 mV. The same behavior as for TPrA is observed, with slowing of the tail currents and the appearance of a hook at the beginning of the repolarization. Dotted lines are fits to Eq. 4. (C) Tail currents obtained in the absence (black trace) and presence (gray trace) of 250 and 500 µM TPA at −100 mV. Channel closure kinetics is slower in the presence of TPA than in its absence, just as for TPrA and TBA. (D) The rate k_{-1} from fits of Eq. 4 to data as in A was plotted against voltage as an index of the channel's closing rate. The straight lines are fits of equation:

$$k_{-1} = k_{-1}(0)\exp(-z_{-1}V/kT).$$

The symbols and parameters of the fit are ($n = 5$): No TPrA, $k_{-1}(0) = 179.86\ s^{-1}$, $z_{-1} = 0.12\ e_o$ (solid circles); 900 µM TPrA, $k_{-1}(0) = 164.1\ s^{-1}$, $z_{-1} = 0.093\ e_o$ (solid diamonds); 2 mM TPrA, $k_{-1}(0) = 130.3\ s^{-1}$, $z_{-1} = 0.09\ e_o$ (solid squares); 10 mM TPrA, $k_{-1}(0) = 128.02\ s^{-1}$, $z_{-1} = 0.045\ e_o$ (solid triangles). (E) As with TPrA, k_{-1} is plotted as an index of the closing rate as a function of voltage in the presence of TBA. The fit parameters and symbols are ($n = 4$): No TBA, $k_{-1}(0) = 148.01\ s^{-1}$, $z_{-1} = 0.09\ e_o$ (solid circles); 250 µM TBA, $k_{-1}(0) = 96.4$, $z_{-1} = 0.08\ e_o$ (solid diamonds); 500 µM TBA, $k_{-1}(0) = 51.2$, $z_{-1} = 0.16\ e_o$ (solid squares); 2.5 mM TBA, $k_{-1}(0) = 60.2$, $z_{-1} = 0.13\ e_o$ (solid triangles). Group data are presented as mean ± SEM.

in potassium-selective channels, an increase of the size of the blocker and its hydrophobic character produces a corresponding increase in the affinity of the blocker for the channel. In the case of *Shaker* potassium channels, it has been shown that the affinities of Q_n-TEA blockers increase with size in a manner that is consistent with the expectation that each methylene group should add 1.2 RT units to the absolute value of the apparent binding energy of the blocker (Choi et al., 1993). A similar analysis of our data shows that this energy is larger, in the order of 2 RT. This value is remarkably close to what is expected from the energy of hydration of the blocker molecules using the Born theory of ion solvation (Hille, 2001). This similarity probably arises from the fact that hydrophobic interactions are the main determinants of the interaction of the blockers with the channel pore. Our experiments show that the kinetic reason for the increase in apparent affinity with increasing blocker size is mainly the result of a decrease in the rate at which the blocker leaves the channel, with the smaller size blockers TEA and TPrA having dissociation rates at 0 mV in the order of 10^5 and $10^4\ s^{-1}$, respectively, whereas TBA and TPA have dissociation rates of 84 and $10\ s^{-1}$, respectively.

Voltage Dependence of Block

All four blockers produce a blockade that is clearly voltage dependent, although they show some differences from the block they induce in other voltage-gated channels. The main difference is the presence of reduced block at positive voltages, which may be explained by a permeant blocker mechanism. A recent paper (Chung et al., 2008) suggests that the permeability of TRPV1 to large cations is increased upon prolonged activation by capsaicin and modulation by PKC, and this is manifested as a time-dependent shift of the reversal potential when Na^+ is only present in the inside and a large cation is in the outside of the membrane. We have not observed shifts of reversal potential in the presence of large concentrations of intracellular blockers, nor changes in the single-channel current size through the duration of the experiment. We suspect that our recording conditions are sufficiently different to explain these observations. In our experiments, Na^+ ions are always present in both the intracellular and extracellular media. Of course, there may still be a fraction of current carried by the blockers, which may contribute to relief of block, but it is too small to be measured as a shift in reversal potential in our experiments.

Kinetics of Block by Small Blockers

To be able to measure the kinetics of the fast blockers TEA and TPrA, we have applied an analysis method that has been shown to work well with similarly fast blockers in BK channels, Ca^{2+} channels, and Na^+ channels (Yellen, 1984; Franco et al., 1991; Winegar et al., 1991; Kimbrough and Gingrich, 2000). To use this method, we had to address two fundamental issues: First, this method was previously applied to Bessel-filtered data, whereas our data were filtered with a Gaussian filter. The validation method we used was to numerically simulate a random two-state process, which is then filtered by a Gaussian filter. We sought to determine if the β distribution can provide a good estimate of the rate constants used to simulate the data. This approach was able to determine rate constants with an error of <1%. The second issue had to do with the validity of considering the blockade observed here a two-state process, where the blocked state has a nominally zero conductance. The evidence we have for this is that at elevated TEA and TPrA concentrations there is no residual current flowing though TRPV1 channels. This is also true when we examined the slower blockers, TBA and TPA, at the single-channel level. Here, the blocking events can readily be observed and the blocker produces a blocked state with conductance indistinguishable from that of the closed-channel noise level.

A very interesting observation is the fact that the blocker association rates (on-rates) for TEA and TPrA are so fast that blockade is manifested as a reduction of the single-channel current. Fast blocker kinetics indicates that there is a small energy barrier to the entrance and exit of the blocker molecule. An estimate of the blocker association rate constant using the β distribution method indicates that these rates are on the order of $10^6\ M^{-1}s^{-1}$ at 0 mV for both blockers. These on-rates are similar to rates observed for other QAs in voltage-dependent potassium channels (Choi et al., 1993; Kutluay et al., 2005; Faraldo-Gomez et al., 2007). The blocker dissociation rate constant (off-rate) is also very fast, on the order of $10^5\ s^{-1}$ for TEA and $10^4\ s^{-1}$ for TPrA. These very fast off-rate constants are responsible for the observed fast block and are many orders of magnitude faster than those observed in inward rectifier potassium channels (Guo and Lu, 2001), although they are similar to TEA off-rates reported for the RCK2 voltage-dependent K^+ channel (Kirsch et al., 1991) and the KcSA channel (Kutluay et al., 2005).

The blocker association constant shows saturation at voltages more positive than 60 mV. A similar phenomenon has been observed in the blockade by QAs of the Anthrax toxin channel. In that case, it was shown that the saturation occurred at the value of blocker association rate predicted by diffusion and that indeed the on-rate constant was diffusion limited (Blaustein and Finkelstein, 1990a; Blaustein et al., 1990). In the present experiments, saturation of the on-rate of TEA and TPrA occurs at a value well below the calculated diffusion-limited rate constant for association of a blocker molecule with an absorbing disc of 6 Å diameter (Berg, 1983). This is a simplified calculation that assumes that the TEA and TPrA molecules are spherically symmetric and provides a lower bound for the value of the on-rate constant.

In the case of TPrA, our experiments using low concentrations of extracellular Na^+ clearly show that the rate of TPrA association increases exponentially with voltage, reaching values almost an order of magnitude larger at 100 mV than at high extracellular Na^+ concentrations, and not showing evidence of saturation with voltage. We interpret this result as an indication that, indeed, the entry of positively charged blocker molecules to the inner pore of TRPV1 is limited by interactions with the permeant ion, in this case Na^+. This is analogous to the knockoff effect observed in potassium channels, where increasing the extracellular concentration of permeant ions decreases the affinity of the blocker molecule (Armstrong, 1971; Hille and Schwarz, 1978). These results are also consistent with previous data indicating ion–blocker interactions in the pore of TRPV1 between Na^+ and TBA, and indicate that the permeation pathway of TRPV1 channels has multi-ion pore characteristics.

Both for TEA and TPrA, most of the voltage dependence of the blocking reactions is related to the association rate (k_{on}), with z_{on} values of 0.94 and 0.69, respectively. These very high valences cannot be explained by the traditional interpretation that relates them to the voltage drop across the inner channel pore. It has been shown that for the open potassium channels, the voltage drop across this region is at most 15% (Jiang et al., 2002). If this is also the case for TRPV1 channels, the very high apparent blocking valences may be the result of coupling between blocker binding and charge movement in the selectivity filter (Spassova and Lu, 1998).

The fact that most of the voltage dependence is associated with the blocker on-rate constant can be understood if the energy barrier for entry of TEA and TPrA is highly asymmetrical and may reflect the fact that the charge displacement due to permeant ions occurs when the blocker first enters the pore and subsequent exit of the blocker is not accompanied by a strictly coupled rearrangement of permeant ions. In contrast with TEA and TPrA, block by TBA and TPA is less voltage dependent and this voltage dependence is observed both in the blocker association as well as in the dissociation rate constants (Table I).

Closure Kinetics in the Presence of Blockers

Our experiments measuring the effects of blockers on closure kinetics provide evidence that the mechanism of channel block is different for each blocker and that it depends on the size of the blocker. The bigger blockers, like TBA and TPA, very clearly affect the kinetics of tail currents at negative voltages in a manner that is consistent with a state-dependent mechanism. The tail currents become

slower and the kinetics can be explained with a model in which the channel has to let the blocker dissociate before it can close (Scheme 1), an effect that has been previously observed with open-state block of potassium channels, particularly by QAs (Armstrong, 1971; Choi et al., 1993; Clay, 1995). The smaller blocker TPrA produces a less dramatic effect on the shape of the tail current, but it still slows tail currents as is observed with TBA and TPA. This indicates that TPrA is able to occupy its binding site in the open channel and interferes with channel closure.

For TEA, the mechanism of block is clearly different from the other QAs. Tail currents in the presence of TEA were not slowed down, and in fact the channels were able to close faster with TEA in the pore. This kinetic effect can be also observed in single-channel burst kinetics as a progressive shortening of the burst length with increasing TEA concentrations. In spite of the very fast dissociation rates of TEA, we know that the channels are blocked at the beginning of the hyperpolarizing pulse because the amplitude of the tail current is reduced with respect to the tail current in the absence of TEA (Fig. 8 A). The fact that channels remain blocked by this fast blocker at negative potentials and that they are able to close with faster kinetics suggests that TRPV1 can close with TEA still in its binding site.

A mechanism in which the blocker can only access its binding site when the channel is open, but becomes trapped upon channel deactivation, has been demonstrated in Kv and HCN potassium channels (Holmgren et al., 1997; Shin et al., 2001). Alternatively, the faster closing kinetics with TEA can be explained if this blocker is able to gain access to closed channels as well as open channels. To differentiate between these possibilities, we attempted to measure trapping of TEA, TBA, or TPA, but two problems prevented us from achieving this goal. TRPV1 channels cannot be completely opened or closed with voltage alone. We measured a ligand-independent open probability in the order of 0.01 at 100 mV, and this is reduced to ~0.005 at −140 mV (not depicted). Second, removal of capsaicin cannot be achieved fast enough to close channels in this manner, so we suspect that TEA can leave the open channels before they can be closed by capsaicin washout. However, both possible mechanisms for TEA block require that the channel can accommodate this QA ion in the closed state. The fact that TEA may be able to reside in the closed channel, combined with the observation that TPrA interferes with channel closure, suggests that the inner pore cavity of TRPV1 can comfortably accommodate an ion of ~8 Å in the closed state, but not a 9-Å molecule.

Significance for the Structure of the Gate and the Dimensions of the Inner Pore

What do these experiments tell us about the probable structure of the inner pore of TRPV1 channels? In principle, probing the channel with varying sizes of blocker molecules should provide us with a way to size the pore in an analogous manner to what was achieved for Na^+ channels (Hille, 1971). We observed that both the association and dissociation rate constants decrease in a monotonic fashion as a function of the blocker size (Fig. 10, A and B). Based on the shape of this relationship, it could be argued that the inner pore of an open channel has an admission cutoff size between the size of TPrA and TBA, with 9 and 10 Å, respectively, which corresponds to the region where the association and dissociation rates have their largest reduction. This does not

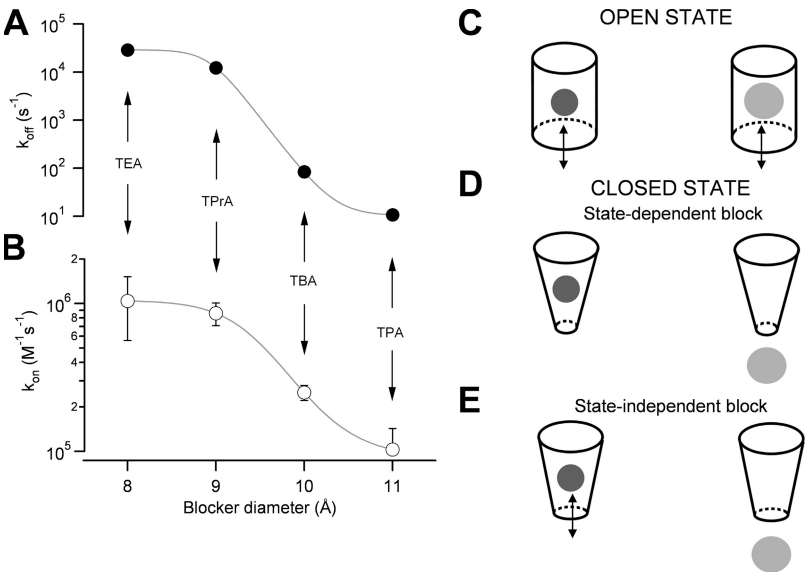

Figure 10. Dependence of the on- and off-rates of QA blockers on their size. The blocker dissociation (A) or association rates (B) are plotted as a function of their ionic radii. The continuous lines are drawn as a visual guide and have no theoretical significance. The decrease of the rates as a function of size is monotonic and there is not a clear cut-off size. Data are mean ± SEM of five to six experiments. (C–E) Cartoon depicting the possible ways in which the QAs may interact with the channel pore. (C) Cartoon of the open-channel pore with a blocker the size of TEA (right) or TPrA (left). (D) A model in which all QAs are only able to access the blocking site when the channel is in the open state, but TEA can reside inside the closed channel (left), whereas larger QAs cannot (right). (E) Alternative model in which the TEA molecule can block the channel in a state-independent manner, whereas the rest of the QAs can only access the blocking site when the channel is open, and hence interact with channel gating. In any way, TEA can reside in its blocking site when the channel is closed, whereas the other QAs do not.

mean that larger organic compounds cannot enter the inner pore. In fact, TPA is able to block TRPV1, and we have observed that QAs as large as tetraoctylammonium (14 Å) can also block this channel (not depicted). This approximate size of the inner pore of open TRPV1 is consistent with the size of the inner pore of the open MthK potassium channel, which is 12 Å (Jiang et al., 2002).

Our observation that TEA may remain in the closed channel, but TPrA already interferes with channel deactivation, would also suggest that the inner pore becomes smaller than 9 Å when the channel is closed. The structure of the closed KcsA channel suggests that the inner pore in this conformation has dimensions from 12 to 14 Å, so that depending on how deep the QA binding site is in TRPV1 channels, it may not be able to accommodate TPrA in the closed state.

The possibility that the closed TPRV1 channel can accommodate TEA but not TPrA is not surprising. It has been shown that wild-type *Shaker* K^+ channels cannot trap TEA, but the mutant I470C, which presumably has a larger pore, is able to do it (Holmgren et al., 1997; Melishchuk and Armstrong, 2001). This would suggest that the main determinant of trapping may be the pore size (or blocker size), and a size difference of just a few angstroms is all that is needed for the closed pore to accommodate a blocker molecule. Fig. 10 (C–E) shows a cartoon of the ways in which the blockers may be interacting with the channel and affecting channel gating. Fig. 10 D represents the case in which all blocker molecules, including TEA, can only access their binding site when the channel is in the open state; however, TEA can become trapped inside the channel when it closes. The other possibility (Fig. 10 D) is that the TEA molecule can block the channel in a state-independent manner, whereas the rest of the QAs can only access their blocking site when the channel is open.

Interestingly, the blocking characteristics of these molecules suggest the existence of an intracellular gate that may or may not be a gate for permeant ions. It remains to be seen if the gate of these channels is like that of the voltage-gated potassium channels (Holmgren et al., 1998; Yellen, 2002) or more like the pore gate in CNG-activated channels (Contreras et al., 2008), or the bacterial-nonselective channels, which apparently are closer to TRP channels in their pore sequence and probable structure.

We thank Félix Sierra, Laura Ongay, Sergio Rojas, Juan Manuel Barbosa, Ivette Rosas, Adrián Aguilera Jiménez, and Aurey Galván at Instituto de Fisiología Celular of UNAM for valuable technical support. We are grateful to Miguel Holmgren at the National Institutes of Health for invaluable discussions of this manuscript.

This study was supported by CONACyT grants 48990 (to L.D. Islas) and 46004 (to T. Rosenbaum), and DGAPA (PAPIIT) grants IN201705 (to T. Rosenbaum) and IN202006-3 (to L.D. Islas).

Angus C. Nairn served as editor.

Submitted: 22 May 2008
Accepted: 9 October 2008

REFERENCES

Armstrong, C.M. 1971. Interaction of tetraethylammonium ion derivatives with the potassium channels of giant axons. *J. Gen. Physiol.* 58:413–437.

Armstrong, C.M., and B. Hille. 1972. The inner quaternary ammonium ion receptor in potassium channels of the node of Ranvier. *J. Gen. Physiol.* 59:388–400.

Berg, H.C. 1983. Random Walks in Biology. Princeton University Press, Princeton, NJ. 142 pp.

Bezanilla, F., and C.M. Armstrong. 1972. Negative conductance caused by entry of sodium and cesium ions into the potassium channels of squid axons. *J. Gen. Physiol.* 60:588–608.

Bhave, G., W. Zhu, H. Wang, D.J. Brasier, G.S. Oxford, and R.W. Gereau. 2002. cAMP-dependent protein kinase regulates desensitization of the capsaicin receptor (VR1) by direct phosphorylation. *Neuron.* 35:721–731.

Blaustein, R.O., and A. Finkelstein. 1990a. Diffusion limitation in the block by symmetric tetraalkylammonium ions of anthrax toxin channels in planar phospholipid bilayer membranes. *J. Gen. Physiol.* 96:943–957.

Blaustein, R.O., and A. Finkelstein. 1990b. Voltage-dependent block of anthrax toxin channels in planar phospholipid bilayer membranes by symmetric tetraalkylammonium ions. Effects on macroscopic conductance. *J. Gen. Physiol.* 96:905–919.

Blaustein, R.O., E.J. Lea, and A. Finkelstein. 1990. Voltage-dependent block of anthrax toxin channels in planar phospholipid bilayer membranes by symmetric tetraalkylammonium ions. Single-channel analysis. *J. Gen. Physiol.* 96:921–942.

Caterina, M.J., M.A. Schumacher, M. Tominaga, T.A. Rosen, J.D. Levine, and D. Julius. 1997. The capsaicin receptor: a heat-activated ion channel in the pain pathway. *Nature.* 389:816–824.

Cheng, W., F. Yang, C.L. Takanishi, and J. Zheng. 2007. Thermosensitive TRPV channel subunits coassemble into heteromeric channels with intermediate conductance and gating properties. *J. Gen. Physiol.* 129:191–207.

Choi, K.L., C. Mossman, J. Aube, and G. Yellen. 1993. The internal quaternary ammonium receptor site of Shaker potassium channels. *Neuron.* 10:533–541.

Chuang, H.H., E.D. Prescott, H. Kong, S. Shields, S.E. Jordt, A.I. Basbaum, M.V. Chao, and D. Julius. 2001. Bradykinin and nerve growth factor release the capsaicin receptor from PtdIns(4,5)P2-mediated inhibition. *Nature.* 411:957–962.

Chung, M.K., A.D. Guler, and M.J. Caterina. 2008. TRPV1 shows dynamic ionic selectivity during agonist stimulation. *Nat. Neurosci.* 11:555–564.

Clay, J.R. 1995. Quaternary ammonium ion blockade of IK in nerve axons revisited. Open channel block vs. state independent block. *J. Membr. Biol.* 147:23–34.

Colquhoun, D., and B. Sakmann. 1985. Fast events in single-channel currents activated by acetylcholine and its analogues at the frog muscle end-plate. *J. Physiol.* 369:501–557.

Colquhoun, D., and F. Sigworth. 1995. Fitting and statistical analysis of single-channel records. *In* Single-channel Recording. B. Sakmann and E. Neher, editors. Plenum Press, New York. 483–587.

Contreras, J.E., D. Srikumar, and M. Holmgren. 2008. Gating at the selectivity filter in cyclic nucleotide-gated channels. *Proc. Natl. Acad. Sci. USA.* 105:3310–3314.

Cortright, D.N., J.E. Krause, and D.C. Broom. 2007. TRP channels and pain. *Biochim. Biophys. Acta.* 1772:978–988.

Faraldo-Gomez, J.D., E. Kutluay, V. Jogini, Y. Zhao, L. Heginbotham, and B. Roux. 2007. Mechanism of intracellular block of the KcsA K+ channel by tetrabutylammonium: insights from X-ray crystallography, electrophysiology and replica-exchange molecular dynamics simulations. *J. Mol. Biol.* 365:649–662.

Ferrer-Montiel, A., C. Garcia-Martinez, C. Morenilla-Palao, N. Garcia-Sanz, A. Fernandez-Carvajal, G. Fernandez-Ballester, and R. Planells-Cases. 2004. Molecular architecture of the vanilloid receptor. Insights for drug design. *Eur. J. Biochem.* 271:1820–1826.

Fitzhugh, R. 1983. Statistical properties of the asymmetric random telegraph signal, with applications to single-channel analysis. *Math. Biosci.* 64:75–89.

Franco, A. Jr., B.D. Winegar, and J.B. Lansman. 1991. Open channel block by gadolinium ion of the stretch-inactivated ion channel in mdx myotubes. *Biophys. J.* 59:1164–1170.

French, R.J., and J.J. Shoukimas. 1981. Blockage of squid axon potassium conductance by internal tetra-N-alkylammonium ions of various sizes. *Biophys. J.* 34:271–291.

French, R.J., and J.J. Shoukimas. 1985. An ion's view of the potassium channel. The structure of the permeation pathway as sensed by a variety of blocking ions. *J. Gen. Physiol.* 85:669–698.

Garcia-Martinez, C., C. Morenilla-Palao, R. Planells-Cases, J.M. Merino, and A. Ferrer-Montiel. 2000. Identification of an aspartic residue in the P-loop of the vanilloid receptor that modulates pore properties. *J. Biol. Chem.* 275:32552–32558.

Gunthorpe, M.J., M.H. Harries, R.K. Prinjha, J.B. Davis, and A. Randall. 2000. Voltage- and time-dependent properties of the recombinant rat vanilloid receptor (rVR1). *J. Physiol.* 525:747–759.

Guo, D., and Z. Lu. 2000. Mechanism of IRK1 channel block by intracellular polyamines. *J. Gen. Physiol.* 115:799–814.

Guo, D., and Z. Lu. 2001. Kinetics of inward-rectifier K+ channel block by quaternary alkylammonium ions. Dimension and properties of the inner pore. *J. Gen. Physiol.* 117:395–406.

Heginbotham, L., and E. Kutluay. 2004. Revisiting voltage-dependent relief of block in ion channels: a mechanism independent of punchthrough. *Biophys. J.* 86:3663–3670.

Hille, B. 1971. The permeability of the sodium channel to organic cations in myelinated nerve. *J. Gen. Physiol.* 58:599–619.

Hille, B. 2001. Ion Channels of Excitable Membranes. Sinauer, Sunderland, MA. 814 pp.

Hille, B., and W. Schwarz. 1978. Potassium channels as multi-ion single-file pores. *J. Gen. Physiol.* 72:409–442.

Holmgren, M., P.L. Smith, and G. Yellen. 1997. Trapping of organic blockers by closing of voltage-dependent K+ channels: evidence for a trap door mechanism of activation gating. *J. Gen. Physiol.* 109:527–535.

Holmgren, M., K.S. Shin, and G. Yellen. 1998. The activation gate of a voltage-gated K+ channel can be trapped in the open state by an intersubunit metal bridge. *Neuron.* 21:617–621.

Hwang, S.W., H. Cho, J. Kwak, S.Y. Lee, C.J. Kang, J. Jung, S. Cho, K.H. Min, Y.G. Suh, D. Kim, and U. Oh. 2000. Direct activation of capsaicin receptors by products of lipoxygenases: endogenous capsaicin-like substances. *Proc. Natl. Acad. Sci. USA.* 97:6155–6160.

Jiang, Y., A. Lee, J. Chen, M. Cadene, B.T. Chait, and R. MacKinnon. 2002. The open pore conformation of potassium channels. *Nature.* 417:523–526.

Kedei, N., T. Szabo, J.D. Lile, J.J. Treanor, Z. Olah, M.J. Iadarola, and P.M. Blumberg. 2001. Analysis of the native quaternary structure of vanilloid receptor 1. *J. Biol. Chem.* 276:28613–28619.

Kimbrough, J.T., and K.J. Gingrich. 2000. Quaternary ammonium block of mutant Na+ channels lacking inactivation: features of a transition-intermediate mechanism. *J. Physiol.* 529:93–106.

Kirsch, G.E., M. Taglialatela, and A.M. Brown. 1991. Internal and external TEA block in single cloned K+ channels. *Am. J. Physiol.* 261:C583–C590.

Kutluay, E., B. Roux, and L. Heginbotham. 2005. Rapid intracellular TEA block of the KcsA potassium channel. *Biophys. J.* 88:1018–1029.

Li, W., and R.W. Aldrich. 2004. Unique inner pore properties of BK channels revealed by quaternary ammonium block. *J. Gen. Physiol.* 124:43–57.

Macpherson, L.J., B.H. Geierstanger, V. Viswanath, M. Bandell, S.R. Eid, S. Hwang, and A. Patapoutian. 2005. The pungency of garlic: activation of TRPA1 and TRPV1 in response to allicin. *Curr. Biol.* 15:929–934.

Melishchuk, A., and C.M. Armstrong. 2001. Mechanism underlying slow kinetics of the OFF gating current in Shaker potassium channel. *Biophys. J.* 80:2167–2175.

Mohapatra, D.P., S.Y. Wang, G.K. Wang, and C. Nau. 2003. A tyrosine residue in TM6 of the Vanilloid Receptor TRPV1 involved in desensitization and calcium permeability of capsaicin-activated currents. *Mol. Cell. Neurosci.* 23:314–324.

Moriyama, T., T. Iida, K. Kobayashi, T. Higashi, T. Fukuoka, H. Tsumura, C. Leon, N. Suzuki, K. Inoue, C. Gachet, et al. 2003. Possible involvement of P2Y2 metabotropic receptors in ATP-induced transient receptor potential vanilloid receptor 1-mediated thermal hypersensitivity. *J. Neurosci.* 23:6058–6062.

Numazaki, M., and M. Tominaga. 2004. Nociception and TRP channels. *Curr. Drug Target. CNS Neurol. Disord.* 3:479–485.

Oseguera, A.J., L.D. Islas, R. Garcia-Villegas, and T. Rosenbaum. 2007. On the mechanism of TBA block of the TRPV1 channel. *Biophys. J.* 92:3901–3914.

Owsianik, G., K. Talavera, T. Voets, and B. Nilius. 2006. Permeation and selectivity of TRP channels. *Annu. Rev. Physiol.* 68:685–717.

Piper, A.S., J.C. Yeats, S. Bevan, and R.J. Docherty. 1999. A study of the voltage dependence of capsaicin-activated membrane currents in rat sensory neurones before and after acute desensitization. *J. Physiol.* 518:721–733.

Premkumar, L.S., and G.P. Ahern. 2000. Induction of vanilloid receptor channel activity by protein kinase C. *Nature.* 408:985–990.

Premkumar, L.S., Z.H. Qi, J. Van Buren, and M. Raisinghani. 2004. Enhancement of potency and efficacy of NADA by PKC-mediated phosphorylation of vanilloid receptor. *J. Neurophysiol.* 91:1442–1449.

Price, T.J., A. Patwardhan, A.N. Akopian, K.M. Hargreaves, and C.M. Flores. 2004. Modulation of trigeminal sensory neuron activity by the dual cannabinoid-vanilloid agonists anandamide, N-arachidonoyl-dopamine and arachidonyl-2-chloroethylamide. *Br. J. Pharmacol.* 141:1118–1130.

Salazar, H., I. Llorente, A. Jara-Oseguera, R. Garcia-Villegas, M. Munari, S.E. Gordon, L.D. Islas, and T. Rosenbaum. 2008. A single N-terminal cysteine in TRPV1 determines activation by pungent compounds from onion and garlic. *Nat. Neurosci.* 11:255–261.

Shin, K.S., B.S. Rothberg, and G. Yellen. 2001. Blocker state dependence and trapping in hyperpolarization-activated cation channels: evidence for an intracellular activation gate. *J. Gen. Physiol.* 117:91–101.

Sigworth, F.J., and S.M. Sine. 1987. Data transformations for improved display and fitting of single-channel dwell time histograms. *Biophys. J.* 52:1047–1054.

Spassova, M., and Z. Lu. 1998. Coupled ion movement underlies rectification in an inward-rectifier K+ channel. *J. Gen. Physiol.* 112:211–221.

Susankova, K., R. Ettrich, L. Vyklicky, J. Teisinger, and V. Vlachova. 2007. Contribution of the putative inner-pore region to the gating of the transient receptor potential vanilloid subtype 1 channel (TRPV1). *J. Neurosci.* 27:7578–7585.

Szallasi, A., and P.M. Blumberg. 1999. Vanilloid (Capsaicin) receptors and mechanisms. *Pharmacol. Rev.* 51:159–212.

Szallasi, A., B. Conte, C. Goso, P.M. Blumberg, and S. Manzini. 1993. Characterization of a peripheral vanilloid (capsaicin) receptor in the urinary bladder of the rat. *Life Sci.* 52:PL221–PL226.

Szallasi, A., S. Nilsson, T. Farkas-Szallasi, P.M. Blumberg, T. Hokfelt, and J.M. Lundberg. 1995. Vanilloid (capsaicin) receptors in the rat: distribution in the brain, regional differences in the spinal cord, axonal transport to the periphery, and depletion by systemic vanilloid treatment. *Brain Res.* 703:175–183.

Szallasi, A., D.N. Cortright, C.A. Blum, and S.R. Eid. 2007. The vanilloid receptor TRPV1: 10 years from channel cloning to antagonist proof-of-concept. *Nat. Rev. Drug Discov.* 6:357–372.

Szolcsanyi, J., A. Szallasi, Z. Szallasi, F. Joo, and P.M. Blumberg. 1990. Resiniferatoxin: an ultrapotent selective modulator of capsaicin-sensitive primary afferent neurons. *J. Pharmacol. Exp. Ther.* 255:923–928.

Szolcsanyi, J., A. Szallasi, Z. Szallasi, F. Joo, and P.M. Blumberg. 1991. Resiniferatoxin. An ultrapotent neurotoxin of capsaicin-sensitive primary afferent neurons. *Ann. NY Acad. Sci.* 632:473–475.

Tominaga, M., and T. Tominaga. 2005. Structure and function of TRPV1. *Pflugers Arch.* 451:143–150.

Tominaga, M., M.J. Caterina, A.B. Malmberg, T.A. Rosen, H. Gilbert, K. Skinner, B.E. Raumann, A.I. Basbaum, and D. Julius. 1998. The cloned capsaicin receptor integrates multiple pain-producing stimuli. *Neuron.* 21:531–543.

Tominaga, M., M. Wada, and M. Masu. 2001. Potentiation of capsaicin receptor activity by metabotropic ATP receptors as a possible mechanism for ATP-evoked pain and hyperalgesia. *Proc. Natl. Acad. Sci. USA.* 98:6951–6956.

Voets, T., G. Droogmans, U. Wissenbach, A. Janssens, V. Flockerzi, and B. Nilius. 2004. The principle of temperature-dependent gating in cold- and heat-sensitive TRP channels. *Nature.* 430:748–754.

Winegar, B.D., R. Kelly, and J.B. Lansman. 1991. Block of current through single calcium channels by Fe, Co, and Ni. Location of the transition metal binding site in the pore. *J. Gen. Physiol.* 97:351–367.

Woodhull, A.M. 1973. Ionic blockage of sodium channels in nerve. *J. Gen. Physiol.* 61:687–708.

Yeh, J.Z., and T. Narahashi. 1977. Kinetic analysis of pancuronium interaction with sodium channels in squid axon membranes. *J. Gen. Physiol.* 69:293–323.

Yellen, G. 1984. Ionic permeation and blockade in Ca2+-activated K+ channels of bovine chromaffin cells. *J. Gen. Physiol.* 84:157–186.

Yellen, G. 2002. The voltage-gated potassium channels and their relatives. *Nature.* 419:35–42.

Zhang, N., S. Inan, A. Cowan, R. Sun, J.M. Wang, T.J. Rogers, M. Caterina, and J.J. Oppenheim. 2005. A proinflammatory chemokine, CCL3, sensitizes the heat- and capsaicin-gated ion channel TRPV1. *Proc. Natl. Acad. Sci. USA.* 102:4536–4541.

nature structural & molecular biology

Structural determinants of gating in the TRPV1 channel

Héctor Salazar[1,4], Andrés Jara-Oseguera[2,4], Enrique Hernández-García[1,4], Itzel Llorente[1], Imilla I Arias-Olguín[1], Manuel Soriano-García[3], León D Islas[2] & Tamara Rosenbaum[1]

Transient receptor potential vanilloid 1 (TRPV1) channels mediate several types of physiological responses. Despite the importance of these channels in pain detection and inflammation, little is known about how their structural components convert different types of stimuli into channel activity. To localize the activation gate of these channels, we inserted cysteines along the S6 segment of mutant TRPV1 channels and assessed their accessibility to thiol-modifying agents. We show that access to the pore of TRPV1 is gated by S6 in response to both capsaicin binding and increases in temperature, that the pore-forming S6 segments are helical structures and that two constrictions are present in the pore: one that impedes the access of large molecules and the other that hampers the access of smaller ions and constitutes an activation gate of these channels.

Transient receptor potential (TRP) channels participate in a wide variety of physiological processes, including detection of sensory stimuli, osmoregulation, intracellular calcium homeostasis, chemotaxis and cell proliferation, among others[1]. A member of the TRP family, the TRPV1 nonselective cation channel, is expressed in sensory neurons and in several other tissues[1–3], where it functions as an integrator of noxious chemical and physical stimuli[4–9]. TRPV1 has been linked to processes mediating inflammatory and neuropathic pain[8,10], a finding that has led to a recent surge in research aimed at designing TRPV1-targeted pain-relieving therapies[11,12].

Despite the clear physiological relevance of TRPV1 and of TRP channels in general, little structural information is currently available[13–17]. Sequence homology of TRPV1 to ion channels of known structure suggests a subunit topology similar to that of voltage-activated potassium (Kv) channels, with each subunit formed by six transmembrane domains (S1–S6), intracellular N and C termini, and a pore domain formed by S5, S6 and the loop between them. Nonetheless, the topology of the pore and the location of the activation gate of TRPV1 or of any other TRP channel remain unknown. Therefore, we set out to establish the location of the molecular determinants of channel gating to obtain insight into the structural properties of the pore of TRPV1 channels.

Using the substituted cysteine accessibility method (SCAM) to scan the entire S6 segment of the rat TRPV1, we have made the following discoveries, which constitute the first molecular characterization of the activation gate of a TRP channel. First, the finding that the accessibility of the introduced cysteines is state-dependent indicated the presence of two intracellular constrictions: the most intracellular one located at Leu681, which closes the ion conduction pathway for large molecules (~6 Å), and one located at Tyr671, which obstructs the conduction pathway for small permeating ions (~2 Å) and constitutes the activation gate of TRPV1. An important result is that the region we define as the activation gate of TRPV1 gates the channel in response to both capsaicin and heat, revealing the physical point of convergence of these two pathways of activation.

Second, use of our recently engineered cysteine-less TRPV1 (18^{-}TRPV1)[4] has allowed us to study the formation of disulfide bonds between cysteines introduced at key S6 locations, unequivocally confirming proximity among the residues involved in gated access of ions in these channels. Third, we have observed a marked periodicity in our accessibility data that is consistent with an α-helical structure for the S6. Our results allow us to propose a structural homology model that neatly incorporates our observations and provides a structural basis to explain gating in TRPV1, which will prove useful in understanding gating of other TRP channels.

RESULTS

TRPV1-C157A as a tool for SCAM analysis

Our previous experiments using blocking ions of known dimensions suggested the existence of gated access to the pore of TRPV1 channels from the intracellular side[18], as observed in Kv channels. We sought to identify the existence of such an activation gate by probing the S6 transmembrane domain using SCAM to insert cysteines into the TRPV1-C157A background. **Figure 1a**, above, shows the sequence of the putative S6 region of the TRPV1 channel.

TRPV1-C157A yields adequate expression levels and is unresponsive to cysteine-modifying compounds such as methanethiosulfonate (MTS) reagents, as no shift in the response to capsaicin or changes in channel conductance were observed after exposure to these molecules[4] (**Figs. 1b,c**). Notably, TRPV1-C157A resembles wild-type TRPV1 in its core biophysical properties, such as voltage-dependence, single-channel conductance (data not shown) and its response to capsaicin[4] (**Supplementary Fig. 1**).

[1]Departamento de Biofísica, Instituto de Fisiología Celular, [2]Departamento de Fisiología, Facultad de Medicina and [3]Departamento de Bioquímica, Instituto de Química, Universidad Nacional Autónoma de México, México, D.F., México. [4]These authors contributed equally to this work. Correspondence should be addressed to T.R. (trosenba@ifc.unam.mx).

Received 15 January; accepted 4 June; published online 28 June 2009; doi:10.1038/nsmb.1633

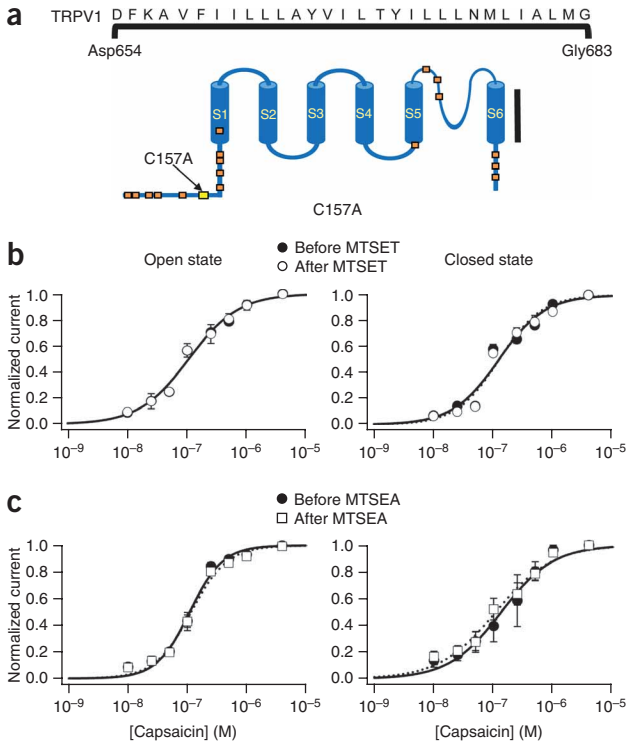

Figure 1 TRPV1-C157A can be used as a template for SCAM analysis of the channel pore. (**a**) Above, amino acid sequence of the putative S6 segment of the TRPV1. Below, cartoon of one TRPV1 subunit. Transmembrane segments are shown in blue, approximate positions of 17 of the 18 native cysteines in orange and Cys157 in yellow. (**b**) TRPV1-C157A dose-response curves to capsaicin obtained before (filled symbols) and after (open symbols) exposure to MTSET applied in the open (left) or closed (right) state. Lines are fits to the Hill equation before (solid lines) and after (dotted lines) treatment with MTS reagents. K_d values before and after MTSET applied in the open state are 106 ± 28 nM and 106 ± 20 nM, respectively. K_d values before and after MTSET applied in the closed state are 124 ± 21 nM and 125 ± 28 nM, respectively. (**c**) TRPV1-C157A dose-response curves to capsaicin obtained before and after exposure to MTSEA applied in the open or closed state. K_d values before and after MTSEA applied in the open state are 116 ± 27 nM and 134 ± 37 nM, respectively. K_d values before and after MTSEA applied in the closed state are 134 ± 10 nM and 109 ± 9 nM, respectively. No statistically significant differences were found between data obtained before and after treatment with MTS reagents (Student's *t*-test, $P > 0.1$). Group data are presented as mean ± s.e.m., $n = 5$.

When we exposed TRPV1-C157A to either MTSET (2-(trimethylammonium) ethyl methanethiosulfonate) or MTSEA (2-aminoethyl methanethiosulfonate) (**Fig. 1b,c**), we observed no changes in the capsaicin dose response in either the open or closed state. The response of TRPV1-C157A to capsaicin remained unchanged even during exposure to the MTS reagents for periods as long as 30 min (data not shown).

State-dependence of S6 cysteine reactivity

We introduced cysteines along the putative S6 segment of TRPV1-C157A (**Fig. 1a**) as targets for chemical modification by MTS reagents. All mutants were functional and had a response to capsaicin that did not substantially differ from that of the wild-type channel (**Supplementary Fig. 1**).

On the basis of our previous findings suggesting the presence of an intracellular gate for large cations (~9 Å)[18], we initially used MTSET to probe the pore of TRPV1. First, we measured the dose-response relationships for capsaicin before and after treatment with MTSET in either the open or closed state for channels in which one of the two most intracellular residues of the S6 segment was substituted by a cysteine (**Fig. 2a,b**). The effect of MTSET on G683C was an almost complete inhibition of the current. On the other hand, M682C showed a strong potentiation of the current upon MTSET exposure. However, both mutants had

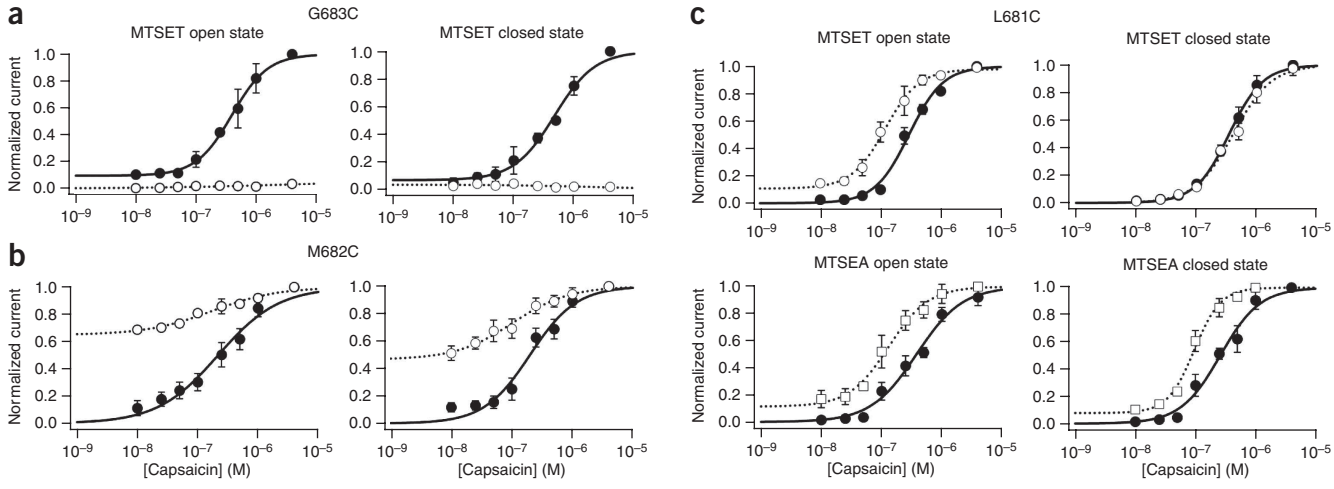

Figure 2 Residue Leu681 restricts the entrance of large cations. Dose-response curves for G683C (**a**) and M682C (**b**) mutants before and after treatment with MTSET (filled and empty circles, respectively) in the open (left) or closed state (right). (**a**) K_d values for G683C before MTSET application in the open or closed states of the channels were 397 ± 55 and 397 ± 8 nM, respectively. After MTSET, currents were abolished and fits could not be performed. (**b**) K_d values of M682C for MTSET applied in the open state were 218 ± 24 nM before treatment and 2 ± 10 nM after. K_d values for MTSET applied in the closed state were 199 ± 52 nM before treatment and 11 ± 7 nM after. (**c**) Above, L681C K_d values were 295 ± 18 nM before and 98 ± 9 nM after MTSET was applied in the open state. K_d values in the closed state were 347 ± 34 nM before and 405 ± 74 nM after MTSET treatment. Modification is significantly state-dependent (Student's *t*-test, $P < 0.01$). Below, dose-response curves for L681C before (filled circles) and after treatment with MTSEA (empty squares) in the open or the closed state were not significantly different (Student's *t*-test, $P > 0.1$). K_d values were 356 ± 48 nM before and 131 ± 16 nM after MTSEA in the open state and 259 ± 87 nM before and 98 ± 4 nM after MTSEA in the closed state. Group data are presented as mean ± s.e.m., $n = 5$.

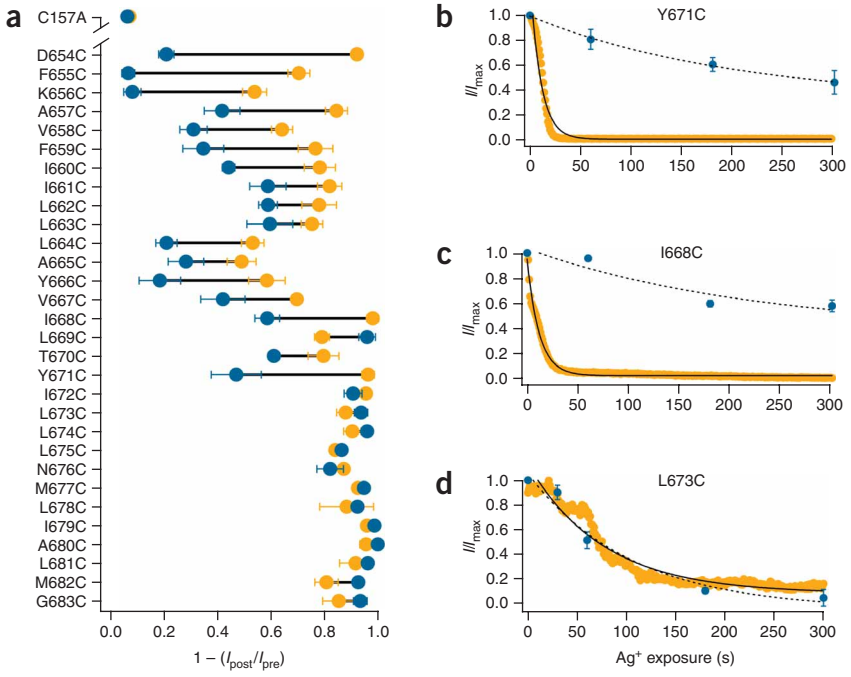

Figure 3 Ag^+ modification reveals the presence of an intracellular gate for small ions at Tyr671. (**a**) Fractional modification for C157A and each of the 30 S6 mutants by treatment with Ag^+ in the presence (orange symbols) or absence (blue symbols) of 4 μM capsaicin. Thick black bars serve as a visual aid. (**b**–**d**) Time courses of modification of the Y671C (**b**), I668C (**c**) and L673C (**d**) mutants by Ag^+ in the open (orange symbols) and closed state (blue symbols). Open-state modification data are from a representative experiment for each mutant, whereas closed-state modification data are from averages (mean ± s.e.m., $n = 6$–8 for each data point) obtained as described in the Online Methods section. Open-state modification second-order rates (k_O) are expressed as mean ± s.e.m., $n = 6$–8. Closed-state modification second-order rates (k_C) are the result of an exponential fit (dashed lines) to the final time course curve. In **b**, Y671C shows state-dependent modification, with $k_O = 8.6 \pm 0.8 \times 10^6\ M^{-1}\ s^{-1}$ and $k_C = 0.13 \times 10^6\ M^{-1}\ s^{-1}$. In **c**, Modification of I668C is state-dependent, with $k_O = 13.8 \pm 3.4 \times 10^6\ M^{-1}\ s^{-1}$ and $k_C = 0.4 \times 10^6\ M^{-1}\ s^{-1}$. In **d**, modification of L673C is state-independent, with $k_O = 0.86 \pm 0.08 \times 10^6\ M^{-1}\ s^{-1}$and $k_C = 1.02 \times 10^6\ M^{-1}\ s^{-1}$. I, current obtained after Ag^+ treatment; I_{max}, current obtained with 4 μM capsaicin.

a state-independent response, indicating that there is no change in accessibility for MTSET during gating in this region.

The mutant L681C, corresponding to the next residue in S6, showed a notable response: MTSET had a potentiating effect when applied in the open state but had no effect at all in the closed state (**Fig. 2c**, top). This state-dependent behavior suggests that the accessibility of L681C to MTSET may be hindered by a constriction of the pore in the closed state. To further validate this hypothesis, we performed the same experiment with MTSEA, which has a smaller diameter (3.6 Å)[19], and found that MTSEA also had a potentiating but state-independent effect (**Fig. 2c**, below). These data suggest that access to Leu681 is restricted for cations the size of MTSET but not for molecules the size of MTSEA, suggesting the presence of an intracellular constriction located near this residue that controls the access for large cations. Nonetheless, in contrast to MTSET, which is positively charged at any pH, MTSEA is neutral at pH 7, allowing it to access residues in the protein through pathways other than the pore[20]. Moreover, MTSEA is still a large molecule when compared with ions such as Na^+ (0.97 Å), Ca^{2+} (0.94 Å) or even K^+ (1.33 Å)[21,22]. For this reason, MTSEA does not constitute an adequate reagent for probing the pore for state-dependent accessibility of smaller ions than MTSET. We decided to perform SCAM analysis of S6 using Ag^+ because it reacts effectively with cysteines, it is nearly the same size of the permeant ions Na^+ and K^+ and it has been previously used as a probe for the accessibility of small ions in Kv channels[21–23].

Gated access of small ions through the TRPV1 pore

We first confirmed that Ag^+ does not affect the activity of TRPV1-C157A by measuring the effects of Ag^+ applied in the open or the closed state. We repeated this same measurement in each of the 30 cysteine-substituted mutants of the S6 and, in all cases where it had an effect, the presence of Ag^+ caused a reduction of the initial capsaicin-activated current (**Fig. 3a**).

L681C and the following nine mutants (A680C to I672C) showed state-independent modification by Ag^+, in agreement with the results obtained with MTSEA. However, when we tested the Y671C mutant for state-dependent modification by Ag^+, a strong effect became apparent: as Ag^+ was applied in the open state, we observed an almost complete reduction of the current upon subsequent activation with capsaicin. When the patches were exposed to Ag^+ in the closed state, only a fraction of the current was eliminated. Notably, all mutants above Tyr671 (less intracellular) showed the same state-dependent behavior (**Fig. 3a**). These data argue that access to Tyr671 and the residues above is gated for small permeant ions the size of Ag^+, indicating that the activation gate of the TRPV1 channel resides just below the region where this tyrosine residue is located.

The data in **Figure 3a** were obtained by comparing the degree of modification between the open and closed states at a single time point. However, if the limiting effect of Ag^+ is attained before the measured 5-min time point, a state-dependent modification could be falsely interpreted as state-independent. To discount this possibility, we measured the rates of modification in the closed and open states of key sites in the S6 segment (**Fig. 3b–d** and **Supplementary Fig. 2**). In accordance with our previous results, the modification rates of Y671C and of the more N-terminal I668C remain clearly state-dependent (**Fig. 3b,c** and **Supplementary Fig. 2**), whereas for residues that are more intracellular (L673C and L675C) than Tyr671, these rates remain basically unchanged in the closed and open states (**Fig. 3d** and **Supplementary Fig. 2**).

If the pore of TRPV1 had two constrictions located at Leu681 and Tyr671, it might be expected that disulfide bonds may be formed in a state-dependent manner between cysteines at any of these two sites because this type of interaction occurs if the two sulfhydryl groups are up to 4 Å apart[24,25]. We explored this possibility by inducing the formation of disulfide bonds using copper phenantroline (CuP), an oxidizing agent.

We introduced cysteines at positions 681 or 671 of the cysteine-less TRPV1 channel, 18⁻TRPV1, and determined the effects of CuP on formation of disulfide bonds in the open state (**Fig. 4a**) (**Supplementary Methods**). CuP failed to produce a response in the

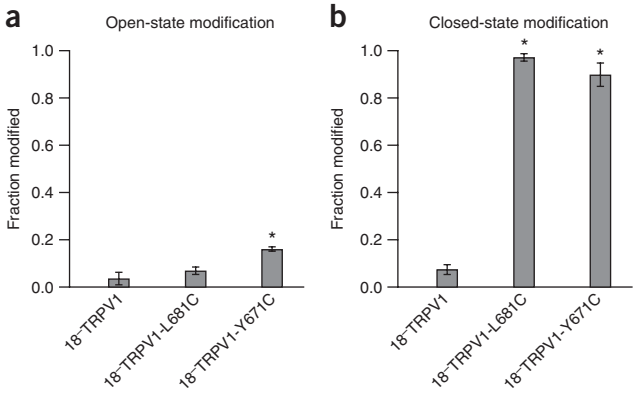

Figure 4 CuP induces state-dependent disulfide bonds in 18⁻TRPV1-L681C and 18⁻TRPV1-Y671C. (**a**) Bar graphs representing the fraction of current modified by copper phenanthroline (CuP) applied concomitantly with 4 μM capsaicin (open state) for the 18⁻TRPV1, 18⁻TRPV1-L681C and 18⁻TRPV1-Y671C mutants. There are no significant differences between the cysteine-less channel 18⁻TRPV1 (0.035 ± 0.025) and 18⁻TRPV1-L681C (0.069 ± 0.016) after CuP treatment (Student's *t*-test, $P > 0.1$). A statistically significant difference (Student's *t*-test, $P < 0.005$) is seen when CuP is applied to 18⁻TRPV1-Y671C (0.16 ± 0.009) as compared to 18⁻TRPV1. (**b**) Bar graphs representing the effect of CuP applied in the absence of agonist (closed state) for the 18⁻TRPV1 (0.075 ± 0.02), 18⁻TRPV1-L681C (0.97 ± 0.01) and 18⁻TRPV1-Y671C (0.89 ± 0.05) mutants. A statistically significant (Student's *t*-test, $P < 0.001$) reduction of the current is seen for 18⁻TRPV1-L681C and 18⁻TRPV1-Y671C as compared to 18-TRPV1. Group data are presented as mean ± s.e.m., $n = 5–7$.

18⁻TRPV1 background and in the 18⁻TRPV1-L681C mutant. In the case of 18⁻TRPV1-Y671C, however, we observed a small but statistically significant ($P < 0.005$; **Fig. 4a**) reduction in the current after treatment with CuP at saturating capsaicin concentration. This may be explained either by the unfavorable formation of a disulfide bond in the open state or, alternatively, by bonds formed cumulatively during the brief dwells of the channels into the closed state. Thus, we next analyzed the effects of CuP applied to the closed state of the channels. As expected, the treatment had no effect on activation of 18⁻TRPV1 channels (**Fig. 4b**). Conversely, both 18⁻TRPV1-L681C and 18⁻ TRPV1-Y671C showed a strong sensitivity to CuP treatment, as evidenced by an almost complete reduction in the current. This reduction was not reversed by washout of CuP but was partially upturned by treating the patches with 20 mM DTT (that is, DTT application recovered 52 ± 10% and 50 ± 4% of channel function in 18⁻TRPV1-L681C and 18⁻TRPV1-Y671C, respectively). DTT had no effect on capsaicin-activated currents before CuP treatment (data not shown). These results support the hypothesis that both Leu681 and Tyr671 are part of regions that constrict upon closure of the channel, blocking the ion-conduction pathway.

If indeed Leu681 serves as a gate for large molecules such as MTSET, it is intriguing that CuP, a larger molecule, can reach the more intracellular residue at position 671 to induce disulfide bond formation in the closed state. The ability of CuP to form these disulfide bonds may reside in the fact that it is far more hydrophobic (polar area of 2.7 Å^2 and apolar area of 601.3 Å^2) than the MTSET molecule (polar area of 103.9 Å^2 and apolar area of 311.9 Å^2). Consequently, CuP may gain access to the 671 site using alternative pathways of lower dielectric constant than the pore, whereas MTSET can access this site only through the pore. If modification by MTSET of cysteines in S6 is gated at Leu681, then a state-dependence of modification should be observed for residues above this position. In fact, the rates of modification of Y671C and other mutants above Leu681 by MTSET are faster in the open state than in the closed state. Moreover, the rates of modification of G683C by MTSET when applied in the open or the closed state do not differ (**Supplementary Fig. 3** and **Supplementary Methods**), in accordance with the presence of a constriction located at Leu681.

Role of Leu681 and Tyr671 in temperature gating

TRPV1 gating is also controlled by temperature, implying that this channel responds to stimuli that are very different in nature. However, because these activation mechanisms are allosterically coupled[26], these two stimuli are expected to converge in the opening of the pore so that conformational changes in the pore domain by either one should not be markedly different.

An implication of the above is that the capsaicin-activated gate should also function as a gate for temperature activation. To test this hypothesis, we measured the rates of modification by Ag^+ in the closed and open states for the I668C, Y671C and L673C mutants when the channel is gated by temperature. We found that I668C and Y671C were modified at a faster rate in the open state as compared to in the closed state, whereas the rate of modification of L673C showed no state-dependence (**Fig. 5**).

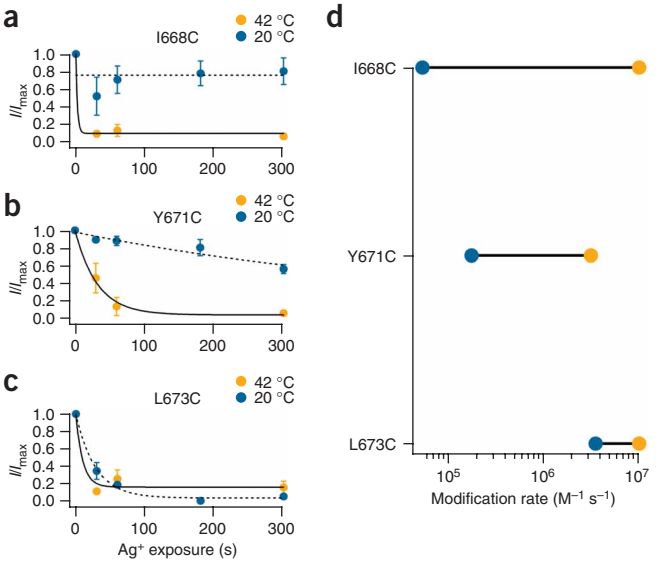

Figure 5 Gating of the TRPV1 channel by temperature. (**a**–**c**) Time courses of modification of the I668C (**a**), Y671C (**b**) and L673C (**c**) mutants by Ag^+ applied in either the open (42 °C, orange symbols) or the closed state (20 °C, blue symbols). Continuous or dashed lines are fits of the open- or closed-state modification data to an exponential, respectively. (**a**) I668C. The open-state modification second-order rate (k_O) of 10.0×10^6 M^{-1} s^{-1} is a lower limit because the modification is faster than the earliest obtained data point. The closed-state modification second-order rate (k_C) was estimated to be 0.05×10^6 M^{-1} s^{-1}, although the process is too slow to be accurately measured. In **b**, modification of Y671C is state-dependent, with $k_O = 3.1 \times 10^6$ M^{-1} s^{-1} and $k_C = 0.17 \times 10^6$ M^{-1} s^{-1}. In **c**, L673C modification has rates $k_O = 10.0 \times 10^6$ M^{-1} s^{-1}, which is within the lower limit, as in **a**, and $k_C = 3.5 \times 10^6$ M^{-1} s^{-1}. (**d**) Comparison of the rates of open-state (orange symbols) or closed-state (blue symbols) modification obtained from (**a**–**c**). Thick black bars serve as a visual aid. $n = 3$ for each data point. Group data are presented as mean ± s.e.m.

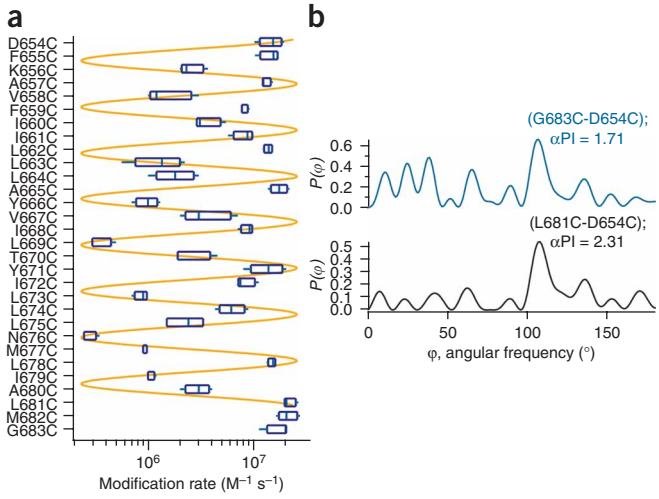

Figure 6 The S6 segment has an α-helical character. (**a**) Box plot of the open-state modification rates with Ag^+ for each of the 30 mutant channels. The vertical line within each box indicates the median, boxes show the twenty-fifth and seventy-fifth percentiles, and whiskers show the fifth and ninety-fifth percentiles of the data ($n = 5$). A sine function with a period of 3.4 was superimposed to the data (orange line) as a visual aid. (**b**) Analysis of the periodicity of the S6 segment. The blue trace is the power spectrum of all the S6 residues; the numbering is indicated in the figure, as is the α-periodicity index, αPI. The black spectrum is obtained when the three C-terminal residues (683–681) are removed.

The α-helical character of S6

The membrane-spanning domains of ion channels are often organized as α-helices[27,28]. Thus, an α-helical S6 would be exposed to the aqueous hydrophilic environment of the inner pore, to the membrane and to the rest of the protein, with the residues facing the aqueous cavity being more accessible. If the S6 is indeed an α-helix, a periodicity of nearly 3.6 residues per turn would be expected[29] in the accessibility of the residues to modifying reagents. To test the helical character of the S6, we measured the rate of modification of each mutant by Ag^+ in the open state (**Fig. 6a**). As expected, there was a large variation in the time courses for each of the mutants. Consistent with our previous results, both L681C and Y671C are among the residues with the highest modification rates, in agreement with these amino acids facing the pore.

To obtain a quantitative measurement of the periodicity of the modification data, we performed harmonic analysis using a discrete Fourier transform[30]. The power spectrum, P(φ), shows a strong peak at 107° (**Fig. 6b**), which has been suggested to be more typical for membrane-spanning α-helices than the 100° seen in α-helices from soluble proteins[31]. The α-helical character can be quantified by evaluating an α-periodicity index, αPI, where values greater than 2 have been shown to represent amphipathic helices[30]. The αPI value for all 30 residues is 1.71, which suggests a poor α-helical organization. However, if the three most C-terminal residues (683–681), which have high modification rates, are omitted from the analysis, αPI becomes 2.31, suggesting that those residues do not form part of an α-helix.

An unexpected result is that the modification of some of the uppermost residues in the pore occurs rapidly, although steric hindrances are expected to be larger owing to the presence of the selectivity filter and the putative pore helix. It may be possible that Ag^+ accesses these residues by a non–pore-dependent pathway. On the other hand, if Ag^+ were accessing these residues through the pore, then the presence of an intracellular pore blocker would protect these sites from modification. Consistent with the rest of our data, we found that the rates of modification for two of these more N-terminally located mutants (A657C and D654C) in the presence of capsaicin and the pore-blocker tetrabutylammonium (TBA) are, at least, one order of magnitude slower than in the absence of blocker (**Supplementary Fig. 4** and **Supplementary Methods**), confirming that Ag^+ reaches these sites through the pore. It is possible that this region of S6 is loosely packed against the pore, allowing for rapid modification of cysteines introduced in this region. Notably, the TRPV1 pore has been shown to be dynamic, as evidenced by gating-induced selectivity changes[32]. Precise structural data concerning the topology of the upper pore of the channel are required to completely solve this conundrum.

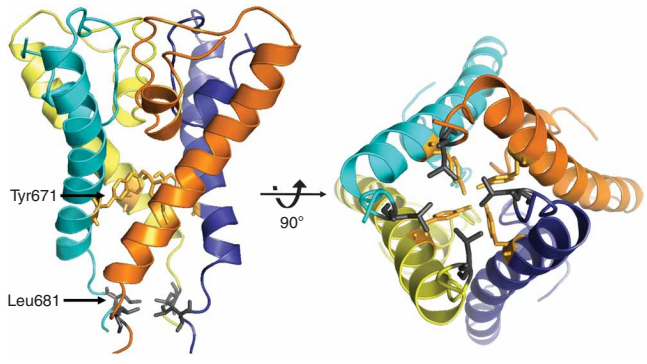

Figure 7 Homology model of TRPV1 based on the Kv1.2 structure. Lateral (left) and bottom (right) views of the helical S6 transmembrane segments are depicted in different colors. Residues Leu681 and Tyr671, which give rise to the two main constrictions in the TRPV1 pore, are depicted as black and orange side chains, respectively.

A SCAM-based model for the S6 region of the TRPV1

To include all of our results in a single functional model, we used the Kv1.2 channel as a template to construct a homology model of the pore domain of TRPV1. Our model (**Fig. 7** and **Supplementary Methods**) is consistent with our experimental data showing that the four aromatic residues, Tyr671 located at the middle of the S6 segments, face the hydrophilic lumen of the pore and are close enough to each other to permit interactions between them. Another feature of the model is that the four Leu681 side chains fit well into a large internal hydrophobic pocket at the bottom of the pore domain. Additionally, residues 681–683 are not part of an α-helix, consistent with our periodicity data.

DISCUSSION

We performed a cysteine-accessibility study to gain structural insight into the architecture and possible gating rearrangements of the S6 of TRPV1. This approach revealed that the S6 segment undergoes capsaicin- and temperature-dependent conformational transitions that change its accessibility, suggesting that these movements are responsible for channel activation.

To date, there are only a handful of models describing the activation gate of ion channels based on functional data[21,33–36]. For TRP channels, such a description is not yet available.

It was previously suggested[37] that residues within the inner-pore helix are candidates for sites of the gating apparatus of TRPV1. However, owing to the fact that TRPV1 does not show a canonical

point of flexibility such as glycine or proline, as typically found in K^+ channels[38], this study could not provide functional support for identifying a gating hinge.

We show that Leu681, located quite intracellularly, impedes the access of ions of the size of MTSET (5.8 Å) in the closed state but not of the size of MTSEA (3.6 Å) or Ag^+ (1.26 Å). Moreover, the state-dependent modification of L681C by MTSET, together with the apparent state-independent block of the TRPV1 by tetraethylammonium (TEA)[18], indicates that a molecule at least the size of TEA (8 Å) can remain inside the closed channel pore.

By using Ag^+, we were able to determine that a region located further up the S6 segment (near residue 671) does indeed impede the access of smaller ions such as Ag^+ in a state-dependent fashion. Moreover, we have probed Leu681 and Tyr671 for proximity, using the formation of disulfide bonds as a reporter, and our results support the idea that these regions comprise physical constrictions. Tyr671 has been found to affect Ca^{2+}-permeation properties in the TRPV1[39], in accordance with this residue facing the lumen of the pore.

Does state-dependence of Ag^+ accessibility at Tyr671 necessarily imply that this residue provides an energy barrier for the access of permeant ions? Gated access of Ag^+ may reflect gated access of a permeant ion such as K^+ or Na^+, as it shares physical-chemical properties with them. It has been pointed out that, if Ag^+ ions behave in the channel in a similar manner to the permeant ions, then the fold change in modification rates from the closed to the open state is expected to reflect the conductance fold change for the same process[21]. In our experiments, the rate fold change for Y671C is 0.028. Under our recording conditions, the open single-channel current is ~10 pA, so the current of the channel upon closure of the 671 gate would be ~0.3 pA, and thus indistinguishable from the recording noise, effectively behaving as a closed state.

A notable observation in our Ag^+-modification experiments is the 'inverted' state-dependence of modification of L669C (**Fig. 3a** and **Supplementary Fig. 2**). A possible explanation is that Ag^+ uses a path other than the pore to gain access to this site and there is a state-dependent conformational change that exposes the residue in the closed state, whereas it remains inaccessible in the open state. A different possibility is that this residue faces the pore lumen in the closed state but not in the open state, as a consequence of the conformational changes in the pore during gating. Because the open probability in the absence of capsaicin is not zero[40], Ag^+ would be able to gain access to the channel and stabilize the closed state, raising the rate of modification in the closed as compared to the open state, where the residue remains inaccessible. This 'reversed' state-dependence has been previously observed in similar experiments with other mutant ion channels[41].

Another interesting observation is that a couple of mutants (L681C and M682C) show potentiation in response to capsaicin when treated with MTSEA or MTSET but are inhibited when treated with Ag^+. These variations may be explained by charge differences between cysteine-modifying agents because both MTSEA and MTSET are charged at pH 7 (ref. 20), whereas Ag^+ is neutral after reacting with a cysteine. Under this notion, the positive charges from the MTS reagents would come closer to each other during the closed state of the channels, causing electrostatic repulsion and thus destabilizing this state[35].

Previous work[42] showed that some residues of the S6 segment have an important role in the response of TRPV3 to temperature but not to other agonists. We did not explore the effect of mutations in the S6 on temperature sensitivity. However, consistent with the idea that the regions located near Leu681 and Tyr671 are important in the regulation of access of ions into the TRPV1 pore, we have also demonstrated that, when the channel is activated by heat, these regions continue to behave as physical constrictions for ion flux. It has been suggested that TRP channels are modular proteins in which the different domains or modules are allosterically coupled to each other but function independently[26,43]. The data presented here are in line with this idea.

By using similar cysteine-accessibility methods, other groups have suggested a role for the pore helix and selectivity filter in the gating process of TRP channels[44]. These data do not conflict with ours because the presence of an intracellular activation gate at the S6 does not preclude state-dependent conformational changes in other regions of the channel such as the S5-S6 loop, as occurs in Kv channels with C-type inactivation[45] or in the conformational changes of the pore of mutant *Shaker* channels[46]. Notably, the TRPV1 pore is dynamic, allowing changes in selectivity in response to different agonists and exposure times[32]. Still, we did not observe this phenomenon in our studies, probably because we used only a single permeant ion in our experiments[18,40].

The S6 transmembrane region of voltage-gated ion channels has been described as an α-helix[27]. Studies of accessibility in K^+-selective channels have also detected α-helical periodicity in other transmembrane segments[47]. We find that some of the cysteines (including Y671C) introduced along S6 contribute to the lining of the pore. We have observed differences in modification rates of introduced cysteines with, presumably, the pore-lining ones being modified at faster rates than those that probably face the lipid interface and show slow modification rates because they might be subjected to stronger steric hindrances. These data reflect the helical character of the S6 domain of TRPV1.

Functional and structural studies in K^+ channels have provided valuable information on the location and nature of the activation gate in ion channels. In this regard, we have used the Kv1.2 structure[27] to produce a model of TRPV1 that correlates with our functional data. Sequence alignment of the S6 of Kv1.2 and TRPV1 reveals conservation of this region among these channels. Notably, the 'Pro-Val-Pro' region of Kv1.2, which is responsible for the flexibility and gated access of ions into the pore of this channel, aligns near Tyr671 of TRPV1 (**Supplementary Fig. 5a**). Moreover, this residue is found in an identical position in another channel of the TRPV subfamily, TRPV2, and coincides with a phenylalanine, another aromatic residue, in TRPV3 and TRPV4 (**Supplementary Fig. 5b**). Further investigations should clarify the importance of this region in the rest of the TRP channel family.

The final model we present here, supported by our experimental results, constitutes a new description of structural elements of the S6 transmembranal segment, which gate the access of ions to the pore of a member of the TRP channel family. Our model may prove useful for future understanding of the structure-function relationships in TRP channels.

METHODS

Methods and any associated references are available in the online version of the paper at http://www.nature.com/nsmb/.

Note: Supplementary information is available on the Nature Structural & Molecular Biology website.

ACKNOWLEDGMENTS

We thank D. Julius at the University of San Francisco for providing the TRPV1 cDNA, and S. Simon at Duke University and M. Rosenbaum at Instituto de Ciencias Nucleares of Universidad Nacional Autónoma de México for thoughtful discussion of this manuscript. We also thank L. Ongay, S. Rojas, A. Aguilera

Jiménez, J. Barbosa, A.M. Escalante and F. Sierra at Instituto de Fisiología Celular, Universidad Nacional Autónoma de México, for expert technical support. This work was supported by grants from La Dirección General de Asuntos del Personal Académico (DGAPA)-Universidad Nacional Autónoma de México (UNAM) IN200308-3 to T.R. and IN202006–3 to L.D.I., and CONACyT No. 58038 to T.R. and No. 48990 to L.D.I. This study was performed in partial fulfillment of the requirements for the Doctorate degree in Biomedical Sciences of H.S. at the UNAM.

AUTHOR CONTRIBUTIONS

H.S., A.J.-O., E.H.-G. and T.R. performed experiments; I.L. did molecular biology and cell culture; M.S.-G. and I.I.A.-O. performed molecular modeling; L.D.I. and T.R. designed experiments, analyzed data and wrote the paper; all authors discussed the data.

Published online at http://www.nature.com/nsmb/
Reprints and permissions information is available online at http://npg.nature.com/reprintsandpermissions/

1. Clapham, D.E., Runnels, L.W. & Strubing, C. The TRP ion channel family. *Nat. Rev. Neurosci.* **2**, 387–396 (2001).
2. García-Martínez, C., Morenilla-Palao, C., Planells-Cases, R., Merino, J.M. & Ferrer-Montiel, A. Identification of an aspartic residue in the P-loop of the vanilloid receptor that modulates pore properties. *J. Biol. Chem.* **275**, 32552–32558 (2000).
3. Montell, C. The TRP superfamily of cation channels. *Sci. STKE* **2005**, re3 (2005).
4. Salazar, H. *et al.* A single N-terminal cysteine in TRPV1 determines activation by pungent compounds from onion and garlic. *Nat. Neurosci.* **11**, 255–261 (2008).
5. Macpherson, L.J. *et al.* The pungency of garlic: activation of TRPA1 and TRPV1 in response to allicin. *Curr. Biol.* **15**, 929–934 (2005).
6. Clapham, D.E. TRP channels as cellular sensors. *Nature* **426**, 517–524 (2003).
7. Montell, C. Thermosensation, hot findings make TRPNs very cool. *Curr. Biol.* **13**, 476–478 (2003).
8. Caterina, M.J. & Julius, D. The vanilloid receptor: a molecular gateway to the pain pathway. *Annu. Rev. Neurosci.* **24**, 487–517 (2001).
9. Julius, D. & Basbaum, A.I. Molecular mechanisms of nociception. *Nature* **413**, 203–210 (2001).
10. Huang, J., Zhang, X. & McNaughton, P.A. Inflammatory pain: the cellular basis of heat hyperalgesia. *Curr. Neuropharmacol.* **4**, 197–206 (2006).
11. Jara-Oseguera, A.S., S.A. & Rosenbaum, T. TRPV1: on the road to pain relief. *Curr. Mol. Pharmacol.* **1**, 255–269 (2008).
12. Szallasi, A., Cortright, D.N., Blum, C.A. & Eid, S.R. The vanilloid receptor TRPV1: 10 years from channel cloning to antagonist proof-of-concept. *Nat. Rev. Drug Discov.* **6**, 357–372 (2007).
13. Gaudet, R. A primer on ankyrin repeat function in TRP channels and beyond. *Mol. Biosyst.* **4**, 372–379 (2008).
14. Lishko, P.V., Procko, E., Jin, X., Phelps, C.B. & Gaudet, R. The ankyrin repeats of TRPV1 bind multiple ligands and modulate channel sensitivity. *Neuron* **54**, 905–918 (2007).
15. McCleverty, C.J., Koesema, E., Patapoutian, A., Lesley, S.A. & Kreusch, A. Crystal structure of the human TRPV2 channel ankyrin repeat domain. *Protein Sci.* **15**, 2201–2206 (2006).
16. Jin, X., Touhey, J. & Gaudet, R. Structure of the N-terminal ankyrin repeat domain of the TRPV2 ion channel. *J. Biol. Chem.* **281**, 25006–25010 (2006).
17. Moiseenkova-Bell, V.Y., Stanciu, L.A., Serysheva, I.I., Tobe, B.J. & Wensel, T.G. Structure of TRPV1 channel revealed by electron cryomicroscopy. *Proc. Natl. Acad. Sci. USA* **105**, 7451–7455 (2008).
18. Jara-Oseguera, A., Llorente, I., Rosenbaum, T. & Islas, L.D. Properties of the inner pore region of TRPV1 channels revealed by block with quaternary ammoniums. *J. Gen. Physiol.* **132**, 547–562 (2008).
19. Dodier, Y. *et al.* Outer pore topology of the ECaC-TRPV5 channel by cysteine scan mutagenesis. *J. Biol. Chem.* **279**, 6853–6862 (2004).
20. Holmgren, M., Liu, Y., Xu, Y. & Yellen, G. On the use of thiol-modifying agents to determine channel topology. *Neuropharmacology* **35**, 797–804 (1996).
21. del Camino, D. & Yellen, G. Tight steric closure at the intracellular activation gate of a voltage-gated K^+ channel. *Neuron* **32**, 649–656 (2001).
22. Greenwood, A. & Earnshaw, N. *Chemistry of the Elements* 2nd edn. 1341 (Butterworth-Heinemann, Oxford, 1997).
23. Lu, Q. & Miller, C. Silver as a probe of pore-forming residues in a potassium channel. *Science* **268**, 304–307 (1995).
24. Careaga, C.L. & Falke, J.J. Thermal motions of surface α-helices in the D-galactose chemosensory receptor. Detection by disulfide trapping. *J. Mol. Biol.* **226**, 1219–1235 (1992).
25. Kobashi, K. Catalytic oxidation of sulfhydryl groups by o-phenanthroline copper complex. *Biochim. Biophys. Acta* **158**, 239–245 (1968).
26. Latorre, R., Brauchi, S., Orta, G., Zaelzer, C. & Vargas, G. ThermoTRP channels as modular proteins with allosteric gating. *Cell Calcium* **42**, 427–438 (2007).
27. Long, S.B., Campbell, E.B. & Mackinnon, R. Crystal structure of a mammalian voltage-dependent Shaker family K^+ channel. *Science* **309**, 897–903 (2005).
28. Doyle, D.A. *et al.* The structure of the potassium channel: molecular basis of K^+ conduction and selectivity. *Science* **280**, 69–77 (1998).
29. Eisenberg, D. The discovery of the α-helix and β-sheet, the principal structural features of proteins. *Proc. Natl. Acad. Sci. USA* **100**, 11207–11210 (2003).
30. Cornette, J.L. *et al.* Hydrophobicity scales and computational techniques for detecting amphipathic structures in proteins. *J. Mol. Biol.* **195**, 659–685 (1987).
31. Komiya, H., Yeates, T.O., Rees, D.C., Allen, J.P. & Feher, G. Structure of the reaction center from *Rhodobacter sphaeroides* R-26 and 2.4.1: symmetry relations and sequence comparisons between different species. *Proc. Natl. Acad. Sci. USA* **85**, 9012–9016 (1988).
32. Chung, M.K. & Caterina, M.J. TRP channel knockout mice lose their cool. *Neuron* **54**, 345–347 (2007).
33. Ding, S., Ingleby, L., Ahern, C.A. & Horn, R. Investigating the putative glycine hinge in Shaker potassium channel. *J. Gen. Physiol.* **126**, 213–226 (2005).
34. Contreras, J.E., Srikumar, D. & Holmgren, M. Gating at the selectivity filter in cyclic nucleotide-gated channels. *Proc. Natl. Acad. Sci. USA* **105**, 3310–3314 (2008).
35. Flynn, G.E. & Zagotta, W.N. A cysteine scan of the inner vestibule of cyclic nucleotide-gated channels reveals architecture and rearrangement of the pore. *J. Gen. Physiol.* **121**, 563–582 (2003).
36. Li, M., Chang, T.H., Silberberg, S.D. & Swartz, K.J. Gating the pore of P2X receptor channels. *Nat. Neurosci.* **11**, 883–887 (2008).
37. Susankova, K., Ettrich, R., Vyklicky, L., Teisinger, J. & Vlachova, V. Contribution of the putative inner-pore region to the gating of the transient receptor potential vanilloid subtype 1 channel (TRPV1). *J. Neurosci.* **27**, 7578–7585 (2007).
38. Magidovich, E. & Yifrach, O. Conserved gating hinge in ligand- and voltage-dependent K^+ channels. *Biochemistry* **43**, 13242–13247 (2004).
39. Mohapatra, D.P., Wang, S.Y., Wang, G.K. & Nau, C. A tyrosine residue in TM6 of the vanilloid receptor TRPV1 involved in desensitization and calcium permeability of capsaicin-activated currents. *Mol. Cell. Neurosci.* **23**, 314–324 (2003).
40. Oseguera, A.J., Islas, L.D., Garcia-Villegas, R. & Rosenbaum, T. On the mechanism of TBA block of the TRPV1 channel. *Biophys. J.* **92**, 3901–3914 (2007).
41. Liu, Y., Holmgren, M., Jurman, M.E. & Yellen, G. Gated access to the pore of a voltage-dependent K^+ channel. *Neuron* **19**, 175–184 (1997).
42. Grandl, J. *et al.* Pore region of TRPV3 ion channel is specifically required for heat activation. *Nat. Neurosci.* **11**, 1007–1013 (2008).
43. Brauchi, S., Orio, P. & Latorre, R. Clues to understanding cold sensation: thermodynamics and electrophysiological analysis of the cold receptor TRPM8. *Proc. Natl. Acad. Sci. USA* **101**, 15494–15499 (2004).
44. Yeh, B.I., Kim, Y.K., Jabbar, W. & Huang, C.L. Conformational changes of pore helix coupled to gating of TRPV5 by protons. *EMBO J.* **24**, 3224–3234 (2005).
45. Yellen, G., Sodickson, D., Chen, T.Y. & Jurman, M.E. An engineered cysteine in the external mouth of a K^+ channel allows inactivation to be modulated by metal binding. *Biophys. J.* **66**, 1068–1075 (1994).
46. Zheng, J. & Sigworth, F.J. Selectivity changes during activation of mutant Shaker potassium channels. *J. Gen. Physiol.* **110**, 101–117 (1997).
47. Cortes, D.M., Cuello, L.G. & Perozo, E. Molecular architecture of full-length KcsA: role of cytoplasmic domains in ion permeation and activation gating. *J. Gen. Physiol.* **117**, 165–180 (2001).

ONLINE METHODS

Molecular biology. We defined a putative S6 region for the rat TRPV1 channel from residues Gly683 to Asp654, based on previous[37,48] and our own amino acid alignments. We individually substituted each of the 30 S6 residues for a cysteine in the rTRPV1-C157A background[4], unless otherwise stated in the text, and carried out mutagenesis according to described PCR-based methods[49].

Electrophysiology and channel expression. We transfected HEK293 cells expressing large T antigen with wild-type or mutant rTRPV1-pCDNA3 and pIRES-GFP (BD Biosciences) with lipofectamine (Invitrogen) as described[40].

We carried out electrophysiological recordings using an EPC10 amplifier (HEKA Elektronik GMBH) and acquired and analyzed data with PULSE software (HEKA Elektronik) and IgorPro (Wavemetrics), respectively. Recordings were performed in the inside-out configuration of the patch-clamp technique at 20 °C. Symmetrical solutions consisted of 130 mM NaCl, 3 mM HEPES and 1 mM EDTA (pH 7.2 with NaOH) for recording except when Ag^+ was applied. We obtained all chemicals from Sigma unless otherwise stated. Solutions were changed with an RSC-200 rapid solution changer (Molecular Kinetics). Patch pipettes had a resistance of 2–4 MΩ. Currents were low-pass filtered at 2 kHz and sampled at 10 kHz.

We prepared capsaicin stock solutions (4 mM) in ethanol and diluted them to the desired concentration in recording solution. MTSET-chloride and MTSEA-chloride (Toronto Research Chemicals) stock solutions (100 mM) were prepared in water and immediately frozen at −70 °C. We diluted aliquots in recording solution to a final concentration of 2 mM before each experiment with either a saturating concentration of capsaicin (4 μM) for open-state modification or in the absence of capsaicin for closed-state modification.

We measured dose-response curves at 120 mV as the steady-state current. This was normalized to the response to 4 μM capsaicin. Capsaicin was washed off and the MTS reagents applied either in the presence or absence of capsaicin for 5 min and the dose-response was remeasured. We obtained the K_d from fits to the Hill equation:

$$\frac{I}{I_{max}} = \frac{[\text{Capsaicin}]^n}{[\text{Capsaicin}]^n + K_d^n}$$

where n is the Hill coefficient and [Capsaicin] is the agonist concentration. Leak subtraction was performed by subtracting the initial current trace in the absence of capsaicin from the traces obtained in the presence of the agonist.

For experiments using Ag^+, we followed the method described[34,35]. We prepared a stock of $AgNO_3$ (10 mM) in water before each experiment, protected it from light and diluted it in an intracellular solution consisting of 130 mM $NaNO_3$, 3 mM HEPES and 1 mM EDTA (pH 7.2 with NaOH). Using the MaxChelator software (http://maxchelator.stanford.edu), we calculated the free concentration of Ag^+ at 1 mM EDTA to be 100 nM. We measured the initial current in the absence of capsaicin at 120 mV, measured the current with 4 μM capsaicin and then either applied Ag^+ for 5 min in the presence of the agonist for open-state modification, or we washed the capsaicin off and then applied Ag^+ for 5 min in the closed state. Finally, we assessed the effects of modification using 4 μM capsaicin to activate the remaining currents. The fraction of current modified, F_m, was calculated from:

$$F_m = 1 - \frac{I_{post}}{I_{pre}},$$

where I_{post} is the current after Ag^+ treatment and I_{pre} is the current before treatment.

We measured modification rates in the open state by applying a train of 100-ms pulses at 120 mV from a holding potential of 0 mV and a frequency of 1 Hz in the presence of Ag^+ and 4 μM capsaicin, and we constructed time courses of modification in the closed state by measuring data points at a single exposure time for each patch. Several patches were averaged to obtain the whole curve. We calculated the second-order modification rate constants as the inverse of the product of the time constant obtained from fits of an exponential to the data and the modifier concentration.

For heat-activation experiments, we used a temperature-controlling recording chamber (Bipolar Temperature Controller TC-202, Medical Systems Corp). We used a thermistor (Warner Instruments) to monitor bath temperature and carried out the experiments by measuring initial currents at 42 °C. For open-state modification experiments, we applied a solution containing Ag^+ to the membrane patch at 42 °C for 0.5 min, 1 min, 3 min or 5 min. We washed out Ag^+ and remeasured current at 42 °C. For closed-state modification, the temperature was lowered to 20 °C and Ag^+ was then applied for 0.5 min, 1 min, 3 min or 5 min. Then, we remeasured the current at 42 °C to evaluate the degree of modification in the closed state and constructed time courses of modification by plotting the data at different exposure times, as mentioned above.

Periodicity analysis. We evaluated periodicity of the S6 segment using the rate of Ag^+ modification of cysteines as an index, and we carried out the analysis using discrete Fourier transform methods[30,31,50] as follows. If r_k is the rate of modification of the k-th residue and $\hat{r}$ is the mean value of r, the power spectrum $P(\varphi)$ for all the n − 1 residues is given by:

$$A(\varphi) = \sum_{k=0}^{n-1} (r_k - \hat{r}) \cos(k2\pi\varphi/360)$$

$$B(\varphi) = \sum_{k=0}^{n-1} (r_k - \hat{r}) \sin(k2\pi\varphi/360)$$

$$P(\varphi) = [A(\varphi)]^2 + [B(\varphi)]^2$$

Here φ is the angle, in degrees, subtended between each pair of amino acids. For a typical α-helix, the value of $P(\varphi)$ is expected to be maximal at 100°, which corresponds to 3.6-amino-acids per turn of the α-helix. An index of the α-helical character is the α-periodic index (αPI), which is defined as[30]:

$$\alpha\text{PI} = \frac{\left[\frac{1}{30^\circ}\right] \int_{90^\circ}^{120^\circ} P(\varphi) d\varphi}{\left[\frac{1}{180^\circ}\right] \int_{0^\circ}^{180^\circ} P(\varphi) d\varphi}$$

A value greater than 2 is typical of a segment with a high likelihood of being an amphipathic α-helix[30].

Statistical analysis. Groups of data are presented as mean ± s.e.m. We performed statistical comparisons with the Student's t-test. A value of $P < 0.05$ was considered statistically significant.

48. Brauchi, S. *et al.* Dissection of the components for PIP2 activation and thermosensation in TRP channels. *Proc. Natl. Acad. Sci. USA* **104**, 10246–10251 (2007).
49. Rosenbaum, T. & Gordon, S.E. Dissecting intersubunit contacts in cyclic nucleotide-gated ion channels. *Neuron* **33**, 703–713 (2002).
50. Li-Smerin, Y. & Swartz, K.J. Helical structure of the COOH terminus of S3 and its contribution to the gating modifier toxin receptor in voltage-gated ion channels. *J. Gen. Physiol.* **117**, 205–218 (2001).

doi:10.1038/nsmb.1633

Channels 3:5, 311-313; September/October 2009; © 2009 Landes Bioscience

The helical character of the S6 segment of TRPV1 channels

León D. Islas,[1] Héctor Salazar,[2] Andrés Jara-Oseguera,[1] Andrés Nieto-Posadas,[2] Itzel Llorente,[2] Gisela Rangel-Yescas[1] and Tamara Rosenbaum[2,*]

[1]Departamento de Fisiología; [2]Instituto de Fisiología Celular; Universidad Nacional Autónoma de México; México D.F., México

The era of molecular structure of ion channels has revealed that their transmembrane segments are alpha helices, as was suspected from hydropathy analysis and experimental data. TRP channels are recent additions to the known families of ion channels, and little structural data is available. In a recent work, we explored the conformational changes occurring at the putative S6 segment of TRPV1 channels; and we observed a periodicity of chemical modification of residues suggestive of an alpha helical structure. Further analysis of the periodicity of the disposition of hydrophobic residues in the S6 segment, suggests that the general architecture of the TRPV1 S6 segment, is very similar to that of voltage-dependent channels of known structure—an aqueous cavity lined by an amphipathic alpha helix, with most of the hydrophobic residues pointing into it.

Key words: amphipatic helix, channel gating, capsaicin receptor, channel structure, TRP channel

Submitted: 07/29/09

Accepted: 07/29/09

Previously published online: www.landesbioscience.com/journals/channels/article/9659

*Correspondence to: Tamara Rosenbaum; Email: trosenba@ifc.unam.mx

Addendum to: Salazar H, Jara-Oseguera A, Hernández-García E, Llorente I, Arias-Olguín II, Soriano-García M, et al. Structural determinants of gating in the TRPV1 channel. Nat Struct Mol Biol 2009; 16:704–10; PMID: 19561608; DOI: 10.1038/nsmb.1633.

Ion channels are membrane proteins composed of several subunits, each of which is formed by several transmembrane segments. In most know ion channels, the membrane-spanning parts of the protein were hypothesized to be alpha helices, based solely on the hydrophobic profile of their component amino acids.[1-4] In recent years, a number of potassium channels and other non-selective channels, have been studied at the structural level. The known x-ray diffraction structures of these proteins have confirmed that the transmembrane segments of ion channels are indeed alpha helical in character.[5-8] Although TRP channels were cloned initially in 1992,[9] the structural information available is scant,[10-13] and it does not include high-resolution structures of transmembrane regions. On the basis of sequence similarity with voltage-gated potassium (K_V) channels, TRP channels are thought to be tetrameric—each tetramer being formed by six transmembrane alpha helices. The pore region, again based on similarity with K_V channels and some experimental evidence,[14-16] is presumed to be formed by two transmembrane segments, equivalent to S5 and S6 and a pore loop and pore helix between them. These two transmembrane helices molecular motifs have been shown to be present in all the pores of potassium and non-selective channels whose atomic structure is known; and are also expected to be the structural basis for the pores of voltage-dependent Na^+ and Ca^{++} channels.[17-19]

Recent cryo-electron microscopic 3D reconstruction studies of TRPV1 channels at 19 Å resolution[12] reveal a large intracellular domain, possibly formed by the N- and C-termini and a smaller region consistent with the transmembrane domains. A similar albeit less well-defined bulk structure has been reported in TRPC3 channels.[20] These studies, while providing some structural information, do not clarify the architecture of the pore or other transmembrane domains. A systematic experimental approach based on the SCAM technique[15] has characterized the opening conformational changes occurring in the S6 segment of TRPV1 in a manner resembling the gating of K_V channels.[21-26] The pattern of accessibility of S6 residues shows a strong periodicity (around 3.36 residues per turn) consistent with a possible alpha helical structure for this transmembrane segment. Furthermore, this periodicity is typical

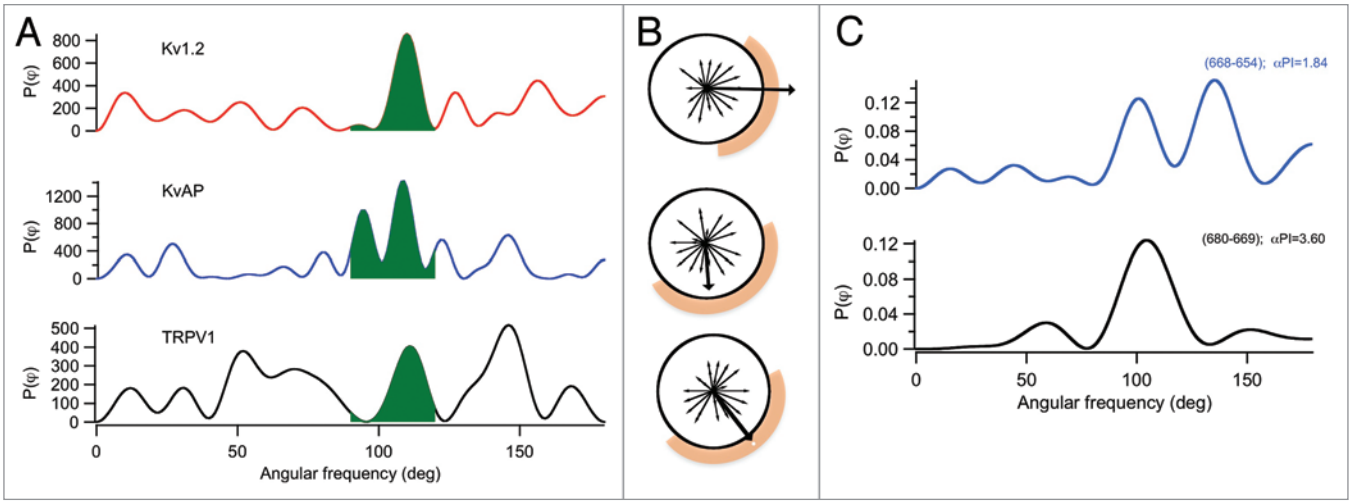

Figure 1. Analysis of periodicity of the S6 helix of K_V1.2, K_VAP and the TRPV1 model. (A) Periodicity of the hydrophobicity based on the Kite-Dolittle scale. P(ϕ) is the power spectrum as a function of the angular frequency, ϕ in degrees. The shaded area represents the region of the power spectrum corresponding to an alpha-helical structure, between 90 and 120 degrees. (B) Orientation of the hydrophobic residues of the S6 segments. Each vector has a magnitude equal to the hydrophobicity of the amino acid it represents. The angle is measured from the centre of the helix to the alpha carbon of each residue. The thick arrow is the resultant hydrophobic vector. The shaded area is the region of the S6 helix exposed to water in the lumen of the pore, estimated from the PDB files. (C) Power spectra of the two accessibility data (reviewed in ref. 15) of two halves of the TRPV1 model S6. The region of the sequence used is indicated, along with the alpha periodicity index. Upper trace is the N-terminal half and the lower trace is the more intracellular half.

of the more "open" alpha helices found in membrane proteins, which normally experience both hydrophobic and hydrophilic environments and interactions.[27]

Based on the sequence similarity between TRPV1 and K_V1.2, a homology model of the pore domain was advanced.[15] Several features of this model are supported by experimental constraints mainly provided by the accessibility data from SCAM experiments. One interesting characteristic of the pore model is that the S6 alpha helix of TRPV1 is highly amphiphilic. There are several apolar amino acids facing into the water filled inner pore cavity; a configuration that is (presumably) thermodynamically expensive. In order to assess the plausibility of such architecture, one can calculate the amphipatic character of the model TRPV1 S6 and compare it to the S6 segments of channels of known structure. While we used the Kyte-Dolittle hydrophobicity scale,[28] the results are qualitatively similar using the Eisenberg scale.[29] The S6 of the K_V1.2 and K_VAP potassium channels shows a periodic distribution of apolar residues along an alpha helix. Discrete Fourier analysis of this distribution reveals a strong peak in the power spectrum at around an angular frequency corresponding to 110° for K_V1.2 and 108° for K_VAP corresponding to a periodicity of 3.27 residues/turn and 3.33 residues/turn, respectively. This periodicity is consistent with 3.36 residues/turn periodicity observed in the accessibility data (**Fig. 1A**).[15] The amphipatic nature of the S6 helix is characterized by an amphipatic index, aPI, which is calculated in the same way as the alpha periodicity index.[30] The K_V1.2 S6 has an aPI of 1.59, while K_VAP's is 2.67. TRPV1 has an aPI of 0.98. It is generally considered that a value of aPI ≥2 represents a completely amphipatic alpha helix. Although this is clearly the case for the K_VAP S6, K_V1.2 and TRPV1, S6 segments have aPI values ≤2, indicating less amphipatic helices. This is due to the fact that these two channels have many more hydrophobic residues that tend to be distributed in hydrophobic patches, rather than on just one side of the helix. This gives rise to the other peaks at different angles in TRPV1. Nevertheless, if resulting "hydrophobic vectors" are calculated for the K_V1.2 and K_VAP S6 helices, they end up pointing in the same direction as the area of the helix that is exposed to the solvent in the pore (**Fig. 1B**). Interestingly, this is also the case for the TRPV1 S6 model helix (**Fig. 1B**, bottom), indicating that this is a general feature of the two transmembrane segments pore motif, and suggesting that the homology model of the TRPV1 pore is a good approximation.

The experimental accessibility data of the TRPV1 S6 has a strong alpha-helical periodicity, but the data also suggests that the helix may have a broken symmetry of the helix.[15] In order to assess this possibility, we split the S6 segment in two and analyzed the periodicity separately. **Figure 1C** shows that the power spectra of the two halves possess a very pronounced peak at 107°, especially the very high alpha periodicity index, αPI ≥3 of the more intracellular half. These results suggest that the S6 alpha helix of TRPV1 may have a region where the helix is bent, as can be observed on the structure of the K_V1.2 channel; however, this feature was not incorporated into our original homology model, and until an atomic detail structure of TRPV1 is available, it remains speculative.

The orientation of the side chains of the S6 helices of ion channels affects ion permeation and activation. In the case of TRPM2 and TRPM8 channels, the substitution of a hydrophobic amino acid residue with a positively charged one at the C-terminal end of the putative transmembrane segment S6, converts the ion

selectivity of both TRPM2 and TRPM8 from cation selective to anion selective.[14] On the other hand, in voltage-gated channels, hydrophobic residues in the S6 segments seem to play an important role in channel gating. For example, for $Ca_V2.3$ and $K_V1.2$, hydrophobic residues seem to control the stability of the closed and open states.[31,32] The data presented here suggest that the proposed S6 segment in TRPV1 has the same organization and properties of the S6 segments of voltage-gated channels of known structure, and it is in agreement with the proposed role of the S6 as the activation gate of TRPV1 channels.

Acknowledgements

We thank Laura Ongay, Sergio Rojas, Adrián Aguilera Jiménez, Juan Barbosa, Ana María Escalante and Félix Sierra at Instituto de FisiologíaCelular, UNAM, for expert technical support. This work was supported by grants from DGAPA-UNAM IN200308-3 to Tamara Rosenbaum and IN209209 to León D. Islas and CONACyT No. 58038 to Tamara Rosenbaum and No. 48990 to León D. Islas.

References

1. Papazian DM, Schwarz TL, Tempel BL, Jan YN, Jan LY. Cloning of genomic and complementary DNA from Shaker, a putative potassium channel gene from Drosophila. Science 1987; 237:749-53.
2. Kayano T, Noda M, Flockerzi V, Takahashi H, Numa S. Primary structure of rat brain sodium channel III deduced from the cDNA sequence. FEBS letters 1988; 228:187-94.
3. Pongs O. Molecular biology of voltage-dependent potassium channels. Physiol Rev 1992; 72:69-88.
4. Catterall WA. Cellular and molecular biology of voltage-gated sodium channels. Physiol Rev 1992; 72:15-48.
5. Doyle DA, Morais Cabral J, Pfuetzner RA, Kuo A, Gulbis JM, Cohen SL, et al. The structure of the potassium channel: molecular basis of K^+ conduction and selectivity. Science 1998; 280:69-77.
6. Dutzler R, Campbell EB, Cadene M, Chait BT, MacKinnon R. X-ray structure of a ClC chloride channel at 3.0 A reveals the molecular basis of anion selectivity. Nature 2002; 415:287-94.
7. Jiang Y, Lee A, Chen J, Ruta V, Cadene M, Chait BT, et al. X-ray structure of a voltage-dependent K^+ channel. Nature 2003; 423:33-41.
8. Long SB, Campbell EB, Mackinnon R. Crystal structure of a mammalian voltage-dependent Shaker family K^+ channel. Science 2005; 309:897-903.
9. Hardie RC, Minke B. The trp gene is essential for a light-activated Ca^{2+} channel in Drosophila photoreceptors. Neuron 1992; 8:643-51.
10. Tominaga M, Tominaga T. Structure and function of TRPV1. Pflugers Arch 2005; 451:143-50.
11. Lishko PV, Procko E, Jin X, Phelps CB, Gaudet R. The ankyrin repeats of TRPV1 bind multiple ligands and modulate channel sensitivity. Neuron 2007; 54:905-18.
12. Moiseenkova-Bell VY, Stanciu LA, Serysheva II, Tobe BJ, Wensel TG. Structure of TRPV1 channel revealed by electron cryomicroscopy. Proc Natl Acad Sci USA 2008; 105:7451-5.
13. Jin X, Touhey J, Gaudet R. Structure of the N-terminal ankyrin repeat domain of the TRPV2 ion channel. J Biol Chem 2006; 281:25006-10.
14. Kuhn FJ, Knop G, Luckhoff A. The transmembrane segment S6 determines cation versus anion selectivity of TRPM2 and TRPM8. J Biol Chem 2007; 282:27598-609.
15. Salazar H, Jara-Oseguera A, Hernandez-Garcia E, Llorente I, Arias O, II, Soriano-Garcia M, et al. Structural determinants of gating in the TRPV1 channel. Nature structural & molecular biology 2009; 16:704-10.
16. Susankova K, Ettrich R, Vyklicky L, Teisinger J, Vlachova V. Contribution of the putative inner-pore region to the gating of the transient receptor potential vanilloid subtype 1 channel (TRPV1). J Neurosci 2007; 27:7578-85.
17. Guy HR, Seetharamulu P. Molecular model of the action potential sodium channel. Proc Natl Acad Sci USA 1986; 83:508-12.
18. Shafrir Y, Durell SR, Guy HR. Models of the structure and gating mechanisms of the pore domain of the NaChBac ion channel. Biophys J 2008; 95:3650-62.
19. Beyl S, Timin EN, Hohaus A, Stary A, Kudrnac M, Guy RH, et al. Probing the architecture of an L-type calcium channel with a charged phenylalkylamine: evidence for a widely open pore and drug trapping. J Biol Chem 2007; 282:3864-70.
20. Mio K, Ogura T, Sato C. Structure of six-transmembrane cation channels revealed by single-particle analysis from electron microscopic images. Journal of synchrotron radiation 2008; 15:211-4.
21. Rothberg BS, Shin KS, Phale PS, Yellen G. Voltage-controlled gating at the intracellular entrance to a hyperpolarization-activated cation channel. The Journal of general physiology 2002; 119:83-91.
22. Liu Y, Holmgren M, Jurman ME, Yellen G. Gated access to the pore of a voltage-dependent K^+ channel. Neuron 1997; 19:175-84.
23. Holmgren M, Smith PL, Yellen G. Trapping of organic blockers by closing of voltage-dependent K^+ channels: evidence for a trap door mechanism of activation gating. The Journal of general physiology 1997; 109:527-35.
24. Rothberg BS, Shin KS, Yellen G. Movements near the gate of a hyperpolarization-activated cation channel. The Journal of general physiology 2003; 122:501-10.
25. Yellen G. The moving parts of voltage-gated ion channels. Q Rev Biophys 1998; 31:239-95.
26. Yellen G. The voltage-gated potassium channels and their relatives. Nature 2002; 419:35-42.
27. Komiya H, Yeates TO, Rees DC, Allen JP, Feher G. Structure of the reaction center from Rhodobacter sphaeroides R-26 and 2.4.1: symmetry relations and sequence comparisons between different species. Proc Natl Acad Sci USA 1988; 85:9012-6.
28. Kyte J, Doolittle RF. A simple method for displaying the hydropathic character of a protein. Journal of molecular biology 1982; 157:105-32.
29. Eisenberg D, Weiss RM, Terwilliger TC. The hydrophobic moment detects periodicity in protein hydrophobicity. Proc Natl Acad Sci USA 1984; 81:140-4.
30. Cornette JL, Cease KB, Margalit H, Spouge JL, Berzofsky JA, DeLisi C. Hydrophobicity scales and computational techniques for detecting amphipathic structures in proteins. Journal of molecular biology 1987; 195:659-85.
31. Hackos DH, Chang TH, Swartz KJ. Scanning the intracellular S6 activation gate in the shaker K^+ channel. The Journal of general physiology 2002; 119:521-32.
32. Raybaud A, Baspinar EE, Dionne F, Dodier Y, Sauve R, Parent L. The role of distal S6 hydrophobic residues in the voltage-dependent gating of $Ca_V2.3$ channels. J Biol Chem 2007; 282:27944-52.

THE JOURNAL OF BIOLOGICAL CHEMISTRY VOL. 286, NO. 28, pp. 24966–24976, July 15, 2011

Identification of a Binding Motif in the S5 Helix That Confers Cholesterol Sensitivity to the TRPV1 Ion Channel*[S]

Received for publication, March 4, 2011, and in revised form, April 25, 2011 Published, JBC Papers in Press, May 9, 2011, DOI 10.1074/jbc.M111.237537

Giovanni Picazo-Juárez[‡1], Silvina Romero-Suárez[‡], Andrés Nieto-Posadas[‡], Itzel Llorente[‡], Andrés Jara-Oseguera[§], Margaret Briggs[¶], Thomas J. McIntosh[¶], Sidney A. Simon[‖], Ernesto Ladrón-de-Guevara[§], León D. Islas[§], and Tamara Rosenbaum[‡2]

From the [‡]Departamento de Neurodesarrollo y Fisiología, División Neurociencias, Instituto de Fisiología Celular and the [§]Departamento de Fisiología, Facultad de Medicina, Universidad Nacional Autónoma de México, D.F. 04510, México and the Departments of [¶]Cell Biology and [‖]Neurobiology, Duke University Medical Center, Durham, North Carolina 27710

The TRPV1 ion channel serves as an integrator of noxious stimuli with its activation linked to pain and neurogenic inflammation. Cholesterol, a major component of cell membranes, modifies the function of several types of ion channels. Here, using measurements of capsaicin-activated currents in excised patches from TRPV1-expressing HEK cells, we show that enrichment with cholesterol, but not its diastereoisomer epicholesterol, markedly decreased wild-type rat TRPV1 currents. Substitutions in the S5 helix, rTRPV1-R579D, and rTRPV1-F582Q, decreased this cholesterol response and rTRPV1-L585I was insensitive to cholesterol addition. Two human TRPV1 variants, with different amino acids at position 585, had different responses to cholesterol with hTRPV1-Ile^{585} being insensitive to this molecule. However, hTRPV1-I585L was inhibited by cholesterol addition similar to rTRPV1 with the same S5 sequence. In the absence of capsaicin, cholesterol enrichment also inhibited TRPV1 currents induced by elevated temperature and voltage. These data suggest that there is a cholesterol-binding site in TRPV1 and that the functions of TRPV1 depend on the genetic variant and membrane cholesterol content.

The transient receptor potential (TRP)[3] family of ion channels is found throughout the animal kingdom and has been shown to subserve numerous functions. One extensively studied member of this family is the TRPV1 (Vanilloid 1) channel. Structurally, TRPV1 is thought to be a tetramer comprised of subunits each with six transmembrane domains (S1–S6), with the putative pore of the channel located between S5 and S6. It also contains large intracellular amino and carboxyl termini that have been shown to be involved both in channel gating and regulation (for review, see Ref. 1). Electrophysiological studies have shown that TRPV1 is an outwardly rectifying, non-selective, and calcium-permeable cation channel (2).

Although TRPV1 is found in many organs, it is predominantly expressed in primary sensory neurons where it acts as a sensor and integrator for noxious stimuli (2). In addition to being a temperature sensor and weakly voltage-dependent, TRPV1 is sensitive to a variety of chemicals (1). Among its many chemical agonists is capsaicin, the principal pungent compound in chili peppers. The intracellular binding pocket for capsaicin has been identified in a region that spans from S2 to S4 (for review, see Ref. 1). In addition to capsaicin, many complex amphiphilic molecules have been shown to activate or inhibit TRPV1. These include polyring compounds such as resiniferatoxin (3), quinazolinone (4), evodiamine (5), 17-β-estradiol (6), as well as molecules with long acyl and amide chains such as anandamide (7, 8), olvanil, and omega-3 polyunsaturated fatty acids (for review, see Ref. 1). Moreover, TRPV1 activity is regulated by the membrane lipid phosphatidylinositol 4,5-bisphophate (9–11).

Another important membrane lipid in terms of TRPV1 activity is cholesterol (Fig. 1). Cholesterol is a major component of plasma membranes where it increases bilayer mechanical strength, thereby helping to prevent cell lysis (12). Importantly, cholesterol has been shown to modify the function of many classes of ion channels (for review, see Ref. 13). Cholesterol can modify channel activity indirectly by altering the thickness and elastic properties of the surrounding lipid bilayer (14). In addition, in recent years compelling evidence has shown a specific interaction between cholesterol and several protein channels (13, 15). That is, based on experiments with structural analogs of cholesterol and channels with specific point mutations, it has been found that cholesterol binds to certain channel proteins, including some with structural similarities to TRPV1 (16). For either of these indirect or direct mechanisms, cholesterol modifies the energy difference between the open and closed states of the channel.

Previous studies of the effect of cholesterol on TRPV1 in whole cells showed that cholesterol depletion by incubation with methyl-β-cyclodextrin (MβCD) causes large decreases in capsaicin-evoked responses (17, 18). Both studies suggest that these effects could be due to TRPV1 being functional only when present in cholesterol-rich plasma membrane microdomains (rafts) that can modulate the activity of some receptors and

* This work was supported, in whole or in part, by National Institutes of Health Grants GM27278 (to T. J. M.) and DC-01065 (to S. A. S.) and grants Dirección General de Asuntos del Personal Académico-PAPIIT IN204111-3, Consejo Nacional de Ciencia y Tecnologia 129474, and Consejo Nacional de Ciencia y Tecnologia-SNI 102152, and a grant from Fundación Miguel Alemán (to T. R.), and IN209209 and Instituto de Ciencia y Technología del Distrito Federal PIFUTP09-262 (to L. D. I.).

[S] The on-line version of this article (available at http://www.jbc.org) contains supplemental Figs. S1–S4.

[1] Performed in partial fulfillment of the requirements for a Doctoral degree in Biomedical Sciences at the Universidad Nacional Autónoma de México.

[2] To whom correspondence should be addressed. Tel.: 52-55-5622-56-24; Fax: 52-55-5622-56-07; E-mail: trosenba@ifc.unam.mx.

[3] The abbreviations used are: TRP, transient receptor potential; MβCD, methyl-β-cyclodextrin; CRAC, cholesterol recognition amino acid consensus; DRM, detergent-resistant membranes; DSM, detergent-soluble membranes.

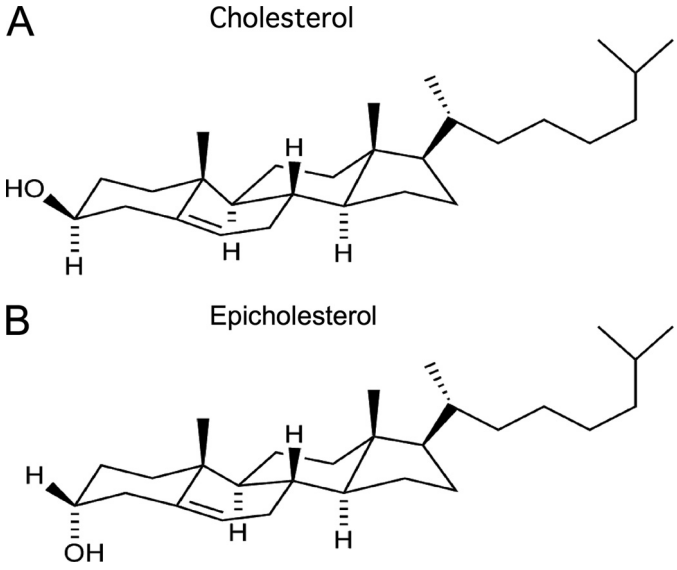

FIGURE 1. **Molecular structures of cholesterol (*A*) and epicholesterol (*B*) (α-3-OH-cholesterol epimeric form).**

transport proteins. However, cholesterol depletion from whole cells also reduces TRPV1 concentration in the plasma membrane, thus making it difficult to determine whether the observed results are due to cholesterol effects on: 1) TRPV1 located in the plasma membrane or 2) TRPV1 trafficking in the cell (17).

Given this information, we thought it important to further explore the mechanisms by which cholesterol modifies TRPV1 activity. To avoid possible effects of TRPV1 cellular trafficking, we measured capsaicin-activated currents by patch clamping excised plasma membranes from HEK293 cells containing heterologously expressed rTRPV1. We found that the rTRPV1 currents were not changed by cholesterol depletion, but were markedly decreased by cholesterol enrichment, indicating that rTRPV1 function was modulated by cholesterol concentration in the plasma membrane. Therefore we also determined the membrane microdomain location of rTRPV1.

To determine whether there were specific cholesterol-binding sites in rTRPV1 three additional series of patch clamp experiments were performed. First, epicholesterol (α-3-OH-cholesterol epimeric form) was substituted for cholesterol (see Fig. 1), as previously done with other channels (16, 19). Second, capsaicin-induced currents were measured for membranes transfected with rTRPV1s with specific point mutations in the S5 transmembrane helix, which has a sequence consistent with the cholesterol recognition amino acid consensus (CRAC) sequence found in several transmembrane proteins that bind cholesterol (20, 21). Third, currents were measured for two common hTRPV1 variants with the same S5 sequence as wild-type rTRPV1 except for one amino acid residue in the hydrophobic region of the helix. In addition, experiments were performed to determine whether cholesterol enrichment also modified heat-activated and voltage-activated TRPV1. The results from these experiments indicate that there is a cholesterol-binding site in the TRPV1 S5 helix that when occupied by cholesterol prevents the channels from opening.

EXPERIMENTAL PROCEDURES

HEK293 Cell Culture and Capsaicin-induced Currents—HEK293 cells expressing large T antigen were transfected with wild-type and mutant pCDNA3-rTRPV1 and pIRES-GFP (BD Biosciences) with Lipofectamine (Invitrogen) following previously described methods (22, 23). Inside-out and outside-out patch clamp recordings of TRPV1 were made using Ca^{2+}-free symmetrical solutions consisting of 130 mM NaCl, 3 mM HEPES (pH 7.2), and 1 mM EDTA. Solutions were changed with an RSC-200 rapid solution changer (Molecular Kinetics, Pullman, WA). Unless otherwise indicated, all chemicals were purchased from Sigma.

Capsaicin-activation curves were measured at 120 mV and normalized to a saturating capsaicin concentration (4 μM). Dose-response relationships were fitted with the Hill equation,

$$\frac{I}{I_{max}} = \left(\frac{[cap]}{[cap] + K_{1/2}}\right)^{n_H} \quad \text{(Eq. 1)}$$

where I is the mean current, I_{max} is the maximum current, $K_{1/2}$ is the capsaicin concentration at $I = I_{max}/2$, n_H is the Hill coefficient, and [cap] is the capsaicin concentration.

Currents were low-pass filtered at 2 kHz and sampled at 10 kHz with an EPC 10 amplifier (HEKA Elektronik GMBH, Pfalz, Germany). For macroscopic current recordings, the following voltage protocol was used: patches were initially held at 0 mV for 10 ms, and voltage was then stepped from 0 to −120 to 120 mV in 10-mV increments for 100 ms, and then returned back to 0 mV for 10 ms. These recordings were performed at room temperature (19 ± 3 °C). For all experiments, leak currents in the absence of capsaicin were subtracted from currents in the presence of capsaicin.

Time courses of modification by cholesterol and epicholesterol were obtained by holding the membrane potential to 0 mV and then pulsing to +120 mV for 100 ms every 10 min in the presence of 4 μM capsaicin. Data were acquired and analyzed with PULSE software (HEKA Elektronik, Germany) and were plotted and analyzed with programs written using Igor Pro (Wavemetrics Inc., Portland, OR).

Noise Analysis—To determine the value of the open probability (P_o), the number of channels in the patch (N), and the single-channel current (i), we performed stationary noise analysis of macroscopic current traces activated by capsaicin at a voltage of 100 mV. Because currents activated instantaneously with voltage pulses, we changed the open probability by varying the concentration of capsaicin. For each patch, the mean (I) and variance (δ^2) were determined from 50 to 80 current traces using the algorithm of Heinemann and Conti (24). Traces were recorded for increasing capsaicin concentrations of 0.01, 0.025, 0.05, 0.1, 0.25, 0.5, 1, and 4 μM before application of MβCD:cholesterol and again after 60 min in the presence of MβCD:cholesterol. Mean *versus* variance plots were fitted to the function in Equation 2.

$$\delta^2 = iI - \frac{I}{N} \quad \text{(Eq. 2)}$$

The open probability was calculated from the relationship in Equation 3.

$$P_o = I/iN \quad \text{(Eq. 3)}$$

Single-channel currents were recorded at room temperature in inside-out patches using the same solutions as for macroscopic currents. Pipettes were pulled from borosilicate glass, covered with dental wax to reduce stray capacitance, and fire polished to a resistance of 10–15 MΩ (22, 23). Currents were filtered at 2 kHz and sampled at 5 kHz. Thirty to fifty 500 ms pulses obtained at 60 mV were delivered every 200 ms and collected continuously in the presence 4 μM capsaicin before and after exposure to cholesterol:MβCD. Single-channel openings were detected with the 50% threshold crossing technique (25). Single channel traces were leak subtracted with a leak template formed by the average of 5–10 null sweeps. The open probability of each sweep was calculated and plotted as a function of time.

Temperature- and Voltage-induced Currents—For heat activation experiments, we used a temperature controlling recording chamber (Bipolar Temperature Controller TC-202, Medical Systems Corp, Greenvale, NY). The bath temperature was measured with a thermistor (Warner Instruments, Hamden, CT). Experiments were conducted at 52 °C for initial and cholesterol:MβCD-exposed currents (60 min). At this temperature the maximal thermally induced current is evoked.

Currents activated exclusively by voltage were recorded at room temperature in the presence of Ca^{2+}-free symmetrical solutions consisting of 200 mM NaCl, 3 mM HEPES (pH 7.2), and 1 mM EDTA. The voltage protocol used was: patches were initially held at 0 mV for 10 ms, and voltage was then stepped from −120 to 200 mV in 20-mV increments for 50 ms, and then returned back to 0 mV for 10 ms.

Modeling of TRPV1-Cholesterol Interaction—The structure of TRPV1 used for docking is that proposed by Fernández-Ballester and Ferrer-Montiel (26), which is a homology model based on the x-ray crystal structure of Kv1.2 (27). All dockings were carried out with the program Autodock 4.2 (28) with a Lamarckian genetic algorithm running on a desktop PC. Autodock Tools (ADT) was used to prepare files. The calculation was performed with 2.5 million evaluation steps for each conformation. The resulting 200 low-energy structures were grouped into clusters with structural deviations below 2.0-Å root mean square deviations (28). A highly populated cluster is used by Autodock as a criterion to validate the possibility of a real interaction (28). Our calculations resulted in several docking sites with similar conformations, including a single cluster of 36 conformations with cholesterol bound to the CRAC site (20, 21) in the S5 helix. Only the more populated clusters with lowest energy dockings were analyzed for protein-ligand contacts (LPC/CSU server) (see Ref. 29) (data not shown).

Cholesterol and Epicholesterol Treatments—To decrease or increase the membrane cholesterol (Avanti Polar Lipids, Alabaster, AL) content the patch was incubated with MβCD (Sigma) or 10:1 MβCD:cholesterol, respectively (30). For all experiments the concentration of MβCD was 3.3 mg/ml and for MβCD:cholesterol the concentration was 0.08 mg/ml. Epicholesterol (Fig. 1*B*) (Steraloids Inc., Newport, RI) was added to the membrane by incubating the patch with 10:1 MβCD:epicholesterol (0.08 mg/ml) (31, 32).

Site-directed Mutagenesis—Constructs were generated by introducing mutations into the wild-type rTRPV1 and into the hTRPV1-Ile^{585} channels. Point mutations were constructed by a two-step PCR procedure as previously described (33).

Detergent Isolation—Detergent-resistant membranes (DRMs) and detergent-soluble membranes (DSMs) were separated by standard techniques (34). HEK293 cells were treated with 1% Triton X-100 for 30 min at 4 °C and then applied to a discontinuous (5/35/45%) sucrose density gradient and analyzed by Western blots using a TRPV1 antibody obtained from Santa Cruz Biochemicals. Raft fractions were identified by blotting of the raft lipid GM1 with HRP-labeled cholera toxin (35, 36). Detergent isolations were performed with no pretreatments, as well as with the same treatments with MβCD:cholesterol and MβCD used in the patch clamp experiments.

Statistical Analysis—Statistical comparisons were made with an analysis of variance test. $p < 0.05$ was considered statistically significant. All pooled data are presented as mean ± S.E.

RESULTS

Increased Membrane Cholesterol Decreased Capsaicin-induced rTRPV1 Currents—Cholesterol is known to modify the trafficking of TRPV1 to the plasma membrane (17), as well as regulate the activity of some classes of channels (13). To isolate the effects of cholesterol on TRPV1 in the membrane from cellular trafficking processes, we measured currents from excised membrane patches of HEK293 cells containing heterologously expressed rat or human TRPV1. These patches were incubated with MβCD or 10:1 MβCD:cholesterol to modify membrane cholesterol content (30).

Depletion of membrane cholesterol with MβCD had no effect on capsaicin-induced rTRPV1 currents (supplemental Fig. S1*A*). However, at room temperature, augmentation of cholesterol with MβCD:cholesterol significantly decreased capsaicin-evoked currents (Fig. 2). Representative current traces at 120 mV (Fig. 2*A*) showed that after a 60-min incubation with MβCD:cholesterol the capsaicin-induced current decreased about 70% (Fig. 2*B*). Control experiments showed that even after longer incubation times in the absence of MβCD:cholesterol, the currents did not markedly decrease (rundown) (Fig. 2*B*). In the presence of 10:1 MβCD:cholesterol, the capsaicin-evoked current decreased exponentially with a time constant of $\tau = 29$ min (shown in Fig. 4*C*). Importantly, we found that the decrease in current seen upon cholesterol addition was reversible. That is, after a subsequent 10-min incubation of the cholesterol-enhanced patch with MβCD alone, the current increased to 83 ± 8% of control values (Fig. 2*E* and supplemental Fig. S1*B*).

We also measured the effects of cholesterol on capsaicin dose-response curves and current-voltage (I-V) relationships. Dose-response relationships showed that the cholesterol-induced reduction in current at 30 and 60 min incubation with MβCD:cholesterol occurred over a range of capsaicin concentrations (Fig. 2*C*). The capsaicin dose-response curves were fit to the Hill equation (Equation 1) and the $K_{1/2}$ values were 317 ±

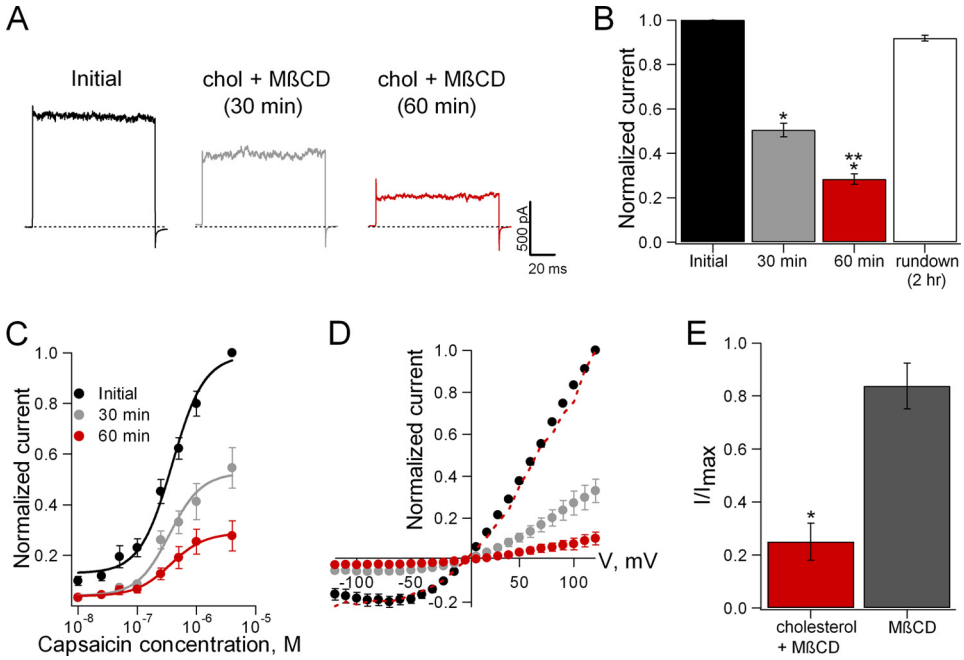

FIGURE 2. **Cholesterol enhancement reduced currents in TRPV1-expressing plasma membrane patches.** *A,* representative current traces elicited by 4 μM capsaicin at 120 mV from inside-out patches before (*black*), 30 min (gray), and 60 min (*red*) after the application of 10:1 MβCD:cholesterol (0.08 mg/ml). *B,* bar chart of average currents as in *A* before (*black*, $n = 38$) and after 30 min (*dark gray*, 0.5 ± 0.03, $n = 38$) and 60 min (*red*, 0.28 ± 0.02, $n = 31$) of MβCD:cholesterol exposure. The *white bar* is current "rundown" after 2 h in the absence of MβCD:cholesterol (0.92 ± 0.01, $n = 5$). Data were normalized to initial currents (*black bar*). * denotes $p < 0.01$ between the initial current and 30 or 60 min with MβCD:cholesterol, and ** between 30 and 60 min with MβCD:cholesterol. *C,* dose-response relationship for capsaicin activation before (*black*, $K_{1/2} = 317 \pm 33$ nM, $n_H = 1.6 \pm 0.1$) and after 30 min (*gray*, $K_{1/2} = 349 \pm 35$ nM, $n_H = 1.5 \pm 0.1$) or 60 min (*red circles*, $K_{1/2} = 323 \pm 23$ nM, $n_H = 1.5 \pm 0.3$) exposure to MβCD:cholesterol. Smooth curves are fits with the Hill equation (Equation 1) ($n = 6$). *D,* current-voltage relationships before (*black*), after 30 (*gray*) and 60 min incubation with MβCD:cholesterol (*red*). The *red dotted curve* represents normalized currents after 60 min of cholesterol with respect to its own maximal current value. *E,* cholesterol-induced current-reduction was reversible (also see supplemental Fig. S1); the *red bar* is the average current after 60 min of MβCD:cholesterol (0.25 ± 0.07) and the *gray bar* represents currents after subsequent 1 mM MβCD treatment for 10–30 min (0.83 ± 0.08, $n = 5$).

33 nM (mean ± S.E.) before MβCD:cholesterol treatment, 323 ± 23 nM after a 30-min MβCD:cholesterol treatment, and 349 ± 35 nM after a 60-min MβCD:cholesterol treatment, respectively. The Hill coefficients (n_H values) were 1.6 ± 0.1 before MβCD:cholesterol treatment, 1.5 ± 0.1 after 30 min MβCD:cholesterol treatment, and 1.5 ± 0.3 after 60 min MβCD:cholesterol treatment, respectively. The observation that these values of $K_{1/2}$ and n_H were not statistically changed ($p > 0.05$) provides evidence that the binding of capsaicin to its sites on TRPV1 was not markedly altered by the addition of cholesterol. In the absence of additional cholesterol, the observed TRPV1 current-voltage relationship was, as expected, outwardly rectifying with a reversal potential of near 0 mV (Fig. 2*D*). Although the addition of cholesterol decreased the capsaicin-evoked current over 60 min, it did not appreciably alter the outwardly rectifying nature of the I-V relationship (Fig. 2*D*), as the scaling of the I-V relationship at 30 and 60 min gave shapes similar to the initial I-V relationship (see *red dotted line* representing normalization of data for 60 min of cholesterol exposure to its own maximal current value). Thus, the addition of cholesterol reversibly decreased the capsaicin-induced current, without changing the binding of capsaicin to the channel or the outwardly rectifying nature of the current-voltage relationship.

To further explore the underlying cause of these observed cholesterol decreases in capsaicin-induced rTRPV1 currents, we performed noise analysis on rTRPV1 channels (37) in the presence and absence of cholesterol. Fig. 3*A* presents the experimental results at varying concentrations of capsaicin, showing good parabolic fits to current-variance *versus* the mean current both before and after MβCD:cholesterol incubation. Note that the initial slope of the curves before (*black*) and after MβCD:cholesterol incubation (*gray*) were almost the same, suggesting that the open channels were unchanged. Values of P_o, i, and N obtained from the fits shown in Fig. 3*A* and the relationship $P_{o\,max} = I/iN$ showed that after incorporation of cholesterol both i (6.85 ± 1.41 pA and 7.96 ± 1.75 pA, before and after cholesterol, respectively) and $P_{o\,max}$ (0.95 ± 0.17 and 0.89 ± 0.33 before and after cholesterol, respectively) remained nearly constant, whereas N decreased about 70% after a 60-min incubation ($N_{after}/N_{before} = 0.32 \pm 0.06$) (Fig. 3*B*). The noise data suggests that the effect of cholesterol is to reduce the number of functional channels in the patch. In single-channel recordings we confirmed that cholesterol enhancement did not alter the single-channel current and that there were not appreciable changes in open probability (Fig. 3, *C* and *D*), until the channel suddenly disappeared from the recording after a few minutes in the presence of MβCD:cholesterol (Fig. 3, *C* and *D*).

Thus, the incorporation of cholesterol into the membrane markedly and reversibly decreased capsaicin-induced rTRPV1 currents. We next considered if these current decreases were due to a specific cholesterol interaction with rTRPV1 by measuring currents for: 1) membranes augmented with epicholesterol and 2) membranes containing rTRPV1 with point mutations in the S5 helix at the interface with the plasma membrane.

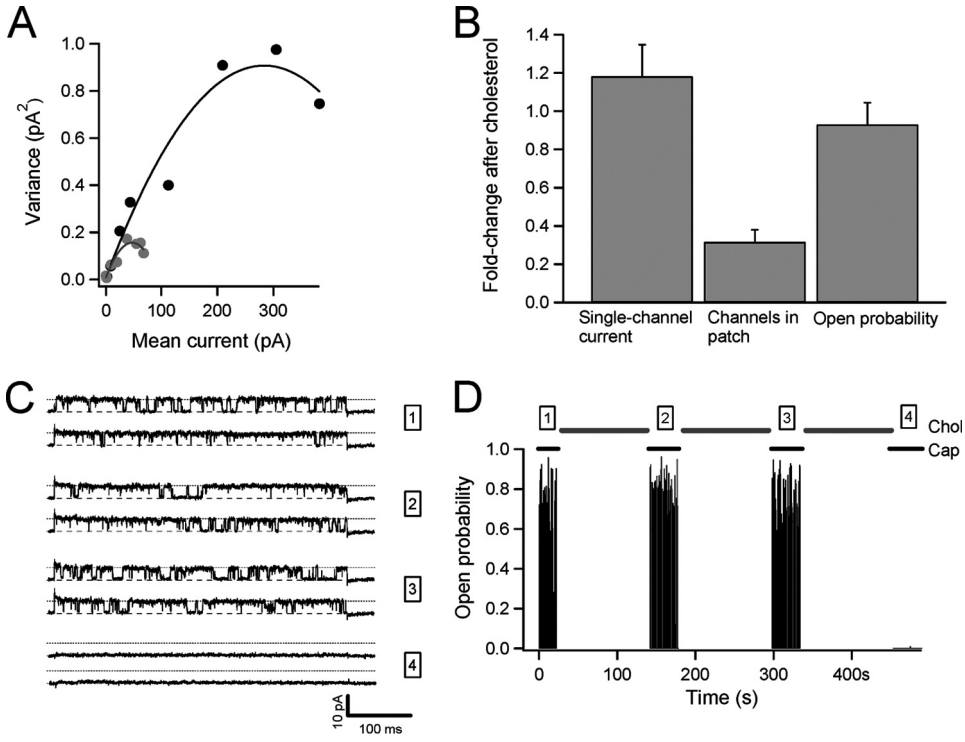

FIGURE 3. **Noise and single-channel analysis of the cholesterol effect on TRPV1 currents.** *A,* the mean variance relationship of membrane patches at 120 mV before (*black*) and after 10:1 MβCD:cholesterol applied for 60 min (*gray*). The fits using Equation 2 under "Experimental Procedures" are shown as *solid curves* and give the following parameters: before cholesterol, single channel current, $i = 6.4$ pA, number of functional channels in the patch, $n = 88$, open probability (4 μM capsaicin), $P_o = 0.67$. After cholesterol, $i = 6.5$ pA, $n = 15$, and $P_o = 0.7$. *B,* bar graph depicting the fold-change in these channel parameters as a result of MβCD:cholesterol application for $n = 5$ patches. *C,* consecutive current traces before (*1*), after 2 min (*2*), 4 min (*3*), and 5 min (*4*) of MβCD:cholesterol application. The channel parameters are not altered by cholesterol until the channel can no longer be opened by capsaicin. The single channel current, *I,* before and after MβCD:cholesterol are 5.96 ± 1.2 and 5.75 ± 1.4 pA, respectively, as estimated from the all points histogram. *D,* single-channel open probability as a function of time calculated from each current trace at 60 mV. 10:1 MβCD:cholesterol was applied for 2 min in three occasions before the channel was unable to open in the presence of 4 μM capsaicin. The *numbers in boxes* correspond to the traces in *C*.

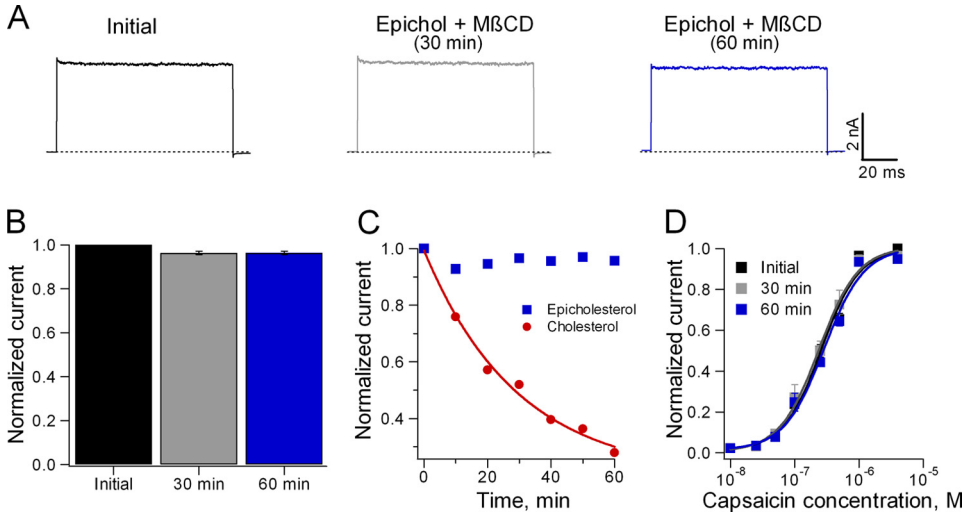

FIGURE 4. **Epicholesterol, a α-3-OH diasteroisomer of cholesterol, does not mimic the effects of cholesterol on TRPV1-mediated currents.** *A,* representative current traces from inside-out excised patches elicited as described in the legend to Fig. 2. The *black trace* represents the initial current before the application of 10:1 MβCD:epicholesterol (0.08 mg/ml) for 30 min (*gray trace*) and 60 min (*blue trace*). *B,* bar chart of average of currents elicited by 4 μM capsaicin before (*black*, $n = 5$), after 30 (*gray*; 0.96 ± 0.007, $n = 5$) and 60 min (*blue*, 0.96 ± 0.008, $n = 5$) of MβCD:epicholesterol exposure. Data were normalized to the initial currents obtained in the presence of 4 μM capsaicin (*black bar*). *C,* time courses for current reduction by treatment with MβCD:cholesterol (*red circles*) and MβCD:epicholesterol (*blue squares*). For MβCD:cholesterol, the *solid curve* represents a single exponential fit with a time constant of $\tau = 27 \pm 5$ min, $n = 6$ for each case. *D,* dose-response curves to capsaicin before (*black*, $K_{1/2} = 263 \pm 9$ nM, $n_H = 1.6 \pm 0.1$) and after incubation with MβCD:epicholesterol for 30 min (*gray*, $K_{1/2} = 260 \pm 16$ nM, $n_H = 1.5 \pm 0.4$), and for 60 min (*blue*, $K_{1/2} = 234 \pm 34$ nM, $n_H = 1.6 \pm 0.11$) at 120 mV. Data were normalized to the current obtained in the presence of 4 μM capsaicin. The *solid curves* are fits of the data with the Hill equation, $n = 5$ for each case.

Epicholesterol Had No Effects on Capsaicin-induced rTRPV1 Currents—The incubation of a membrane patch with MβCD:epicholesterol produced no significant decreases in capsaicin-evoked currents (Fig. 4, *A* and *B*) over the same time course used for cholesterol treatment (Fig. 4*C*). Moreover, the observed capsaicin dose-response relationship overlapped in

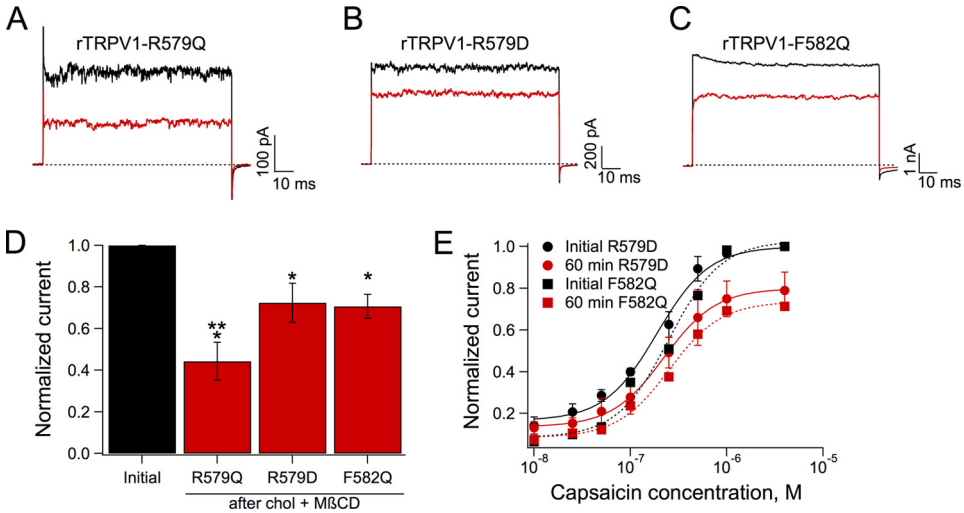

FIGURE 5. **Amino acids Arg^{579} and Phe^{582} in S5 constitute part of a binding site for cholesterol.** Representative current traces (as in Fig. 1) for *A,* rTRPV1-R579Q, *B,* rTRPV1-R579D, and *C,* rTRPV1-F582Q in inside-out excised patches before (*black*) and after incubation with 10:1 MβCD:cholesterol for 60 min (*red*). *D,* bar chart of average of currents elicited by 4 μM after 60 min of exposure to MβCD:cholesterol for rTRPV1-R579Q (0.44 ± 0.09, $n = 5$), rTRPV1-R579D (0.72 ± 0.09, $n = 5$), and rTRPV1-F582Q (0.70 ± 0.06, $n = 5$) mutants. Data were normalized to the initial currents obtained in the presence of 4 μM. * denotes significant differences with respect to initial values ($p < 0.01$) and ** with respect to R579D and F582Q ($p < 0.01$). *E,* capsaicin dose-response curves before (*black circles* and *squares*, $K_{1/2} = 192 \pm 14$ nM, $n_H = 1.6 \pm 0.25$ and 237 ± 49 nM, $n_H = 1.7 \pm 0.3$ for rTRPV1-R579D and rTRPV1-F582Q, respectively) and after treatment with MβCD:cholesterol (*red circles* and *squares*, $K_{1/2} = 218 \pm 32$ nM, $n_H = 1.5 \pm 0.15$ and 250 ± 32 nM, $n_H = 1.7 \pm 0.23$ for rTRPV1-R579D and rTRPV1-F582Q, respectively). $n = 5$ for each case.

the absence and presence of epicholesterol (Fig. 4*D*), giving $K_{1/2} = 260 \pm 16$ nM, $n_H = 1.5 \pm 0.4$, and $K_{1/2} = 234 \pm 34$ nM, $n_H = 1.6 \pm 0.11$ after MβCD:epicholesterol incubation for 30 and 60 min, respectively. That cholesterol and epicholesterol had significantly different effects on capsaicin-induced rTRPV1 currents (Fig. 4) suggests that there is stereospecificity in the ability of cholesterol to inhibit the capsaicin-evoked currents.

Currents from rTRPV1 with Point Mutations in Transmembrane Helix S5—We next measured capsaicin-induced currents from control and MβCD:cholesterol-treated patches containing heterologously expressed rTRPV1 with point mutations at different positions in transmembrane helix S5 where we had found a CRAC sequence (Fig. 7*A*). Fig. 5 shows the effects of changing the positively charged arginine (Arg) with the negatively charged aspartic acid (Asp) at residue 579 (near the edge of the transmembrane region), and the aromatic phenylalanine (Phe) with the polar amino acid glutamine (Gln) at position 582 (in the hydrophobic region). Cholesterol augmentation reduced the measured currents for both rTRPV1-R579D and rTRPV1-F582Q (Fig. 5, *B–D*). Both mutants gave similar capsaicin dose-response curves (Fig. 5*E*). The coefficients before MβCD:cholesterol treatment were $K_{1/2} = 192 \pm 14$ nM, $n_H = 1.6 \pm 0.25$ and 237 ± 49 nM, $n_H = 1.7 \pm 0.3$ for rTRPV1-R579D and rTRPV1-F582Q, respectively, and after treatment with MβCD:cholesterol $K_{1/2} = 218 \pm 32$ nM, $n_H = 1.5 \pm 0.15$ and 250 ± 32 nM, and $n_H = 1.7 \pm 0.23$ for rTRPV1-R579D and rTRPV1-F582Q, respectively. Moreover, when residue 579 was changed to an electically neutral amino acid (R579Q), the effects of cholesterol on capsaicin-activated currents were augmented with respect to the R579D mutation, thereby pointing to the importance of the presence of the charge at this site (Fig. 5, *A* and *D*).

Representative current traces (Fig. 6*A*) and normalized currents (Fig. 6*B*) from membrane patches containing rTRPV1-L585I showed that the capsaicin-induced current was essentially unchanged after MβCD:cholesterol treatment, as were the capsaicin dose-response curves (Fig. 6*C*), giving $K_{1/2} = 382 \pm 16$ nM, $n_H = 1.6 \pm 0.03$ before treatment and $K_{1/2} = 396 \pm 5$ nM, $n_H = 1.5 \pm 0.02$ after MβCD:cholesterol for 60 min. Thus, this single point mutation at residue 585 in S5 essentially abolished the large inhibitory cholesterol effects of wild-type rTRPV1 (Fig. 2). Consistently, the addition of cholesterol did not noticeably alter the shape of the I-V relationship in this mutant (data not shown).

Comparisons of rTRPV1 and hTRPV1 Variants—Human TRPV1 has two common variants containing natural point mutations at residue 585, with isoleucine (variant 1) or valine (variant 2) at that residue (38) (Fig. 7*A*). Cholesterol augmentation with MβCD:cholesterol had quite different effects for variant 1 and for this variant mutated at position 585 to have the same S5 sequence as variant 2 (hTRPV1-I585V). Specifically, cholesterol augumentation had no appreciable effect on capsaicin-induced currents for membranes containing hTRPV1-Ile^{585} (Fig. 7, *B* and *D*), whereas cholesterol augumentation reduced by about 35% the currents for membranes with hTRPV1-I585V (Fig. 7, *C* and *D*). However, the decrease in currents produced by cholesterol augmentation was greater for wild-type rTRPV1 than for either hTRPV1 variant (Fig. 7*D*). The values of $K_{1/2}$ were not significantly different for the two hTRPV1 variants before (217 ± 28 and 232 ± 26 nM for hTRPV1-Ile^{585} and hTRPV1-I585V, respectively) and after treatment with MβCD:cholesterol (185 ± 30 and 204 ± 37 nM for hTRPV1-Ile^{585} and hTRPV1-I585V, respectively) (Fig. 7*E*). Incubation with MβCD:cholesterol did not alter the shape of the I-V relationship for either hTRPV1-Ile^{585} or hTRPV1-I585V (Fig. 7, *F* and *G*).

We next measured capsaicin-induced currents and cholesterol sensitivity for hTRPV1-I585L, which was of interest because it has the same S5 sequence as wild-type rTRPV1 (Fig.

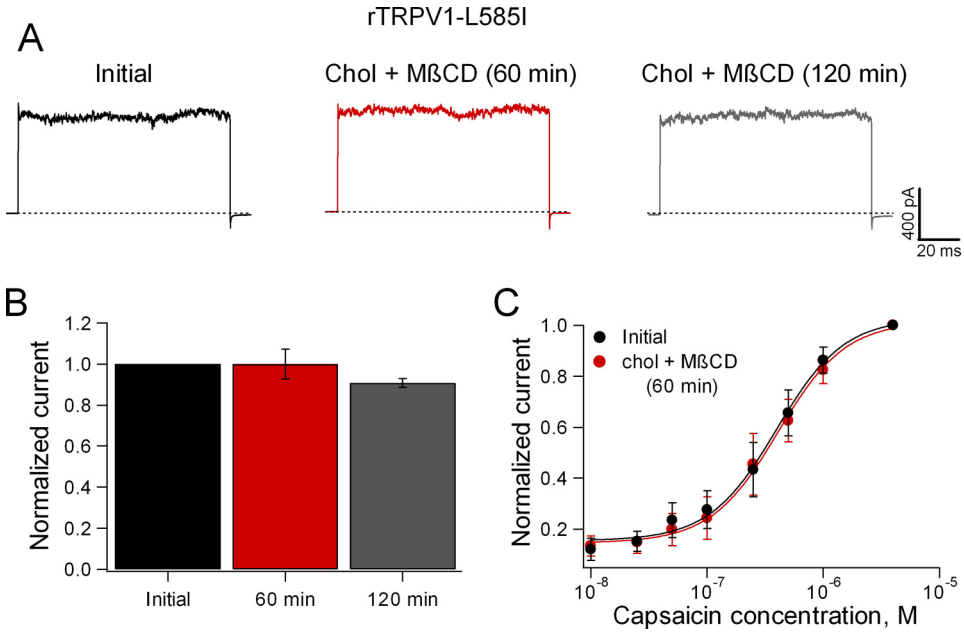

FIGURE 6. **Mutation of amino acid Leu^{585} in the S5 transmembrane segment abolished the effects of cholesterol on rTRPV1-mediated currents.** *A*, representative current traces from inside-out excised patches expressing the rTRPV1-L585I mutant elicited as described in the legend to Fig. 2 before (*black*) and after incubation of membrane patches for 60 (*red*) and 120 min (*gray*) with 10:1 MβCD:cholesterol. *B*, bar chart of average currents elicited by 4 μM capsaicin before (*black*, $n = 5$), after 60 (*red*, 1 ± 0.07, $n = 10$) and 120 min (*gray*, 0.91 ± 0.02, $n = 5$) MβCD:cholesterol exposure. Data were normalized to the initial currents obtained in the presence of 4 μM (*black bar*). *C*, dose-response curves to capsaicin with Hill equation fits before (*black*, $K_{1/2} = 382 \pm 16$ nM, $n_H = 1.6 \pm 0.03$) and after MβCD:cholesterol for 60 min (*red*, $K_{1/2} = 396 \pm 5$ nM, $n_H = 1.5 \pm 0.02$). Data were normalized to the current obtained in the presence of 4 μM capsaicin ($n = 4$ for each case).

7*A*). For hTRPV1-I585L augmentation of cholesterol decreased the capsacin-induced currents (Fig. 8*A*) to about the same extent and with the same time course as wild-type rTRPV1 (Fig. 8*B*). Moreover, the Hill parameters were unchanged from that of rTRPV1 (Fig. 8*C*) and so was the I-V relationship (data not shown). These electrophysiological data demonstrate the importance of residue 585 in S5 for the cholesterol sensitivity of TRPV1. Importantly, the inhibitory effects of cholesterol enhancement on capsaicin-induced rTRPV1 currents were also found in the absence of capsaicin when rTRPV1 was activated thermally at 52 °C (supplemental Fig. S2, *A* and *B*) as well as by voltage (supplemental Fig. 2, *C* and *D*).

Model of Cholesterol-binding Site—The three residues we show here to be important for cholesterol binding are predicted to be in the S5 transmembrane segment and would be facing the same side of this α-helix. In other proteins (20) a cholesterol consensus motif has been proposed to be formed by a cleft in the membrane protein located at a membrane interfacial region and containing at least a positively charged residue and an aromatic residue.

To get an idea of the physical appearance of the CRAC sequence in TRPV1, we examined the two available homology models of the transmembrane domains of TRPV1 (26, 39). In both cases, amino acids Arg^{579}, Phe^{582}, and Leu^{585} are facing the lipid-exposed side of the S5 helix and the sequence is very similar to the cholesterol consensus motif in β-adrenergic receptors (20). We carried out a docking experiment using the model of Fernández-Ballester and Ferrer-Montiel (26) as a docking template and cholesterol as the ligand. Fig. 9 shows the 5 best structures of cholesterol docked in the S5 of TRPV1. These correspond to a larger cluster (36 of 200 results with root mean square deviations below 2 Å) interacting at the site identified by mutagenesis, calculated with the Autodock suite. In this model of cholesterol binding, the OH group makes a possible electrostatic interaction with Arg^{579} and the flat α-face of cholesterol is stacked against Phe^{582}, which is an interaction seen very often in crystal structures of proteins bound to cholesterol and other sterols (20, 40). The important interaction with residue Leu^{585} seems to be mediated by the aliphatic tail of cholesterol, which enters an incipient cavity formed by Leu^{585} and other hydrophobic residues. When Leu^{585} is mutated to an Ile residue, the cavity is reduced in size, suggesting an explanation for the lack of effect of cholesterol in L585I and the Ile^{585} human isoform. Modeling also suggests a reason why epicholesterol might not be able to favorably interact with TRPV1. Epicholesterol can be docked in the same general site as cholesterol with poor clustering results (9/200 below 2-Å root mean square deviations, see "Experimental Procedures") (supplemental Fig. S3). The aliphatic tail of epicholesterol makes an interaction with Leu^{585}, but the position of the OH group on the α-face (Fig. 9) increases its van der Waals volume, as compared with cholesterol, making it difficult for Phe^{582} to interact with the α-face of epicholesterol. The increased volume also makes the simultaneous interaction with all three residues more energetically unfavorable.

TRPV1 Was in Detergent-soluble Membranes—Because previous electrophysiological studies have suggested that rTRPV1 is primarily localized in membrane raft microdomains (17, 18), we performed studies to determine whether rTRPV1 extracts with DSMs or DRMs from HEK293 cells. DSMs, which contain relatively low concentrations of cholesterol, and DRMs, which have higher cholesterol concentrations, are thought to corre-

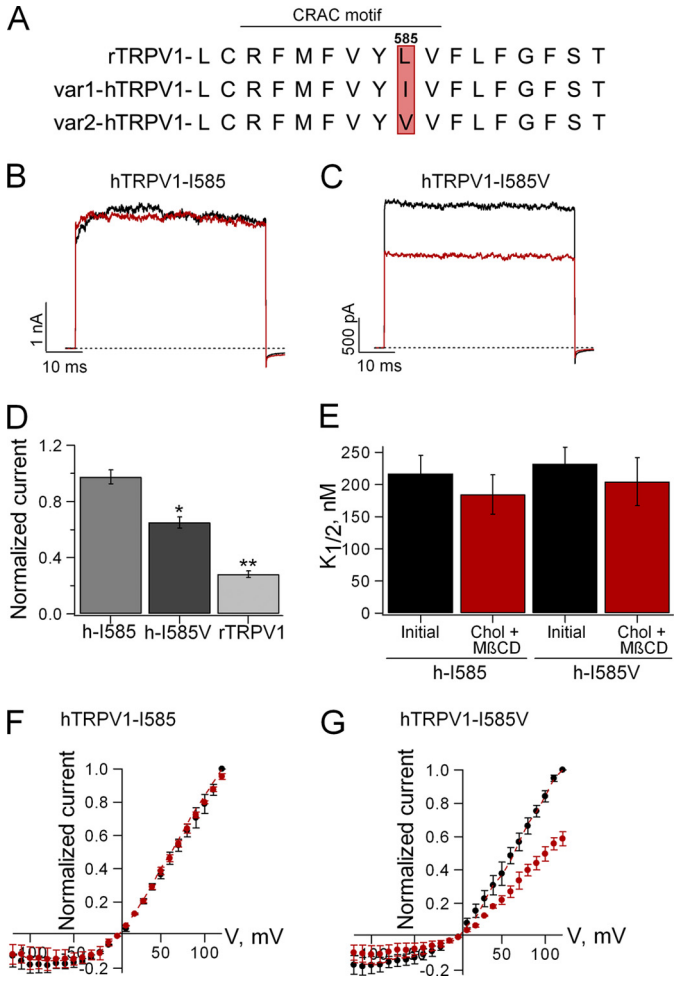

FIGURE 7. **Cholesterol enhancement of responses for two human TRPV1 variants.** *A,* sequence alignment of the S5 transmembrane segment of rTRPV1 and two common hTRPV1 variants, variant "1" with Ile^{585} and variant "2" with Val^{585}. The CRAC motif is noted. The *red box* highlights amino acid 585. Representative current traces from inside-out excised patches elicited by 4 μM capsaicin before (*black*) and after 60 min (*red*) incubation with 10:1 MβCD:cholesterol for *B,* hTRPV1-I585, and *C,* hTRPV1-I585V. *D,* bar chart of average currents elicited by 4 μM after 60 min of exposure to MβCD:cholesterol for hTRPV1-Ile^{585} (0.97 $\pm$ 0.05, $n = 9$) and hTRPV1-I585V (0.65 $\pm$ 0.04, $n = 8$) variants and rTRPV1 (0.28 $\pm$ 0.02, $n = 31$). MβCD:cholesterol data were normalized to the initial currents obtained in the presence of 4 μM. * denotes significant differences with respect to hTRPV1-Ile^{585} ($p < 0.05$) and ** denotes a difference of rTRPV1 with respect to both human variants ($p < 0.01$). *E,* capsaicin sensitivities before (*black*, $K_{1/2} = 217 \pm 28$ nM, $n_H = 1.4 \pm 0.08$ and 232 $\pm$ 26 nM, $n_H = 1.4 \pm 0.07$ for hTRPV1-Ile^{585} and hTRPV1-I585V, respectively) and after treatment with MβCD:cholesterol (*red,* $K_{1/2} = 185 \pm 30$ nM, $n_H = 1.5 \pm 0.08$ and 204 $\pm$ 37 nM, $n_H = 1.4 \pm 0.09$ for hTRPV1-Ile^{585} and hTRPV1-I585V). $n = 5$ for each case. *F* and *G*, current to voltage relationships for hTRPV1-Ile^{585} and hTRPV1-I585V variants, respectively, before (*black symbols*) and after (*red symbols*) a 60-min MβCD:cholesterol treatment. *Dotted curves* are the data after cholesterol application normalized to their maximal value.

spond to putative non-raft and raft microdomains, respectively (34). Both before and after MβCD or MβCD:cholesterol treatment, rTRPV1 was found in DSM fractions and there was no detectable rTRPV1 in DRM fractions (supplemental Fig. S4).

DISCUSSION

In these studies we have shown that cholesterol, an important component of cell plasma membranes, modulates the function of the cation-selective channel TRPV1. Although depletion of membrane cholesterol had no effect on capsaicin-induced TRPV1 currents, augmentation of cholesterol markedly reduced these currents in both wild-type rat TRPV1 and one of the major human variants of TRPV1. Specifically, we found that the addition of cholesterol inhibits TRPV1 by binding to specific sites along the S5 helix having a putative CRAC motif. These data suggest the extent cholesterol alters the function of TRPV1 is dependent on the species and membrane cholesterol content.

All of the electrophysiology experiments reported in this article were performed on patches excised from HEK293 cells with heterologously expressed rTRPV1 channels. Therefore, the observed effects of membrane cholesterol depletion or augmentation had to be due to changes within this excised membrane, rather than to possible modifications in cell trafficking. We found that cholesterol depletion had no effect on the currents (Fig. 2), which contrasts to electrophysiological data from whole cells where cholesterol depletion reduced capsaicin-induced currents (17, 18). We argue that this means that the observed results in whole cells upon MβCD treatment were due to the role of cholesterol in membrane trafficking in the cell, consistent with the observation that cholesterol depletion decreased the concentration of rTRPV1 in the plasma membrane (17). Moreover, this interpretation is consistent with the results of Liu *et al.* (41) who found for whole cells that cholesterol removal caused no appreciable change in temperature-induced rTRPV1 currents over a range of temperatures (44 to 50 °C).

In contrast to the non-effect of cholesterol depletion, cholesterol augmentation significantly and reversibly reduced capsaicin-induced rTRPV1 currents (Fig. 2). In terms of molecular mechanism, the similarity in shape of the dose-response curves before and after cholesterol augmentation (Fig. 2*C*) suggests that cholesterol addition had no appreciable effect on the affinity of capsaicin to its binding site. The similar shapes of the I-V curves (Fig. 2*D*) suggest that there was little change in the voltage-sensing domain. Importantly, the noise analysis experiments revealed that the decrease in current with cholesterol addition did not arise from a significant change in the conducting channels as reflected in no appreciable changes in the single channel current (i) or open probability (P_o), but rather a decrease in the number of agonist-responsive channels in the patch (Fig. 3*B*). Our single-channel recordings also suggest that cholesterol sequesters the channel in a non-conducting state. These data could be interpreted to mean that cholesterol impedes channel opening (see Refs. 19 and 42).

Unlike cholesterol, epicholesterol did not modify the capsaicin-evoked current (Fig. 4), indicating that the effect of cholesterol is not due to a nonspecific membrane effect, but rather to a stereospecific binding site. Similar results with other channels, including inward-rectifier K^+ channels and large-conductance voltage/Ca^{2+}-gated K^+ channels, have also been interpreted to mean that the effect of cholesterol are not due to an indirect modification of lipid bilayer properties, but rather to a stereospecific interaction at the surface of the protein (19, 32).

We consequently explored rTRPV1 for possible cholesterol-binding sites. One established sequence selective for binding cholesterol is the putative CRAC motif, first identified in the

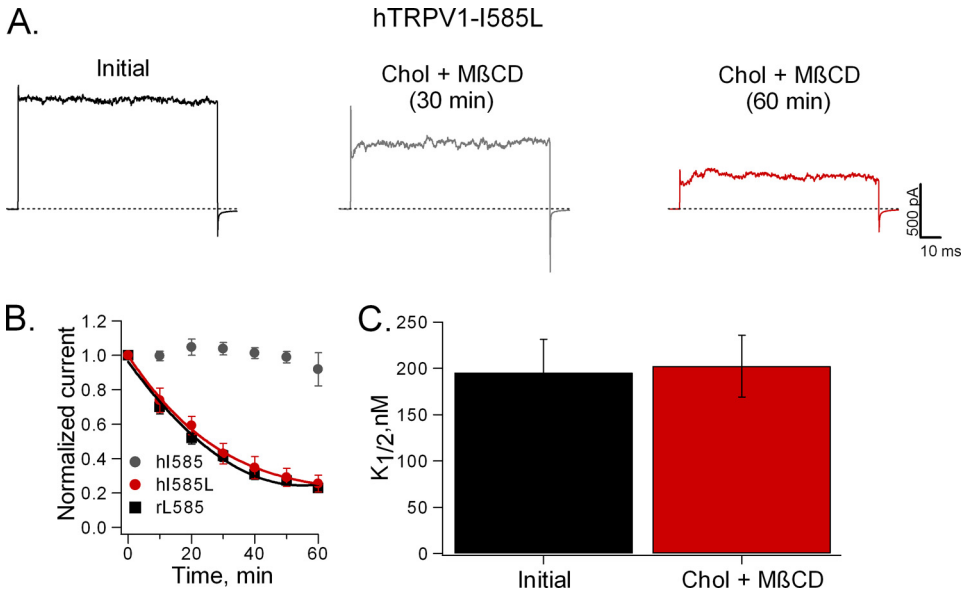

FIGURE 8. **The I585L substitution in hTRPV1 renders the channel cholesterol-sensitive.** *A,* representative current traces from inside-out excised patches before (*black*) and after incubation with 10:1 MβCD:cholesterol for 30 (*gray*) and 60 min (*red*). *B,* time course for effects of cholesterol. Application of MβCD: cholesterol for 60 min to the hTRPV1-Ile^{585} variant did not decrease the current (*gray circles*, $n = 5$). The hTRPV1-I585L mutant responded to cholesterol with a τ of 32 $\pm$ 7 min (*red circles*, $n = 5$), similar to that of the rat TRPV1 (*black squares*, $\tau = 27 \pm 5$ min; $n = 5$). Data were fit to a single exponential. *C,* capsaicin sensitivity of hTRPV1-I585L before (*black*, $K_{1/2} = 195 \pm 36$ nM and $n_H = 1.5 \pm 0.3$) and after cholesterol (*red*, $K_{1/2} = 202 \pm 34$ nM and $n_H = 1.5 \pm 0.3$). $n = 5$ for each case.

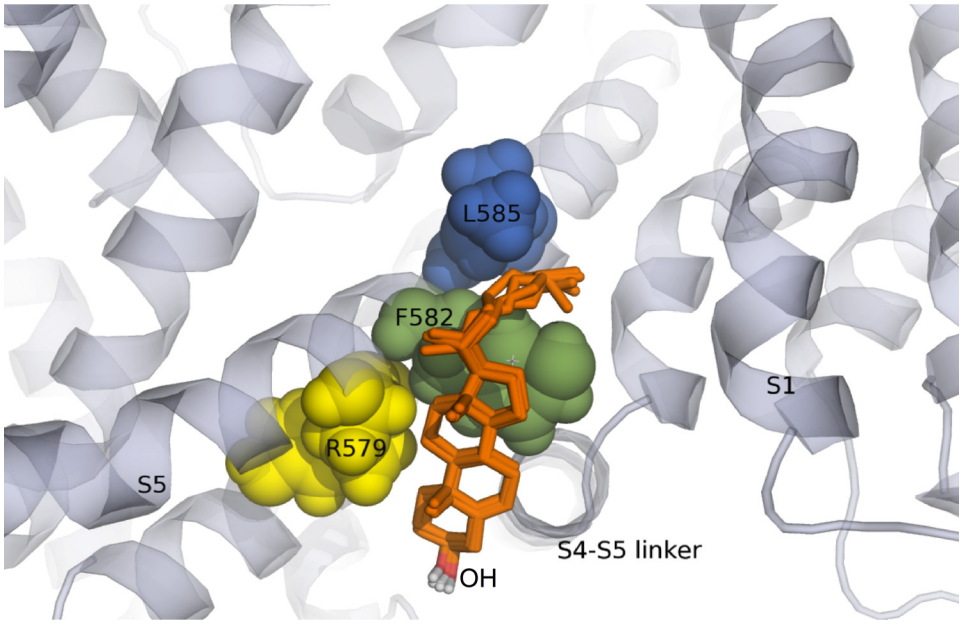

FIGURE 9. **Model for cholesterol binding to S5 in TRPV1.** The best five conformations of cholesterol docked to the S5 of the TRPV1 model. These are the lowest energy conformations (between -7.15 and -7.06 kcal/mol) taken from the cluster of 36 similar dockings. In this binding conformation, cholesterol occupies a groove formed between S5 and the putative voltage-sensing domain of the adjacent subunit. The bulky β-face of cholesterol points away from the S5 helix, the OH group (*red* and *white*) points toward Arg^{579} (*yellow*), possibly establishing an electrostatic interaction. The α-face of cholesterol, which is essentially flat, makes a hydrophobic π-aliphatic interaction with Phe^{582} (*green*). The aliphatic tail in cholesterol occupies a small cavity in which it interacts with Leu^{585} (*blue*) of the rat TRPV1, a position in which I and V can be found for the human TRPV1 orthologue.

benzodiazepine receptor (43) and later identified in many other proteins and peptides (40, 44, 45). This motif is defined as a sequence pattern of -(Leu/Val-$(X)_{1-5}$-Tyr-$(X)_{1-5}$-Arg/Lys)-, in which $(X)_{1-5}$ represents between one and five residues of any amino acid (40, 45). Cholesterol interacts with the CRAC motif with both attractive van der Waals interactions between hydrophobic surfaces and electrostatic interactions between the positively charged Arg or Lys residue and the cholesterol -OH group (40, 45). In a study of a peptide from the fusogenic gp41 protein of HIV-1, Epand *et al.* (40) found that the single Leu to Ile substitution in the CRAC motif (from LWYIK to IWYIK) resulted in no preferential interaction with cholesterol (33). Another cholesterol binding motif, called the cholesterol consensus motif, also found in many proteins, has three sites (Trp/Tyr)–(Ile/Val/Leu)–(Lys/Arg) on one helix and one site (Phe/Tyr/Trp) on an adjoining helix (20). For example, in the crystal

structure of the human β_2-adrenergic receptor, Hanson *et al.* (20) found that cholesterol binds in a shallow groove between these helices. As with the CRAC motif, key features of the cholesterol consensus motif are the van der Waals interactions of the cholesterol with the aromatic residues and electrostatic interactions with positively charged residues (20).

A cholesterol-binding motif in rTRPV1 is located in the S5 helix, which contains a CRAC sequence from residue 579 to 586 (Fig. 7*A*). Our experiments showing different sensitivities to cholesterol augmentation of specific rat mutants (Figs. 5 and 6) and human variants (Figs. 7 and 8) provide strong evidence for the presence of a cholesterol-binding site in helix S5. Two points here are worth discussing. First, the abrogation of most of the sensitivity to cholesterol augmentation by the rTRPV1-L585I mutation (Fig. 6) and the restoration of this sensitivity by the inverse mutation in hTRPV1-I585L (Fig. 8), shows the importance of hydrophobic interactions for this cholesterol effect. Given that the Leu to Ile mutation is rather subtle, its effect also highlights the importance of steric factors in the interaction. Second, given that the CRAC sequence contains a positively charged (Arg or Lys) residue, it might seem surprising that the R579D mutation (positive to negative charge with different side chain volumes) retained sensitivity to cholesterol augmentation, albeit reduced (Fig. 5*B*). However, the interaction with the -OH dipole can occur with charges of either sign (20) in a manner that may be enough to stabilize the interaction of cholesterol with the protein. Our data imply that in the case of rTRPV1, the positive charge Arg^{579} contributed a fraction of the stabilization energy because charge neutralization (R579Q) rendered TRPV1 more sensitive to cholesterol than charge reversal (R579D) (Fig. 5).

Recently, Rosenhause-Dankster *et al.* (46) have further characterized the interaction of Kir2.1 channels with cholesterol. By using a combination of electrophysiological recordings and mutagenesis as well as modeling based on the crystal structure of Kir2.1 they have concluded that cholesterol does not appear to have a typical binding pocket in Kir2.1. Rather they found that a more complex belt-like structure is formed to contain the apex of the flexible G-loop near the interface with the transmembrane region, affecting channel gating in a manner that stabilizes the closed state of the channel (46). The question remains whether other regions of TRPV1 also interact with the S5 CRAC motif to form a more complex cholesterol-stabilizing structure.

Although there are many variants of human hTRPV1 subunits (47), two very common alleles (I and V) were identified at position 585 (see Fig. 7*A*). In a genetic and functional screening of hTRPV1 variants obtained from a human population, Cantero-Recasens *et al.* (48) found that at amino acid 585, 51% are heterozygous (Ile/Val), 15% are homozygous for Val/Val, and 34% homozygous for Ile/Ile. They found these variants could be activated by capsaicin, which we have confirmed. Moreover, we found that the two variants had different responses to cholesterol addition (Fig. 7, *B–D*), which represents, to our knowledge, the first demonstrated functional difference between these two variants. Given that rTRPV1-L585I was insensitive to cholesterol augmentation (Fig. 6), it was gratifying to find that hTRPV1-Ile^{585}, with the same S5 sequence as rTRPV1-L585I, was also insensitive to cholesterol augmentation (Fig. 7*B*). Thus, a single amino acid substitution dramatically altered the sensitivity of TRPV1 to cholesterol among species.

It follows that the observed decreases in capsaicin-induced currents by cholesterol augmentation were due to specific interactions with a cholesterol-binding site in the S5 transmembrane helix of TRPV1. We have identified critical amino acids on the S5 helix that greatly affected how TRPV1 responds in the presence of cholesterol. Based on the similarities of capsaicin dose-response and I-V curves before and after cholesterol addition, the cholesterol effects are not due to changes in capsaicin binding or channel selectivity. Rather we argue that cholesterol binding must cause a conformational change in TRPV1 that stabilizes the closed state(s) (41) of the channel. A similar conclusion was reached in a noise analysis study of Kir2.1 channels (19).

The time required to inhibit rTRPV1 with MβCD:cholesterol incubation was greater than the time for recovery of the current with the same concentration of MβCD (Fig. 2 and supplemental Fig. S1). Let us consider possible reasons for this observation. First, the membrane bilayer contains many more cholesterol-binding sites (each monolayer with its raft and non-raft regions) than do the TRPV1 channels embedded in the bilayer. Thus, from mass action principle, it follows that cholesterol would initially preferentially partition into the bilayer sites and the channel sites would take longer to fill. The TRPV1 channel is formed from tetramers, and cholesterol has to partition between subunits to get to its sites within the protein. Moreover, it may take all four sites to be occupied for the channels to fully close. We argue that this latter process may be the rate-limiting step. One possibility for the faster recovery time is that the removal of cholesterol from only one (or two) of the subunits may be sufficient for the channel to reopen.

Our result (see supplemental Fig. S4) that rTRPV1 is primarily located in cholesterol-poor DSMs (thought to be related to non-raft microdomains) is similar to results for TRPC3 and TRPC6 (49), but in contrast to other TRP channels, such as TRPC1, TRPC4, and TRPC5 (49) and TRPM8 (42), that have been associated with cholesterol-rich DRMs. Although the reasons for these different microdomain locations are not clear, the different locations can impact on the TRP channels' response to cholesterol. Thus, the cholesterol-rich raft microdomain location of TRPM8 helps to explain why MβCD treatment increases cold-evoked TRPM8 currents in cells (42), whereas the non-raft localization of rTRPV1 (data seen in supplemental Fig. S4) helps explain why MβCD treatment does not modify the capsaicin-induced current of this channel in HEK293 cells (Fig. 2 and supplemental Fig. S1).

TRPV1 is known to serve many physiological functions and is also involved in pathological conditions (for review, see Ref. 1). Here we consider the physiological significance of the observations that the activity of both rTRPV1 and hTRPV1 can be diminished by cholesterol. This is relevant because different cells have different cholesterol concentrations, with the cholesterol unequally partitioned between plasma and organelle membranes. Moreover, many plasma membranes contain transient cholesterol-rich raft and cholesterol-poor non-raft microdomains. Here we have shown that rTRPV1 is located in

DSM (non-raft) fractions (supplemental Fig. S4). We speculate that the activity of TRPV1 could be regulated by expression of the Val/Val or Ile/Ile variants in cells with different cholesterol concentrations, or by transferring them between non-raft (low cholesterol) and raft (high cholesterol) microdomains within a given plasma membrane. For example, after exposure to bradykinin TRPM7 channels have been shown to relocalize from cholesterol-poor (non-raft) to cholesterol-rich (raft) domains (50). In the future, these variants may prove to display a physiologically important role in humans containing both variants of TRPV1 under conditions of hypercholesterolemia, for instance. Our data also argue in favor of a species-specific sensitivity of TRPV1 to cholesterol as happens for the Kir6 channel, which shows differences in cholesterol sensitivity in a porcine model (51) as compared with a rabbit model (52). These findings and our own suggest that the same channel can be differentially regulated by cholesterol in different species.

Acknowledgments—We thank David Julius, University of California at San Francisco, for providing the TRPV1 cDNA and Dr. Wolfgang Liedtke, Duke University, for supplying cells for the detergent extraction experiments. We also thank Félix Sierra, Laura Ongay, Guadalupe Códiz, Ana Escalante, and Francisco Pérez, Instituto de Fisiología Celular, UNAM and Sukhee Lee, Duke, for expert technical support, and Hiram Picazo for artwork.

REFERENCES

1. Jara-Oseguera, A., Simon, S. A., and Rosenbaum, T. (2008) *Curr. Mol. Pharmacol.* **1,** 255–269
2. Caterina, M. J., Schumacher, M. A., Tominaga, M., Rosen, T. A., Levine, J. D., and Julius, D. (1997) *Nature* **389,** 816–824
3. Szallasi, A., and Blumberg, P. M. (1989) *Neuroscience* **30,** 515–520
4. Culshaw, A. J., Bevan, S., Christiansen, M., Copp, P., Davis, A., Davis, C., Dyson, A., Dziadulewicz, E. K., Edwards, L., Eggelte, H., Fox, A., Gentry, C., Groarke, A., Hallett, A., Hart, T. W., Hughes, G. A., Knights, S., Kotsonis, P., Lee, W., Lyothier, I., McBryde, A., McIntyre, P., Paloumbis, G., Panesar, M., Patel, S., Seiler, M. P., Yaqoob, M., and Zimmermann, K. (2006) *J. Med. Chem.* **49,** 471–474
5. Pearce, L. V., Petukhov, P. A., Szabo, T., Kedei, N., Bizik, F., Kozikowski, A. P., and Blumberg, P. M. (2004) *Org. Biomol. Chem.* **2,** 2281–2286
6. Xu, S., Cheng, Y., Keast, J. R., and Osborne, P. B. (2008) *Endocrinology* **149,** 5540–5548
7. De Petrocellis, L., Bisogno, T., Davis, J. B., Pertwee, R. G., and Di Marzo, V. (2000) *FEBS Lett.* **483,** 52–56
8. Ross, R. A. (2003) *Br. J. Pharmacol.* **140,** 790–801
9. Stein, A. T., Ufret-Vincenty, C. A., Hua, L., Santana, L. F., and Gordon, S. E. (2006) *J. Gen. Physiol.* **128,** 509–522
10. Ufret-Vincenty, C. A., Klein, R. M., Hua, L., Angueyra, J., and Gordon, S. E. (2011) *J. Biol. Chem.* **286,** 9688–9698
11. Yao, J., and Qin, F. (2009) *PLoS Biol.* **7,** e46
12. Salton, M. R. (1968) *J. Gen. Physiol.* **52,** (suppl.) 227–252
13. Levitan, I., Fang, Y., Rosenhouse-Dantsker, A., and Romanenko, V. (2010) *Subcell. Biochem.* **51,** 509–549
14. Levitan, I., Christian, A. E., Tulenko, T. N., and Rothblat, G. H. (2000) *J. Gen. Physiol.* **115,** 405–416
15. Levitan, I. (2009) *IUBMB Life* **61,** 781–790
16. Singh, D. K., Rosenhouse-Dantsker, A., Nichols, C. G., Enkvetchakul, D., and Levitan, I. (2009) *J. Biol. Chem.* **284,** 30727–30736
17. Liu, M., Huang, W., Wu, D., and Priestley, J. V. (2006) *Eur. J. Neurosci.* **24,** 1–6
18. Szoke, E., Börzsei, R., Tóth, D. M., Lengl, O., Helyes, Z., Sándor, Z., and Szolcsányi, J. (2010) *Eur. J. Pharmacol.* **628,** 67–74
19. Romanenko, V. G., Fang, Y., Byfield, F., Travis, A. J., Vandenberg, C. A., Rothblat, G. H., and Levitan, I. (2004) *Biophys. J.* **87,** 3850–3861
20. Hanson, M. A., Cherezov, V., Griffith, M. T., Roth, C. B., Jaakola, V. P., Chien, E. Y., Velasquez, J., Kuhn, P., and Stevens, R. C. (2008) *Structure* **16,** 897–905
21. Oddi, S., Dainese, E., Fezza, F., Lanuti, M., Barcaroli, D., De Laurenzi, V., Centonze, D., and Maccarrone, M. (2011) *J. Neurochem.* **116,** 858–865
22. Salazar, H., Llorente, I., Jara-Oseguera, A., García-Villegas, R., Munari, M., Gordon, S. E., Islas, L. D., and Rosenbaum, T. (2008) *Nat. Neurosci.* **11,** 255–261
23. Salazar, H., Jara-Oseguera, A., Hernández-García, E., Llorente, I., Arias-Olguí, II, Soriano-García, M., Islas, L. D., and Rosenbaum, T. (2009) *Nat. Struct. Mol. Biol.* **16,** 704–710
24. Heinemann, S. H., and Conti, F. (1992) *Methods Enzymol.* **207,** 131–148
25. Colquhoun, D., and Sigworth, F. J. (1995) *Fitting and Statistical Analysis of Single-channel Records,* Second Ed., Plenum Publishing Corp., New York
26. Fernández-Ballester, G., and Ferrer-Montiel, A. (2008) *J. Membr. Biol.* **223,** 161–172
27. Long, S. B., Tao, X., Campbell, E. B., and MacKinnon, R. (2007) *Nature* **450,** 376–382
28. Huey, R., Morris, G. M., Olson, A. J., and Goodsell, D. S. (2007) *J. Comput. Chem.* **28,** 1145–1152
29. Sobolev, V., Sorokine, A., Prilusky, J., Abola, E. E., and Edelman, M. (1999) *Bioinformatics* **15,** 327–332
30. Christian, A. E., Haynes, M. P., Phillips, M. C., and Rothblat, G. H. (1997) *J. Lipid Res.* **38,** 2264–2272
31. Romanenko, V. G., Rothblat, G. H., and Levitan, I. (2002) *Biophys. J.* **83,** 3211–3222
32. Bukiya, A. N., Belani, J. D., Rychnovsky, S., and Dopico, A. M. (2011) *J. Gen. Physiol.* **137,** 93–110
33. Rosenbaum, T., and Gordon, S. E. (2002) *Neuron* **33,** 703–713
34. Brown, D. A., and Rose, J. K. (1992) *Cell* **68,** 533–544
35. Tkachenko, E., and Simons, M. (2002) *J. Biol. Chem.* **277,** 19946–19951
36. Tong, J., Briggs, M. M., Mlaver, D., Vidal, A., and McIntosh, T. J. (2009) *Biophys. J.* **97,** 2493–2502
37. Oseguera, A. J., Islas, L. D., García-Villegas, R., and Rosenbaum, T. (2007) *Biophys. J.* **92,** 3901–3914
38. Hayes, P., Meadows, H. J., Gunthorpe, M. J., Harries, M. H., Duckworth, D. M., Cairns, W., Harrison, D. C., Clarke, C. E., Ellington, K., Prinjha, R. K., Barton, A. J., Medhurst, A. D., Smith, G. D., Topp, S., Murdock, P., Sanger, G. J., Terrett, J., Jenkins, O., Benham, C. D., Randall, A. D., Gloger, I. S., and Davis, J. B. (2000) *Pain* **88,** 205–215
39. Brauchi, S., Orta, G., Mascayano, C., Salazar, M., Raddatz, N., Urbina, H., Rosenmann, E., Gonzalez-Nilo, F., and Latorre, R. (2007) *Proc. Natl. Acad. Sci. U.S.A.* **104,** 10246–10251
40. Epand, R. F., Thomas, A., Brasseur, R., Vishwanathan, S. A., Hunter, E., and Epand, R. M. (2006) *Biochemistry* **45,** 6105–6114
41. Liu, B., Hui, K., and Qin, F. (2003) *Biophys. J.* **85,** 2988–3006
42. Morenilla-Palao, C., Pertusa, M., Meseguer, V., Cabedo, H., and Viana, F. (2009) *J. Biol. Chem.* **284,** 9215–9224
43. Jamin, N., Neumann, J. M., Ostuni, M. A., Vu, T. K., Yao, Z. X., Murail, S., Robert, J. C., Giatzakis, C., Papadopoulos, V., and Lacapère, J. J. (2005) *Mol. Endocrinol.* **19,** 588–594
44. Epand, R. M. (2008) *Biochim. Biophys. Acta* **1778,** 1576–1582
45. Epand, R. M. (2006) *Prog. Lipid Res.* **45,** 279–294
46. Rosenhouse-Dantsker, A., Logothetis, D. E., and Levitan, I. (2011) *Biophys. J.* **100,** 381–389
47. Schumacher, M. A., and Eilers, H. (2010) *Front. Biosci.* **15,** 872–882
48. Cantero-Recasens, G., Gonzalez, J. R., Fandos, C., Duran-Tauleria, E., Smit, L. A., Kauffmann, F., Antó, J. M., and Valverde, M. A. (2010) *J. Biol. Chem.* **285,** 27532–27535
49. Brownlow, S. L., and Sage, S. O. (2005) *Thromb. Haemost.* **94,** 839–845
50. Yogi, A., Callera, G. E., Tostes, R., and Touyz, R. M. (2009) *Am. J. Physiol. Regul. Integr. Comp. Physiol.* **296,** R201–207
51. Mathew, V., and Lerman, A. (2001) *Atherosclerosis* **154,** 329–335
52. Genda, S., Miura, T., Miki, T., Ichikawa, Y., and Shimamoto, K. (2002) *J. Am. Coll. Cardiol.* **40,** 1339–1346

ARTICLE
PUBLISHED ONLINE: 20 NOVEMBER 2011 | DOI: 10.1038/NCHEMBIO.712
nature chemical biology

Lysophosphatidic acid directly activates TRPV1 through a C-terminal binding site

Andrés Nieto-Posadas[1], Giovanni Picazo-Juárez[1], Itzel Llorente[1], Andrés Jara-Oseguera[2], Sara Morales-Lázaro[1], Diana Escalante-Alcalde[1]*, León D Islas[2]* & Tamara Rosenbaum[1]*

Since 1992, there has been growing evidence that the bioactive phospholipid lysophosphatidic acid (LPA), whose amounts are increased upon tissue injury, activates primary nociceptors resulting in neuropathic pain. The TRPV1 ion channel is expressed in primary afferent nociceptors and is activated by physical and chemical stimuli. Here we show that in control mice LPA produces acute pain-like behaviors, which are substantially reduced in *Trpv1*-null animals. Our data also demonstrate that LPA activates TRPV1 through a unique mechanism that is independent of G protein–coupled receptors, contrary to what has been widely shown for other ion channels, by directly interacting with the C terminus of the channel. We conclude that TRPV1 is a direct molecular target of the pain-producing molecule LPA and that this constitutes, to our knowledge, the first example of LPA binding directly to an ion channel to acutely regulate its function.

Neuropathic pain can occur after trauma to the nervous system or as a result of diseases such as multiple sclerosis and stroke. It is quite common among the human population and includes symptoms such as continuous burning pain, allodynia and hyperalgesia[1].

The release of certain bioactive lipids contributes to the generation and maintenance of neuropathic pain. However, many of the molecular targets of these molecules remain unknown. Among the molecules for which a role in neuropathic pain has been described is LPA[1].

LPA is found in serum and plasma where it is synthesized mainly by the enzyme autotaxin from precursor lysophospholipids, which in turn are produced by phospholipases A_1 and A_2 (ref. 2). Activated platelets[3] and other cell types such as microglia[4] stimulate LPA production, leading to accumulation of micromolar concentrations of the lipid upon tissue damage[3].

LPA's actions are mediated by G protein–coupled receptors that are specific to LPA (LPA_1–LPA_6)[5] and include the regulation of some ion channels through the activation of pathways downstream of the receptors. Effects of LPA on TRP channels have also been reported[6,7]. For example, high concentrations of LPA (100 μM) stimulate Ca^{2+} mobilization in B-lymphoblast cell lines by regulating the activity of a TRPC channel[6]. Although they do not experimentally demonstrate it, these authors suggest that LPA-induced Ca^{2+} mobilization could be due to direct channel activation as the process was not sensitive to $G_{i/o}$ protein or PLC inhibition[6]. On the other hand, LPA decreases TRPM7 activity in fibroblasts. Because these cells express the LPA_3 (also called EDG-7) receptor, the authors suggest that regulation of TRPM7 by LPA could be due to activation of the G_q-associated signaling pathway[7].

The TRPV1 ion channel is activated by a variety of stimuli such as high temperature[8,9], low pH and pungent compounds[8]. Also, multiple signals that originate from inflammatory processes converge on TRPV1, whose activation in sensory neurons has the final consequence of pain perception.

Because TRPV1 receptors in neurons contribute to hyperalgesia, a connection between TRPV1 and LPA-induced neuropathic pain has been hypothesized[1]. A recent study suggests that pain-related responses in dorsal root ganglion (DRG) neurons from a rat bone cancer model are due to enhanced expression as well as potentiation of the capsaicin and thermal responses of TRPV1 in this disease. These changes in TRPV1 expression and function were suggested to be caused by the activation of the protein kinase Cε (PKCε) pathway downstream of the LPA_1 receptor[10].

Because LPA is linked to painful processes involving pain generation during tissue injury and damage and because other lipids such as PIP_2 are known to interact directly with TRPV1 (refs. 11–13), we set out to determine whether LPA could modify TRPV1 function through direct binding to the channel.

The present study shows that LPA does in fact activate TRPV1 by acting directly on its C-terminal region, and this effect contrasts with all other examples of LPA action on ion channels as it is independent of LPA-receptor activation.

RESULTS

TRPV1 mediates LPA-induced pain behavior

To investigate the acute effects of LPA on TRPV1-mediated pain-related behavior, we assessed capsaicin- and heat-elicited pain behavior by means of the paw-licking and paw-withdrawal assays in control and littermate mice lacking expression of LPP3 (*Lpp3*$^{-/-}$, or *Ppap2b*$^{-/-}$), an enzyme which degrades LPA[14], in the nervous system.

We measured the paw-licking time immediately after injection of the test solution. Whereas both wild-type and *Lpp3*$^{-/-}$ animals showed a greater painful response when injected with capsaicin than did those injected with saline, *Lpp3*$^{-/-}$ mice showed longer paw-licking times after capsaicin injection than did control animals (**Fig. 1a**). When pain behavior was assayed by the paw-withdrawal assay, we also observed a hyperalgesic response to increased temperature in *Lpp3*$^{-/-}$ mice (**Fig. 1b**). As expected, *Trpv1*$^{-/-}$ mice showed no differences with respect to control animals, consistent with what had been demonstrated for low-intensity (5.5 A) stimulation[15] (**Fig. 1b**). To confirm that the painful responses to capsaicin and temperature in the *Lpp3*$^{-/-}$ mouse model are due to TRPV1, we produced *Trpv1*$^{-/-}$ *Lpp3*$^{-/-}$ mice and tested their responses to painful stimuli. These double-knockout animals showed no differences

[1]Departamento de Neurodesarrollo y Fisiología, División Neurociencias, Instituto de Fisiología Celular, Universidad Nacional Autónoma de México, Distrito Federal, México. [2]Departamento de Fisiología, Facultad de Medicina, Universidad Nacional Autónoma de México, Distrito Federal, México. *e-mail: trosenba@ifc.unam.mx or descalante@ifc.unam.mx or islas@liceaga.facmed.unam.mx

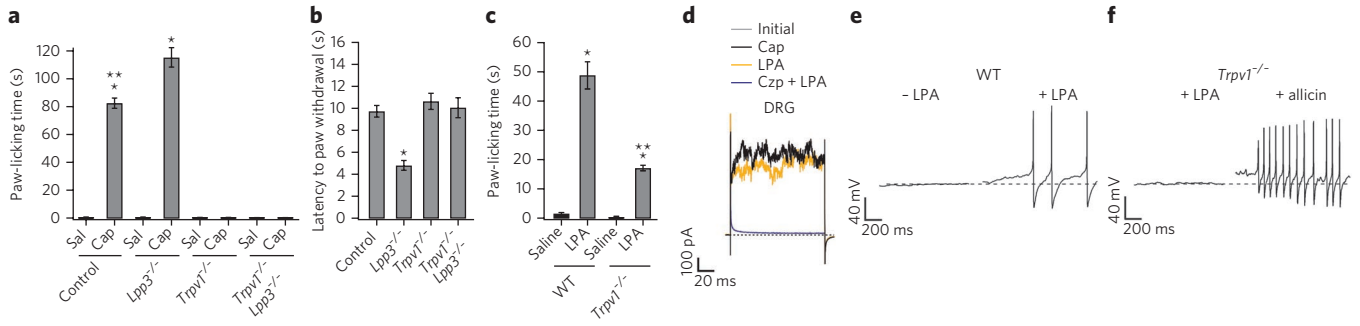

Figure 1 | TRPV1 responds to LPA. (**a**) Paw-licking times for saline and capsaicin, respectively, were: control, 0.8 ± 0.1 s and 82.5 ± 4 s ; *Lpp3*$^{-/-}$, 0.8 ± 0.2 s and 115.42 ± 7 s; *Trpv1*$^{-/-}$, 0.3 ± 0.1 s and 0.4 ± 0.2 s; *Trpv1*$^{-/-}$ *Lpp3*$^{-/-}$, 0.3 ± 0.1 s and 0.4 ± 0.2 s. *P < 0.01 for saline-injected versus capsaicin-injected control and *Lpp3*$^{-/-}$ animals; **P < 0.01 for control mice injected with capsaicin versus *Lpp3*$^{-/-}$ and *Trpv1*$^{-/-}$ mice injected with capsaicin; ANOVA (n = 12). Sal, saline injection; Cap, capsaicin injection. (**b**) Radiant paw-heating (Hargreaves) assay. Latencies were: control, 9.7 ± 0.5 s; *Lpp3*$^{-/-}$, 4.8 ± 0.4 s; *Trpv1*$^{-/-}$, 10.6 ± 0.7 s; *Trpv1*$^{-/-}$ *Lpp3*$^{-/-}$, 10.1 ± 0.9 s. *P < 0.01 *Lpp3*$^{-/-}$ versus all other groups; ANOVA (n = 20). (**c**) Paw-licking times for saline and LPA, respectively, were: control, 1.5 ± 0.3 s and 49 ± 5 s; *Trpv1*$^{-/-}$, 0.4 ± 0.2 s and 17 ± 0.9 s. *P < 0.01 for saline-injected versus LPA-injected animals; **P < 0.01 for control versus *Trpv1*$^{-/-}$ animals injected with LPA; ANOVA (n = 12). (**d**) Representative (n = 5) TRPV1 currents (120 mV) from inside-out DRG neuron membrane patches exposed to capsaicin (Cap, 4 μM), LPA (5 μM, after wash) and LPA (5 μM) and capsazepine (Czp, 30 μM) together. (**e**) Membrane potential in a wild-type DRG neuron with or without 5 μM LPA. (**f**) Membrane potential in a *Trpv1*$^{-/-}$ DRG neuron with LPA and with allicin (200 μM). Resting potential (dashed line) was near −40 mV (n = 8). Group data are reported as the mean ± s.e.m.

in their responses to the injection of saline or capsaicin solutions, and their reaction to changes in temperature (paw withdrawal) were similar to those in *Trpv1*$^{-/-}$ and control mice (**Fig. 1a**,**b**).

Finally, we assayed whether injection of LPA into the paws of wild-type and *Trpv1*$^{-/-}$ mice elicited pain-like behavior. We found that LPA produces a robust (P <0.01) increase in paw-licking time in wild-type animals compared to controls injected with saline (**Fig. 1c**). A nearly 60% decrease in the response to LPA was observed in *Trpv1*$^{-/-}$ mice compared to wild-type animals, although a remnant of the response to LPA was observed in *Trpv1*$^{-/-}$ mice compared to those injected with saline (**Fig. 1c**). Furthermore, we acutely inhibited the TRPV1 channel by injecting the TRPV1 inhibitor capsazepine together with capsaicin or LPA in wild-type mice and measured paw-licking time. Consistently, capsazepine reduced the pain-associated responses to both capsaicin and LPA (**Supplementary Results**; **Supplementary Fig. 1a**).

These data show that more than half of the response to acute LPA delivery is mediated by TRPV1. Thus, the question arises as to how behavioral phenotypes relate to responses at the cellular level. We first sought to answer this question by applying LPA to inside-out membrane patches from dissociated wild-type mouse DRG neurons. LPA elicited currents from membrane patches, and this effect was blocked in all experiments by 30 μM capsazepine applied together with 5 μM LPA (**Fig. 1d**), suggesting that TRPV1 may indeed be a target of LPA.

To establish the physiological role of TRPV1 in the response of DRG neurons to LPA, we performed whole-cell current-clamp recordings in wild-type and *Trpv1*$^{-/-}$ mice. Application of 5 μM LPA to DRG neurons from wild-type mice elicited a depolarization in the range of 7–20 mV and subsequent action potential firing (**Fig. 1e**). DRG neurons that responded to LPA also responded to capsaicin (8 out of 8). In contrast, cells that did not respond to capsaicin did not respond to LPA either (10 out of 10). Although no response to LPA in *Trpv1*$^{-/-}$ neurons was observed, a clear response to allicin (which is also mediated by TRPA1 channels) was present, confirming that LPA was applied to the correct subset of small-diameter DRG neurons (**Fig. 1f**) and indicating that TRPV1 contributes to the electrical response to LPA in DRG neurons.

LPA activates heterologously expressed TRPV1 channels

LPA applied to inside-out patches from TRPV1-transfected HEK293 cells induced robust channel activation at both hyperpolarizing and depolarizing voltages (left and right of **Fig. 2a**, respectively). Furthermore, LPA activated a similar fraction of current with respect to the maximal response to 4 μM capsaicin when applied to patches from TRPV1-expressing HEK cells or wild-type mouse DRG neurons (0.93 ± 0.09 for DRG and 0.93 ± 0.03 for HEK cells; 120 mV, n = 10). In contrast, HEK cells expressing only green fluorescent protein (GFP; **Supplementary Fig. 1b**) did not respond to LPA, and the vehicle used to deliver LPA did not produce TRPV1 channel activation (**Supplementary Fig. 1c**). Moreover, we measured the response to LPA in heterologously expressed TRPV2, TRPV3 and TRPA1 channels, which in many cases colocalize with TRPV1 in native cells, and found that application of LPA to these channels did not produce current activation (**Supplementary Fig. 1d**).

LPA activated a larger fraction of current when it was applied intracellularly than when it was applied extracellularly (**Fig. 2a**,**b**). The time constants of activation (**Fig. 2c**) indicate that LPA is more effective from the inside than from the outside and that LPA applied extracellularly may cross the membrane to act on the intracellular side.

The observed TRPV1 current-voltage relationship was outwardly rectifying with a reversal potential of near 0 mV in the presence of either capsaicin or LPA (**Fig. 2d**). Activation of TRPV1 by LPA occurs in a dose-dependent fashion, with an apparent dissociation constant (K_D) of 754 nM at 120 mV (**Fig. 2e**).

We then probed whether TRPV1 responded to molecules with similar structures to LPA and to molecules that are also substrates or products of the LPP3 enzyme. Intracellular application of 5 μM of glycerol phosphate, oleic acid, lysophosphatidylcholine, diacylglycerol, ceramide-1-phosphate or sphingosine-1-phosphate did not activate TRPV1, but 5 μM phosphatidic acid promoted a small activation of TRPV1 currents (**Supplementary Fig. 1e**).

These data led us to conclude that a robust and specific activation of TRPV1 can be achieved by LPA. We further studied whether LPA could activate TRPV1 through an LPA receptor–independent pathway.

LPA receptors are not involved in TRPV1 activation

So far, our data suggest that LPA acts as a ligand of TRPV1 by promoting a conformational change that leads to the opening of the channel. We then asked whether LPA activates endogenous LPA receptors or whether it interacts directly with the channel.

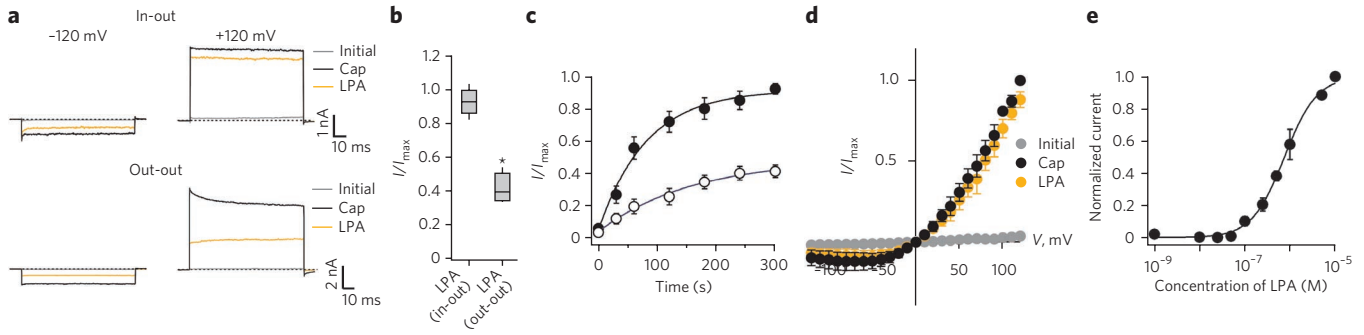

Figure 2 | Heterologously expressed TRPV1 channels respond to LPA. (**a**) Traces shown are representative of five experiments. Currents from inside-out and outside-out HEK cell patches were obtained as in **Figure 1** at −120 mV (left) and 120 mV (right). Patches were first exposed to capsaicin (Cap), washed, and then exposed to LPA. (**b**) Box plot of the fraction of current activated by LPA applied to the intracellular or extracellular face of the channel, normalized to the current with 4 μM capsaicin (120 mV). The horizontal line within each box indicates the median, boxes show the 25th and 75th percentiles, and whiskers show the 5th and 95th percentiles of the data ($n = 6$). *$P < 0.01$, ANOVA. (**c**) Time course of activation by 5 μM LPA in the inside-out (filled symbols) and outside-out (empty symbols) configurations at 120 mV ($n = 5$). Data were fit to a single exponential with time constants 80.5 ± 24 s (inside-out) and 167 ± 77 s (outside-out). LPA application started at $t = 0$ in the abscissa. (**d**) Current-voltage relationships for initial currents (gray), 4 μM capsaicin (black) and 5 μM LPA (orange) after capsaicin was washed off in the inside-out configuration ($n = 5$). (**e**) Dose response for activation by LPA at 120 mV in the inside-out configuration. Smooth curve is a fit with the Hill equation. The K_D value was 754 nM and the slope was 1.2. Owing to seal instability, a single LPA concentration was tested per membrane patch and normalized to the current at 10 μM LPA in the same patch ($n = 5$). Group data are reported as the mean ± s.e.m.

To establish a direct interaction of LPA with the channel, we used the molecule BrP-LPA, which not only closely resembles LPA in structure (**Fig. 3a**) but also is an antagonist of several LPA receptors (LPA_1–LPA_4)[16] and an inhibitor of autotaxin[16].

Unexpectedly, BrP-LPA applied to inside-out membrane patches from DRG neurons (which express LPA_1, LPA_3 and LPA_5)[1,17] and TRPV1-expresing HEK293 cells (which express LPA_1)[18], activated the channel similarly to LPA (**Fig. 3b**). The fraction of current activated by BrP-LPA with respect to the currents activated by 4 μM capsaicin in the same membrane patch at 120 mV was 0.9 ± 0.04 for DRG neurons and 0.91 ± 0.01 for HEK cells. Also, the dose response to BrP-LPA (K_D = 1.1 ± 0.25 μM) was comparable to that for LPA (K_D = 754 nM) (**Fig. 3c**).

Compelled by these results, we studied whether BrP-LPA could mimic LPA's effects at the physiological level. We first examined whether injection of BrP-LPA into the paws of wild-type and *Trpv1*$^{-/-}$ mice mimicked the effects of LPA and found that BrP-LPA produced a significant increase in paw-licking time in wild-type animals compared to saline ($P < 0.01$). The response of *Trpv1*$^{-/-}$ mice to BrP-LPA was only about 20% of that in wild-type animals (**Supplementary Fig. 2**), indicating that BrP-LPA induces a painful sensation that is largely mediated through the activation of TRPV1.

It was also shown that BrP-LPA induces action potential firing in DRG neurons from wild-type mice (**Fig. 3d**, top right) and that these effects are not observed when it is applied to neurons from *Trpv1*$^{-/-}$ mice (**Fig. 3d**, bottom left), although sensitivity to allicin remains (**Fig. 3d**, bottom right).

The data obtained with BrP-LPA suggest that, owing to its structural similarities with LPA, it can activate the channel through the same mechanism as LPA, independently of LPA receptors. To further support our hypothesis, we next performed experiments in which we added both BrP-LPA (BrP-LPA_{out}) to the patch pipette in inside-out patches to act as an antagonist of the LPA receptors and LPA to the intracellular face of the patch (LPA_{in}). Our results show

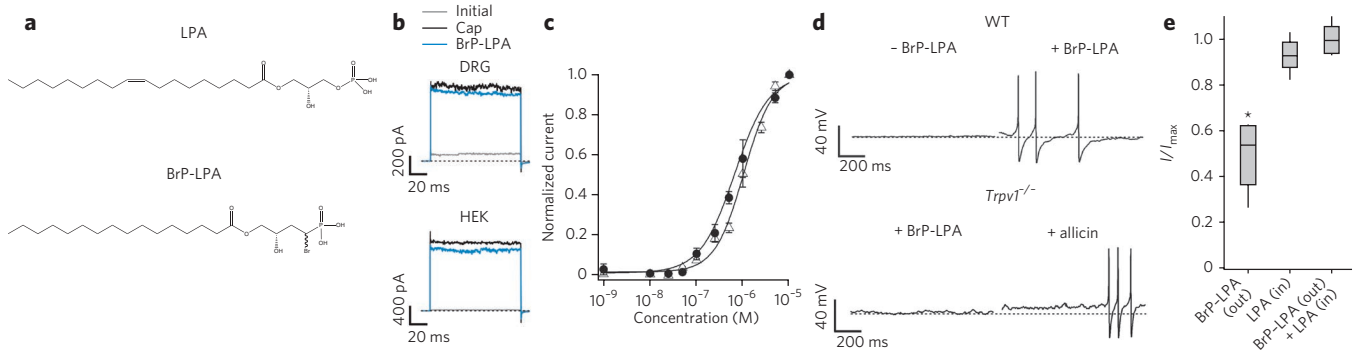

Figure 3 | An antagonist of LPA receptors with a similar structure to LPA activates TRPV1. (**a**) Stick representation of the chemical structures of LPA and BrP-LPA. (**b**) BrP-LPA (5 μM) activates currents in inside-out patches from DRG neurons (top) and HEK cells (bottom) at 120 mV. Representative traces, $n = 8$. Membrane patches were first exposed to 4 μM capsaicin (Cap) and washed, and then BrP-LPA was applied. (**c**) Comparison of BrP-LPA (triangles) and LPA (circles) dose responses at 120 mV obtained from inside-out patches from TRPV1-expressing HEK cells. Data for each patch was normalized to the current at 10 μM of either LPA or BrP-LPA. Smooth lines are fits with the Hill equation. The K_D for BrP-LPA is 1.1 ± 0.25 μM (slope is 1.3 ± 0.21, $n = 5$). (**d**) Membrane potential in a wild-type (WT) DRG neuron before (top left) and during (top right) application of BrP-LPA and in a *Trpv1*$^{-/-}$ DRG neuron during the exposure to BrP-LPA (bottom left) and in the presence of allicin (200 μM; bottom right). Resting membrane potential (dashed lines) was around −40 mV ($n = 9$ per genotype). (**e**) Activation of TRPV1 (120 mV) by external BrP-LPA (5 μM, out) and by internal LPA (5 μM, in) in inside-out patches from HEK cells. Data are normalized to activation with saturating capsaicin. The horizontal lines are as in **Figure 2b**. *$P < 0.01$ with respect to BrP-LPA (out) and LPA (in); ANOVA ($n = 6$). Group data are reported as the mean ± s.e.m.

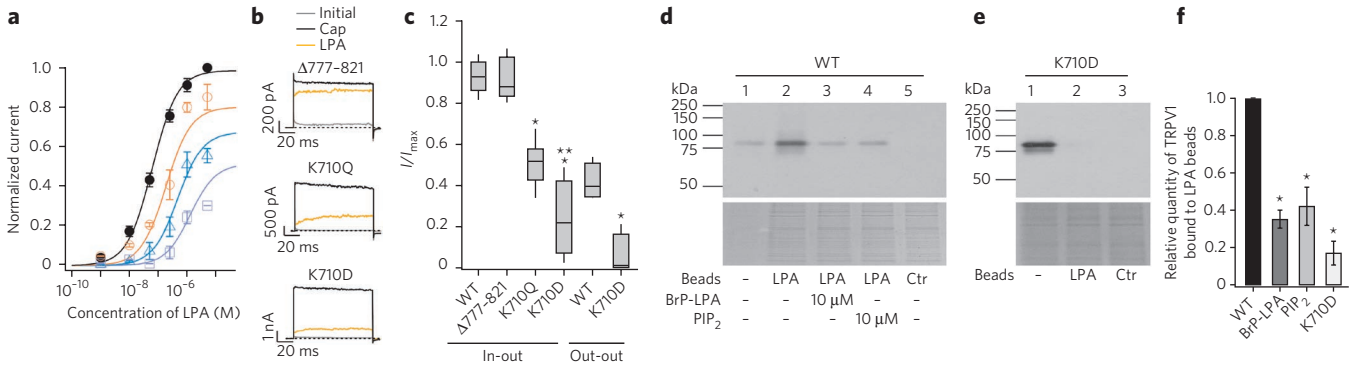

Figure 4 | Interaction site for LPA in the C terminus of TRPV1. (**a**) TRPV1 activation by intracellular LPA after polyK at 120 mV without (filled circles) or with PIP_2 (empty circles, 50 nM; triangles, 100 nM; squares, 200 nM). Curves are fits to **Scheme 1**. (**b**) Representative currents (120 mV, inside-out patches) containing the deletion mutant (Δ777–821) and the mutations K710Q and K710D, activated by 5 μM LPA or 4 μM capsaicin (Cap). (**c**) Fraction of current activated by intracellular LPA in wild-type and mutant TRPV1 channels (normalized to 4 μM capsaicin) and extracellular LPA in K710D mutants and wild type (n = 6–10). Horizontal lines are as in **Figure 2b**. *P < 0.01 versus wild-type (WT) and **P < 0.05 versus $TRPV1^{K710Q}$; ANOVA test. (**d**) TRPV1 interaction with LPA-coated beads. Lane 1, input (1 μg); 2, TRPV1 bound to LPA beads; 3 and 4, competition of BrP-LPA and PIP_2 for beads, respectively; 5, interaction with control beads. Lanes 2, 3, 4 and 5 contained 30 μg of membrane protein. Lower panel shows Coomassie blue–stained supernatant fraction. (**e**) Interaction of the K710D mutant with LPA-coated beads. Lane 1, the input (5 μg) of the K710D mutant; 2, pull-down of $TRPV1^{K710D}$ with LPA beads; 3, control beads. Lanes 2 and 3 contain 60 μg of membrane protein. Lower panel as in **d**. (**f**) Bar graph for the relative quantity of pulled-down TRPV1 with LPA beads from experiments as in **d** and **e**. Normalized values with respect to wild-type were: BrP-LPA = 0.35 ± 0.04; PIP_2 = 0.42 ± 0.09 and K710D = 0.17 ± 0.06. n = 4–6 for each case. *P < 0.01 versus wild-type; ANOVA test. Group data are reported as the mean ± s.e.m.

that the magnitude of the currents activated by LPA under these conditions was not different from the magnitude of those activated by intracellular LPA alone (**Fig. 3e**). In fact, extracellular BrP-LPA ($BrP\text{-}LPA_{out}$) could sustain current activation as effectively as extracellular LPA at the same concentration (**Figs. 2b** and **3e**).

The LPA_5 receptor, which is activated by BrP-LPA[19], is expressed in DRG neurons[17] and HEK cells (**Supplementary Fig. 3a**). To rule out any contributions of LPA_5 to our electrophysiological recordings, we determined whether the LPA_5 agonist farnesyl-pyrophosphate (FPP) could activate the TRPV1 channel. **Supplementary Figure 3b** shows that FPP was incapable of eliciting current activation in TRPV1-expressing HEK cells both in the inside-out and on-cell configurations, in accordance with a previous study that also showed a lack of effect of FPP on TRPV1[20]. However, FPP activated heterologously expressed TRPV3 (**Supplementary Fig. 3c**), as previously reported[20]. These data indicate that LPA is able to promote TRPV1 channel function through a mechanism independent of the activation of LPA receptors 1–5 (**Supplementary Fig. 3d**).

To further rule out the involvement of any LPA receptor in TRPV1's response to this lipid, we treated TRPV1-transfected HEK cells with inhibitors of the G protein–coupled signaling pathways that are associated with activation of LPA receptors. We used the inhibitors of phospholipase C (U73122; ref. 21); Rho-associated protein kinases and PKC (Y-27632; ref. 22); G_i, G_o and G_t proteins (pertussis toxin, PTX[23]); the βγ subunit of G proteins (C terminus of β-adrenergic kinase 1, Ctr-βARK1; ref. 24); and adenylyl cyclase (2′,5′-dideoxyadenosine or 2′,5′-dd-Ado[25]). We found that none of the treatments precluded current responses to extracellular LPA in on-cell recordings and that the responses were in fact indistinguishable from those elicited in untreated cells (**Supplementary Fig. 3e**), leading us to conclude that LPA receptor activation is not necessary for TRPV1 activation by LPA.

Because a recent study in an induced bone cancer model shows that LPA might regulate expression and activity of TRPV1 through a PKC-dependent pathway[10], we tested this possibility in our system. Incubation of TRPV1-transfected HEK293 cells with the PKC inhibitors Y27632 (ref. 22) and BIM I[26] had no effect on LPA activation of TRPV1 in on-cell experiments (**Supplementary Fig. 4a**). PKCε has been reported to be responsible for LPA-induced potentiation of TRPV1 by heat and capsaicin[10]. To assess whether this was a possibility, we performed experiments in which we transfected HEK293 cells with a plasmid containing either a dominant-negative form of PKCε[27] or the wild-type functional version of PKCε[27] together with TRPV1. Overexpression of either form of PKCε did not have an effect on acute activation of TRPV1 by LPA (**Supplementary Fig. 4b**,**c**).

To further establish the lack of a role for PKCε in our model, we used the specific inhibitor $εV_{1\text{-}2}$ (ref. 10) in whole-cell recordings of DRG neurons to determine whether blockage of this pathway precluded activation of TRPV1. All DRG neurons tested for TRPV1 activation by LPA responded irrespectively of the presence of the specific inhibitor $εV_{1\text{-}2}$ applied in the recording pipette, leading to the conclusion that PKCε is not necessary for acute LPA activation of TRPV1, contrary to what was previously suggested[10] (**Supplementary Fig. 4d**). Nonetheless, in accordance to the study mentioned above, we, too, observed a potentiating effect of LPA on capsaicin currents (**Supplementary Fig. 5a**).

So far, our data demonstrate that LPA promotes its effects on TRPV1 independently of LPA receptors, most likely through a direct interaction with the channel.

Interaction site for LPA in the C terminus of TRPV1

Some proteins known to interact with LPA share binding sites with other lipids such as PIP_2 (refs. 28,29). PIP_2 binds directly to TRPV1 and enables the channel's response to capsaicin without activating it[13]. Conversely, depletion of PIP_2 results in decreased channel activity induced by capsaicin[30,31] (**Supplementary Fig. 5b**).

To determine whether LPA could share a binding site with PIP_2, we performed a competition assay. Using an established approach[7,13], we constructed a dose-response curve for activation by LPA by first removing endogenous PIP_2 with the scavenger polylysine (polyK) and then applying different concentrations of LPA. Interestingly, removal of PIP_2 with polyK did not preclude TRPV1 activation by LPA (**Fig. 4a**), although polyK did scavenge LPA (**Supplementary Fig. 5c**,**d**). Moreover, the data in **Figure 4a** show that the dose-response curve for TRPV1 activation by LPA after treatment with polyK is shifted to the left, and the K_D of TRPV1 for LPA is lower than that measured in the presence of endogenous PIP_2 (71 nM versus 754 nM). We then repeated the experiment described above but

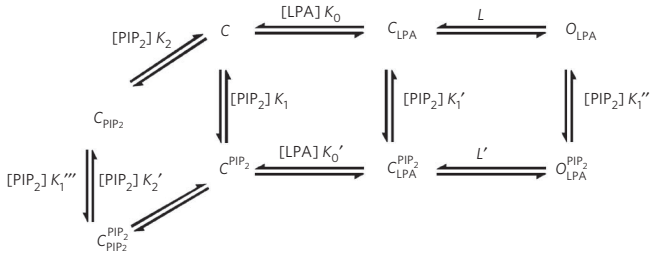

Scheme 1 Model for TRPV1 modulation by LPA and PIP_2. The model considers a shared PIP_2- and LPA-binding site for which both lipids compete and a second PIP_2 binding site from which PIP_2 modulates LPA binding and channel gating. At equilibrium, the relative current is given by

$$\frac{I}{I_{max}} = \frac{[LPA]K_0L(1+[PIP_2]K_1'')}{1+[LPA]K_0+[LPA][PIP_2]K_0'K_1'+[PIP_2](K_1+K_2)+[PIP_2]^2K_1K_2'+[LPA]K_0L(1+[PIP_2]K_1'')}$$

where [LPA] and [PIP_2] are the lipid's molar concentrations, K_0, K_0', K_1, K_1', K_1'', K_1''', K_2 and K_2' are association constants between the channel and LPA or PIP_2, and L and L' are equilibrium constants for channel gating. In the C_X^Y notation used here, C denotes closed states, O denotes open states, X denotes ligand occupancy of the shared LPA- and PIP_2-binding site and Y denotes ligand occupancy of the PIP_2-only site. This equation was used to fit the data in **Figure 4a** with following parameters: $K_0 = 2.3 \times 10^5\ M^{-1}$, $K_0' = 17.5 \times 10^6\ M^{-1}$, $K_1 = 4.2 \times 10^6\ M^{-1}$, $K_1' = 3.2 \times 10^8\ M^{-1}$, $K_1'' = 3.2 \times 10^4\ M^{-1}$, $K_1''' = 5.5 \times 10^8\ M^{-1}$, $K_2 = 1.7 \times 10^6\ M^{-1}$, $K_2' = 2.2 \times 10^8\ M^{-1}$, $L = 70$ and $L' = 7 \times 10^{-3}$.

applied LPA together with different concentrations of DiC8-PIP_2, a water-soluble form of PIP_2 (**Fig. 4a** and **Supplementary Fig. 5c**,**d**).

These data show that with increasing PIP_2 concentrations, the apparent affinity for LPA is diminished, as evidenced by a rightward shift in the dose responses for activation by LPA (**Fig. 4a**). However, the magnitude of the maximum response to LPA was also decreased in the presence of PIP_2.

In a simple competition, the LPA dose-response curves are expected to be shifted to the right upon increasing PIP_2 concentrations without a change in the maximum response (that is, there should be a concentration of LPA than can actually displace PIP_2 from the binding site). Our results can be explained by the allosteric effect of PIP_2 on the binding of LPA to TRPV1 together with the competition between PIP_2 and LPA for the same binding region (described further in Discussion; **Fig. 4a**, **Scheme 1**).

As LPA is a negatively charged molecule, we mutated sites proposed to interact with PIP_2 because these contain positively charged residues that could bind LPA. We first removed residues 777–821 in the C terminus, which contains several positively charged amino acids[32], and tested the effects of LPA. LPA activated this deletion mutant similarly to its activation of wild-type channels (**Fig. 4b**,**c**). We then mutated another positive residue in the C terminus, Lys710 (ref. 11). A charge-neutralization mutation (K710Q) produced a channel with a markedly decreased (nearly 50%) response to LPA (**Fig. 4**,**c**) that retained normal capsaicin activation (**Supplementary Fig. 6a**). We then explored the effects of the charge-reversal mutation K710D and found that it also behaved similarly to the wild type in its response to capsaicin (**Supplementary Fig. 6a**), but nearly 80% of the response of the channel to LPA (**Fig. 4b**,**c**) and to BrP-LPA (**Supplementary Fig. 6b**) was abolished. Moreover, when we applied LPA to the K710D mutant from the extracellular side, we found that a smaller fraction of current was activated compared to when extracellular LPA was applied to the wild-type channel. These data indicate that the intracellular Lys710 residue accounts for most of the effects of LPA on TRPV1 (**Fig. 4c**).

Finally, we took a biochemical approach to confirm a direct interaction between TRPV1 and LPA. Using membrane-protein extracts from HEK293 cells transfected with TRPV1, we performed pull-down experiments to test for LPA-TRPV1 interactions with agarose beads bound to LPA (LPA beads).

The LPA beads bound to the TRPV1 channel significantly ($P < 0.01$) more than control beads without the lipid (**Fig. 4d** and **Supplementary Fig. 7a**), as evidenced by the differences in signal intensity of the TRPV1 band (molecular mass of 85–90 kDa[33]), suggesting that TRPV1 physically interacts with LPA.

So far, these results constitute strong evidence for direct interaction of the channel with LPA. To further support this hypothesis, we decided to explore whether BrP-LPA, which seems to activate TRPV1 through the same mechanism as LPA, was able to diminish channel binding to the LPA beads by competing for the same site. As expected, preincubation of membrane-protein extracts with BrP-LPA reduced binding of TRPV1 to LPA beads and decreased the intensity of the TRPV1 signal on the immunoblot (**Fig. 4d** and **Supplementary Fig. 7a**).

Furthermore, we used this assay to test for competition of the LPA-beads with PIP_2 for binding to TRPV1. The data in **Figure 4d** show that PIP_2 can diminish the signal associated with LPA-bead binding to TRPV1, indicating that PIP_2 antagonizes LPA at the level of channel binding, probably in competition for a binding site.

Finally, we tested for a correlation between the lack of a functional response of the K710D mutant to LPA and the effects of this mutation on the binding of TRPV1 to the LPA beads. We found that this charge-reversal mutant bound to LPA beads very poorly (**Fig. 4e** and **Supplementary Fig. 7b**). A quantitative analysis of our pull-down assays is presented in **Figure 4f**. The data obtained strongly suggest that LPA binds to the TRPV1 channel and that the Lys710 site is important for LPA binding.

DISCUSSION

Many TRP channels play a pivotal role in the detection of environmental stimuli and pain perception. TRPV1 is implicated in several painful processes, and interactions of this channel with some exogenous pain-producing molecules have been demonstrated[8]. However, our knowledge of the molecular mechanisms of TRPV1 activation by substances released during injury or inflammation remains scarce. LPA has an important role in the development of neuropathic pain[34]. It has been suggested that during the development of neuropathic hyperalgesia, an upsurge in LPA production occurs, leading to myelinated Aδ fiber hypersensitivity that is partially due to upregulation of TRPV1 (ref. 35). Despite this clear proposition, to date, the role of TRPV1 in LPA-induced chronic pain had remained unclear and, in the case of acute pain, unaddressed.

Actions of LPA on ion channels in peripheral nociceptors have been classically circumscribed to the activation of receptor-mediated signaling pathways[21,36]. Our work constitutes the first study to show a direct and physiologically relevant interaction of an ion channel and LPA, and several lines of evidence presented here support this

idea: (i) BrP-LPA, an antagonist of LPA receptors structurally similar to LPA, activates TRPV1; (ii) inhibitors of the G protein–coupled receptor signaling pathways, which are coupled to LPA-receptor activation, do not preclude actions of LPA on TRPV1; (iii) blockers and dominant-negative forms of PKC and PKCε, previously linked to activation of TRPV1 by LPA, had no effects on both a heterologous expression system and the native DRG neurons; (iv) TRPV1 interacts directly with LPA, as shown by pull-down assays; and (v) mutation of a charged residue in the C terminus of TRPV1 considerably reduces the effects of LPA and BrP-LPA on the channel and eliminates interactions of the channel with LPA in pull-down assays.

A recent study shows that application of a LPA receptor antagonist attenuates thermal hyperalgesia in a rat model of bone cancer. On the basis of this observation, the authors propose a possible role for the regulation of TRPV1 activity by LPA receptor–mediated signaling pathways, specifically PKCε-dependent pathways[10]. However, we did not observe any role of PKCε for TRPV1 activation by LPA in our experiments. In that respect, the study mentioned above shows experiments performed in a model involving the induction of a cancerous process[10], which complicates interpretation of the results. For example, after only 9 days of introducing cancerous cells to the animal model, the authors were able to observe an increase in paw-withdrawal latency when animals were injected with an LPA_1-receptor antagonist[10]. Cancerous processes are accompanied by inflammatory responses, and bone cancers induce demyelination of sensory fibers, a phenomenon that leads to hyperalgesic responses[37]. Furthermore, most osteolytic tumors cause extracellular acidification[38], which may potentiate TRPV1 activity independently of LPA. The hyperalgesic responses observed in ref. 10 could also be due to the already-demonstrated overexpression of TRPV1 in some cancerous processes[10,39] and the potentiated response of the channel to inflammatory mediators known to modulate its activity through the activation of PKC-dependent pathways[8]. We were able to reproduce the potentiating effect of LPA on the TRPV1 capsaicin response reported in ref. 10, but we conclude that this is just an additive effect of two agonists binding to different regions in the channel.

Other studies in which LPA was delivered intraplantarly to mice show that LPA-induced pain responses can be blocked either by injection of LPA together with PTX or by inhibition of LPA_1 expression[40], suggesting that acute peripheral nociceptor responses to LPA depend on the $G_{i/o}$-coupled LPA_1 receptor. These data seem to exclude a major role for direct activation of TRPV1 by LPA in nocifensive behavior generation.

However, different lines of evidence from our experiments point to the contrary. First, our findings show that TRPV1, which is expressed in peripheral nociceptors, is robustly and directly activated by LPA and BrP-LPA, an inhibitor of LPA_1. Second, BrP-LPA produced similar responses to LPA in our behavioral assays and triggered action-potential firing in cultured DRG neurons, indicating that LPA_1 is not essential for the generation of acute pain responses triggered by LPA. Furthermore, the experimental recordings in ref. 40 were performed after prolonged nociceptor stimulation, which favors TRPV1 channel desensitization. The resulting decrease in TRPV1 channel responsiveness to agonists could have obscured its role in the acute response to LPA.

Moreover, the authors in ref. 40 measured pain responses after LPA and PTX were injected together into the paws of mice and showed that, after only 20 min, PTX was able to produce a decrease in the pain response. The pain-related behavior up to 10 min was the same as the control response obtained in the presence of only LPA, consistent with our observations that LPA causes acute pain partly through TRPV1. Responses at longer LPA exposures could indeed stem from other molecular entities such as LPA_1. It is certain that it is not only a single effector that controls the responses to LPA and other painful stimuli. Our own data show that there are residual responses in the behavioral assay in the TRPV1-null mice after LPA and BrP-LPA injection (**Fig. 1c** and **Supplementary Fig. 2**) that could be due to other molecules affected by the activation of the signaling pathways resulting from LPA-receptor activation, such as LPA_1 or LPA_5.

With regard to the nature of the interaction between channel and lipid, we established that one of the proposed PIP_2 binding sites in the TRPV1 channel, the residue Lys710 (ref. 11), in fact mediates binding of LPA. This interaction possibly occurs partly through an electrostatic mechanism, as a charge neutralization of this site is not as effective as a charge reversal in precluding LPA activation of TRPV1, and probably also through hydrophobic interactions with the acyl chain of LPA.

Lys710 is located in the region that constitutes the TRP-like domain and is also a tetramerization domain for the protein, and deletions in this region hinder the formation of stable multimers[41]. From our experiments with the K710D mutant, we observed that nearly 80% (but not all) of the response to LPA is abolished. It is possible that other residues also participate in the stabilization of LPA binding to TRPV1. To determine this, we mutated other charged residues in this region, including the nearby Arg701 residue as well as Lys694, Lys698, Lys714 and Arg718. However, none of these mutations produced functional channels. The deletion of a stretch of residues in the distal C terminus, previously reported as important for interactions of TRPV1 with PIP_2 (ref. 32), also had no effect on LPA activation of TRPV1.

Regarding the effects of PIP_2 on the channel's response to LPA, we found that PIP_2 reduces the apparent affinity of the channel for LPA. This is observed as a reduction in both the affinity for LPA obtained from the dose-response curves and the channel binding to LPA beads when PIP_2 is present. Moreover, the presence of PIP_2 also reduces the channel's maximum response to LPA. The effects on apparent affinity could be due to overlapping binding sites for LPA and PIP_2. However, the reduction in the maximal response indicates that a complex allosteric interplay between LPA and PIP_2 might be taking place. Allosteric modulation of the effects of LPA by PIP_2 is not surprising because PIP_2 allosterically modulates the activation of TRPV1 by capsaicin through binding to several sites throughout the channel. In accordance with this interpretation, we produced a model that considers the competition between LPA and PIP_2 for a site in the channel and the allosteric modulation of LPA binding and channel activation through a second PIP_2 binding site (**Fig. 4a** and **Scheme 1**) and found that it satisfactorily accounts for our data.

How does LPA reach its intracellular binding site under physiological conditions? Intracellular LPA is produced mainly as a precursor of membrane phospholipids in the endoplasmic reticulum and mitochondria. The role for the intracellular LPA pool in cell signaling is not clear. Moreover, its effects on intracellular protein receptors such as PPARγ have been ascribed to the extracellular LPA pool, which finds its way into the cell[42]. Although LPA is present in serum at elevated concentrations, the large protein-bound fraction thereof reduces its effective concentration and its potency to activate some of its receptors[43]. Nonetheless, autotaxin associates with integrins[44] in the plasma membrane and contains a hydrophobic channel connected with the active site, which has a flat entrance that could interact with the membrane. On the basis of these findings, it has been proposed that the enzyme could locally deliver LPA, which could elevate the local concentration of the lipid above the maximal reported values for serum LPA[45,46]. Although the flip-flop rate of LPA is unknown, activation of the nuclear PPARγ receptor by extracellular LPA has been shown to be physiologically relevant, suggesting that efficient mechanisms of transbilayer movement of LPA exist. The apparent lack of a delay in channel activation by extracellular LPA in our experiments also indicates that the rate of transbilayer movement of LPA is comparable to the rate of channel activation. Also, these mechanisms for extracellular delivery of LPA do not preclude the possible role of intracellularly synthesized LPA in TRPV1 activation.

In this study we provide strong evidence that TRPV1 is directly activated by LPA, a mechanism that further broadens our understanding of how bioactive lipids act on nociceptors to produce and maintain pain. Our results also suggest a broader role of LPA in acute pain responses such as angina pectoris (the atherosclerotic plaque that produces ischemia contains high concentrations of LPA[47]), bites from animals whose venoms contain enzymes that convert lysophosphatidylcholine to LPA (such as those of the brown recluse or violin spider, *Loxosceles reclusa*[48]) or snake venoms that contain phospholipase A_2 (ref. 49), which also catalyzes the formation of LPA.

METHODS

Mice strains and genotyping. C57BL/6J and *Trpv1*$^{-/-}$ mice were obtained from The Jackson Laboratory (Bar Harbor, Maine). Animals with neural inactivation of *Ppap2b* (*Ppap2b*$^{tm3Stw/tm3Stw}$; Nes-cre mouse line), named here for simplicity *Lpp3*$^{-/-}$, were obtained from our animal facility[14]. *Lpp3*$^{-/-}$ and *Trpv1*$^{-/-}$ animals were mated to obtain double-mutant mice. The C57BL/6J mice were used as controls for the behavioral experiments on *Trpv1*$^{-/-}$ mice, and *Ppap2b*$^{tm3Stw/tm3Stw}$ littermates were used as controls for *Lpp3*$^{-/-}$ and *Trpv1*$^{-/-}$ as well as *Lpp3*$^{-/-}$ mouse experiments. For PCR genotyping of complete *Ppap2b* Cre-mediated recombination as well as *Trpv1*$^{-/-}$ and Cre genotyping, we followed previously described methods[14,15].

Pain-related behavioral assays. 10 µl of either saline solution (0.9% w/v of NaCl) or capsaicin (2.8 µg), LPA (4.1 µg), BrP-LPA (3 µg) or capsazepine (2.2 µg) diluted in saline was injected intraplantarly using a 30-gauge needle, and paw-licking behavior was quantified for 10 min immediately after injection. Animals were handled according to institutional standards from the US National Institutes of Health (NIH). Thermal hyperalgesia was assessed by measuring paw withdrawal latency to radiant heat (University of California San Diego Thermal Paw stimulator) as previously described[15]. A current of 5.5 A was applied to each of the hind paws, and the mean of the withdrawal latencies was defined as paw-withdrawal latency.

Mutagenesis. Point mutations and deletions in the rTRPV1 channel were constructed by a two-step PCR method as previously described[50].

DRG and HEK293 cell culture and recording. DRG neurons were obtained following previously described procedures[12]. HEK293 cells were transfected with wild-type and mutant pcDNA3-rTRPV1, pIRES-GFP (BD Biosciences) and with FLAG.PKCepsilon (Addgene plasmid 10795) or FLAG.PKCepsilon.K/W (Addgene plasmid 10796) with JetPei (Polyplus Transfection). Currents were recorded using the inside-out, outside-out and on-cell configurations of the patch-clamp technique[44]. Solutions were changed with a RSC-200 rapid solution changer (Molecular Kinetics). The solution for both inside-out and on-cell recording under isometric conditions comprised 130 mM NaCl, 3 mM HEPES (pH 7.2) and 1 mM EDTA. Capsazepine and capsaicin were diluted in DMSO and ethanol, respectively. Experiments were performed at 24 °C. Mean current values for LPA were measured after channel activation had reached the steady state (~5 min). Currents were obtained using voltage protocols with a holding potential of 0 mV. Steps from −120 to 120 mV were applied for 100 ms, and then the voltage was returned to 0 mV. Currents were low-pass filtered at 2 kHz, sampled at 10 kHz with an EPC 10 amplifier (HEKA Elektronik), and plotted and analyzed with Igor Pro (Wavemetrics Inc.).

Whole-cell currents from DRG neurons were recorded following previously described methods[10]. Action potentials were recorded in the whole-cell configuration from acutely dissociated DRG neurons from wild-type or *Trpv1*$^{-/-}$ mice following methods previously described[44]. The membrane potential was recorded continuously, and LPA or allicin were applied directly to the bath solution.

LPA binding assay. Plasma membrane proteins from HEK293 cells transfected with wild-type TRPV1 or the K710D mutation were biotinylated and extracted using the Pierce cell-surface protein isolation kit according to manufacturer instructions with minor modifications (elution of proteins was performed with non-ionic detergents). Total membrane-protein extracts were incubated with LPA or control beads (Echelon Biosciences) for 3 h at 4 °C and were washed five times with binding buffer containing 0.5% Igepal (Sigma). To ensure equal protein input between conditions, proteins in equivalent volumes of the first supernatant (50 µl) were separated by SDS-PAGE and analyzed by Coomasie blue staining of the gel.

For competition assays, protein extracts were incubated with 10 µM BrP-LPA or DiC8-PIP_2 prior to the addition of LPA or control beads. Pulled-down protein from each sample was eluted from the beads by adding an equal volume of 2× Laemmli sample buffer to beads and heating to 95 °C for 5 min. Eluted proteins were separated by SDS-PAGE and analyzed by immunoblotting using a TRPV1-specific antibody (Alomone Labs). For each experiment, a small sample of the total membrane-protein extract was loaded into the gel as a positive control of TRPV1 protein expression (lane 1 in **Fig. 4d,e**). Immunoblots were developed by enhanced chemiluminesence, and densitometric analysis was done using ImageJ software (NIH) and expressed as relative amounts of protein versus the amount of TRPV1 bound to LPA beads.

Lipids and polylysine. LPA (Avant Polar Lipids or Sigma) and BrP-LPA (Echelon) dilutions were freshly prepared every day and sonicated in a cold bath. Stock solutions of LPA (10 mM) were prepared in DMEM with 1% fatty acid–free BSA (Roche), and BrP-LPA was prepared in water. Stock solutions were sonicated and frozen before use. DiC8-PIP_2 (Echelon Biosciences) was solubilized in recording solution and frozen at −20 °C. Phosphatidic acid and diacylcglycerol (both from Avanti Polar Lipids) were diluted in chloroform, glycerol phosphate in water, sphingosine-1-phosphate in DMEM, oleic acid in ethanol and ceramide-1-phosphate (Avanti Polar Lipids) and lysophosphatidylcholine in chloroform:methanol (1:1), and a final concentration of 5 µM was obtained by diluting in recording solution. FPP (Echelon Biosciences) was used at a concentration of 1.5 µM.

Experiments to determine the effects of PIP_2 on TRPV1 activation by LPA were performed following previously established methods[13]. Briefly, we applied polyK (15 µg ml^{-1}) to inside-out membrane patches and then measured the response to different concentrations of LPA in the absence and presence of different concentrations of PIP_2 to construct a dose-response curve. Data were normalized to the maximal current obtained in the presence of 5 µM LPA without PIP_2.

Statistical analysis. Statistical comparisons were made with a one-way ANOVA test. $P < 0.05$ was considered statistically significant. Group data are reported as the mean ± s.e.m. Additional experimental procedures can be found in **Supplementary Methods**.

Received 4 April 2011; accepted 29 August 2011;
published online 20 November 2011; corrected online 15 June 2012

References

1. Inoue, M. *et al.* Initiation of neuropathic pain requires lysophosphatidic acid receptor signaling. *Nat. Med.* **10**, 712–718 (2004).
2. Okudaira, S., Yukiura, H. & Aoki, J. Biological roles of lysophosphatidic acid signaling through its production by autotaxin. *Biochimie* **92**, 698–706 (2010).
3. Lin, M.E., Herr, D.R. & Chun, J. Lysophosphatidic acid (LPA) receptors: signaling properties and disease relevance. *Prostaglandins Other Lipid Mediat.* **91**, 130–138 (2010).
4. Ma, L., Nagai, J. & Ueda, H. Microglial activation mediates de novo lysophosphatidic acid production in a model of neuropathic pain. *J. Neurochem.* **115**, 643–653 (2010).
5. Chun, J., Hla, T., Lynch, K.R., Spiegel, S. & Moolenaar, W.H. International Union of Basic and Clinical Pharmacology. LXXVIII. Lysophospholipid receptor nomenclature. *Pharmacol. Rev.* **62**, 579–587 (2010).
6. Roedding, A.S., Li, P.P. & Warsh, J.J. Characterization of the transient receptor potential channels mediating lysophosphatidic acid-stimulated calcium mobilization in B lymphoblasts. *Life Sci.* **80**, 89–97 (2006).
7. Runnels, L.W., Yue, L. & Clapham, D.E. The TRPM7 channel is inactivated by PIP(2) hydrolysis. *Nat. Cell Biol.* **4**, 329–336 (2002).
8. Jara-Oseguera, A., Simon, S.A. & Rosenbaum, T. TRPV1: on the road to pain relief. *Curr. Mol. Pharmacol.* **1**, 255–269 (2008).
9. Yao, J., Liu, B. & Qin, F. Modular thermal sensors in temperature-gated transient receptor potential (TRP) channels. *Proc. Natl. Acad. Sci. USA* **108**, 11109–11114 (2011).
10. Pan, H.L., Zhang, Y.Q. & Zhao, Z.Q. Involvement of lysophosphatidic acid in bone cancer pain by potentiation of TRPV1 via PKCε pathway in dorsal root ganglion neurons. *Mol. Pain* **6**, 85 (2010).
11. Brauchi, S. *et al.* Dissection of the components for PIP2 activation and thermosensation in TRP channels. *Proc. Natl. Acad. Sci. USA* **104**, 10246–10251 (2007).
12. Stein, A.T., Ufret-Vincenty, C.A., Hua, L., Santana, L.F. & Gordon, S.E. Phosphoinositide 3-kinase binds to TRPV1 and mediates NGF-stimulated TRPV1 trafficking to the plasma membrane. *J. Gen. Physiol.* **128**, 509–522 (2006).
13. Ufret-Vincenty, C.A., Klein, R.M., Hua, L., Angueyra, J. & Gordon, S.E. Localization of the PIP2 sensor of TRPV1 ion channels. *J. Biol. Chem.* **286**, 9688–9698 (2011).
14. Escalante-Alcalde, D., Sanchez-Sanchez, R. & Stewart, C.L. Generation of a conditional Ppap2b/Lpp3 null allele. *Genesis* **45**, 465–469 (2007).
15. Caterina, M.J. *et al.* Impaired nociception and pain sensation in mice lacking the capsaicin receptor. *Science* **288**, 306–313 (2000).
16. Jiang, G. *et al.* α-substituted phosphonate analogues of lysophosphatidic acid (LPA) selectively inhibit production and action of LPA. *ChemMedChem* **2**, 679–690 (2007).
17. Oh, D.Y. *et al.* Identification of farnesyl pyrophosphate and N-arachidonylglycine as endogenous ligands for GPR92. *J. Biol. Chem.* **283**, 21054–21064 (2008).
18. Alderton, F., Sambi, B., Tate, R., Pyne, N.J. & Pyne, S. Assessment of agonism at G-protein coupled receptors by phosphatidic acid and lysophosphatidic acid in human embryonic kidney 293 cells. *Br. J. Pharmacol.* **134**, 6–9 (2001).
19. Zhang, H. *et al.* Dual activity lysophosphatidic acid receptor pan-antagonist/autotaxin inhibitor reduces breast cancer cell migration in vitro and causes tumor regression in vivo. *Cancer Res.* **69**, 5441–5449 (2009).

20. Bang, S., Yoo, S., Yang, T.J., Cho, H. & Hwang, S.W. Farnesyl pyrophosphate is a novel pain-producing molecule via specific activation of TRPV3. *J. Biol. Chem.* **285**, 19362–19371 (2010).
21. Cohen, A., Sagron, R., Somech, E., Segal-Hayoun, Y. & Zilberberg, N. Pain-associated signals, acidosis and lysophosphatidic acid, modulate the neuronal K(2P)2.1 channel. *Mol. Cell. Neurosci.* **40**, 382–389 (2009).
22. Uehata, M. *et al.* Calcium sensitization of smooth muscle mediated by a Rho-associated protein kinase in hypertension. *Nature* **389**, 990–994 (1997).
23. Bourinet, E., Soong, T.W., Stea, A. & Snutch, T.P. Determinants of the G protein-dependent opioid modulation of neuronal calcium channels. *Proc. Natl. Acad. Sci. USA* **93**, 1486–1491 (1996).
24. Koch, W.J., Hawes, B.E., Inglese, J., Luttrell, L.M. & Lefkowitz, R.J. Cellular expression of the carboxyl terminus of a G protein-coupled receptor kinase attenuates Gβγ-mediated signaling. *J. Biol. Chem.* **269**, 6193–6197 (1994).
25. Chaytor, A.T., Edwards, D.H., Bakker, L.M. & Griffith, T.M. Distinct hyperpolarizing and relaxant roles for gap junctions and endothelium-derived H_2O_2 in NO-independent relaxations of rabbit arteries. *Proc. Natl. Acad. Sci. USA* **100**, 15212–15217 (2003).
26. Tang, L. *et al.* Antinociceptive pharmacology of *N*-(4-chlorobenzyl)-*N*′-(4-hydroxy-3-iodo-5-methoxybenzyl) thiourea, a high-affinity competitive antagonist of the transient receptor potential vanilloid 1 receptor. *J. Pharmacol. Exp. Ther.* **321**, 791–798 (2007).
27. Cenni, V. *et al.* Regulation of novel protein kinase C ε by phosphorylation. *Biochem. J.* **363**, 537–545 (2002).
28. Mintzer, E., Sargsyan, H. & Bittman, R. Lysophosphatidic acid and lipopolysaccharide bind to the PIP2-binding domain of gelsolin. *Biochim. Biophys. Acta* **1758**, 85–89 (2006).
29. Kumar, N., Zhao, P., Tomar, A., Galea, C.A. & Khurana, S. Association of villin with phosphatidylinositol 4,5-bisphosphate regulates the actin cytoskeleton. *J. Biol. Chem.* **279**, 3096–3110 (2004).
30. Klein, R.M., Ufret-Vincenty, C., Hua, L. & Gordon, S. Determinants of molecular specificity in phosphoinositide regulation. *J. Biol. Chem.* **283**, 26208–26216 (2008).
31. Yao, J. & Qin, F. Interaction with phosphoinositides confers adaptation onto the TRPV1 pain receptor. *PLoS Biol.* **7**, e46 (2009).
32. Prescott, E.D. & Julius, D. A modular PIP2 binding site as a determinant of capsaicin receptor sensitivity. *Science* **300**, 1284–1288 (2003).
33. Tominaga, M. *et al.* The cloned capsaicin receptor integrates multiple pain-producing stimuli. *Neuron* **21**, 531–543 (1998).
34. Inoue, M. *et al.* Lysophosphatidylcholine induces neuropathic pain through an action of autotaxin to generate lysophosphatidic acid. *Neuroscience* **152**, 296–298 (2008).
35. Ueda, H. Peripheral mechanisms of neuropathic pain—involvement of lysophosphatidic acid receptor-mediated demyelination. *Mol. Pain* **4**, 11 (2008).
36. Chemin, J. *et al.* Lysophosphatidic acid-operated K^+ channels. *J. Biol. Chem.* **280**, 4415–4421 (2005).
37. Kelly, J.J. Jr., Kyle, R.A., Miles, J.M. & Dyck, P.J. Osteosclerotic myeloma and peripheral neuropathy. *Neurology* **33**, 202–210 (1983).
38. Schwei, M.J. *et al.* Neurochemical and cellular reorganization of the spinal cord in a murine model of bone cancer pain. *J. Neurosci.* **19**, 10886–10897 (1999).
39. Marincsák, R. *et al.* Increased expression of TRPV1 in squamous cell carcinoma of the human tongue. *Oral Dis.* **15**, 328–335 (2009).
40. Renbäck, K., Inoue, M., Yoshida, A., Nyberg, F. & Ueda, H. Vzg-1/lysophosphatidic acid-receptor involved in peripheral pain transmission. *Brain Res. Mol. Brain Res.* **75**, 350–354 (2000).
41. García-Sanz, N. *et al.* A role of the transient receptor potential domain of vanilloid receptor I in channel gating. *J. Neurosci.* **27**, 11641–11650 (2007).
42. McIntyre, T.M. *et al.* Identification of an intracellular receptor for lysophosphatidic acid (LPA): LPA is a transcellular PPARγ agonist. *Proc. Natl. Acad. Sci. USA* **100**, 131–136 (2003).
43. Hama, K., Bandoh, K., Kakehi, Y., Aoki, J. & Arai, H. Lysophosphatidic acid (LPA) receptors are activated differentially by biological fluids: possible role of LPA-binding proteins in activation of LPA receptors. *FEBS Lett.* **523**, 187–192 (2002).
44. Salazar, H. *et al.* A single N-terminal cysteine in TRPV1 determines activation by pungent compounds from onion and garlic. *Nat. Neurosci.* **11**, 255–261 (2008).
45. Nishimasu, H. *et al.* Crystal structure of autotaxin and insight into GPCR activation by lipid mediators. *Nat. Struct. Mol. Biol.* **18**, 205–212 (2011).
46. Hausmann, J. *et al.* Structural basis of substrate discrimination and integrin binding by autotaxin. *Nat. Struct. Mol. Biol.* **18**, 198–204 (2011).
47. Karliner, J.S. Lysophospholipids and the cardiovascular system. *Biochim. Biophys. Acta* **1582**, 216–221 (2002).
48. Sams, H.H., Dunnick, C.A., Smith, M.L. & King, L.E. Jr. Necrotic arachnidism. *J. Am. Acad. Dermatol.* **44**, 561–573 (2001).
49. Caccin, P., Rigoni, M., Bisceglie, A., Rossetto, O. & Montecucco, C. Reversible skeletal neuromuscular paralysis induced by different lysophospholipids. *FEBS Lett.* **580**, 6317–6321 (2006).
50. Rosenbaum, T. & Gordon, S.E. Dissecting intersubunit contacts in cyclic nucleotide-gated ion channels. *Neuron* **33**, 703–713 (2002).

Acknowledgments

We thank D. Julius at University of California, San Francisco for providing the TRPV1 and TRPV2 cDNA, A. Patapoutian at the Scripps Research Institute for the TRPA1 cDNA, A. Toker at Harvard Medical School for PKCε dominant-negative and wild-type plasmids, J.A. García-Sáinz for his kind gift of BIM I and M. Calcagno for helpful discussion. We also thank L. Ongay, A. Escalante and F. Pérez at Instituto de Fisiología Celular, Universidad Nacional Autónoma de México (UNAM) for expert technical support and F. Sierra for expert help with DRG neuron culture. We are grateful to C.C. Durán and V.G. Soto for very valuable help with paw-withdrawal experiments. This work was supported by Dirección General de Asuntos del Personal Académico–Programa de Apoyo a Proyectos de Investigación e Innovación Tecnológica (DGAPA-PAPIIT) grant IN209209 and Instituto de Ciencia y Tecnología del Distrito Federal (ICYT-DF) grant PIFUTP09-262 to L.D.I., PAPIIT grants IN216009 and CONACyT 53777 to D.E.-A., and PAPIIT grants IN294111-3 and CONACyT CB-129474 and a grant from Fundación Miguel Alemán to T.R. This study was performed in partial fulfillment of the requirements for A.N.-P.'s doctoral degree in biomedical sciences at the UNAM.

Author contributions

A.N.-P., G.P.-J. and A.J.-O. performed electrophysiological experiments. I.L. carried out all site-directed mutagenesis. S.M.-L. performed all animal matings, genotyping and biochemical assays. D.E.-A., L.D.I. and T.R. jointly conceived the study, performed recordings and analysis, and wrote the paper.

Competing financial interests

The authors declare no competing financial interests.

Additional information

Supplementary information is available online at http://www.nature.com/naturechemicalbiology/. Reprints and permissions information is available online at http://www.nature.com/reprints/index.html. Correspondence and requests for materials should be addressed to T.R., D.E.-A. or L.D.I.

CORRIGENDUM

Lysophosphatidic acid directly activates TPRV1 through a C-terminal binding site

Andrés Nieto-Posadas, Giovanni Picazo-Juárez, Itzel Llorente, Andrés Jara-Oseguera, Sara Morales-Lázaro, Diana Escalante-Alcalde, León D Islas & Tamara Rosenbaum

Nat. Chem. Biol. **8**, 78–85 (2012); published online 20 November 2011; corrected after print 15 June 2012

In the version of this article initially published, the amount of LPA used in behavioral assays was incorrectly stated in the Methods section as 3 μg when it should have read 4.1 μg. Also, the details of preparation of LPA stock solutions were incomplete in the Methods section. The errors have been corrected in the HTML and PDF versions of the article.